EPFL

Thèse n° 10 266

Testing lepton flavour universality in $B^+ \to K^+ \pi^+ \pi^- \ell^+ \ell^-$ decays with LHCb

Présentée le 23 juin 2023

Faculté des sciences de base
Laboratoire de physique des hautes énergies LS
Programme doctoral en physique

pour l'obtention du grade de Docteur ès Sciences

par

Sara CELANI

Acceptée sur proposition du jury

Prof. L. Villard, président du jury
Prof. L. Shchutska, directrice de thèse
Prof. P. Álvarez Cartelle, rapporteuse
Prof. C. Parkes, rapporteur
Prof. A. de Cosa, rapporteuse

École polytechnique fédérale de Lausanne

2023

A mio padre

Un giorno credi di esser giusto
e di essere un grande uomo,
in un altro ti svegli e devi
cominciare da zero

Acknowledgements

These four years have been an amazing journey, full of emotions and challenges, which definitely contributed to make me the person I am today.

This journey would not even have started without my PhD supervisor, Prof. Lesya Shchutska, who chose me and accompanied me through all this period. Thank you for being always supportive and available for advices, and also for always asking me the most difficult (and of course rightful) questions.

Thank you also to the other professors at the LPHE: Prof. Nakada, Prof. Bay, Prof. Blanc, Prof. Schneider, Prof. Marchevski, for the atmosphere that all of you managed to create among us, it has been an honor for me being part of this group.

Thank you to the wonderful Esther and Corinne. Without you, we would all be completely lost! Thank you for being so great at your work, and for always being gentle and nice.

Elena guided me during my first steps as a scientist, and I will always be grateful for that. Thank you also for having pushed me towards things even I thought I was not good enough for.

I had the opportunity to meet so many incredibly people during the PhD times, among which there is Prof. Rafael Silva Coutinho. I want to thank you, Rafa, for all the physics discussions, for staying positive and for being there for me, for trusting me and making me more and more independent. You definitely made me the physicist I am today.

I can not thank enough all my incredible colleagues at the LPHE, so many friends that made my journey much lighter and enjoyable. Thank you all for the conversations, for the beers after work, for the barbecues and the swimming in the lake. I will miss all of this deeply. Among all I would like to thank Carina, for having shared with me all the good and the bad days. You really were my travelling companion. I also thank you Serhii: we started, and finished, together, and I could have not wished for a better office mate (and friend).

I want also to thank my volleyball teammates. It was amazing to start playing again among such incredible players and scientists! Thank you especially to Marzia, Alessandro, Giulia and Gaia, with you, it really felt like being part of a family.

Now I want to move the people who supported me since a lifetime: Alessia and Ludovica. I know that while everything else can change, you will always be there, by my side, even while living so far away, even in the most difficult times. I don't have words anymore to explain how grateful I am for having you in my life.

Thank you also to Eleonora. We have been together from the first year of physics classes till the end of our PhDs. Who would have told that? (definitely not us!). Thank you because every time we meet, it always feels as if we had just seen each other.

Thank you to Andrea, because you really are the person who pushed me through the most difficult times. Thank you for every time you got angry (and probably you will still get) because I didn't believe enough in myself. Thank you because your calm is the most effective antidote to all of my anxieties.

Finally, my family. Thank you to Marta and Matteo, you have always been the sister and the brother I didn't have. Grazie a nonna Maria, zia Cristina e zio Gigino. Mi sento incredibilmente fortunata ad avere una famiglia così, vi voglio un mondo di bene.

Grazie alla persona piú forte che conosco, mia madre. Grazie mamma per avermi sempre insegnato a lavorare duro, per aver sempre creduto in me, per avermi sempre spinto a inseguire i miei sogni, tutto questo non sarebbe stato possibile senza di te.

Lausanne, June 9, 2023 Sara Celani

Abstract

This PhD thesis aims at testing one of the fundamental properties of the Standard Model (SM) of particle physics: the lepton flavour universality (LFU), which states that W and Z bosons are equally coupled to the three lepton generations. In this work, processes mediated by flavour-changing neutral currents, proceeding through a $b \to s\ell\ell$ quark-level transition, are studied with great precision, probing possible deviations from LFU. Such decay modes are forbidden at tree level in the SM, and can only happen through electroweak loop or box diagrams. Hence, due to their very small SM amplitudes, these processes are sensitive to New Physics contributions that could modify their characteristics.

The measurement presented in this thesis is a LFU test performed in a previously unexplored B^+ decay mode, by measuring the ratio $R_{K\pi\pi}$ between the branching fractions of $B^+ \to K^+\pi^+\pi^-\mu^+\mu^-$ and $B^+ \to K^+\pi^+\pi^-e^+e^-$ decays, using data collected by the LHCb detector. The hadronic system of this decay is very rich in resonances, making these processes of particular interest to help shedding light on the spin structure of hypothetical new particles, that would explain the anomalies previously observed by the LHCb collaboration in decays mediated by the same $b \to s\ell\ell$ transition. In addition, the measurement will provide the first observation of the $B^+ \to K^+\pi^+\pi^-e^+e^-$ decay.

The LHCb experiment has undergone a major upgrade between 2018 and 2022, aimed at making full use of the increased LHC luminosity. This thesis reports in particular on the new scintillating-fibre tracker, built at EPFL and other institutes, and its commissioning.

Keywords: particle physics, LHCb, LHC, rare decays, lepton flavours, flavour changing neutral currents, flavour anomalies, SciFi tracker, scintillating fibres.

Résumé

Cette thèse de doctorat vise à tester l'une des propriétés fondamentales du Modèle Standard (SM) de la physique des particules : l'universalité de la saveur leptonique (LFU), qui stipule que les bosons W et Z sont couplés de manière égale aux trois générations de leptons. Dans ce travail, les processus médiées par des courants neutres changeant de saveur, passant par une transition $b \to s\ell\ell$ au niveau de quarks, sont étudiés avec une grande précision, en sondant éventuelles déviations par rapport à l'LFU. Tels modes de désintégration sont interdits au *tree-level* dans le SM, et ne peuvent se produire qu'à travers des boucles électrofaibles ou des boîtes. Par conséquent, en raison de leurs très petites amplitudes, ces processus sont sensibles aux contributions de Nouvelle Physique qui pourraient modifier leurs caractéristiques.
La mesure présentée dans cette thèse est un test de LFU réalisé dans un mode de désintégration de B^+ jusqu'alors inexploré, en mesurant le rapport $R_{K\pi\pi}$ entre les fractions des désintégrations de $B^+ \to K^+\pi^+\pi^-\mu^+\mu^-$ et $B^+ \to K^+\pi^+\pi^-e^+e^-$, en utilisant les données collectées par le détecteur LHCb. Le système hadronique de cette désintégration est très riche en résonances, ce qui rend ces processus particulièrement intéressants pour aider à éclairer la structure de spin de nouvelles particules hypothétiques, qui expliqueraient les anomalies précédemment observées par la collaboration LHCb dans les désintégrations médiées par la même transition $b \to s\ell\ell$. En outre, la mesure fournira la première observation de la désintégration $B^+ \to K^+\pi^+\pi^-e^+e^-$.
Le détecteur LHCb a fait l'objet d'une mise à jour majeure entre le 2018 et le 2022, visant à exploiter pleinement la luminosité accrue du LHC. Cette thèse présente notamment sur le nouveau trajectographe à fibres scintillantes, construit à l'EPFL et dans d'autres instituts, et sur sa mise en service.

Mots-clés : physique des particules, LHCb, LHC, désintégrations rares, saveur leptonique, courants neutres changeant de saveur, anomalies de saveur, SciFi trajectographe, fibres scintillantes.

Contents

Acknowledgements **i**

Abstract (English/Français) **iii**

Introduction **1**

1 The Standard Model **3**
1.1 A general overview . . . 3
1.2 Formalism . . . 5
1.2.1 Quantum Electrodynamics . . . 6
1.2.2 Quantum Chromodynamics . . . 7
1.2.3 Electroweak Unification . . . 8
1.2.4 Breaking the symmetry: the Higgs mechanism . . . 10

2 Beyond the Standard Model **13**
2.1 $b \to s\ell\ell$ decays: Probes for New Physics . . . 14
2.2 An experimental overview . . . 16
2.2.1 Branching fraction of $b \to s\mu\mu$ decays . . . 16
2.2.2 Angular observables . . . 18
2.2.3 Lepton flavour universality tests . . . 19
2.2.4 Global fits . . . 20

3 The LHCb detector **23**
3.1 The Large Hadron Collider . . . 23
3.2 The LHCb detector in Runs 1 and 2 . . . 25
3.2.1 The tracking system . . . 27
3.2.2 Particle Identification . . . 31
3.2.3 The Trigger System . . . 37
3.3 The LHCb detector upgrade . . . 38
3.3.1 The tracking system upgrade . . . 39
3.3.2 The Scintillating fibre Tracker . . . 41
3.3.3 SciFi control and monitoring . . . 47

4 The $R_{K\pi\pi}$ measurement **53**
4.1 Introduction . . . 53

4.2 Analysis strategy . . . 55
4.2.1 Events Simulation . . . 57
4.2.2 Dilepton invariant mass regions . . . 57
4.3 Selection . . . 61
4.3.1 Stripping . . . 61
4.3.2 Trigger . . . 62
4.3.3 Preselection . . . 65
4.3.4 Background studies . . . 66
4.3.5 Multivariate Selection . . . 84
4.4 Corrections to the simulation . . . 88
4.4.1 Statistical background subtraction . . . 91
4.4.2 Particle Identification response . . . 94
4.4.3 $K^+\pi^+\pi^-$ resonance structure . . . 95
4.4.4 Electron tracking efficiency . . . 98
4.4.5 B^+ kinematics and multiplicity . . . 98
4.4.6 Trigger efficiencies . . . 101
4.4.7 Residual reconstruction effects . . . 107
4.4.8 Smearing of the $J/\psi \to e^+e^-$ mass . . . 107
4.5 Calculation of the event selection efficiency . . . 112
4.5.1 Geometrical acceptance . . . 112
4.5.2 Reconstruction and stripping efficiency . . . 114
4.5.3 Selection efficiency . . . 114
4.6 Mass modelling and fit strategy . . . 117
4.6.1 Fit of the resonant decay modes . . . 118
4.6.2 Fit of the rare decay modes . . . 123
4.6.3 Fit stability . . . 132
4.7 Cross-checks . . . 134
4.7.1 $r_{J/\psi}$ . . . 134
4.7.2 $r_{\psi(2S)}$ and $R_{\psi(2S)}$ . . . 137
4.8 Systematic uncertainties . . . 140
4.8.1 Systematic uncertainties associated to the fit model . . . 140
4.8.2 Systematic uncertainties related to the calculation of the efficiency . . . 144
4.9 Outlook . . . 153

5 Conclusions **155**

A MVA sensitivity studies **157**

Bibliography **161**

Curriculum Vitae **169**

Introduction

"Nel mezzo del cammin di nostra vita
mi ritrovai per una selva oscura,
ché la diritta via era smarrita"

—Inferno, canto I, vv 1-3

The current knowledge of the building blocks that constitute our Universe, and of the forces through which they interact, is based on the Standard Model (SM) of particle physics. The SM is a very successful theory elaborated in the 1960s, which has been thoroughly tested during the last decades by a variety of experiments operating in different energy ranges. The theory has proven to be capable of predicting the existence of particles before they were experimentally observed, like the famous Higgs boson, discovered only in 2012 at the LHC by the CMS and ATLAS collaborations [1, 2].

Nevertheless, the SM fails to properly describe several observed phenomena, with one of the most striking examples being the matter-antimatter asymmetry of the Universe. For these reasons, one of the main focuses of the particle physics community in the past years has been to search for possible signs of New Physics beyond the SM, which could address its shortcomings. The search for new particles usually happens along two complementary paths. The first approach relies on *direct* searches, which aim at observing new particles created in high-energy collisions. The second approach uses *indirect* searches, *i.e.* testing the Standard Model predictions with very high accuracy in observables accessible at lower energy, to look for possible contributions from New Physics particles.

In this thesis, an indirect search for New Physics is presented, which is performed by looking at decays happening via $b \to s\ell\ell$ quark-level transitions. Such processes belong to a category of phenomena called flavour-changing neutral currents (FCNC), which are forbidden at tree level in the SM and happen only via loops. Hypotetical new particles can enter these loops and significantly shift the values of some observables. FCNC decays are thus ideal laboratories to indirectly look for New Physics effects, and they are used here to test one of the cardinal properties of the SM: the lepton flavour universality (LFU). The couplings of the fundamental

forces are in fact predicted to be the same for all three lepton generations, but such *universality* does not necessarily hold for interactions mediated by physics beyond the SM.

One way to look for potential LFU violation is to construct experimental observables whose values can be predicted with very high precision in the SM. Ratios of branching fractions of $B \to X_s \ell\ell$ decays, where X_s is a hadron containing a strange quark and $\ell = e, \mu$, have become in recent years the most famous example of such observables. They are in fact predicted to be equal to unity within a $\mathcal{O}(1\%)$ precision in the SM, as the mass of both leptons can be neglected with respect to that of the decaying b quark. These ratios can be experimentally measured in a very accurate way due to the cancellation of many systematic uncertainties. Any observed deviation from unity would thus be a clear sign of the presence of New Physics. Several ratios of this type have been measured in the past years by using different strange hadrons, *e.g.* $X_s = K^+, K^*, \Lambda^0$ *etc.*, with the most precise results having been provided by the LHCb collaboration. The LHCb experiment is in fact highly suited for these purposes, being a forward spectrometer with high acceptance for the large variety of b hadrons produced in pp collisions at the LHC.

This thesis presents a LFU ratio measurement in a particular final state: $B^+ \to K^+\pi^+\pi^-\ell^+\ell^-$, with $\ell = e, \mu$. This ratio, hereinafter referred to as $R_{K\pi\pi}$, is the first *inclusive* LFU test ever performed, since the $K^+\pi^+\pi^-$ hadronic system is considered inclusively without selecting any of the many resonances contributing to it. The inclusiveness is what makes this measurement particularly interesting, as it can provide complementary information on the spin structure of new particles. Furthermore, the work performed for this thesis also provides the first observation of the $B^+ \to K^+\pi^+\pi^- e^+ e^-$ decay mode.

The thesis is structured as follows. Chapter 1 describes the theoretical framework of the Standard Model, with a focus on the LFU. Chapter 2 shows how $b \to s\ell\ell$ decays can be used to probe New Physics scenarios, and it presents a state-of-the-art of the experimental measurements in this context. Chapter 3 describes the LHCb detector, used to collect the data analysed in the thesis. Here, focus is also put on the upgrade of the downstream tracking detector, which has been the other main project undertaken during this PhD. Finally, Chapter 4 describes the strategy adopted to measure the LFU ratio $R_{K\pi\pi}$, describing each step of the procedure in detail.

1 The Standard Model

"Dico che quando l'anima mal nata
li vien dinanzi, tutta si confessa;
e quel conoscitor de le peccata

vede qual loco d'inferno è da essa;
cignesi con la coda tante volte
quantunque gradi vuol che giù sia messa."

— Inferno, canto V, vv 7-12

The Standard Model of particle physics is the theory that describes the fundamental particles and their interactions. In Section 1.1 an overview of this theoretical framework is given. Sections 1.2.1–1.2.3 describe the formalism of the electromagnetic, the strong and the weak interactions, while Section 1.2.4 addresses the Higgs mechanism and the Yukawa interactions. This chapter in general focuses on the gauge symmetries which underpin the Standard Model properties, notably the one investigated in this thesis work: the lepton flavour universality (LFU).

1.1 A general overview

The Standard Model (SM) is build on the foundations of Quantum Field Theories (QFT), and it is determined by specifying a set of particles and how they interact among each other. The interaction is mediated by three distinct forces, namely strong, weak and electromagnetic force. Figure 1.1 shows an overview of the elementary particles, *i.e.* particles that can not be divided in smaller parts, described by the theory. The electromagnetic charge and the mass of each particle are also shown in the same sketch. The first substantial classification of the

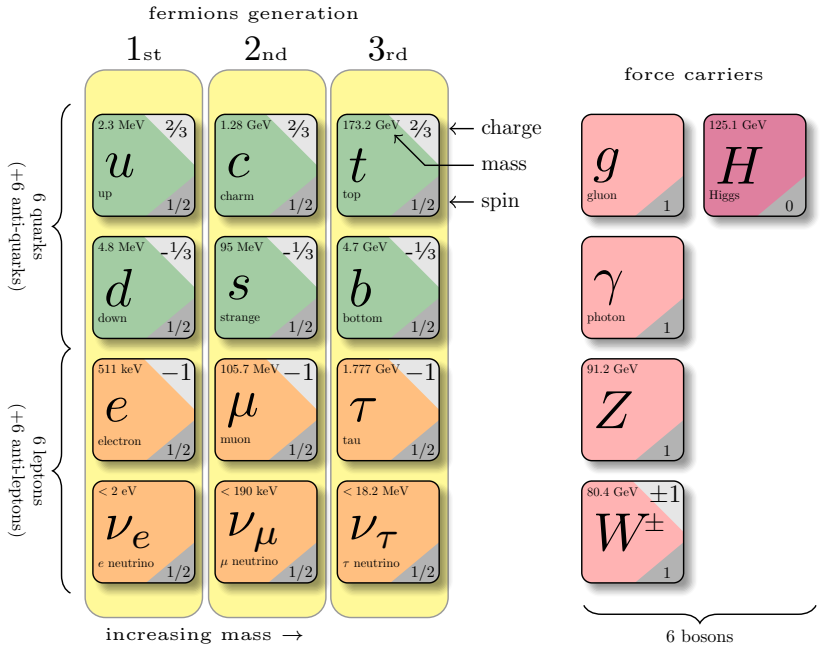

Figure 1.1: Overview of the Standard Model and its fundamental particles [3].

particles is based on the value of their spin[1]. Particles with half-integer spin are the *fermions*, the ones with integer spin are the *bosons*.

- **Half-integer spin – Fermions**, the very constituents of matter. Depending on which forces they are subject to, they are further divided in: quarks, interacting both via electroweak and strong forces, and leptons, interacting via the electroweak force. Both quarks and leptons come in three generations, also called *families*, the first of which contains the components of the ordinary matter. Every lepton family is made of a charged lepton (electron e, muon μ and tauon τ), with an electromagnetic charge of -1, and its respective neutrino (electron neutrino ν_e, muon neutrino ν_μ, tau neutrino ν_τ), that carries no electromagnetic charge and that are predicted to be massless. Quark families are also made of two particles with different electromagnetic charges: the *up*-type quarks have a charge of $+2/3$ (up u, charm c, top t) and the *down*-type ones have a charge of $-1/3$ (down d, strange s, bottom/beauty b). These six varieties of quarks or leptons are known as *flavours*. For quarks and charged leptons, the mass increases in the successive generations. To each charged fermion described corresponds an antiparticle, with same spin and mass value but opposite electromagnetic charge. It is still unknown if the neutrinos have antiparticles or if they are their own antiparticle.

[1]The spin is a quantum number related to the angular symmetry of particle wave function, which does not have a classical analogue, but is often perceived as particle rotation.

- **Integer spin – Bosons**. The different types of interactions among particles, that will be described in the following sections, effectively occur as an exchange of a specific boson, different for each interaction. The vector bosons (spin = 1) $W^{\pm}$ and Z are responsible for the weak interaction, the photon γ for the electromagnetic one and the gluon g for the strong one. The scalar Higgs boson (spin = 0) is the carrier of the interaction between the elementary particles and the Higgs field, thanks to which the elementary particles acquire their masses.

1.2 Formalism

In the SM, elementary particles are represented by fermionic fields ψ and their motion is described by the so-called *Lagrangian*. The classical Lagrangian depends in general on the field itself and of its time-space derivatives:

$$\mathscr{L} = \mathscr{L}(\psi, \partial_\mu \psi), \tag{1.1}$$

where μ runs over the time and space indexes.

The Lagrangian can be used to find the equations of motion (starting from t_1 and ending at t_2), by first building the action S:

$$S = \int_{t_1}^{t_2} \mathrm{d}^4 x \, \mathscr{L}(\psi, \partial_\mu \psi), \tag{1.2}$$

where the integration is over the whole quadri-dimensional time-space, and then by making the action stationary:

$$\delta S = 0, \tag{1.3}$$

where δ is an arbitrary variation of the parameters. The requirement for the action to be stationary leads to the Euler-Lagrange equation, that describes the motion of the field

$$\partial_\mu \left[\frac{\partial \mathscr{L}}{\partial(\partial_\mu \psi)} \right] - \frac{\partial \mathscr{L}}{\partial_\mu \psi} = 0. \tag{1.4}$$

The Lagrangian gives also hints about physical quantities that are conserved during the motion. In fact, the Noether's theorem [4] states that to each symmetry of the Lagrangian corresponds a conserved quantity. A symmetry of the local field ψ that does not modify the action variation δS is called *gauge* symmetry.

The Standard Model is totally specified by the $SU(3)xSU(2)xU(1)$ symmetry group. In the following sections, each part of the group will be described, together with symmetry breaking Higgs mechanism.

1.2.1 Quantum Electrodynamics

The Quantum Electrodynamics (QED) is the quantum field theory that describes the interaction of the fermions and the electromagnetic field. The motion of a free charged particle of spin 1/2 with mass m is described by the Lagrangian

$$\mathscr{L} = \bar{\psi}\left[i\gamma^{\mu}\partial_{\mu} - m\right]\psi, \tag{1.5}$$

where γ^{μ} are the Dirac matrices. This Lagrangian leads to the equation of motion, also known as the Dirac equation

$$(i\gamma^{\mu}\partial_{\mu} - m)\psi = 0. \tag{1.6}$$

One can notice that the Lagrangian in Eq. 1.5 is not invariant under a local transformation of the field ψ of the type

$$\psi \rightarrow e^{i\theta(x)}\psi, \tag{1.7}$$

given the dependence of the angle θ on the coordinates x. To reach an invariance under local transformation of the fields, a covariant derivative is introduced, defined as

$$D_{\mu} = \partial_{\mu} - ieA_{\mu}, \tag{1.8}$$

where e is the electric charge and A_{μ} is the so-called gauge field, representing the electromagnetic potential. For the kind of transformation considered in 1.7, the gauge field is required to transform as

$$A_{\mu} \rightarrow A_{\mu} + \frac{1}{e}\partial_{\mu}\theta(x). \tag{1.9}$$

In this way, if one replaces the derivative in Eq. 1.5 with the derivative in Eq. 1.8, the Lagrangian becomes invariant under local transformation, since $D_{\mu}e^{i\theta(x)}\psi(x) = e^{i\theta(x)}D_{\mu}\psi(x)$. By using the covariant derivative, the Lagrangian becomes

$$\begin{aligned}\mathscr{L} &= \bar{\psi}\left[i\gamma^{\mu}D_{\mu} - m\right]\psi \\ &= \bar{\psi}\left[i\gamma^{\mu}\partial_{\mu} - m\right]\psi + e\bar{\psi}\left(\gamma^{\mu}A_{\mu}\right)\psi.\end{aligned} \tag{1.10}$$

In addition, it is necessary to include a propagation term for the gauge field that has been introduced. This is done using the Maxwell antisymmetric tensor, defined as

$$F_{\mu\nu} = \partial_{\mu}A_{\nu} - \partial_{\nu}A_{\mu}, \tag{1.11}$$

so that a propagation term of the form $F_{\mu\nu}F^{\mu\nu}$ will be invariant under local transformation. Finally, the Lagrangian for Quantum Electrodynamics is given by

$$\mathscr{L} = \underbrace{\bar{\psi}\left[i\gamma^{\mu}\partial_{\mu} - m\right]\psi}_{\text{Free Particle}} + \overbrace{e\bar{\psi}\left(\gamma^{\mu}A_{\mu}\right)\psi}^{\text{Interaction}} - \underbrace{\frac{1}{4}F_{\mu\nu}F^{\mu\nu}}_{\text{Gauge Field Propagation}}. \tag{1.12}$$

From the interaction term in Eq. 1.12, it can be seen that when two charged fermions interact, an A_μ boson is exchanged, without any mass term, which would make the Lagrangian not invariant anymore under local transformation. The boson exchanged is the carrier of the electromagnetic force: the photon, which was indeed experimentally observed to be massless. The symmetry group introduced, that includes the transformations defined in 1.7, is usually referred to as $U(1)$, the group of 1×1 unitary matrix.

1.2.2 Quantum Chromodynamics

The so-called strong force, which is described by Quantum Chromodynamics (QCD), is the fundamental force responsible for holding the quarks together in the nuclei. According to QCD, quarks can exist in three different colour states: Red (R), Green (G) and Blue (B) that can be seen as the "charges" of the strong interaction. QCD is based on the $SU(3)$ symmetry group, and the derivation of its formalism follows the same procedure used for QED (Section 1.2.1) with the replacement of the electromagnetic transformation in Eq. 1.7, that belongs to the symmetry group $U(1)$, with a transformation of the $SU(3)$ group that acts on the quark fields $q(x)$:

$$q(x) \rightarrow e^{-ig_s\theta_a(x)T_a} q(x), \tag{1.13}$$

where g_s corresponds to the strong coupling constant and $\theta_a(x)$ to a set of local parameters. T_a are the 8 generators of the symmetry group: $T_a = \lambda_a/2$ (with a from 1 to 8), where λ_a are the so-called Gell-Mann matrices.

The free Lagrangian is written in the usual way, with the sum over the six quark flavours (j):

$$\mathscr{L} = \sum_j \overline{q}_j \left(i\gamma^\mu \partial_\mu - m_j\right) q_j, \tag{1.14}$$

where quarks can have either the R, B or G color. The covariant derivative of QCD is defined as

$$D_\mu = \partial_\mu - i g_s T_a G_a^\mu, \tag{1.15}$$

where G_a^μ are the eight gauge fields associated to the gluons. Similarly to the Maxwell tensors in the QED case, one can build

$$G_{\mu\nu}^a = \partial_\mu G_\nu^a - \partial_\nu G_\mu^a - g_s f^{abc} G_\mu^b G_\nu^c, \tag{1.16}$$

where f^{abc} are the structure constant of the $SU(3)$ group. The Lagrangian of the QCD is then built in the usual way as

$$\mathscr{L}_{QCD} = -\frac{1}{4} G_{\mu\nu}^a G_a^{\mu\nu} + \overline{q}\left(i\gamma^\mu D_\mu - m\right) q \tag{1.17}$$

An important feature of QCD is the fact that the strong constant g_s decreases with the increase of the energy considered. This behavior produces two effects on the quarks: the so-called

asymptotic freedom and the confinement. The former means that quarks, at sufficiently high energies, act like free particles, not feeling the colour potential. The latter instead implies that at low energies, quarks cannot be observed as free particles, but they always appear in a colourless bound state of two or more quarks. If in the first case it is possible to describe the processes with perturbative methods, in the second case nonperturbative techniques have to be employed.

1.2.3 Electroweak Unification

In the 60s the physicists Glashow, Salam and Weinberg assumed that electromagnetic and weak theory could be described by the same formalism: interactions characterised by Lagrangians that are invariant under gauge transformations. This unified Electroweak theory is related to the symmetry group $SU(2) \times U(1)$, where the $U(1)$ transformations are the same as the ones discussed for the electromagnetic interaction, and the $SU(2)$ group describes the weak interactions, where the different states are identified by the weak isospin I_W. The generators of the $SU(2)$ group (a group of 2×2 unitary matrices with determinant = 1) are three: $\vec{S} = \{S_x, S_y, S_z\}$, and they are related to the Pauli's matrices σ_i

$$\sigma_1 = \begin{pmatrix} 0 & 1 \\ 1 & 0 \end{pmatrix} \qquad \sigma_2 = \begin{pmatrix} 0 & -i \\ i & 0 \end{pmatrix} \qquad \sigma_3 = \begin{pmatrix} 1 & 0 \\ 0 & -1 \end{pmatrix} \tag{1.18}$$

by $\vec{S} = \vec{\sigma}/2$. Given the increase of the group dimensionality, the bosons associated to the weak interaction are the three W_μ^i fields, a triplet of weak isospin $I_W = 1$. The remaining gauge field associated to the $U(1)$ symmetry includes another boson, the B_μ field, which is a singlet of $I_W = 0$. The weak group symmetry is usually also referred to as $SU(2)_L$, where L indicates that the interaction acts only on the left-handed chirality states. That is why fermion fields are split in right-handed and left-handed chirality states, by applying the chirality projector $P_{RL} = (1 \pm \gamma_5)/2$, where γ_5 is defined as $\gamma_5 = i\gamma_0\gamma_1\gamma_2\gamma_3$ (γ_μ are the Dirac matrices), such as

$$\psi = \frac{1-\gamma_5}{2}\psi + \frac{1+\gamma_5}{2}\psi = \psi_L + \psi_R, \tag{1.19}$$

where ψ_L are weak isospin doublets ($I_W = 1/2$), and ψ_R are singlets ($I_W = 0$), that do not interact with the weak bosons. A transformation of the U(1) symmetry group simply changes the left-handed and right-handed fermion fields by a phase $e^{i\alpha(x)Y}$, where α are local parameters and Y is the hypercharge, defined as $Y_W = 2Q - I_W$, where Q is the electric charge. Under a transformation of the $SU(2)_L$ group, only the left-handed fields transform themselves as

$$\psi_L \rightarrow \psi_L e^{i\beta_a(x)S_a}, \tag{1.20}$$

where S_a are the generators of the group ($a = 1,2,3$) and β are local parameters. The covariant derivatives that must be introduced to obtain the gauge invariance are

$$D_\mu^L = \partial_\mu + igYB_\mu + ig'S_\alpha W_\mu^\alpha \qquad D_\mu^R = \partial_\mu + igYB_\mu, \tag{1.21}$$

where g and g' are the coupling constants of the two interactions. Field tensors are then needed to write the final Lagrangian, and they are defined as

$$B_{\mu\nu} = \partial_\mu B_\nu - \partial_\nu B_\mu \qquad W^a_{\mu\nu} = \partial_\mu W^a_\nu - \partial_\nu W^a_\mu - g' \epsilon^{abc} W^b_\mu W^c_\nu, \tag{1.22}$$

where ϵ_{abc} is the structure constant of the $SU(2)_L$ group. Finally, the Lagrangian describing the interaction of the fermion fields with the four gauge fields introduced above is written as:

$$\mathscr{L}_{\text{EW}} = i\bar{\psi}_L \gamma_\mu D^\mu_L \psi_L + i\bar{\psi}_R \gamma_\mu D^\mu_R \psi_R - \frac{1}{4} W^a_{\mu\nu} W^{\mu\nu}_a - \frac{1}{4} B_{\mu\nu} B^{\mu\nu}. \tag{1.23}$$

The bosons mediating the weak and the electromagnetic interactions, $W^\pm$, Z and γ, introduced in Section 1.1, are linear combinations of the W_a and B gauge fields appearing in Eq. 1.23. In particular, $W^\pm$ come from a linear combination of the components W_1 and W_2:

$$W^\pm_\mu = \frac{W^1_\mu \mp W^2_\mu}{\sqrt{2}}, \tag{1.24}$$

while Z and γ are defined as a combination of the W_3 component and B:

$$\begin{pmatrix} W^3_\mu \\ B_\mu \end{pmatrix} = \begin{pmatrix} \cos\theta_\omega & \sin\theta_\omega \\ -\sin\theta_\omega & \cos\theta_\omega \end{pmatrix} \begin{pmatrix} Z_\mu \\ A_\mu \end{pmatrix} \tag{1.25}$$

where θ_ω is the so-called weak mixing angle, defined as:

$$\cos\theta_w = \frac{g}{\sqrt{g^2 + g'^2}} \qquad \text{and} \qquad \sin\theta_\omega = \frac{g'}{\sqrt{g^2 + g'^2}}. \tag{1.26}$$

At this point, it is clear that the Standard Model possesses a flavour degeneracy in its gauge sector (as the electroweak part just described). In fact, one can define 5 independent fermion fields (doublets or singlets of the electroweak interaction):

$$Q_L = \begin{pmatrix} u_L \\ d_L \end{pmatrix}, \quad u_R, \quad d_R, \quad L_L = \begin{pmatrix} \nu_L \\ e_L \end{pmatrix}, \quad e_R, \tag{1.27}$$

where the fermions may belong to any of the three generations. Since in the electroweak Lagrangian there are no terms that distinguish between the different families, the three generations must behave as identical replicas (except for their masses) of the basic fermion family $\psi = [Q_L, u_R, d_R, L_L, e_R]$, when undergoing electroweak interactions. This implies that the gauge bosons must be equally coupled to the three lepton generations. In practical terms, it means that the probability of a decay to happen must be the same regardless the family of the leptons present in the final state, except for mass differences (given the helicity role in the electroweak interactions). This property is referred to as lepton flavour universality (LFU) and it is an accidental symmetry, since there is no a priori motivation for its presence in the SM. Nevertheless, it has been precisely verified [$\sim 0.1\%$] *e.g.* in W and Z decays [5, 6], in light mesons decays (K or π) [7, 8], and in decays of charmonioum resonances, *e.g.* J/ψ decays [9].

Testing if LFU holds also at higher energy scales than the ones within our current reach is the fundamental purpose of this doctoral project, as will be extensively explained in Section 4.

1.2.4 Breaking the symmetry: the Higgs mechanism

In Eq. 1.23, the four gauge bosons introduced are massless. Nevertheless, massive Z and $W^{\pm}$ bosons are observed: $m_Z \sim 91\,\text{GeV}/c^2$ and $m_{W^{\pm}} \sim 80\,\text{GeV}/c^2$ [10]. To solve this puzzle, Higgs, Brout and Englert assumed the existence of a field, the Higgs field, that gives mass to the gauge bosons when interacting with them, and whose vacuum state would break the electroweak symmetry just described. A scalar, complex doublet ϕ is introduced, with an associated Lagrangian written as

$$\mathscr{L}_{\text{Higgs}} = \left(D_\mu \phi^\dagger\right)\left(D^\mu \phi\right) - \mu^2\left(\phi^\dagger \phi\right) - \lambda\left(\phi^\dagger \phi\right)^2, \tag{1.28}$$

where the kinematic term is the one already introduced for the electroweak interaction, and μ and λ are the free parameters of the Higgs potential, with λ assumed to be positive. While for $\mu^2 > 0$ the ground state of the ϕ field, that corresponds to the field value at the minimum of the potential, has only one solution, $\phi = 0$, for $\mu^2 < 0$ the expected value of the ground state corresponds to a circumference of centre 0 and radius $\phi_0^2 = -\mu^2/(2\lambda) = v^2/2$ in the plane $\text{Re}(\phi) - \text{Im}(\phi)$, as shown in Fig. 1.2.

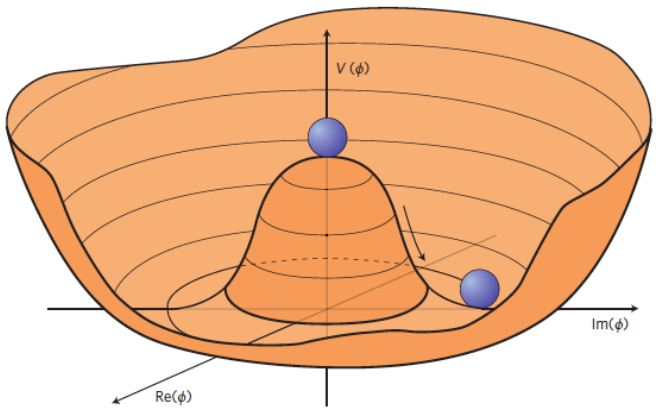

Figure 1.2: Higgs potential $V(\phi)$ with $\lambda > 0$ and $\mu^2 < 0$ [11].

These infinite combinations break the $SU(2)$ symmetry, since a minimum state will be altered by a $SU(2)_L$ local transformation. Among all the minima, one can be chosen as a reference state without loss of generality

$$\phi_{\text{min}} = \begin{pmatrix} 0 \\ \frac{v}{\sqrt{2}} \end{pmatrix}. \tag{1.29}$$

It is possible then to study small fluctuations of the field around this reference minimum

$$\phi = \frac{e^{i\theta_a(x)\frac{\sigma_a}{2}}}{\sqrt{2}} \begin{pmatrix} 0 \\ v + \mathrm{H}(x) \end{pmatrix}, \tag{1.30}$$

where $H(x)$ is the Higgs scalar boson (H) and $\theta_a(x)$ ($a = 1,2,3$) are new fields that can be removed thanks to the invariance of the Higgs Lagrangian under $SU(2)$ gauge transformations. By replacing this ϕ expression in the Higgs Lagrangian (Eq. 1.28) and using the covariant derivative from Eq. 1.21 and the bosons expressions from Eq. 1.24-1.25, the mass terms for the H, the $W^{\pm}$ and the Z bosons appear (while the photon remains massless):

$$M_{W^-} = M_{W^+} = \frac{1}{2} v g \qquad M_Z = \frac{1}{2} v \sqrt{g^2 + g'^2} \qquad M_{\mathrm{H}} = \sqrt{2\lambda v^2}. \tag{1.31}$$

In addition, also fermions acquire their masses when interacting with the Higgs field. This interaction is referred to as Yukawa interaction, and the corresponding term in the Lagragian has the following form

$$\mathscr{L}_{\text{Yukawa}} = -\bar{Q}_L^i Y_D^{ik} d_R^k H - \bar{Q}_L^i Y_U^{ik} u_R^k H_c - \bar{L}_L^i Y_\ell^{ik} \ell_R^k + h.c.\,, \tag{1.32}$$

where the i,k labels refer to the flavour generations and the Y_{ik} are complex matrices defining the Yukawa couplings strengths. The first fact to be noted is that the Yukawa eigenstates are not the same as the mass eigenstates, and that in general the Yukawa couplings are not proportional to the identity. For this reason, the Yukawa interaction is the only interaction that breaks the global flavour symmetry of the SM, as it will be shown in the following.

Considering the quark sector, one can diagonalise the Yukawa matrices in the mass basis through a unitary transformation of the form $U_L^{u,d} Y U_R^{u,d\dagger} = M^{u,d}$, where U are unitary independent matrices. The resulting $M_u(M_d)$ matrix will be a matrix containing only the up(down)-type quarks masses on the diagonal. Due to the residual flavour symmetry it is possible to choose a basis where only one of the two couplings is diagonal (either the up or the down one), without breaking the gauge invariance. If one chooses a basis where $M_d = \mathrm{diag}(\mathrm{m_d}, \mathrm{m_s}, \mathrm{m_b})$, a mixing matrix is needed when trying to diagonalise also the second mass matrix: $M_u = V^+ \times \mathrm{diag}(\mathrm{m_u}, \mathrm{m_c}, \mathrm{m_t})$. This mixing matrix, up to arbitrary phase differences, is the Cabibbo-Kobayashi-Maskawa (CKM) matrix, where each element represents the mixing between the quark flavours:

$$V_{CKM} = \begin{pmatrix} V_{ud} & V_{us} & V_{ub} \\ V_{cd} & V_{cs} & V_{cb} \\ V_{td} & V_{ts} & V_{tb} \end{pmatrix}. \tag{1.33}$$

The experimental values of the mixing elements indicate a strong hierarchical structure, where the most off-diagonal terms are smaller and the diagonal terms are larger. This phenomenological fact allows an expansion of the CKM matrix following the so-called Wolfenstein

parametrisation, yielding:

$$V_{CKM} = \begin{pmatrix} 1-\frac{\lambda^2}{2} & \lambda & A\lambda^3(\rho - i\eta) \\ -\lambda & 1-\frac{\lambda^2}{2} & A\lambda^2 \\ A\lambda^3(1-\rho-i\eta) & -A\lambda^2 & 1 \end{pmatrix} + \mathcal{O}(\lambda^4), \tag{1.34}$$

where A, ρ and η are real parameters of order unity, and $\lambda = \sin\theta_c \sim 0.22$, with θ_c known as the Cabibbo angle. There is still no explanation for the peculiar structure observed in the SM Yukawa couplings, making this pattern one of the long-standing open issues in flavour physics.

The CKM matrix naturally appears when considering the electroweak interaction between the quarks and the gauge bosons, in the basis of the quark mass eigenstates. For processes involving charged currents, *i.e.* where a charged boson is exchanged, the quark sector is described by

$$\mathcal{L}_{CC} = -\frac{g}{\sqrt{2}} \bar{u}_L^i \gamma^\mu V_{ij} d_L^j W_\mu^+ + h.c.\,, \tag{1.35}$$

where it is clear how the W boson mediates a transition between up-type and down-type quarks, with a coupling depending on the the relative mixing element of the CKM matrix, V_{ij}. On the other hand, the neutral current does not transform between upper and lower $SU(2)$ components, as the W_3 generator has elements only on the diagonal. This remains true also when moving to the mass eigenstates, where the neutral currents remain flavour diagonal. That is the reason why flavour changing neutral currents (FCNC) cannot happen at tree level in the SM, but they must occur via at least two $W^\pm$ vertices, forming loops and thus being suppressed with respect to charged current processes.

Such effects are what makes the processes mediated by FCNC (as the one studied in this thesis work) ideal laboratories to search for possible New Physics beyond the SM, as it will be discussed in details in the following chapter.

2 Beyond the Standard Model

"Considerate la vostra semenza:
fatti non foste a viver come bruti,
ma per seguir virtute e canoscenza".

— Inferno, canto XXVI, vv 118-120

Despite its great successes in the last decades, culminated with the discovery of the Higgs boson in 2012 at the LHC by the ATLAS ad the CMS collaborations [1, 2], the SM still fails to describe properly some phenomena such as

- The evidence of dark matter and the origin of dark energy, which together compose ~ 96% of the Universe's content [12].
- The abundance of the matter with respect to the antimatter of the Universe.
- The measured neutrino oscillations [13], which are possible only in the presence of massive neutrinos which are not included in the SM.
- A description of quantum gravity, which is not included in the SM formalism.

In addition, the SM contains several free parameters whose values cannot be predicted by the theory itself but rely on experimental measurements. Examples of these parameters are the masses of the quarks and leptons, which take values in an extremely wide range, or the mixing elements of the CKM matrix (see Section 1.2.4), which come with a still unexplained very hierarchical structure.

For all these reasons, the current experimental efforts are focused on the searches for possible extensions to the SM which would explain its aforementioned pitfalls. Such theories are referred to as New Physics (NP) scenarios. One way to study them is to perform measurements of observables predicted by the SM with very high precision, looking for discrepancies between nature and the theory. One of the possible physical processes studied to perform these

measurements is the one mediated by $b \to s\ell\ell$ quark-level loop transitions, studied in this thesis work.

Therefore, an overview of the theoretical aspects describing such decays is given in Section 2.1, while an overview of the experimental results for such processes is given in Section 2.2.

2.1 $b \to s\ell\ell$ decays: Probes for New Physics

Due to the outstanding problems of the SM, the modern point of view on its Lagrangian is to consider it as the low-energy approximation of a more complete theory, living at energy scales much larger than the mass of the W boson (commonly taken as the electroweak energy scale Λ_{EW}):

$$\mathscr{L}_{\text{eff}} = \underbrace{\mathscr{L}_{\text{Gauge}}(A_a, \psi_i) + \mathscr{L}_{\text{Higgs}}(H, A_a, \psi_i)}_{\mathscr{L}_{\text{SM}}} + \overbrace{\sum \frac{c_n}{\Lambda^{d-4}} \mathscr{O}_n^{(d)}(H, A_a, \psi_i)}^{\text{“heavy fields”}}. \tag{2.1}$$

Equation 2.1 combines the Gauge and the Higgs Lagrangians described in the previous chapter with a general parameterisation of new “heavy” degrees of freedom, by means of operators $\mathscr{O}_n$ of dimensions $d \geq 5$, containing SM fields only, and of effective couplings c_n. Since these new degrees of freedom are still unknown, the shown parameterisation comes from integrating out the “heavy dynamics” in the most general way, as it is done in the Fermi theory.

Some physics processes, like the ones mediated by a $b \to s\ell\ell$ transition, are ideal to perform indirect searches of heavy particles, allowing to test the flavour structure of the possible physics beyond the SM. Such decays are mediated by FCNC, and thus can not happen at tree level for the SM (as explained in Section 1.2.4), but they occur with small branching fractions, typically of $\mathscr{O}(10^{-7} - 10^{-6})$. Therefore, possible new mediators *e.g.* Leptoquarks (LQ) [14] or new heavy gauge boson such as Z' [15–18] can contribute with amplitudes comparable or enhanced with respect to the SM ones, modifying physical observables such as processes branching fractions, angular distributions of final particles *etc.*. Examples of SM diagrams and possible New Physics contributions for $b \to s\ell\ell$ transitions are shown in Figure 2.1.

The SM interactions contributing to such decays are of two types: the electroweak part, also known as *short-distance* effects, that mediates the flavour-changing transition at quark level with a scale of $\Lambda_{\text{EW}} \sim 80\,\text{GeV}/c^2$, and the strong part, also known as *long-distance* effects, with scale $\Lambda_{\text{QCD}} \sim \mathscr{O}(10^{-1})\,\text{GeV}/c^2$, that is related to the quark hadronisation. Given the large difference between the b mass and the electroweak scale, the description of rare decays of B hadrons is simplified by constructing a local effective Hamiltonian, integrating out the heavy SM fields W and Z bosons, as well as the top quark. This allows to rewrite the Lagrangian in terms of local operators containing only light SM fields, as

$$\mathscr{L}_{\text{eff}} = -4\frac{G_F}{\sqrt{2}} V_{tb} V_{ts}^* \frac{g_e}{4\pi} \sum C_i(\mu) \mathscr{O}_i(\mu), \tag{2.2}$$

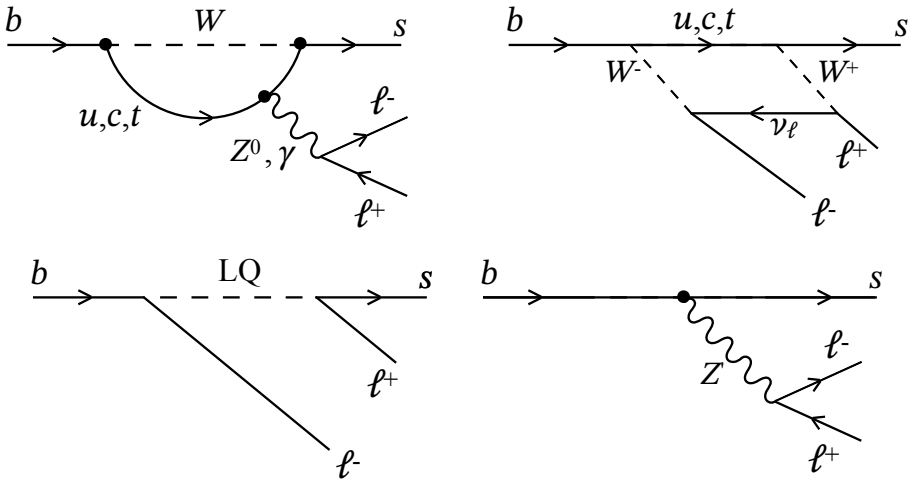

Figure 2.1: SM contributions (top row) for $b \to s\ell\ell$ transition, happening via loop (left) or box (right), involving the electroweak bosons W, Z and γ; New Physics contributions at tree-level (bottom row), mediated by new heavy bosons such as Leptoquark (left), which could couple directly quarks and leptons, or Z' (right). Both new heavy bosons can have different couplings to flavour families.

where G_F is the Fermi constant, g_e the electromagnetic coupling, $V_{tb}V_{ts}^*$ the quark-mixing elements, $\mathcal{O}_i$ a complete basis of local operators encoding the long-distance effects, and C_i the effective couplings encoding the short-distance effects, also known as *Wilson coefficients* (WC). In general, the couplings and the operators depend on the renormalisation energy scale. In fact, the Wilson coefficients are first evaluated at the electroweak scale (Λ_{EW}), by matching the decay amplitudes of the full theory with the effective ones, and then they are evolved down to the energy scale of the physical process ($\sim m_B$) by renormalisation group equations [19]. The presence of new mediators can modify the initial values of the WC, appearing as a shift with respect to the Standard Model predictions: *e.g.* $C_i = C_i^{SM} + C_i^{NP}$. The most relevant operators for the effective weak lagragian in Eq. 2.2 are

$$\begin{aligned} \mathcal{O}_7 &= m_b \bar{s}_L^\alpha \sigma^{\mu\nu} F_{\mu\nu} b_R^\alpha, \\ \mathcal{O}_9 &= \bar{s}_L^\alpha \gamma_\mu b_L^\alpha \bar{\ell}\gamma^\mu \ell, \\ \mathcal{O}_{10} &= \bar{s}_L^\alpha \gamma_\mu b_L^\alpha \bar{\ell}\gamma^\mu \gamma_5 \ell, \end{aligned} \tag{2.3}$$

where b, s and ℓ correspond to the SM fermionic fields, m_b to the mass of the b quark, α and β to the possible color indices, $F_{\mu\nu}$ to the electromagnetic tensor, γ_μ and γ_5 to the Dirac matrices, $\sigma_{\mu\nu} = \frac{i}{2}[\gamma^\mu, \gamma^\nu]$, and the L and R indices to the helicity status. The operators correspond respectively to the photon pole $b \to s\gamma$ and to the *vector* and *axial* leptonic currents.

Given the left-handed nature of the weak interactions, the right-handed operators $\mathcal{O}'$, arising from the swap of the left and the right quark states $q_L(R) \to q_R(L)$, are suppressed in the

SM and thus particularly sensitive to contribution from NP models with a different helicity structure.

2.2 An experimental overview

A large variety of experimental observables is available when looking at $b \to s\ell\ell$ transitions, the most studied being:

- **Relative rates** of $b \to s\mu\mu$ and $b \to see$. Ratios of this type are predicted to be equal to unity with very high precision, due to the LFU of the SM (see Section 1.2.3). Such observables are particularly clean, with the theoretical uncertainties coming from the QCD part of the decay cancelling out in the ratio.
- **Angular observables**. New physics can modify the angular distributions of final state particles. Angular observables are usually studied by parameterising them to reduce the uncertainties coming from the hadronic part of the interaction, encoded by the so-called *form factors*. Nevertheless, higher-order long distance effects such as $b \to sc\bar{c}$ that cannot be described by perturbation techniques, also known as *charm-loop*, can pollute the observables of this type.
- **Single branching fractions**, usually studied with muons in the final states due to their easiest experimental identification and measurement, are the ones suffering the most from theoretical uncertainties. However, some fully leptonic final states *e.g.* $B_s^0 \to \mu^+\mu^-$, with their very clean SM predictions ($\sim \mathcal{O}(4\%)$ uncertainty), are valuable channels to search for New Physics.

During the past few years, a pattern of tensions between SM predictions and experimental results has been observed when looking at b meson decays, usually referred to as *flavour anomalies*, but none of them is large enough to rule out statistical fluctuations. In the following, an overview of such experimental results will be given, mainly showing measurements from the LHCb collaboration, which is currently leading the experimental precision in these kinds of flavour observables.

2.2.1 Branching fraction of $b \to s\mu\mu$ decays

The LHCb collaboration has measured the differential branching fractions for several decay modes mediated by a $b \to s\mu\mu$ transition, namely in $B^{0(+)} \to K^{0(+)}\mu^+\mu^-$ and $B^+ \to K^{*+}\mu^+\mu^-$ [22], in $\Lambda_b^0 \to \Lambda\mu^+\mu^-$ [21], in $B^0 \to K^{*0}\mu^+\mu^-$ [20], and more recently in $B_s^0 \to \phi\mu^+\mu^-$ decays [23]. The branching fractions, measured as a function of the dilepton invariant mass squared $q^2 = m^2(\mu\mu)$, appear to be consistently lower than the SM predictions, with the largest discrepancy of ~ 3.6 standard deviations (σ) observed in $1.1 < q^2 < 6\,\text{GeV}^2/c^4$ for $B_s^0 \to \phi\mu^+\mu^-$ decays [23], shown in Figure 2.2. However, it is worth to stress that SM predictions of branching fractions are affected by large theory uncertainties, mainly coming from the modelling of the

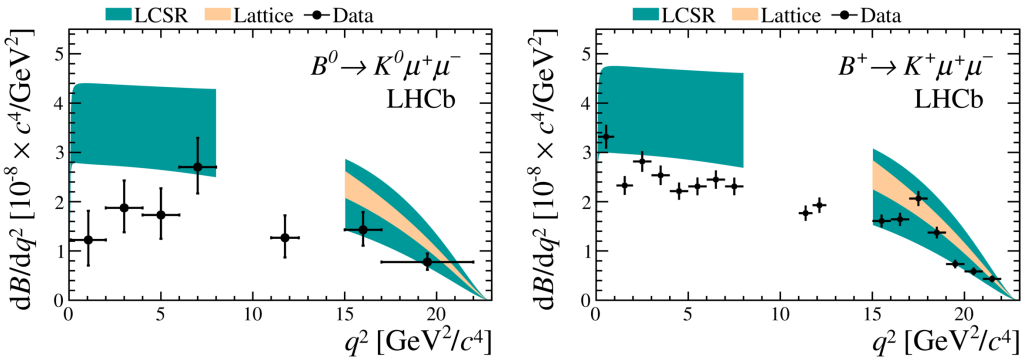

(a) $B^{0(+)} \to K^{0(+)}\mu^+\mu^-$ [20]

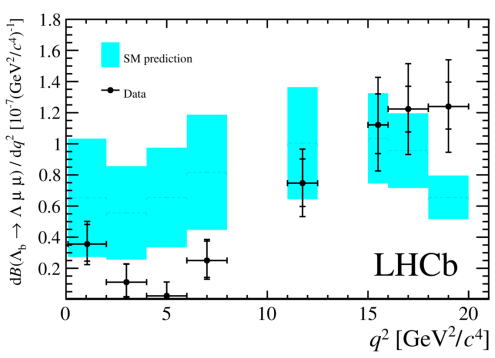

(b) $\Lambda_b^0 \to \Lambda\mu^+\mu^-$ [21]

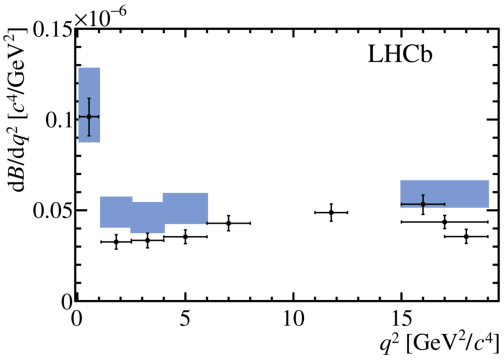

(c) $B^0 \to K^{*0}\mu^+\mu^-$ [22]

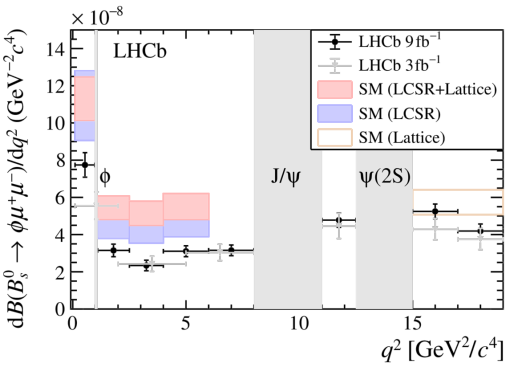

(d) $B_s^0 \to \phi\mu^+\mu^-$ [23]

Figure 2.2: Differential branching fractions measurements as a function of the dilepton invariant mass square (q^2) for several decays studied by the LHCb collaboration. SM predictions are also shown.

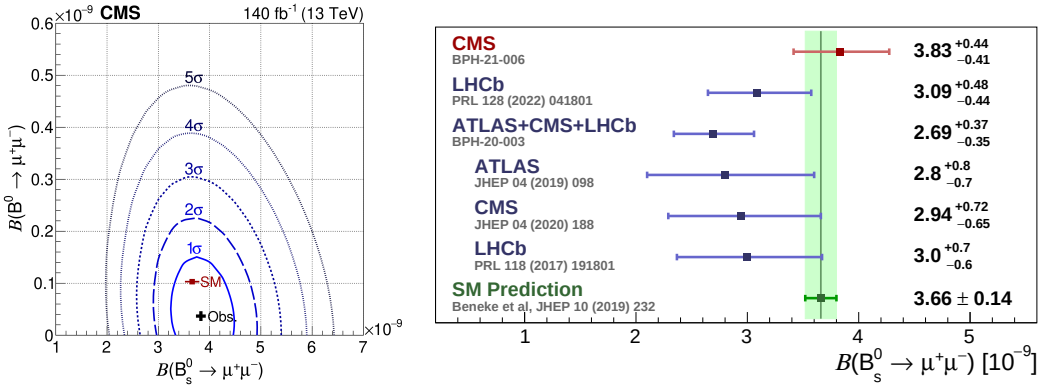

Figure 2.3: The profile likelihood (left) as a function of $B_s^0 \to \mu^+\mu^-$ and $B^0 \to \mu^+\mu^-$ decay branching fractions in 2D. The contours enclose the regions with $1-5\sigma$ coverage, where 1σ, 2σ, and 3σ regions correspond to 68.3, 95.4, and 99.7% confidence levels, respectively [24]. A comparison with the previous measurements and with the SM predictions (right).

hadronic form factors.

Fully leptonic decays

Fully leptonic final states, such as $B_s^0 \to \mu^+\mu^-$, are helicity suppressed and have very clean Standard Model predictions (~ few percent). In fact, thanks to the absence of hadrons in the final state, the decay is described only by the B_s^0 decay constant, that is calculated with high accuracy with lattice QCD techniques. The CMS experiment released the most precise measurement of the branching fractions of $B_s^0 \to \mu^+\mu^-$ decays and of the B_s^0 lifetime [24]. All values are in agreement with the Standard Model predictions within one standard deviation, as shown in Figure 2.3.

2.2.2 Angular observables

The angular observables can be described using a set of parameters that are related to the WCs, thus sensitive to new physics contributions. In some cases, these parameters can be defined such that they minimize the QCD uncertainties at leading order. One such example is the P_5' operator, measured by the LHCb collaboration in $B^0 \to K^{*0}\mu^+\mu^-$ [25] and $B^+ \to K^{*+}\mu^+\mu^-$ decays [26], but also by Belle, ATLAS and CMS collaborations. The LHCb result, which leads the precision of the P_5' observable, is shown in Figure 2.4. The measurements show local tensions with the SM predictions between $2-3\sigma$, depending on the q^2 intervals and the hadronic uncertainties descriptions, but, like the differential branching fractions, none of them is significant enough to be an evidence of New Physics. In addition, there exists a long-standing debate within the theory community about whether non-perturbative QCD contributions from charm-loop could mimic New Physics contributions and thus explain the observed anomalies.

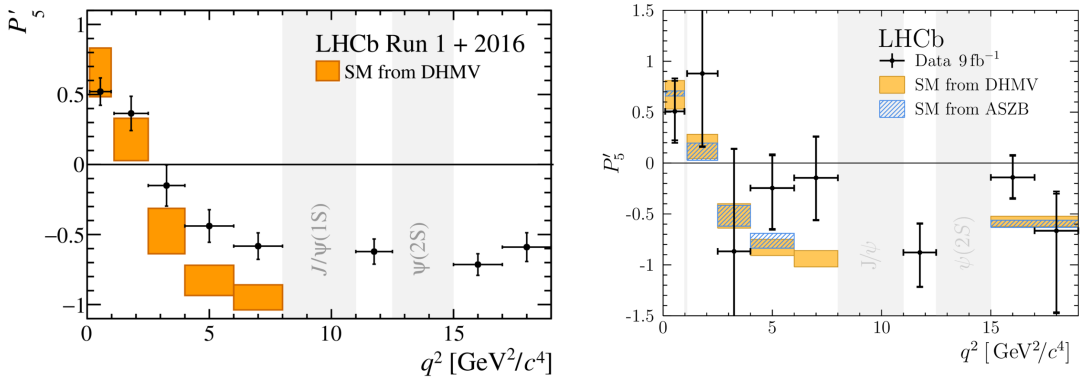

Figure 2.4: P'_5 measured values for $B^0 \to K^{*0}\mu^+\mu^-$ [25] (left) and for $B^+ \to K^{*+}\mu^+\mu^-$ [26] (right) decays in bins of the di-muon invariant mass. SM predictions are also shown.

2.2.3 Lepton flavour universality tests

Another interesting set of measurements are ratios of branching fractions of the form:

$$R_H = \frac{\int_{q^2_{\min}}^{q^2_{\max}} \frac{\mathrm{d}\mathcal{B}(H_b \to H_s ee)\mathrm{d}q^2}{\mathrm{d}q^2}}{\int_{q^2_{\min}}^{q^2_{\max}} \frac{\mathrm{d}\mathcal{B}(H_b \to H_s \mu\mu)\mathrm{d}q^2}{\mathrm{d}q^2}}, \tag{2.4}$$

where $H_{b(s)}$ is a generic hadronic system containing a $b(s)$ quark. In the case above, the numerator and the denominator will have the same theory uncertainties related to the hadronic form factors and charm-loop effects, making the SM predictions very accurate ($\mathcal{O}(1\%)$) [27], thanks also to the smallness of electron and muon masses, that are negligible in a large part of the phase space. In addition, since the gauge interactions of the SM are flavour universal, any departure of the ratio from unity would be a clear sign of presence of New Physics, whose amplitudes would be different depending on the lepton family involved.

Several decays were studied in the past years, with a historical overview given below. The measurements are grouped per published paper.

- $\mathbf{H_b = B^+, H_s = K^+}$ [28]

$$R_K(1.1 < q^2 < 6\ \mathrm{GeV}^2/c^4) = 0.846^{+0.042}_{-0.039}(\mathrm{stat})^{+0.013}_{-0.012}(\mathrm{sys}) \tag{2.5}$$

  The measurement lies at 3.1 standard deviations from the SM predictions and it is compatible with the previous R_K value measured with a smaller part of the data collected [29].

- $\mathbf{H_b = B^0(B^+), H_s = K^0_S(K^{*+})}$ [30]

$$R_{K^0_S}(1.1 < q^2 < 6\ \mathrm{GeV}^2/c^4) = 0.66^{+0.20}_{-0.14}(\mathrm{stat.})^{+0.02}_{-0.04}(\mathrm{syst.}), \tag{2.6}$$

$$R_{K^{*+}}(0.045 < q^2 < 6\ \text{GeV}^2/c^4) = 0.70^{+0.18}_{-0.13}(\text{stat.})^{+0.03}_{-0.04}(\text{syst.}) \tag{2.7}$$

The values agree with the SM predictions at $\sim 1.5\sigma$ level, and with the other tests of lepton universality.

- $\mathbf{H_b} = \mathbf{B^0}, \mathbf{H_s} = \mathbf{K^{*0}}$ [31]

$$R_{K^{*0}} = \begin{cases} 0.66^{+0.11}_{-0.07} \pm 0.03 & \text{for } (0.045 < q^2 < 1.1\ \text{GeV}^2/c^4) \\ 0.69^{+0.11}_{-0.07} \pm 0.05 & \text{for } (1.1 < q^2 < 6\ \text{GeV}^2/c^4) \end{cases} \tag{2.8}$$

The values show a $2.1-2.4\sigma$ tension with the SM, depending on the q^2 range considered.

- $\mathbf{H_b} = \Lambda_\mathbf{b}, \mathbf{H_s} = \mathbf{pK}$ [32]

$$R_{pK}(0.1 < q^2 < 6\ \text{GeV}^2/c^4) = 0.86^{+0.14}_{-0.11} \pm 0.05 \tag{2.9}$$

The value is compatible with the SM.

For the past years the deviations observed, especially in the high-yield decay channel $B^+ \to K^+\ell^+\ell^-$, has sparked the interest of the worldwide physics community. Nevertheless, the LHCb collaboration released, at the end of 2022, a conclusive LFU test, by studying simultaneously the $B^+ \to K^+\ell^+\ell^-$ and $B^0 \to K^{*0}\ell^+\ell^-$ decays, and thus measuring at once the R_K and R_K^* ratios, with the full dataset available. The results, shown in Figure 2.5, supersede the previous values and are in agreement with the SM predictions [33], where the differences with respect to the previous measurements are partly due to the use of tighter electron identification criteria and partly to the modelling of residual backgrounds coming from a misidentification of hadrons to leptons (which will be extensively described in Section 4.3.4).

It is worth to mention that LFU tests have been performed also with charged current decays, as relative rates of $b \to c\tau\nu_\tau$ versus $b \to c\ell\nu_\ell$, where $\ell = e, \mu$. Although these processes have enhanced branching fractions with respect to the $b \to s\ell\ell$ ones, as they can happen at tree level mediated by a $W^\pm$ boson, the missing energy from the neutrino(s) and the very busy environment of the LHC, where the initial B meson momentum is unknown, make their measurement particularly challenging. Figure 2.6 shows the combination of the $R(D^*) = \mathscr{B}(B \to D^*\tau\nu)/\mathscr{B}(B \to D^*\mu\nu)$ and the $R(D) = \mathscr{B}(B \to D\tau\nu)/\mathscr{B}(B \to D\mu\nu)$ measurements, produced by the Heavy Flavour Averaging Group (HFLAV), including results from the LHCb, BaBar and Belle collaborations [35–42]. The combination exhibits a $\sim 3.2\sigma$ global tension with the SM predictions [34].

2.2.4 Global fits

The flavour observables from rare B meson decays, described in the previous sections, can be input to global fits, which allow to estimate possible shifts of the Wilson coefficients with respect to their SM values. Figure 2.7 shows a global fit in a two-dimensional scenario $(C_9^{bs\mu\mu}, C_{10}^{bs\mu\mu})$, updated with the latest measurements of R_K, R_{K^*} and of the $\text{BR}(B_s \to \mu\mu)$ [43].

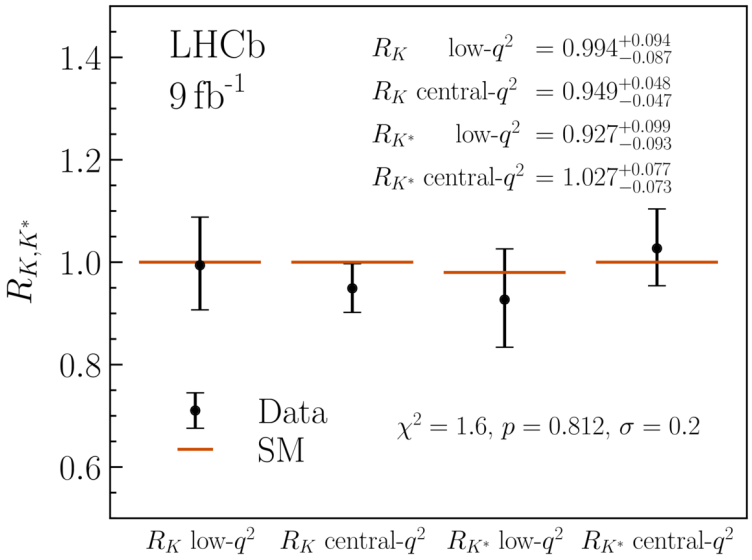

Figure 2.5: R_K and R_K^* most precise values up to date. The label low$-q^2$ stays for a q^2 range of $0.1 < q^2 < 1.1\,\text{GeV}^2/c^4$ and high$-q^2$ for $1.1 < q^2 < 6.0\,\text{GeV}^2/c^4$ [33].

These fits suggest that the experimental measurements are compatible with New Physics scenarios that are lepton flavour universal.

In Ref. [43] several example models for New Physics are studied that would explain the latest experimental results, mainly extending the SM by TeV scale gauge bosons such as Z', or by a (bi)triplet of scalar leptoquarks, which satisfy LFU.

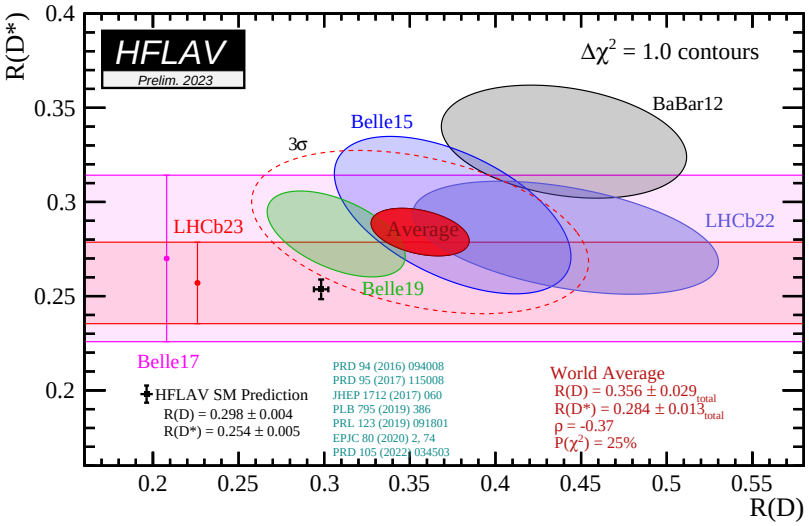

Figure 2.6: $R(D^*)$ and $R(D)$ combination with inputs from LHCb, BaBar and Belle collaboration. The HFLAV average, in red, shows a $\sim 3.2\sigma$ tension with the SM prediction [34].

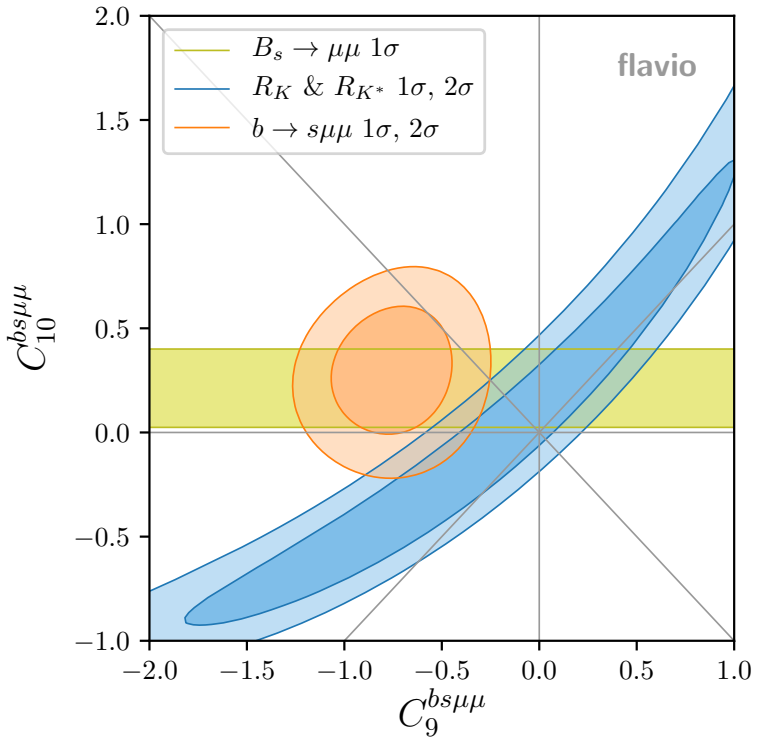

Figure 2.7: Constraints on $C_9^{bs\mu\mu}$ and $C_{10}^{bs\mu\mu}$ Wilson coefficients including the latest LFU ratios (blue), the $b \to s\mu\mu$ measurements (orange) and the recent BR($B_s \to \mu\mu$) (yellow) [43], assuming no NP in the electron channel.

3 The LHCb detector

Così parlar conviensi al vostro ingegno,
però che solo da sensato apprende
ciò che fa poscia d'intelletto degno.

— Paradiso, canto IV, vv 39-42

In this chapter, a brief description will be given of the subdetectors that compose the LHCb detector (Section 3.2), permitting the reconstruction of tracks (Section 3.2.1), the identification of different particle types (Section 3.2.2), and the selection of the interesting events (Section 3.2.3) among the huge amount of particles resulting from proton-proton collision at the Large Hadron Collider (LHC) (Section 3.1).

3.1 The Large Hadron Collider

The Large Hadron Collider (LHC) is the largest and most powerful proton-proton (pp) and heavy-ion collider in the world. The LHC is part of an accelerator complex, shown in Figure 3.1, situated at the Conseil Européen pour la Recherche Nucléaire (CERN), on the border between France and Switzerland.

The protons that circulate in the 27 km long LHC ring, about 100 m underground, are provided by ionisation of hydrogen atoms. They are, at first, accelerated in the Linear Accelerator (LINAC2), that allows them to reach an energy of 50 MeV. Afterwards, they pass through several circular machines: the Proton Synchrotron Booster (PSB), the Proton Synchrotron (PS) and finally the Super Proton Synchrotron (SPS), where they are accelerated to 450 GeV. Then, they get separated into two beams that travel in distinct beam pipes, in opposite directions, which are then merged in a single straight section where the collisions take place. In the four interaction points, the ALICE [45], ATLAS [46], CMS [47] and LHCb [48] detectors are placed, in order to study the products of the collisions. The beams trajectory and focusing

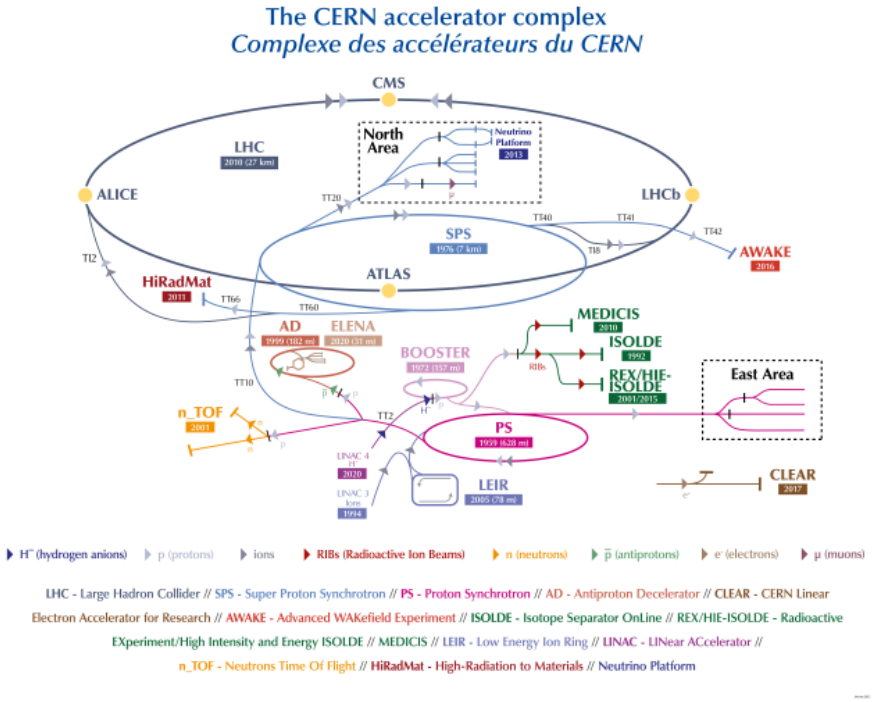

Figure 3.1: The CERN accelerator complex [44].

is guaranteed by a superconducting magnets system, that consists of dipole (to bend the particles) and quadrupole (to squeeze the bunches) and provides a magnetic field of ~ 8 T. Protons are collected in a maximum of 2808 bunches per beam, each of which contains $\sim 1.2 \times 10^{11}$ protons, separated by 25 ns from each other (resulting in a collision frequency of 40 MHz). The proton energy varied during time. The LHC operated with a centre-of-mass energy of 7 TeV in in 2011-2012, referred to as `Run1`. In 2015-2018, referred to as `Run2`, the centre-of-mass energy was increased up to 13 TeV.

One of the main parameters for an accelerator machine is the so-called luminosity ($\mathscr{L}$), which is a measure for how frequently protons collide. For example, the number of B mesons produced after a pp collision, which is the starting point of the physics process studied in this analysis, $B^+ \to K^+\pi^+\pi^-\ell^+\ell^-$, will be given by

$$\frac{\mathrm{d}N}{\mathrm{d}t} = \frac{1}{2}\mathscr{L} \cdot \sigma_{b\bar{b}}, \tag{3.1}$$

where N is the rate of events produced and $\sigma_{b\bar{b}}$ the cross-section for the production of a pair of beauty hadrons, *i.e.* the probability that a pair of beauty hadrons is produced from a pp collision. Figure 3.2 shows the luminosity, integrated per year from 2010 to 2018, recorded by the LHCb detector, which gives an estimation of the amount of the data collected.

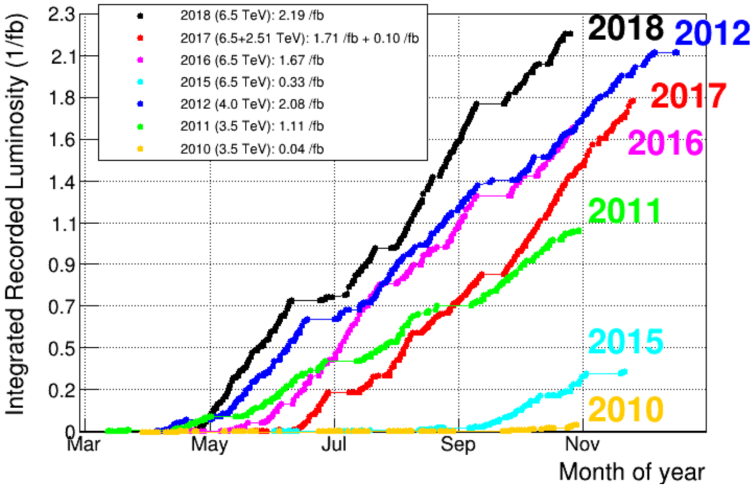

Figure 3.2: Integrated pp luminosity per year, from 2010 to 2018, except for the years when the machines were undergoing upgrades. The centre of mass energies of the pp collisions are also shown in the legend.

3.2 The LHCb detector in Runs 1 and 2

The main purpose of the Large Hadron Collider Beauty (LHCb) detector, shown schematically in Figure 3.3, is the study of heavy mesons decays, such as b hadrons. The angular distribution of $b\bar{b}$ quark pairs produced from proton-proton collisions is shown in Figure 3.4 and it explains the reason behind the forward-arm design of the LHCb detector, which covers a range of pseudorapidity η from 2 to 5[1].

Going forward from the interaction point, *i.e.* from $z = 0$ towards positive values of z, where z is the axis along the beam direction, several subdetectors follow one another, each of which exploits different techniques to obtain the most reliable information on different properties of the particles resulting from the pp interactions.

Given the geometrical precision required for the reconstruction of b hadron decay vertices, the LHCb detector achieves optimal performance at a slightly lower instantaneous luminosity with respect to *e.g.* the ATLAS [46] and CMS [47] detectors. Moreover, it performs best if the instantaneous luminosity is kept constant throughout the LHC fill. These requirements are both achieved using an innovative technique known as "luminosity levelling". This procedure, consisting in shifting the beams transversely based on instantaneous feedback from the detector, is described in Ref. [50]. The process allows LHCb to operate with a lower number of simultaneous pp collisions in a bunch crossing, called *pile-up*, which is usually between one or two, depending on the run conditions.

Table 3.1 summarises the running conditions of the data collected by the LHCb detector from

[1] $\eta = -\ln\left[\tan\frac{\theta}{2}\right]$, θ being the angle between the beam axis and the particle momentum.

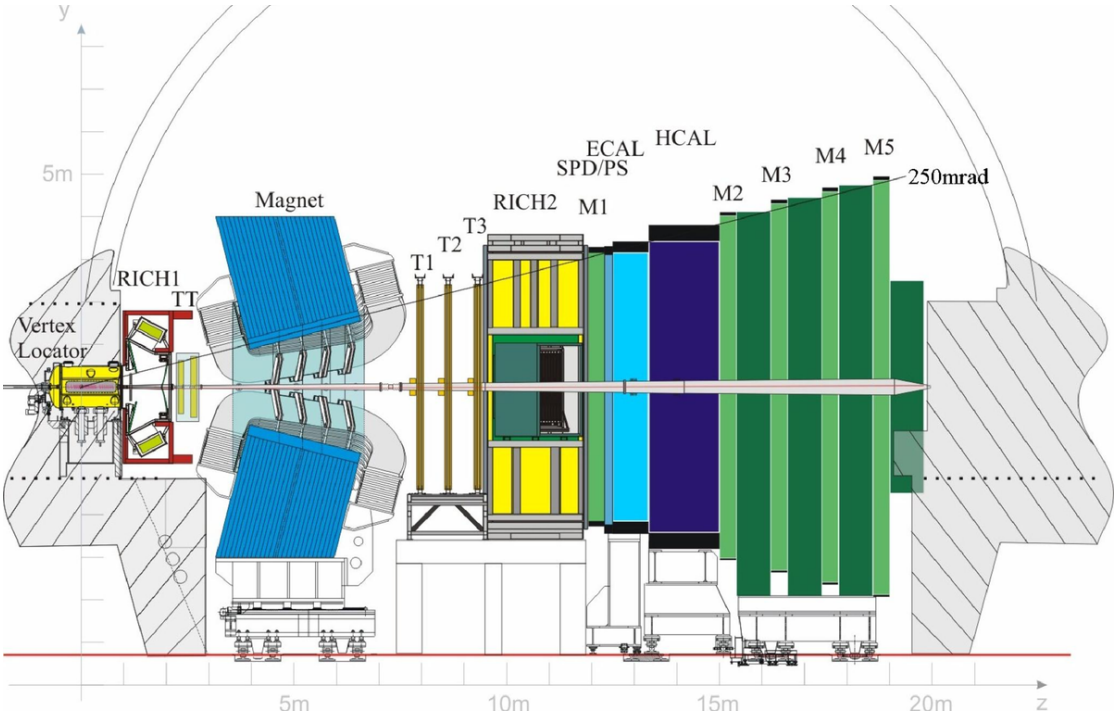

Figure 3.3: Schematic view of the LHCb detector operating in 2011-2018 [48].

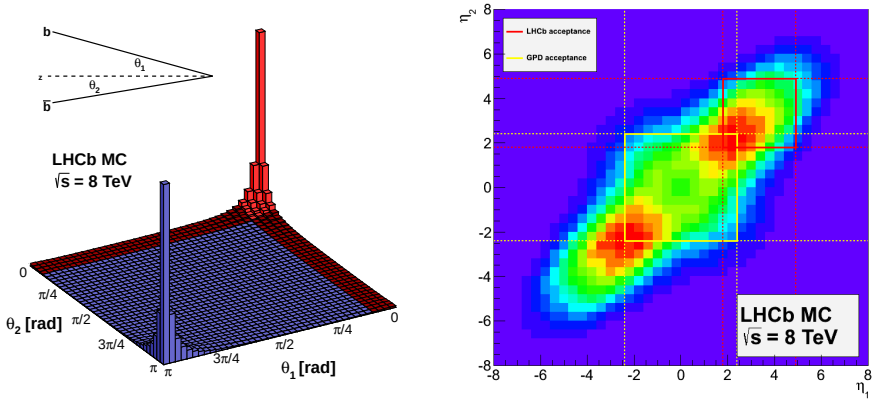

Figure 3.4: Angular distribution of $b\bar{b}$ quark pairs produced from proton-proton collisions at the LHC in terms of polar angles (left) and pseudorapidity (right), where the red areas represent the LHCb angular acceptance and the yellow one the acceptance of the ATLAS and CMS detectors (general purpose detectors) [49].

Table 3.1: Centre of mass energy and recorded luminosity for each year of data taking.

	Year	$\sqrt{s}$ [TeV]	$\mathscr{L}$ [fb^{-1}]
Run1	2011	7	1.0
	2012	8	2.0
Run2p1	2015	13	0.3
	2016	13	1.6
Run2p2	2017	13	1.7
	2018	13	2.2

2011 to 2018. The data collected in this period are used in this thesis work. The table also shows how the data are usually grouped in periods for analysis purposes, essentially by splitting the LHC Run2 period in two parts, called Run2p1 and Run2p2.

3.2.1 The tracking system

Several parts of the LHCb detector are aimed at measuring the trajectory of the particles, from which it is possible to infer their momenta. They are collectively referred to as the tracking system, and during the periods when the data used for this thesis work were collected, they included: the VErtex LOcator (VELO), the detector closest to the interaction point, the Tracker Turicensis (TT), a tracking station before the LHCb dipole magnet, and three tracking stations after the magnet (T1, T2, T3). The tracking system, in combination with the magnetic field, allowed LHCb to achieve an excellent momenta resolution of $\Delta p/p = 0.5\%$ for particles with momenta up to 200 GeV/c. In the following, a brief overview of all the mentioned subdetectors is given.

VErtex LOcator

The VErtex LOcator (VELO) is the closest detector to the pp interaction point, placed at only 8 mm from the beam axis. Its main purpose is to precisely measure the primary vertex (PV), *i.e.* the location of the pp collision, and the displaced secondary vertices (SV), where the heavy hadrons decay. This is particularly important for the LHCb physics program, since b hadrons travel for a non-negligible distance before decaying [51], and thus can be separated from other shorter living particles.

The VELO is structured in 21 modules, each of which is divided in two semi-circular halves of silicon micro-strip sensors. The design is made as such to be retractable, since the two halves will be closed around the beam interaction region only in presence of stable beams and left open otherwise, in order to avoid radiation damage due to beam instabilities.

The sensors provide measurements of the coordinates in the radial (R) and azimuthal (ϕ)

directions thanks to the different arrangement of the strips, as shown in Figure 3.5.

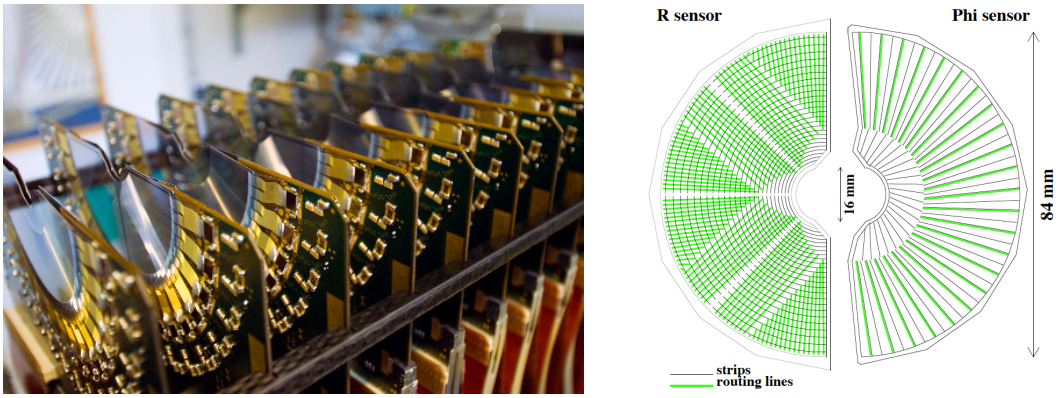

Figure 3.5: A photograph of one side of the VELO showing the silicon sensors and readout hybrids (left). Schematic view of an R and ϕ sensor (right) [52].

The VELO performance is described in details in Ref. [52]. The detector achieves a primary vertex resolution of 71 μm in the plane along $\hat{z}$ and of 13 μm in the transverse plane, for a typical LHCb event with 25 tracks, and an impact parameter [2] resolution of less than 35 μm for particles with transverse momentum larger than 1 GeV/c.

The Tracker Turicensis

The TT [53] is a tracking detector placed between the VELO and the dipole magnet. It is structured in four layers of silicon strip sensors, divided in two stations, TTa and TTb, separated by 27 cm along the beam direction, as shown in Figure 3.6. In the first and last layers the silicon strips are laid out along y direction and therefore provide a measurement of the x coordinate, while in the middle layers they are tilted by $\pm 5°$ in order to provide information also on the y coordinate, which helps reducing ghost hits in the typical events where multiple charged particles cross the detector. Each layer consists of half-layers with an overlap of few millimeters between each other, to avoid empty regions in the acceptance. Each half-layer is composed of 14 staves of 7 sensors (see Figure 3.6). The sensors are wired together in groups of one, three or four sensors depending on the distance from the beam axis, for readout purposes. Each silicon sensor is made of 512 strips with a strip pitch of 183 μm, providing a resolution of 50 μm on the hit position.

The Inner Tracker

The Inner Tracker (IT) [55] corresponds to the central regions, *i.e.* the ones closest to the beam pipe, of the T1,T2 and T3 tracking stations, downstream the dipole magnet. In order to ensure a high granularity, given the high occupancy in these regions, silicon microstrips sensors are used, similar to the ones used in the TT, but with a reduced number of strips (348). The layers

[2] The distance between the track and the PV at the track's point of closest approach to the PV.

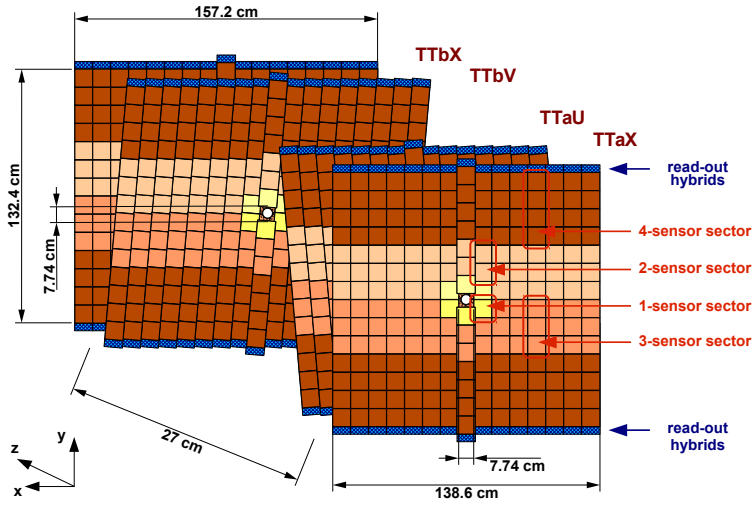

Figure 3.6: Schematic view of the TT layers [54].

follow the same $x-u-v-x$ orientation as in the TT. They consist of one- or two-sensors modules. One-sensor modules are placed at the top and bottom regions of the detector, and two-sensors modules at the two sides (see Figure 3.7). All the four sides contain a total of seven modules. The resolution on the hit position achieved by the IT is of 50 µm.

The Outer Tracker

The Outer Tracker (OT) [56] covers all the rest of the acceptance of the three tracking stations, surrounding the IT. A drift-tube technology is used, since the lower occupancy in this large active area permits a coarser granularity with respect to the IT. The OT number of layers and their orientation are the same as the ones described for the IT. Each layer consist of 18 modules, each containing 128 tubes, where the central ones are shorter to leave space for the IT (see Figure 3.7).

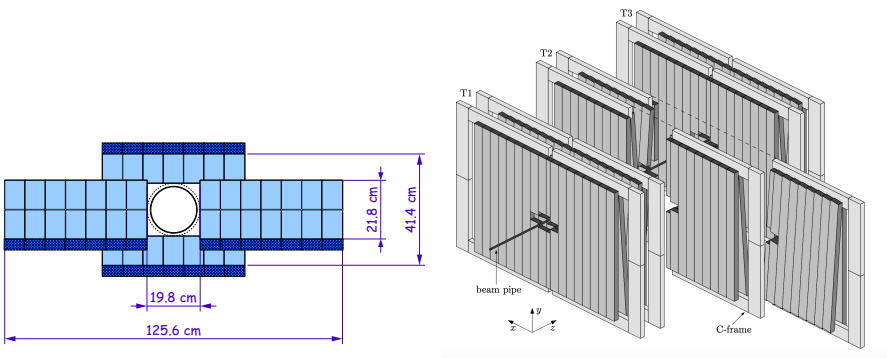

Figure 3.7: Schematic view of one of the IT layers (left) and the OT layout (right) [48].

The gas straw-tubes are 2.4 m long and 4.9 mm in diameter, filled with a mixture of Ar (70%),

CO_2 (28.5%) and O_2 (1.5%). The read-out electronics is sensitive to the drift time of the electron-ion clusters produced when a charged particle passes through the tube and ionises the gas. Then, by comparing the drift time with the bunch-crossing time, the hit position along the straw can be reconstructed with a resolution of 200 μm.

The LHCb dipole magnet

At the LHCb detector, a warm dipole magnet is placed between the TT and the T1–3 stations, to bend the trajectory of charged particles and thus to make it possible to infer their charges and their momenta from the curvature radius. The magnet provides an integrated magnetic field of about 4 Tm along the full tracking system (~ 10 m), bending the particles in the xz plane. Figure 3.8 shows a sketch of the dipole magnet and the intensity of the magnetic field on the z-axis.

The polarity of the magnet is regularly inverted when taking data, leading to two configurations usually called `MagUp` and `MagDown`, in order to check possible asymmetries of the detector performance.

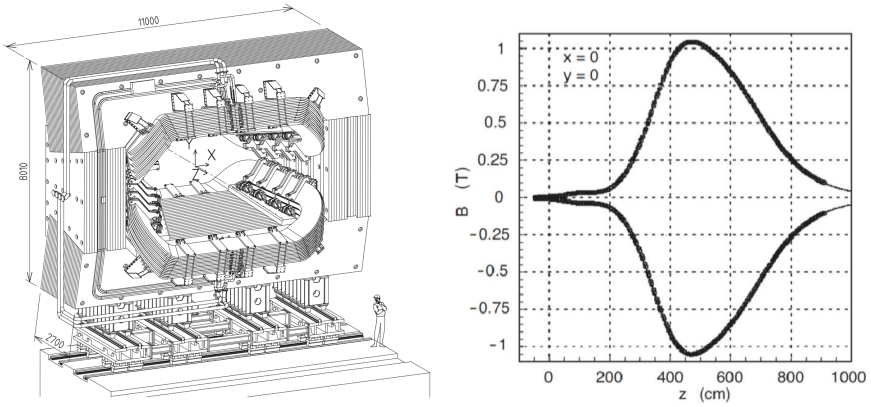

Figure 3.8: Schematic view of the LHCb dipole magnet (left) and magnetic field intensity along the beam axis (right) [48].

Track reconstruction

The pieces of information from the tracking subdetectors, described in the previous sections, are combined to reconstruct the trajectory of a particle travelling through the detector. The track reconstruction is achieved using several particle recognition algorithms, first looking for segments in one tracking detector, *e.g.* VELO seeds, TT seeds *etc.*, and then trying to extrapolate the track into another subdetector, finding the best-matching cluster. Depending on which subdetectors are used by the algorithms during the reconstruction, the tracks are usually divided in (see also Figure 3.9)

- VELO tracks: if only information from the VELO hits is used in the reconstruction. This

means having an accurate identification of the primary vertex, but without momentum estimation.

- Upstream tracks: when VELO hits are combined with TT hits, typical of low momentum particles that are bent out of the detector acceptance by the magnetic field.
- Long tracks: the ones travelling through the whole tracking system and thus with the most precise momentum estimation. They are the ones usually most used for physics analysis (and the type used in this thesis work).
- Downstream tracks: which are similar to the Long Tracks but with hits only in the TT and T stations. They usually refer to those particles that decay outside the VELO, and thus lead to tracks with worse momentum and impact parameter resolution.
- T tracks; with hits only in the T stations.

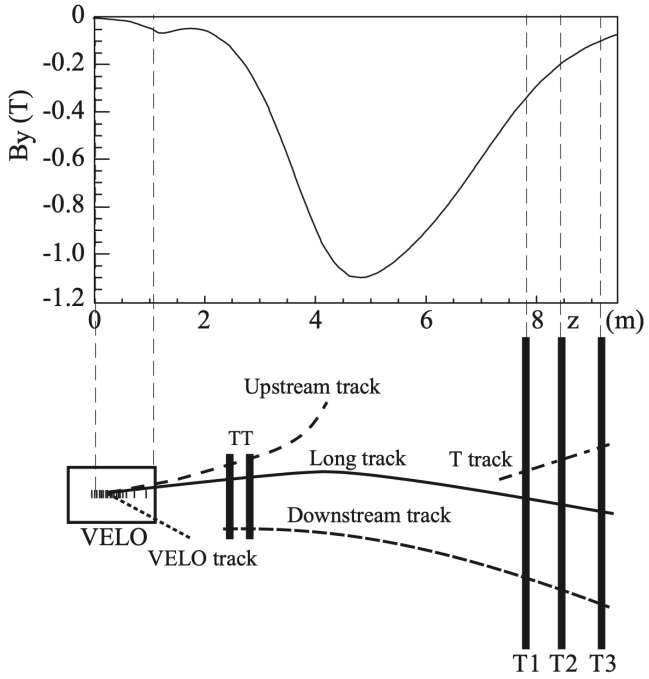

Figure 3.9: Sketch describing the different type of tracks used in LHCb measurements. The magnetic field component B_y is plotted above for reference [48].

3.2.2 Particle Identification

The LHCb physics program heavily relies on the ability of the detector to distinguish between the different types of charged and neutral particles produced from pp collisions. The so-called particle identification (PID) is achieved by combining information from several subdetectors: two Ring Imaging Cherenkov (RICH) detectors, for the identification of charged particles (*e.g.* K, π, p); one electromagnetic calorimeter (ECAL) and one hadronic calorimeter (HCAL), for neutral and charged particles energy measurements; and several muon stations, to specifically

tag muons. In the following, all the mentioned subdetectors are briefly described.

Ring Imaging Cherenkov detectors

A Ring Imaging CHerenkov (RICH) detector exploits the property of charged particles to emit a cone of light, known as Cherenkov radiation, when travelling faster than the velocity of light in the same medium. The opening angle of the radiation cone is related to the refractive index of the medium n, to the velocity of light c/n and to the velocity of the particle v ($v/c = \beta$)), via

$$\cos\theta_c = \frac{1}{n\beta}. \tag{3.2}$$

Hence, by measuring the opening angle of the radiation cone emitted by the particle, it is possible to infer its velocity. The mass of the particle, and thus its type, can be then estimated by combining this information with the momentum measurement from the tracking system.

The LHCb detector includes two RICH detectors [57], filled with different media, also called *radiators*. One is placed between the VELO and the TT, filled with C_4F_{10} ($n = 1.0014$),[3] and the other one is placed after the tracking stations T1–3, filled with CF_4 ($n = 1.0005$). The use of two RICH detectors with different radiators allows LHCb to be sensitive to a wider momentum spectrum: between 2 and 60 GeV for the RICH closest to the interaction point (RICH-1), and between 15 and 100 GeV for the one downstream (RICH-2). The emitted radiation is reflected and focused by a series of mirrors into photomultipliers, where it is detected.

Figure 3.10 shows a schematic view of the RICH1 detector and the excellent performance achieved in the separation of different particles types, especially between charged kaons and pions, which behave similarly in the rest of the detector.

The Cherenkov angles measured in the two RICH detectors are further combined with the momentum information coming from the tracking system, using an overall event log-likelihood algorithm. This allows to assign, for each track in the event, a likelihood for different mass hypotheses, such as the electron, muon, pion, kaon or proton masses.

Calorimeters

The calorimeters system provides measurements of the electron, photon and hadron energies, contributing also to their identification. In addition, the measured energy in the transverse plane E_T is employed as a discriminating variable in the hardware trigger (as explained in Section 3.2.3).

The calorimeters measure the energy loss of a particle that interacts with an absorbing material and produces a cascade of secondary particles (shower), that will hit active materials (scintillators) generating photons, proportionally to the energy of the incoming particle. The

[3] In `Run1` used in combination with (SO_2) ($n = 1.03$)

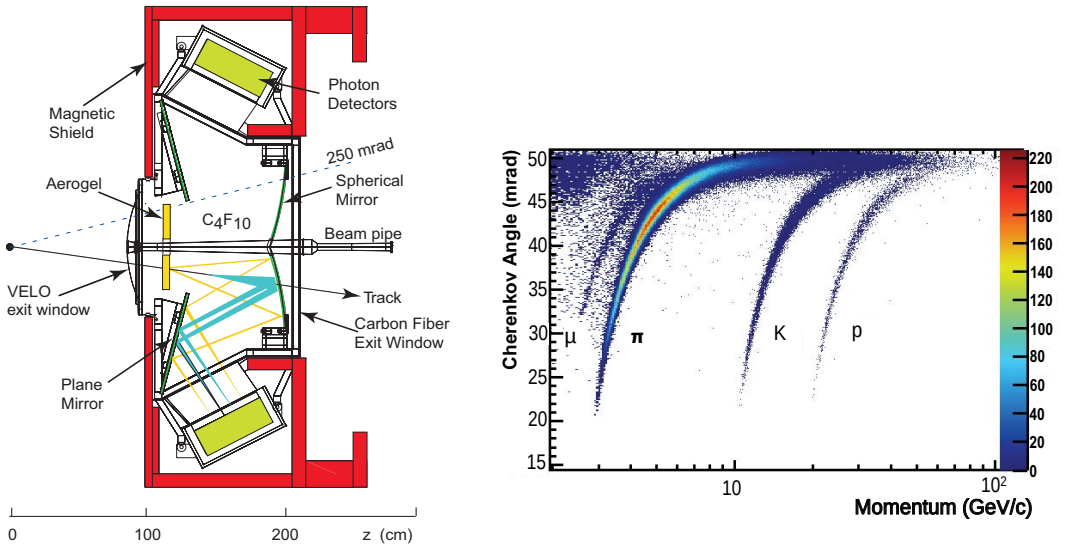

Figure 3.10: Schematic view of the RICH-1 detector (left) [48] and reconstructed Cherenkov angle with respect to the particle momentum (right) [57]. The discriminating power is clearly visible, given the separation of the different bands for the different types of particles.

entire shower, and thus the total energy of the particle, is finally reconstructed by detecting the emitted photons using photomultipliers.

Different types of particles undergo different mechanisms of energy loss, leading to differences in the reconstruction process. This is a crucial point for this thesis work, the aim of which is to precisely measure the relative rates of the same physics process, $B^+ \to K^+\pi^+\pi^-\ell^+\ell^-$, with electrons or muons in the final state (see Section 2.2). Thus, it is worth to mention the differences between the various energy loss mechanisms in the material.

- *Electrons* produce a large quantity of Bremsstrahlung [4] radiation. The emitted photons can convert into e^+e^- by pair production, where each particle of the pair can in turn emit photons by Bremsstrahlung and so on in a cascade, creating the so-called electromagnetic shower. These processes will stop when the mean energy of the particles involved will be lower than the critical energy, that is the energy in which the energy loss by radiation is equal to that by ionisation. A characteristic measure of the material is the so-called radiation length,[5] used to design the length of the calorimeter needed to contain the full shower.
  The measurement of the electron energy can be particularly problematic when electrons emit Bremsstrahlung photons *before* the magnet. In fact, the trajectory of the photons, being neutral particles, will not be affected by the magnetic field, and thus photons will end up in a different calorimeter cell with respect to the electron that produced them. That is why, during reconstruction, a Bremsstrahlung recovery algorithm [48] is applied

[4] Bremsstrahlung is the process in which electrons or positrons lose energy by emitting photons.

[5] After having covered a radiation length (X_0) in an absorber material, the electron energy is reduced by a factor of $1/e$.

to the electron tracks, in order to add possible photon clusters seen in the calorimeter. The momentum of the photon is added to the one of the electron only if the cluster position in the ECAL plane corresponds to the one extrapolated from the direction of the electron before the magnet, and if the photon satisfies loose identification requirements.

- *Hadrons* also produce showers by ionisation and by the interaction with the nuclei of the detector material. These showers are longer and wider than those generated by electrons, including also hadrons (*e.g.* pions) as secondary particles, some of which can in turn develop electromagnetic showers. Similarly to the electron showers, the development of the hadronic showers is measured using the interaction length λ_I.
- *Muons* have small energy loss, travelling thought the whole detector as minimum-ionizing particles (MIPs) throughout the muon momentum range detectable at LHCb.

Figure 3.11 shows the different signatures left by different particle types in the calorimeter system and, in general, in the detector.

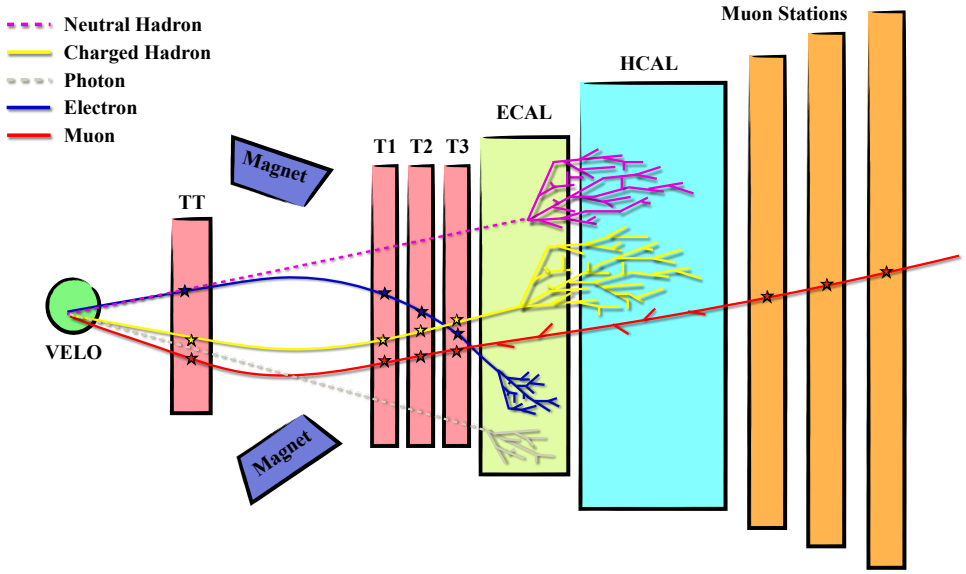

Figure 3.11: A sketch showing the signatures of the different particle types travelling through the LHCb detector (top view). Electrons (blue) and photons (grey) produce electromagnetic showers in the ECAL, with the electrons also leaving hits in the tracking stations. Hadrons also produce showers, but in the HCAL, with the charged ones (yellow) providing also hits in the tracking stations. Muons (red) travel through the detector, providing hits in all the tracking stations and the muon system.

In view of this, the calorimeter system is composed of

i. The Electromagnetic Calorimeter (ECAL) [58], designed as a sampling calorimeter, *i.e.* composed of alternating layers of absorbing materials, in this case lead, and scintillator pads. The total of 66 layers, with a thickness of 2 mm for the absorbing and 4 mm for the

scintillator layers, covers 25 X_0, ensuring the full containment of the electromagnetic shower.

ii. The Hadronic Calorimeter (HCAL) [59], again with a sampling structure but with iron used as absorber material. The 26 layers, for a total length of 19.7 cm, correspond to 5.6 λ_I, providing a good estimation of the energy of the hadronic showers.

iii. The Scintillating Pad (SPD) and Preshower (PS) detectors [60], placed in front of the ECAL and separated from each other by a 15 mm-thick lead layer (corresponding to ~ 2.5 radiation lengths). The main goal of the SPD is to tag charged particles, and thus help the electrons/photons separation, while the PS detector separates hadrons, mainly pions, from electrons, using their different shower lengths.

The cells of the subdetectors of the calorimeter system have increasing dimensions for the inner, middle and outer regions, in order to cope with the variation of the hit density with respect to the radial distance from the beam axis.

The energy resolution obtained by the calorimeter system, as shown in Refs. [58, 59] for the ECAL and HCAL respectively, is

$$\frac{\sigma_E}{E}(\text{ECAL}) = \frac{10\%}{\sqrt{\text{E[GeV]}}} \oplus 1\% \qquad \frac{\sigma_\text{E}}{\text{E}}(\text{HCAL}) = \frac{69\%}{\sqrt{\text{E[GeV]}}} \oplus 10\%. \tag{3.3}$$

The Muon system

The identification of muons is of fundamental importance in general for the LHCb physics program (as shown in Section 2.2), and in particular for this thesis work, which analyses $B^+ \to K^+\pi^+\pi^-\mu^+\mu^-$ decays, together with the $B^+ \to K^+\pi^+\pi^- e^+ e^-$ ones. As already mentioned in the above sections, muons are expected to travel through the whole detector, while the majority of the other particles are expected to be stopped by the detector materials (see Figure 3.11). That is why at the very end of the LHCb detector four stations (M2-M5) of multi-wire proportional chambers are placed, with absorber layers of lead in between. An additional station (M1) is placed upstream the calorimeter system, to provide a precise position measurement before the multiple scattering happening in the following material, where the inner part ($\sim 3\,\text{m}^2$) is equipped with 12 gas electron multiplier (GEM) detectors, given the higher occupancy. Both types of chambers (multi-wire and GEM) detect the electrons avalanches produced when charged particles traverse and ionise the gas filling them. The main difference among the two is the presence of a dielectring foil in the GEM detectors, which separates the movement of the ions from the readout electrode. In the multi-wire chambers, the ions generated in the avalanche remain in the gas for $\mathcal{O}(10^{-5})$ s, while the ones generated in a GEM avalanche leave the hole within $\mathcal{O}(10^{-7})$ s, explaining why the GEMs are placed in the higher occupancy region of the detector.

The layout of the muon system is shown in Figure 3.12. The same figure also shows the different

segmentation in each of the stations, with four regions with dimensions and segmentation scaling as $1:2:4:8$, in order to cope with the different irradiation levels according to the distance from the beam. In general, the M1, M2 and M3 stations provide the main contribution to the measurement of the momentum of the muon candidates, while the main purpose of the M4 and M5 stations is the identification of penetrating particles.

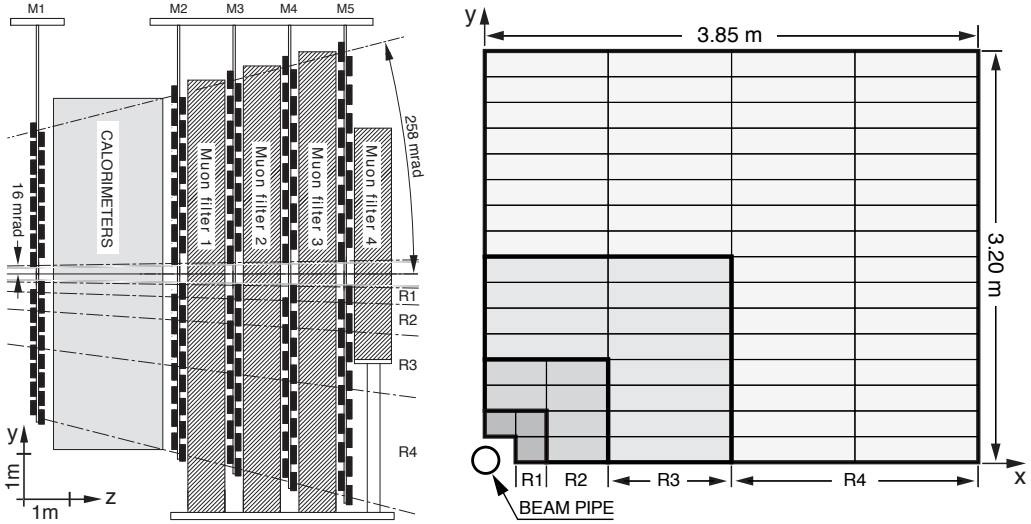

Figure 3.12: Side view of the muon system (left) and the scaling granularity of one muon station (right) [61].

The muon identification can be divided in three steps [62]:

i. A loose binary selection, referred to as *isMuon*, based on the number of stations where a hit is found. The selection depends on the momentum of the particle and on the definition of a field of interest in the station, from track extrapolation. This selection leads to a reconstruction efficiency of $95-98\%$, with a probability of hadrons to be misidentified as muons, mainly pions and kaons, of the level of 1%.

ii. A likelihood computed for the muon and non-muon hypotheses, combining the hits in the different muon stations with charged particles trajectories reconstructed in the tracking system. For a given particle, the logarithm of the ratio between the muon and non-muon hypotheses, called μDLL, is used as discriminating variable.

iii. The muon system likelihoods above, *i.e.* muon and non-muon, are combined with likelihoods provided by the RICH systems and by the calorimeters. The non-muon hypothesis is set to the pion hypothesis. The difference of the combined log-likelihoods for the muon and pions hypotheses (DLL) is then used to identify the muons. This allows to reduce the hadron misidentification probabilities to 0.6%, while preserving a total efficiency above 93%. After this, about 60% of the misidentification comes from real muons produced in decays in flight of pions and kaons.
It has to be noted that DLLs are in general computed not only for muons, but for all the

particles, *e.g.* electrons, kaons, pions, with information from the dedicated subdetectors depending on the particle type.[6]

In addition, the muon system provides a fast measurement of the transverse momentum used by the trigger (as described in Section 3.2.3), achieved by simply requiring hits in all the stations and combining this information with the interaction point position.

3.2.3 The Trigger System

At the LHC, the collisions of proton bunches happen with a very high rate (40 MHz), which makes it necessary to use a series of filters aimed at storing on disk, for later analysis purposes, only the events that are believed to be interesting. These filtering steps, collectively known as the trigger system [63], have the goal to reduce the event rate from 40 MHz to few kHz (as shown in Figure 3.13). The steps include:

- The `Level-0 (L0)` trigger, a hardware-based trigger that uses information on the transverse energy deposits E_T from the calorimeters, combined with hits in the PS and SPD detectors. These measurements aim at checking for high-energy clusters due to the presence of electrons, photons and hadrons in the events. In addition, hits in the muon stations help in selecting events with one or two high-momentum muons. The L0 trigger applies real-time decisions, based on the single subdetectors measurements, reducing the event rates from 40 MHz to 1 MHz, where the whole detector can be read out.
- The `High Level Trigger (HLT)`, a software-based trigger that selects events based on a more complete event reconstruction. The HLT is divided in two steps. The first one (HLT1) uses information from the VELO to partially reconstruct the tracks, checking the quality of the impact parameter and the primary vertex identification. The second one (HLT2) uses a full reconstruction of the event to apply a number of custom selections for specific physics decays, being able to work with higher level variables such as reconstructed masses, decay lengths, secondary vertices *etc*. The HLT reduces the event rates from 1 MHz to 5 kHz for the data collected in the `Run1` period, and from 1 MHz to 12.5 kHz for those taken during `Run2`. The changes in the second period are due to the inclusion of a real-time alignment of the detector, which allows a better calibration, in view of the upgrade of the trigger for `Run3`, where the hardware-based selection is completely removed (as it will be described in Section 3.3).

Finally, another filtering step is added, where loose requirements are applied to fully reconstructed physics events. This step is called *stripping* and the so-called *stripping lines* are a series of criteria that can be different with respect to the physic decay of interest. Only the outputs of the stripping selections are saved to disk and made available to the collaboration.

[6] Where in general the *non-particle* hypothesis is set to the pion hypothesis.

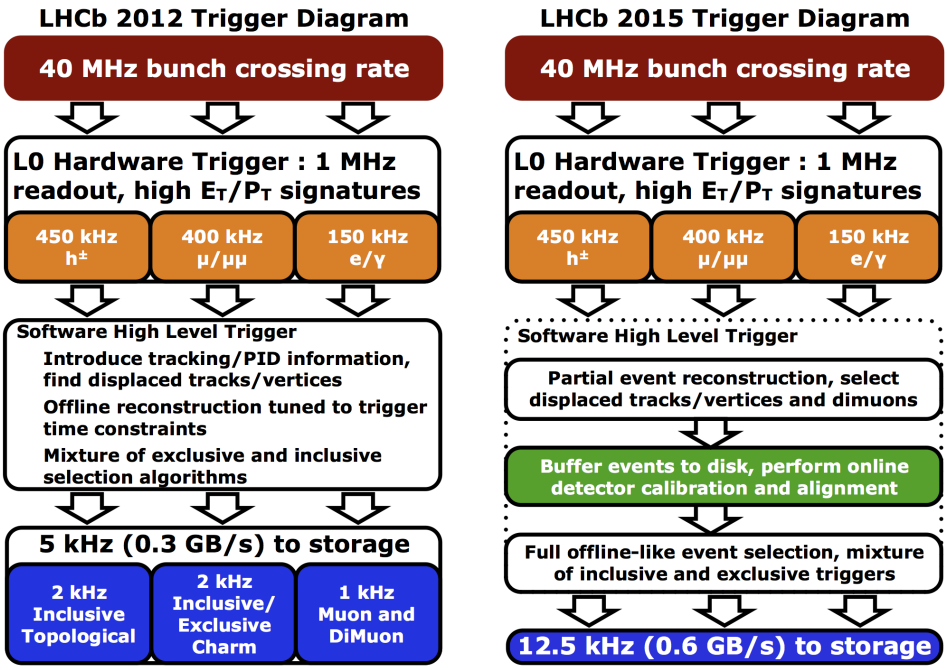

Figure 3.13: A sketch showing the LHCb trigger steps implemented to reduce the event rate from the nominal 40 MHz of the LHC to 5 kHz for Run1 (left) and 12.5 kHz for Run2 (right) [64].

3.3 The LHCb detector upgrade

The LHCb detector, as described in the previous section, operated from 2011 to 2018, successfully recording 9fb^{-1} of data. Nevertheless, many key measurements of flavour physics, like the ones introduced in Section 2, are still highly limited by the size of the available dataset. That is why it is of crucial importance that the detector is able to fully exploit the dataset that will be delivered during the LHC Run3 and Run4 periods, *i.e.* from 2022 to 2032, at the end of which an integrated luminosity of $\sim 50\text{fb}^{-1}$ is expected to be collected.

During these periods, the LHCb detector is required to cope with an instantaneous luminosity five times larger than the one recorded in the previous runs, and to read out the data at the same LHC crossing rate of 40 MHz. An upgrade of most subdetectors was required in order to handle both the increased radiation and the increased occupancy that comes with a five-fold increase in pile-up [65]. The subdetectors upgrades are described in the following sections, with a focus on the upgrade of the downstream tracking stations to a scintillator fibre (SciFi) tracker, relevant for the PhD work.

In addition, to cope with the increased read-out rate, a new trigger system was developed, where the L0 hardware level is completely replaced by a software selection based on a full event reconstruction, and thus much more efficient than the simpler L0 criteria on the particles momenta or energies. Figure 3.14 shows the new trigger system where the full detector is read out at the non-empty bunch crossing rate (30 MHz). The first level of the software trigger

(HLT1), running on GPUs, performs a first reconstruction of the event by using information from the tracking and muon systems. The HLT1 applies one- or two-track based algorithms, selecting high-momenta tracks significantly displaced from the PV. The selected events are buffered on disks for a detector real-time alignment and calibration [66], in order to ensure the quality of the track reconstruction. The second level of the software trigger (HLT2) fully reconstructs tracks from the calibrated events, with improved precision in the entire momentum range, adding particle identification and track quality information. A mix of inclusive and exclusive particle selection algorithms is applied at this point, to finally reduce the event rate to 2-5 GB/s, which are saved for offline analysis. More information on the upgrade of the LHCb trigger system can be found in [66–68].

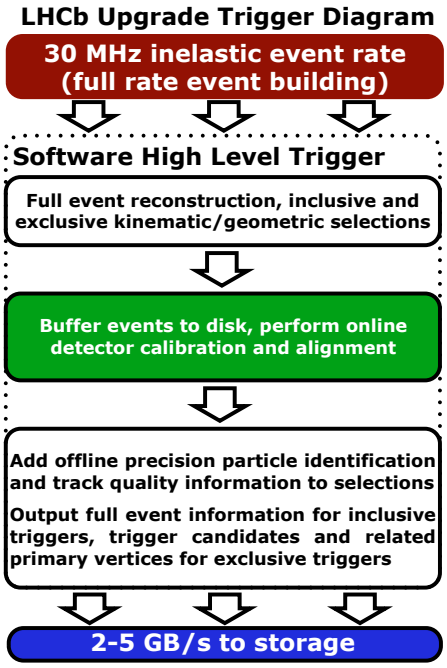

Figure 3.14: Scheme of the upgraded LHCb trigger system operating from Run3. To be compared with Figure 3.13 showing the Run1 and Run2 trigger systems [64].

3.3.1 The tracking system upgrade

All the subdetectors of the tracking system (described in Section 3.2.1) were replaced with upgraded versions, in order to at least maintain the same performance as in the Run1 and Run2 periods while facing the increase of the instantaneous luminosity. In the following, a brief description of the upgrade of each subdetector is given.

- The VELO detector will have to face a radiation dose and a hit multiplicity of approximately one order of magnitude larger than in the previous runs, by maintaining at least the same high efficiency of his predecessor in finding tracks right after the pp collisions take place. A good parameter of the VELO performance is the impact parame-

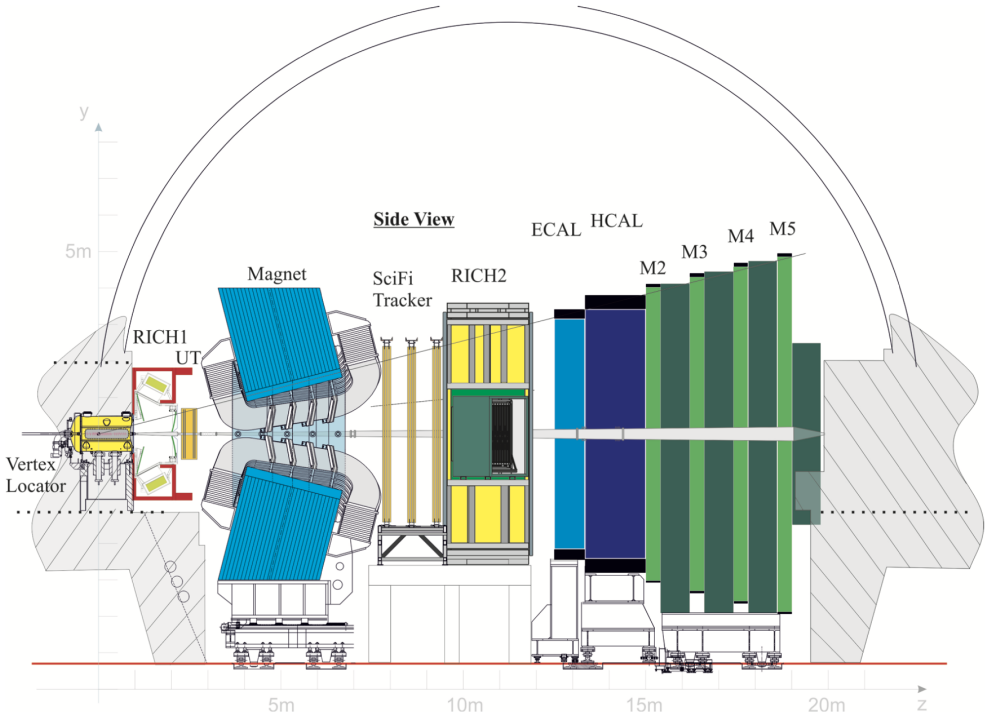

Figure 3.15: The LHCb upgrade detector [69]. To be compared with the LHCb detector operating during the LHC Run1 and Run2 data taking periods (see Figure 3.3).

ter resolution, defined in Section 3.2.1, which heavily depends on the proximity of the first measured hit to the pp interaction point, and on the material contribution of the foil which separates the secondary vacuum of the VELO from the primary beam-pipe vacuum. Therefore, the new VELO was designed to reduce the inner radius of the active silicon detector from 8.2 mm to 5.1 mm, with a new foil with half the material budget of the previous one. In addition, in order to deliver data at 40 MHz in the upgraded conditions, the silicon strip sensors have been replaced with hybrid pixel sensors, thus passing from a segmentation in a R,ϕ geometry to a squared one. The sensors are arranged in modules and cooled down by an innovative silicon micro-channel cooling system with circulating bi-phase CO_2, which has to maintain the sensors at a low temperature for the full detector lifetime. A more detailed description of the VELO upgrade can be found in Ref. [70].

- The Tracker Turicensis (TT) is replaced by the Upstream Tracker (UT), made of four planes of silicon microstrip detectors with the same $x-u-v-x$ orientation as the TT. The UT silicon microstrips, thinner and with a finer segmentation than the TT sensors, are arranged in each plane in vertical units, called *staves*, with the silicon sensors placed on both sides of each stave, in order to ensure a vertical overlap. This arrangement considerably improves the acceptance with respect to the TT and reduces the amount of material seen by the particles. The UT has a very high single hit efficiency ($\sim 99\%$), helping in reducing the rate of fake tracks created by possible mismatches between the

VELO and the downstream tracker hits. More details on the UT can be found in Ref. [69].

- The Inner Tracker (IT) and the Outer Tracker (OT) are both replaced by a single detector, the Scintillating Fibre (SciFi) tracker, made of 2.5 m long scintillating fibres with a diameter of 250 µm. The fibres emit light in the blue spectral region when traversed by a charged particle, which is then read out by silicon photomultipliers. The design was chosen as such to achieve a hit resolution less or equal than 100 µm and a single hit efficiency as large as possible (≈ 99%) over the full 6 m × 5 m detector area, covering the nominal LHCb acceptance. A more comprehensive description of the SciFi tracker is given in the following section and more information can be found in Ref. [69].

Figure 3.15 shows a sketch of the entire Upgrade I LHCb detector with the new tracking systems, while Figure 3.16 shows pictures of the upgraded Velo, UT and SciFi detectors.

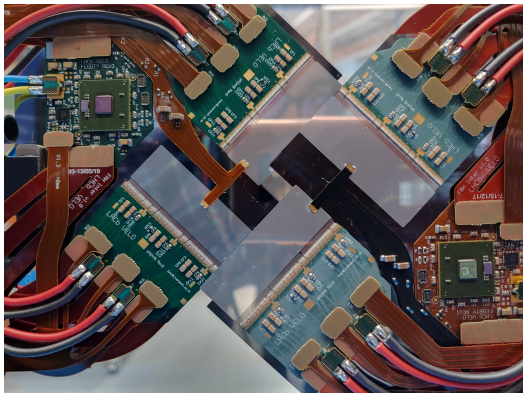

(a) The VELO detector

(b) The Upstream Tracker

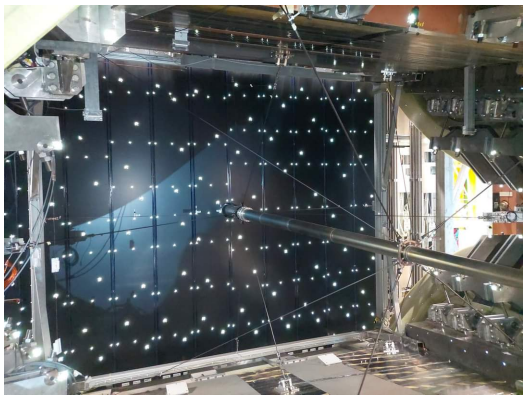

(c) The SciFi Tracker

Figure 3.16: Pictures of the upgraded detectors of the LHCb tracking system.

3.3.2 The Scintillating fibre Tracker

The SciFi tracker serves for measurement of the momenta and charge-sign of charged particles. The SciFi design has been driven by the requirements summarised below.

- A very high hit detection efficiency ($\approx 99\%$) while keeping a low noise over signal rate ($< 10\%$) at any location on the detector.
- A spatial resolution on a single hit less than or equal to 100 μm. In fact, since the matching with the VELO hits is already dominated by the effects of the multiple scattering in the upstream tracker, a better resolution is not needed.
- A thickness X of each detector layer is such that $X/X_0 \leq 1\%$, where X_0 is the radiation length, to reduce the effects of multiple scattering before the calorimeter system.
- Read-out electronics capable of running at a frequency of 40 MHz.
- The capability to operate with the above requirements for the full LHC `Run3` and `Run4` periods, collecting up to 50 fb^{-1} of integrated luminosity.

Detector Layout

Like the previous IT and OT, the SciFi tracker consists of three stations (T1, T2, T3) placed between the magnet and the RICH2 detector. Each station is made of four layers (L0, L1, L2, L3) following the usual $x-u-v-x$ orientation. The layers of each station are separated by 20 mm from each other, and have a circular hole in the centre to allow the passage of the beam-pipe. A schematic view of one station of the SciFi detector is shown in Figure 3.17 (left).

As it can be seen in the figure, each layer consists of a series of 5-metre-long vertical modules, each of which is composed of eight ~ 2.4 m long and ~ 13 cm wide mats made of staggered layers of scintillating fibres, half of them going from the beam pipe position ($y = 0$) upward along the vertical axis y, and the other half downward on the same axis. The layers have 10 modules each, except for the ones in the T3 station which are equipped with an additional module on both sides, for a total of 12 modules, to account for the increasing acceptance in the x direction. Mirrors are placed between the top and the bottom mats, to reflect additional light back to the read-out system.

At the top and at the bottom of each module, the light emitted by the scintillating fibres is read out by 16 arrays of silicon photomultipliers, *i.e.* four arrays per mat, each array containing 128 channels with a channel pitch of 250 μm.

Given the complexity of the SciFi tracker geometry, a naming scheme is used to identify each part of the detector, as shown in Figure 3.17 (right). A given half-module (Mv) will be identified by the combination of the station (Tx), the layer (Ly) and the quadrant (Qz) in which the module is located (where v, x, y, z run over the number of stations, layers, quadrants and modules, respectively).

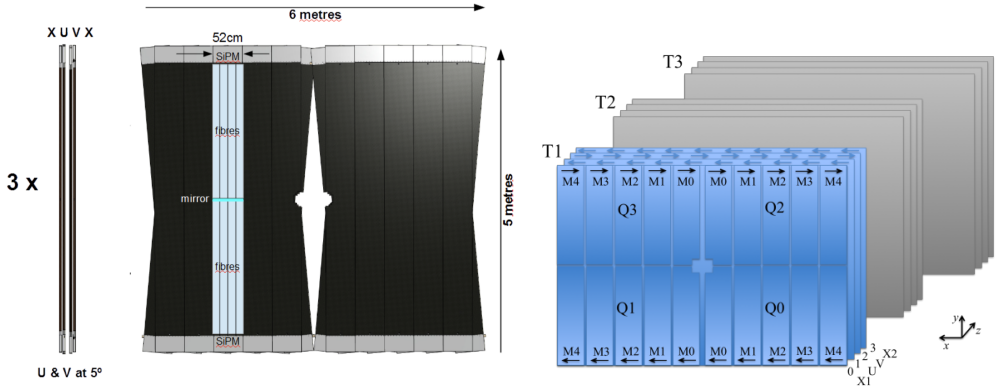

Figure 3.17: Schematic view of one layer of the SciFi tracker (left). Naming scheme used to identify the detector components (right). The pictures are taken from internal material for SciFi presentations.

Scintillating fibres

A schematic view of a scintillating fibre used in the the SciFi tracker is shown in Figure 3.18. The fibres have an average total diameter of 250 µm and they are composed of a scintillating core and a cladding structure with decreasing refractive indices that allows the light produced after the passage of a charged particle to be captured by total internal reflection.

The fibres have been chosen for their high light yield of 8000 photons emitted per MeV of deposited energy after ionisation. This means that, given the dimension of the fibre core, one can estimate that ~ 300 photons are emitted by the passage of a MIP. Furthermore, the fibres have been selected also for their small decay constant, measured to be 2.4 ns. Another important parameter for the performance of a fibre is the attenuation length, *i.e.* the length over which the intensity of the emitted scintillation light is attenuated by $1/e$, which for the chosen fibre is approximately 3.5 m, but is expected to degrade in time due to the radiation doses to which the fibres will be exposed during the whole LHCb operation time.

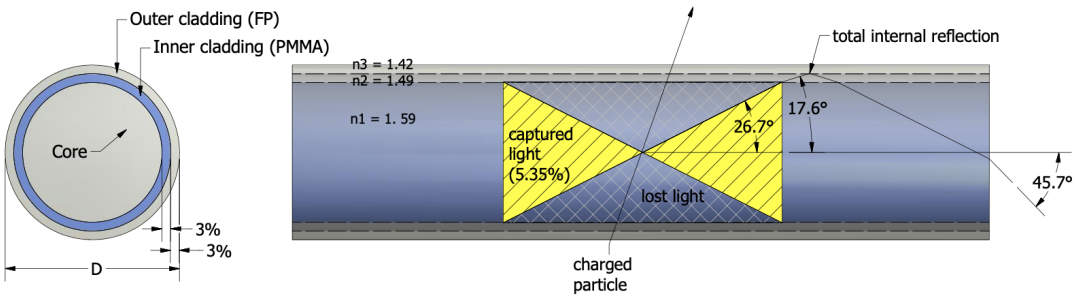

Figure 3.18: Schematic representation of the double-cladded fibre composing the SciFi tracker [71]. The minimum trapping efficiency of 5.3% of the solid angle is also shown, corresponding to the light generated by ionisation of a charged particle emitted with an angle of 26.7°.

Six layers of scintillating fibres are wound together in a honey-comb structure to form a fibre mat, as shown in Figure 3.20. Finally, a mirror is put at one end of the mat in order to reflect residual light back to the read out system, placed at the opposite side of the mat.

Eight fibre mats are combined to form a single vertical module, with four mats going from the beam pipe position upwards and four downwards. The material thickness of a single module is estimated to be 1.03% of a radiation length, for perpendicular tracks, thus fulfilling the design requirements.

Silicon photomultipliers

The photons produced along the direction of the incoming particle are then propagated through the fibres and detected by arrays of silicon photomultipliers (SiPMs), shown in Figure 3.19. An array contains 128 channels, made of two chips of 64 SiPM channels, where each channel is composed of 4×26 pixels of dimension of 62 µm × 57 µm each. One pixel is a reverse-biased single photon avalanche diode which operates in Geiger-Müller mode, *i.e.* is biased above the so-called breakdown voltage. The basic principle is that an absorbed photon can create an electron-hole pair in the depletion region, which is then separated and accelerated by the electric field, resulting in a self-sustaining avalanche. A SiPM channel is read out by combining the detected signals of each pixel, so that the detected current is proportional to the number of incoming photons. The peak value of the photon detection efficiency (PDE) for such SiPMs is measured to be approximately 45%. The PDE, together with the aforementioned light yield, attenuation length and trapping fraction of the scintillating fibres, yields to a number of 2-3 photoelectrons detected in the SiPMs for each fibre.

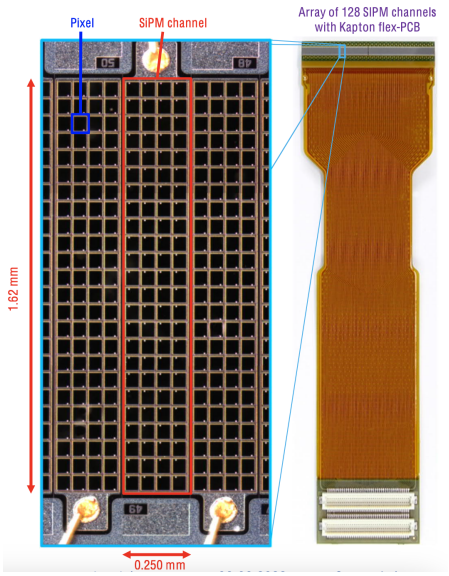

Figure 3.19: Zoom of a single array of SiPMs channels, each formed by 104 photodiodes (pixels), mounted on flex cable [72].

The SiPMs are then coupled to the SciFi modules, encased in *cold-boxes*, which cool down the irradiated SiPMs by means of a cooling liquid circulating in vacuum insulated lines. The SiPMs are cooled to a temperature of −40°C, in order to reduce the dark current rate (DCR), *i.e.* the current circulating in absence of signal photons. It is estimated that the DCR is reduced by a factor of two for every 10 degrees of cooling. By the end of Run4, a DCR of 10 MHz is expected per SiPM array when cooled to this temperature.

Front-end electronics

The Front-end (FE) electronics read out signals from the SiPMs, operating at the upgrade requirement of 40 MHz frequency. The FE electronics consists of three types of boards. The first board includes a custom integrated circuit (ASIC) called PACIFIC, which amplifies, shapes and digitizes the output of two arrays of SiPM channels, integrating the signal over the LHC bunch-crossing rate.

Given the arrangement of the scintillating fibres inside the fibre mats, one single SiPM channel does not read the photons emitted by one fibre, but rather covers a section of the mat including several fibres, as shown in Figure 3.20. A charged particle will thus induce signal in more than one SiPM channels that must then be clustered together. This is the responsibility of the second type of board, called Cluster board, that through Field Programmable Gate Arrays (FPGAs), groups neighboring SiPM channels exceeding customisable current thresholds.

Finally, the cluster data are sent to the Master board, which transfers them through optical links to the data acquisition system (DAQ).

To each end of a vertical module two sets of FE electronics are attached, also called HROBs (Half Read-Out Boxes), each containing four PACIFIC boards, four Cluster boards and one Master board, as shown in Figure 3.21.

The cooling of the FE boards is based on demineralised water at 19°C, which will limit the temperature of the electronics to a maximum of 50°C [69].

During the commissioning of the SciFi tracker, I monitored the temperature of the FE electronics in the first cool down tests of the SiPMs, by analysing the temperatures detected by several sensors placed on the boards. The aim of the study was to check if the board temperatures were independent of location on the detector, stable in time and independent of the temperature of the SiPMs cooling liquid. This was found to be the case, where a stable temperature over time periods (lasted from a minimum of three hours to a maximum of 14 hours) was observed, independent of the temperature of the cooling liquid, studied at −10°C, −30°C and −50°C, and with small differences over the various FE sets of the detector. An example of the trending of the temperatures over time is shown in Figure 3.21 (right), where, as expected, the PACIFIC boards exhibit a slightly higher temperature given their computational effort.

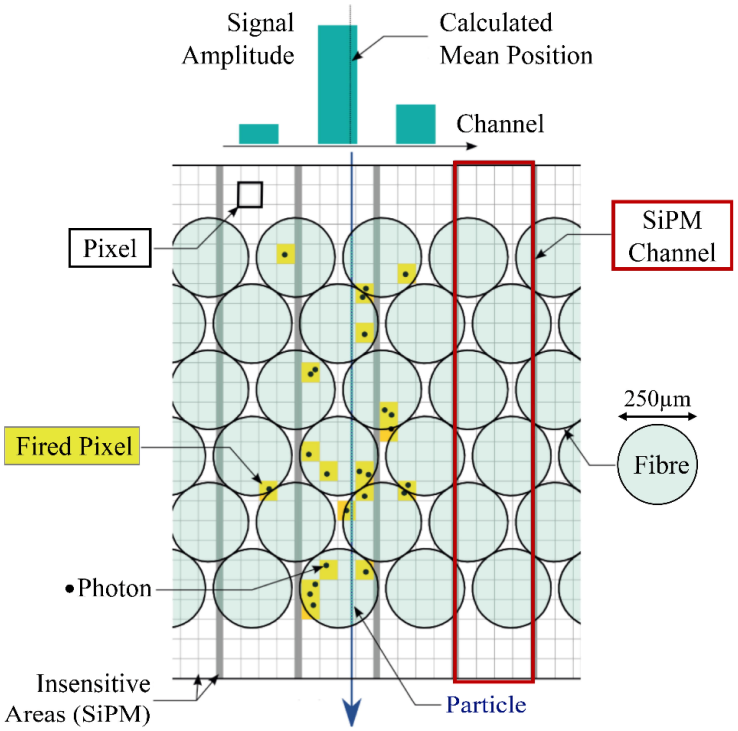

Figure 3.20: Sketch of the clustering of SiPMs channels activated by the passage of a charged particle through the scintillating fibres [72].

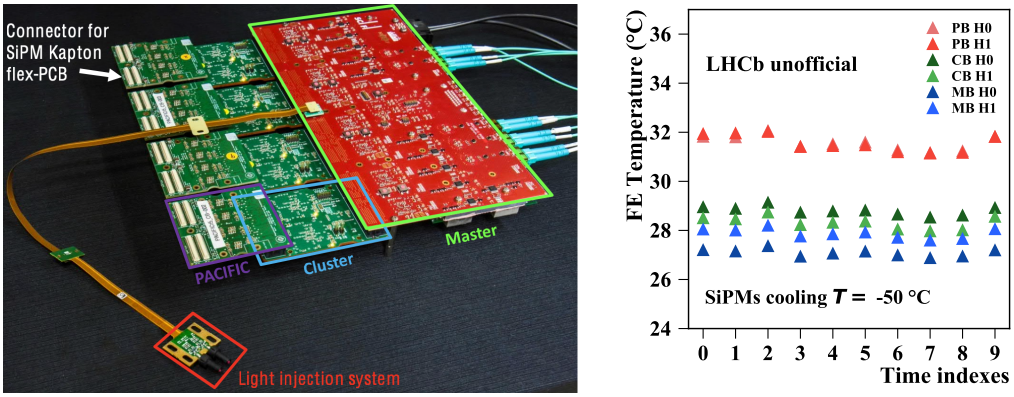

Figure 3.21: Picture of one set of FE electronics (HROB) composed by the three types of FE boards (left) [72]. Trend of the temperatures detected on the FE boards over time, for the different types of boards belonging to two neighbouring sets of FE electronics (H0 and H1). The time indexes correspond to the time intervals used for the data taking, each of which lasted a different amount of hours, between the 23/10/2019 and the 29/10/2019. The temperatures are averaged among boards of the same type.

Performance

Preliminary results on the SciFi performances were obtained by using two SciFi modules with a test beam from the SPS in the CERN area. The mean single hit efficiency was measured to be of $\approx 99\%$ and the hit position resolution of $\sim 64\,\mu m$, thus well within the design requirements [72].

3.3.3 SciFi control and monitoring

A supervisory control and data acquisition (SCADA) architecture is used to operate detectors, especially in the presence of a complex structure of sub-systems as in most cases for the CERN experiments. The usual SCADA system for detectors at CERN is the WinCC Open Architecture (WinCC-OA) [73], which connects to hardware devices in order to monitor and supervise their behaviour, to configure and operate them. The software architecture is composed by several control managers, the main ones being: the Event manager, which is the central processing center responsible for all the communications and the alarm handling; the Database manager, which is the link to the database; and the User Interface manager, composed by a database editor and a graphic editor, which allows to show the values from the devices or to execute user commands. In order to reduce the overall manpower and avoid duplication of possible solutions for common needs, CERN and the LHC experiments collaborated to provide a set of WinCC-OA built-in tools, known as the Joint COntrols Project (JCOP) framework [74], that can be used as a base to develop new control systems.

The whole LHCb detector operation is controlled by the LHCb Experiment Control System (ECS), which includes the control systems of all subdetectors, usually built on JCOP framework with the addition of LHCb specific tools, as in the SciFi system case.

Figure 3.22 shows the SciFi ECS structure, which is a hierarchy of subsystems including: the data acquisition (DAQ), controlling the interaction with the FE electronics; the detector infrastructure (DCS), controlling the correct operation of the detector by measuring the temperatures, humidity and monitoring the FE electronics voltage supplies; the high voltage (HV), controlling the bias voltages of the SiPMs; and the timing control and trigger systems (TFC and HLT), provided centrally and linked to the general LHCb ECS.

During the last years of the commissioning of the SciFi tracker, until the first collisions of the LHC Run3 in 2022, I worked to develop the control and monitoring system of the SiPM bias voltage supplies, referred to as the SF_HV domain in the SciFi ECS. In the following section, the most important features developed for the project are described.

High Voltage control system

The control system for the bias voltage supplied to the SiPMs has been built following the LHCb guidelines for ECS design [76]. An OPC Unified Architecture server (OPC-UA) links the control project to the hardware, allowing the user to switch on or off the channels supplying

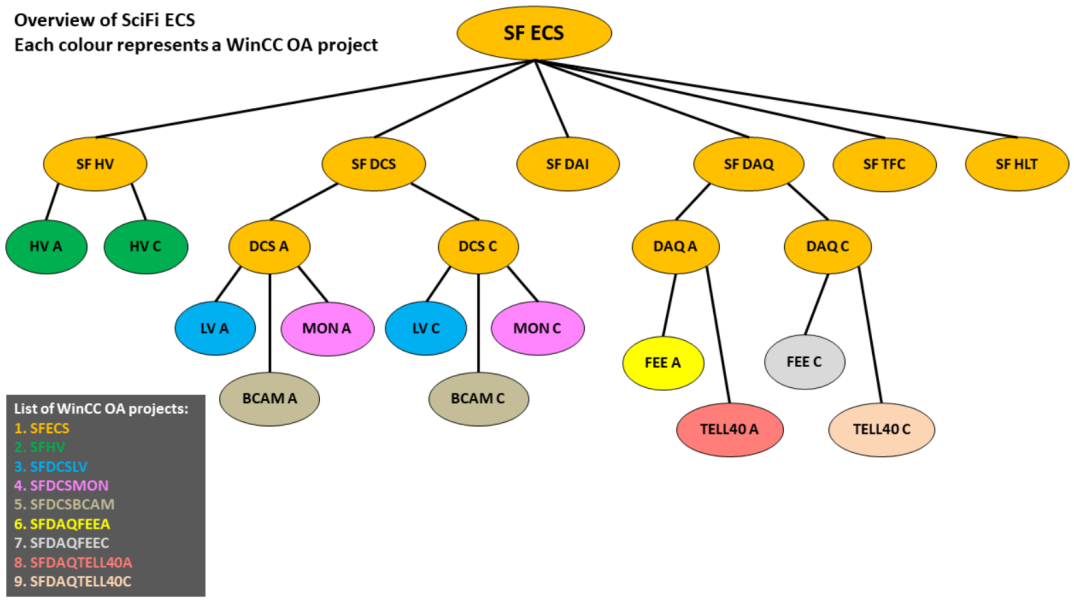

Figure 3.22: Structure of the SciFi ECS architecture [75].

the power to the SiPMs, to set various parameters such as the voltage trip limits and the voltage values, and to monitor the actual current and voltage values.

The SiPMs used in the SciFi tracker perform best at 3.5 V above the breakdown voltage V_{BD}, as it was checked by studying *e.g.* their gain or DCR at different voltages. The V_{BD} was measured for all the SiPMs used in the detector and stored in a database that the control system reads in order to provide the right voltage values. The mean value of the V_{BD} was found to be 51.75 V with a maximum variation of ±300 mV across the SiPM arrays. In addition, a linear dependence of the V_{BD} with temperature has been observed, with a linear coefficient of (60±2) mV/K. Thus, the control system needs to access also the temperature information, detected by the FE electronics, in order to correct the supplied voltage for temperature effects.

The bias voltage is provided by CAEN SY4527 multichannel power supply modules. In order to reduce the amount of cables needed, each channel of a CAEN module supplies 8 arrays of 64 SiPM channels each, thus powering an entire fibre mat. This is possible thanks to two types of splitter panels. The first splitter panels are placed next to the CAEN supplies, where the bias line is split in two lines. From there, the bias lines go to the second type of splitter panels mounted on the detector, that split each bias line in four. Switches are also mounted on the splitter panels, as shown in Figure 3.23, to manually control the splitting of the bias lines.

Figure 3.24 shows a control panel displaying the four layers of the T1 station. From there, the state of the CAEN channels can be modified, from a single channel (which powers an entire fibre mat) till the entire set of channels powering the whole station. The possible CAEN channel states are:

Figure 3.23: The two types of splitter panels used to provide the bias voltage to the SiPMs [72]. The left one, placed next to the CAEN supplies, splits the bias lines in two. The right one, placed on the detector, splits the line in four. The switches to manually switch on or off the splitting are also visible.

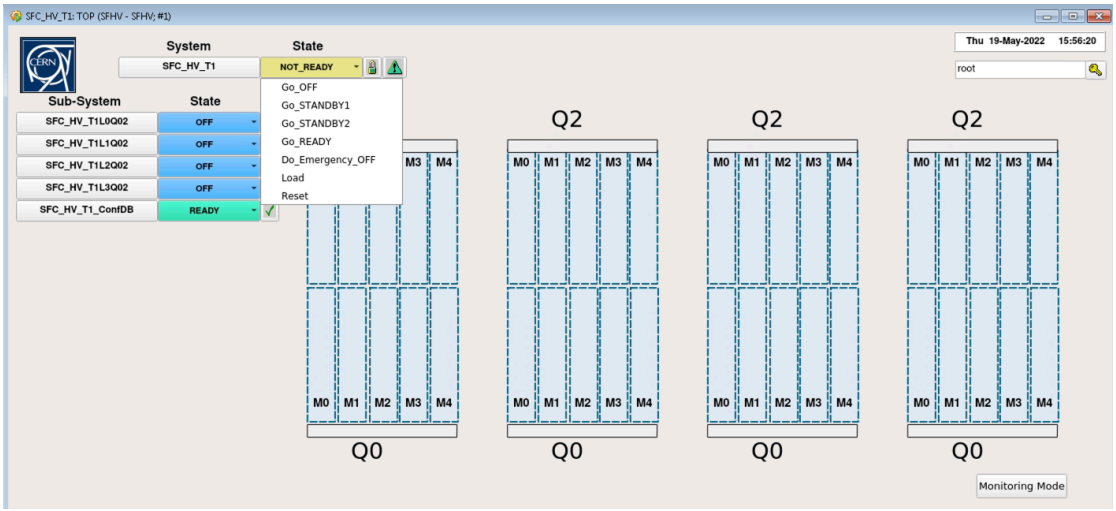

Figure 3.24: Panel showing the four layers of the first station of the SciFi. From here it is possible to change the state of the CAEN channels, through the actions displayed in the drop-down list in the top left corner.

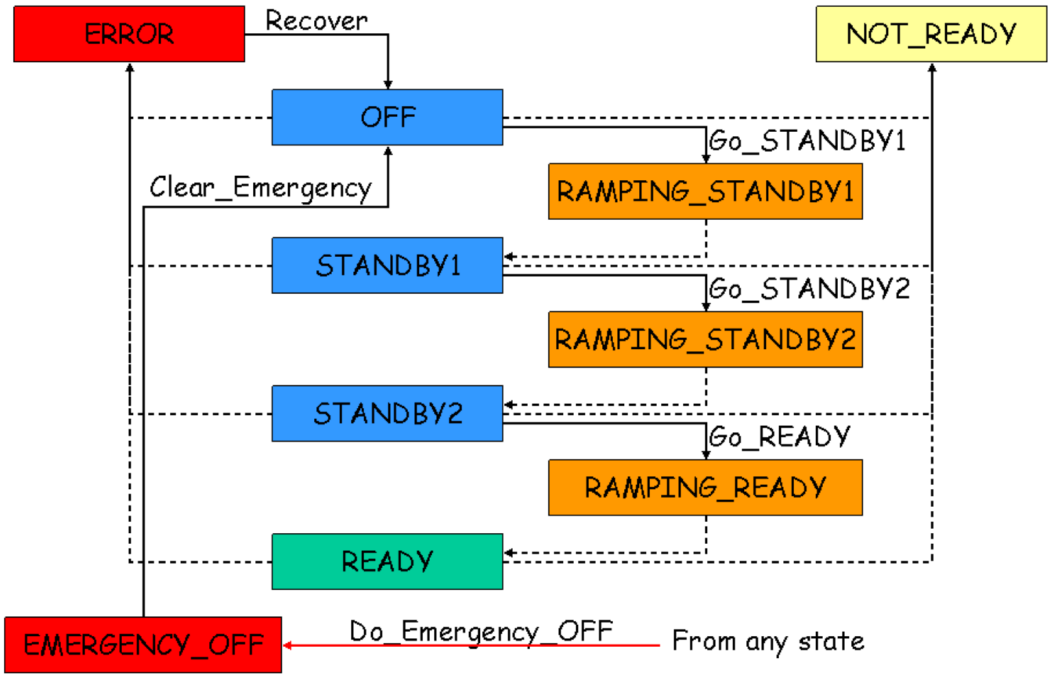

Figure 3.25: Possible states, transitions and actions of the HV channels.

- OFF, where the CAEN channels provide zero power;
- READY, where the CAEN channels provide the nominal bias voltage value for operation, computed as the $V_{BD} + 3.5$ V plus temperature corrections;
- STANDBY_1, STANDBY_2 where the CAEN channels provide an intermediate low (10 V) or high (20 V) voltage. These states are not strictly necessary for the detector operation, but they are in general used to limit the time needed to switch to the READY state;
- RAMPING_READY, RAMPING_STANDBY1, RAMPING_STANDBY2; those are temporary transitions when an action (GO_READY, GO_STANDBY1, GO_STANDBY2) is performed to move the CAEN channel to the steady READY, STANDBY_1, STANDBY_2 states respectively;
- ERROR, where one or more CAEN channels experience problems.

The aforementioned states, transitions and actions are also displayed in Figure 3.25.

Given the complexity of the relation between the power supplies channels and the powered SiPMs channels on the detector, a reliable channel mapping is crucial, in order to link the detector to the CAEN modules. The panel in Figure 3.26 shows an example of such a mapping, displaying for each fibre mat the associated CAEN channel powering it. From the same panel is it also possible to monitor the current and the voltage of the SiPMs, and storing the interesting values in a database for future analysis (an example of voltage and current trends over time is shown in Figure 3.27).

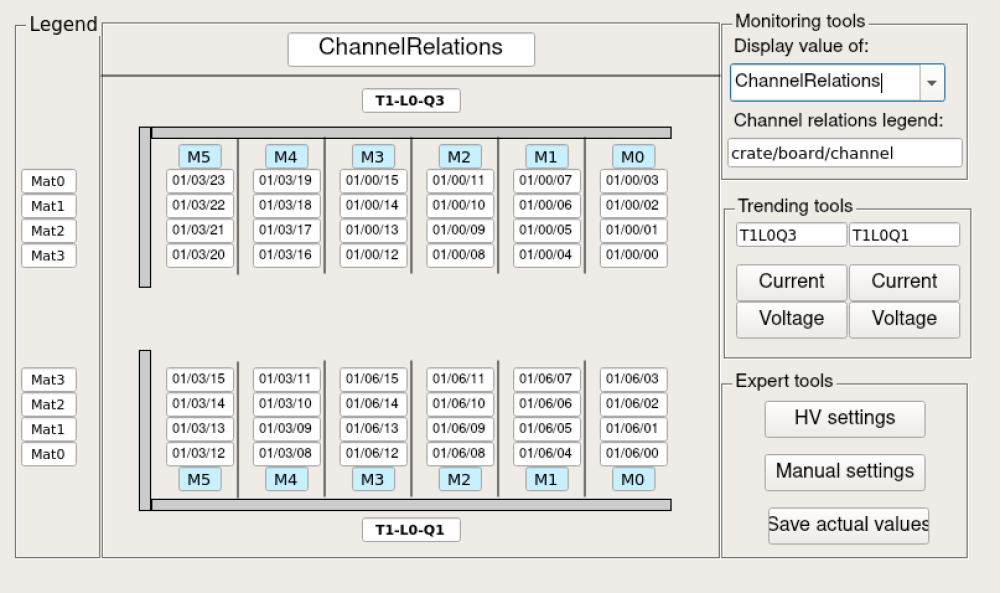

Figure 3.26: Panel showing the relation between a fibre mat and the CAEN channel that powers its SiPMs (identified by the number of crate, board and channel). The panel shows the left half of the first layer of the first station of the SciFi tracker (T1-L0-Q3). The panel possesses many more functionalities, including the display of the current and the voltage values, readout from the CAEN channels, and the status of the channels.

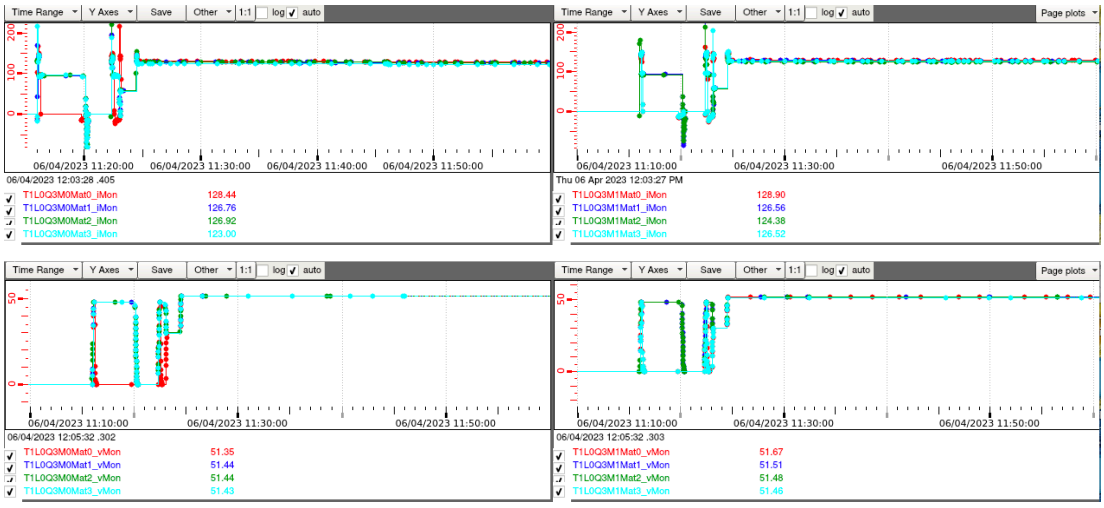

Figure 3.27: Current (top) and voltage (bottom) values stored by the control system on the 06.04.2023 for two neighbouring modules (left and right) placed on the top-left of the first layer of the first station of the detector. For each module the voltage values are shown for each of the four fibre mats composing the half-module.

One of the first tests performed during the commissioning was to check the actual CAEN channel-fibre mat matching by turning on one CAEN channel and observing, from the FE electronics, if the expected SiPMs channels (and not any others) were indeed powered. An example of the panel used for the test is shown in Figure 3.28 - this tool found that some bias cable connections were swapped during detector installation (*i.e.* not powering the expected SiPMs but others), and these could then be fixed by the detector installation team before the start of the Run 3 data-taking period.

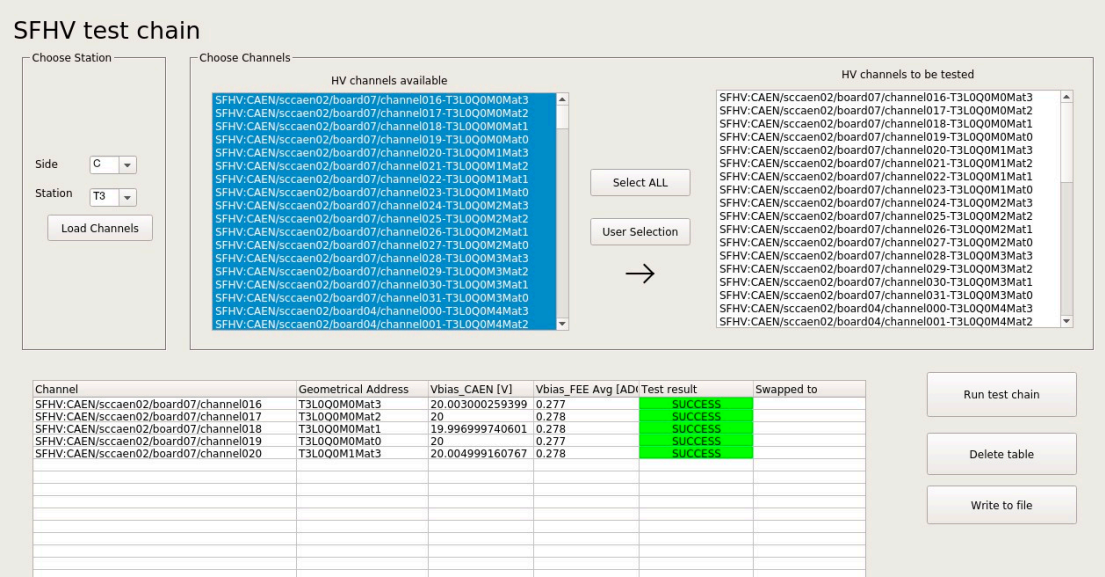

Figure 3.28: Panel used to test the mapping between the CAEN channel and the powered SiPMs. The first column shows the CAEN channel selected, the second column the geometrical position on the detector of the SiPMs that should be powered according to the channel mapping, the third column the voltage of the CAEN channel from the HV control system and the fourth the voltage seen by the SiPMs, read from the FE electronics in ADC counts.

4 The $R_{K\pi\pi}$ measurement

Lo duca e io per quel cammino ascoso
intrammo a ritornar nel chiaro mondo;
e sanza cura aver d'alcun riposo,

salimmo sù, el primo e io secondo,
tanto ch'i' vidi de le cose belle
che porta 'l ciel, per un pertugio tondo.

— Inferno, canto XXXIV, vv 133-138

In this chapter the main work performed during the PhD thesis will be described: the first test of lepton flavour universality using $B^+ \to K^+\pi^+\pi^-\ell^+\ell^-$ decays, with $\ell = e, \mu$, together with the first observation of the electron mode.

4.1 Introduction

The main goal of this work is to perform a LFU test by measuring the ratio of branching fractions of $B^+ \to K^+\pi^+\pi^-\ell^+\ell^-$ decays, where $\ell = \mu, e$. These decays present a more complex spin structure compared to the processes, mediated by the same $b \to s\ell\ell$ transition, used to investigate LFU so far (described in Section 2.2). In fact, the $K^+\pi^+\pi^-$ hadronic system, shown in Figure 4.1, is populated with several resonances with intermediate states such as $K^*(1410)$, $K_0^*(1430)$, $K_2^*(1430)$, $K^*(892)\pi$, $K\rho(770)$ [10].

Given the complexity of the hadronic $K^+\pi^+\pi^-$ system, where no *a priori* knowledge of the several underlying resonances is available, the measurement is carried on in an inclusive way, *i.e.* no particular resonance is selected in the hadronic $K^+\pi^+\pi^-$ spectrum, but they are rather studied in their ensemble. In Ref. [78], it has been recently shown that such inclusive LFU ratios can be still interpreted within the framework of effective Lagrangians (described in

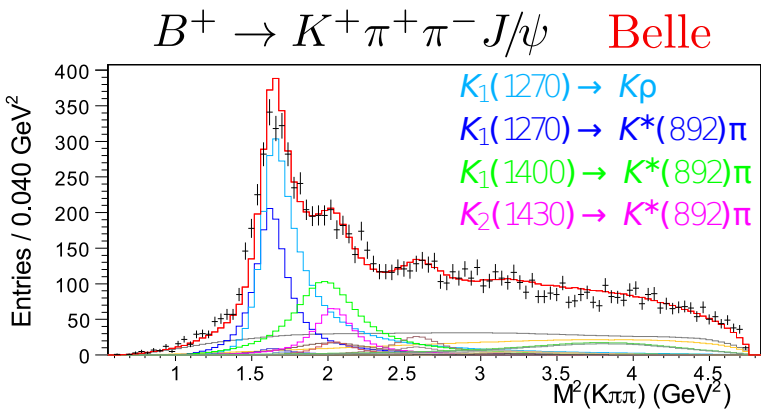

Figure 4.1: $K^+\pi^+\pi^-$ final state in $B^+ \to K^+\pi^+\pi^- J/\psi$ decays [77], where the J/ψ is reconstructed only in its decays to electrons or muons. The different colors show the several resonances composing the system.

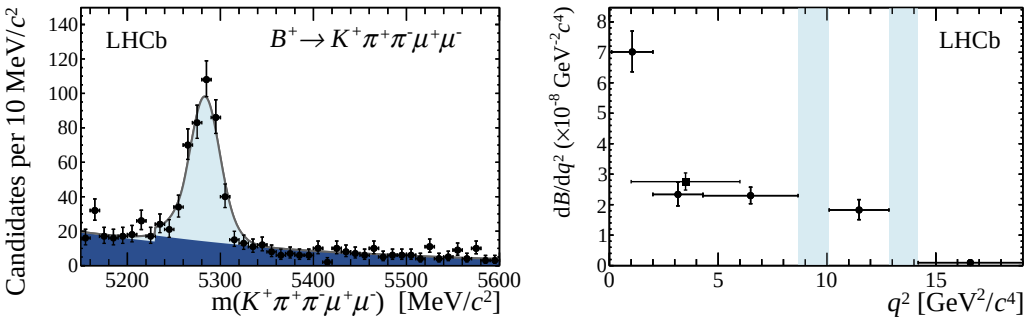

Figure 4.2: Observation of the $B^+ \to K^+\pi^+\pi^-\mu^+\mu^-$ decay with the LHCb `Run1` dataset [79].

Section 2), even if the detailed structure of the hadronic matrix elements is unknown. As a matter of fact, the richness of the hadronic system can provide complementary information with respect to the exclusive modes, being sensitive to an unprobed combination of Wilson coefficients.

The decay $B^+ \to K^+\pi^+\pi^-\mu^+\mu^-$ has been observed at LHCb, using the `Run1` dataset (Figure 4.2), with a measured branching fraction of $\mathcal{B}\left(B^+ \to K^+\pi^+\pi^-\mu^+\mu^-\right) = 4.36^{+0.40}_{-0.39} \times 10^{-7}$ [79], while no evidence for the $B^+ \to K^+\pi^+\pi^- e^+e^-$ mode has been found yet.

In the following, the $B^+ \to K^+\pi^+\pi^-\ell^+\ell^-$ decays are referred to as the "rare" modes, since they happen at loop level with small branching fractions $\sim \mathcal{O}(10^{-7})$. The decays with the same final state but happening through a J/ψ or a $\psi(2S)$ resonance, *i.e.* $B^+ \to K^+\pi^+\pi^- J/\psi\,(\to \ell^+\ell^-)$ and $B^+ \to K^+\pi^+\pi^-\psi(2S)(\to \ell^+\ell^-)$, are referred to as the "resonant" modes. They happen at tree level with the emission of a $c\bar{c}$ pair, hence they are much more abundant than the rare modes, with branching fractions of $\sim \mathcal{O}(10^{-4})$. They have been experimentally proved to satisfy lepton flavour universality [10] with very high precision, thus they are not sensitive to possible new physics contributions. The resonant decay modes play a crucial role in the measurement,

helping in calibrating the detector efficiencies, in reducing the systematic uncertainties and in the validation of the analysis procedure, as it will be explained in detail in the following sections. For these reasons they are also referred to as "control" modes.

4.2 Analysis strategy

The observable measured in this thesis work is $R^{-1}_{K\pi\pi}$ and it is defined as the ratio between the branching fractions of the rare decays $B^+ \to K^+\pi^+\pi^-\ell^+\ell^-$ with different lepton flavours in the final state ($\ell = e, \mu$):

$$\begin{aligned} R^{-1}_{K\pi\pi} &\equiv \frac{\mathscr{B}\left(B^+ \to K^+\pi^+\pi^- e^+e^-\right)}{\mathscr{B}\left(B^+ \to K^+\pi^+\pi^-\mu^+\mu^-\right)} \\ &= \frac{\mathscr{N}\left(B^+ \to K^+\pi^+\pi^- e^+e^-\right)}{\mathscr{N}\left(B^+ \to K^+\pi^+\pi^-\mu^+\mu^-\right)} \cdot \frac{\varepsilon\left(B^+ \to K^+\pi^+\pi^-\mu^+\mu^-\right)}{\varepsilon\left(B^+ \to K^+\pi^+\pi^- e^+e^-\right)}, \end{aligned} \tag{4.1}$$

where $\mathscr{N}$ and ε are the measured yield and detector efficiency for the given decay, respectively. The choice to measure the inverse ratio $R^{-1}_{K\pi\pi}$ is due to the low yield of the electron decay mode, which placed at the numerator makes the uncertainty on the observable better represented by a Gaussian distribution.

To reduce many sources of systematic uncertainty, mainly due to differences in the response of the detector to electrons and muons (described in Section 3), this observable is computed as a double ratio, by normalising the rare mode branching fractions to the ones of the corresponding J/ψ resonant mode. The measured quantity is defined as

$$\begin{aligned} R^{-1}_{K\pi\pi} &\equiv \frac{\mathscr{B}\left(B^+ \to K^+\pi^+\pi^- e^+e^-\right)}{\mathscr{B}\left(B^+ \to K^+\pi^+\pi^-(J/\psi \to e^+e^-)\right)} \frac{\mathscr{B}\left(B^+ \to K^+\pi^+\pi^-(J/\psi \to \mu^+\mu^-)\right)}{\mathscr{B}\left(B^+ \to K^+\pi^+\pi^-\mu^+\mu^-\right)} \\ &\equiv \frac{\mathscr{N}\left(B^+ \to K^+\pi^+\pi^- e^+e^-\right)}{\mathscr{N}\left(B^+ \to K^+\pi^+\pi^-(J/\psi \to e^+e^-)\right)} \frac{\mathscr{N}\left(B^+ \to K^+\pi^+\pi^-(J/\psi \to \mu^+\mu^-)\right)}{\mathscr{N}\left(B^+ \to K^+\pi^+\pi^-\mu^+\mu^-\right)} \\ &\times \frac{\varepsilon\left(B^+ \to K^+\pi^+\pi^-(J/\psi \to e^+e^-)\right)}{\varepsilon\left(B^+ \to K^+\pi^+\pi^- e^+e^-\right)} \frac{\varepsilon\left(B^+ \to K^+\pi^+\pi^-\mu^+\mu^-\right)}{\varepsilon\left(B^+ \to K^+\pi^+\pi^-(J/\psi \to \mu^+\mu^-)\right)}. \end{aligned} \tag{4.2}$$

This approach relies on the experimentally well-tested lepton universality in $J/\psi \to \ell^+\ell^-$ decays, with the $\mathscr{B}(J/\psi \to e^+e^-)/\mathscr{B}(J/\psi \to \mu^+\mu^-)$ ratio being in agreement with unity within sub-percent precision [10].

The LFU of J/ψ decays is also used to perform a stringent validation of the analysis strategy, by measuring the resonant single ratio

$$r_{J/\psi} \equiv \frac{\mathscr{B}\left(B^+ \to K^+\pi^+\pi^- J/\psi\,(\to \mu^+\mu^-)\right)}{\mathscr{B}\left(B^+ \to K^+\pi^+\pi^- J/\psi\,(\to e^+e^-)\right)} \equiv 1. \tag{4.3}$$

A deviation from unity of $r_{J/\psi}$ would be a clear indication of a fault in the analysis procedure. In particular, the use of a single ratio is extremely sensitive to differences in the reconstruction

of the two leptons species and thus it allows to identify potential issues in the measurement.

Another useful validation of the double ratio strategy is given by measuring the double ratio

$$R_{\psi(2S)} \equiv \frac{\mathcal{B}\left(B^+ \to K^+\pi^+\pi^-\psi(2S)(\to \mu^+\mu^-)\right)}{\mathcal{B}\left(B^+ \to K^+\pi^+\pi^- J/\psi\,(\to \mu^+\mu^-)\right)} \cdot \frac{\mathcal{B}\left(B^+ \to K^+\pi^+\pi^- J/\psi\,(\to e^+e^-)\right)}{\mathcal{B}\left(B^+ \to K^+\pi^+\pi^-\psi(2S)(\to e^+e^-)\right)} \equiv 1\,, \quad (4.4)$$

in which the $\psi(2S)$ decays are known to satisfy lepton-flavour universality at order of $\approx$ 10% [10]. Deviations from unity of the $R_{\psi(2S)}$ value not only indicate issues in the analysis procedure, but can also be used to probe the double-ratio strategy itself.

The $r_{J/\psi}$ and $R_{\psi(2S)}$ cross-checks acquire even more importance in light of the fact that the analysis is carried out in a *blind* way: the values of the efficiencies of the rare modes, necessary for the $R^{-1}_{K\pi\pi}$ estimation (Eq. 4.1), are never explicitly looked at, to prevent any artificial bias to be injected into the measurement. The $R^{-1}_{K\pi\pi}$ value is *unblinded* only after the analysis procedure has been fully validated.

The various steps of the analysis strategy, built on the knowledge developed by the different LFU tests performed at LHCb so far (Section 2.2), are summarised below.

i. Selection requirements are needed to isolate the decays of interest from the environment generated by the pp collisions. The selection is designed to account for the multi-body characteristic of this decay, as it will be shown in Section 4.3. In particular, the region $1.1 < m(K^+\pi^+\pi^-) < 2.4\,\text{GeV}/c^2$ is selected, which has been chosen based on the $m(K^+\pi^+\pi^-)$ distribution observed in data in `Run1` [79]. These criteria result in a sample of approximately $\mathcal{O}(800)$ and $\mathcal{O}(400)$ of $B^+ \to K^+\pi^-\pi^+\mu^+\mu^-$ and $B^+ \to K^+\pi^-\pi^+e^+e^-$ candidates, respectively.

ii. The simulation of the decays is corrected to account for some known discrepancies between simulation and data, which originate from the mismodeling of the kinematics/multiplicity of the event and the detector response (*e.g.* particle identification, trigger efficiency *etc.*), as it will be shown in Section 4.4. A novelty of this analysis is the design of a data-driven correction to the underlying dynamics of the phase-space of the hadronic system, used as the first step of the correction chain. Other corrections compare and make use of the experience accumulated in similar measurements performed at LHCb.

iii. Since relative branching ratio measurements rely on the knowledge of the relative efficiency between rare and resonant channels (Eq. 4.2), Section 4.5 will describe the procedure for its determination and the corresponding uncertainties.

iv. The remaining terms in Eq. 4.2 are the measured yields of the rare modes and of the J/ψ control modes. Furthermore, the yields of the resonants modes are used for the computation of the $r_{J/\psi}$ and $R_{\psi(2S)}$ cross-checks, see Eq. 4.3 and Eq. 4.4 respectively. All these yields are obtained by fitting the invariant mass of the final state particles $m(K\pi\pi\ell\ell)$, after having selected the relative invariant mass regions of the dilepton pair (see Section 4.2.2). The models used to parameterise the invariant masses distributions

are reported in Section 4.6, together with validation of the models through pseudo-experiments. A crucial point of this work is the implementation of a dedicated data-driven strategy to model and quantify backgrounds from partially-reconstructed B decays, *i.e.* from $B \to K\pi\pi\ell\ell X$ decays, where X is a missing particle (described in Section 4.6.2).

v. The measurements of the $r_{J/\psi}$ and $R_{\psi(2S)}$ cross-checks are reported in Section 4.7, and provide stringent validations to the analysis procedure. The values of these quantities are given as a function of each step of the data/simulation correction, and the stability of $r_{J/\psi}$ is examined as a function of several kinematical variables too.

vi. Systematic uncertainties are described in Section 4.8. While this measurement is expected to be limited by the statistical uncertainty, these studies include all contributions typically involved in the efficiency determination and in the fits to the B^+ invariant mass line shape.

This thesis work is performed using the full dataset collected by the LHCb detector, corresponding to a total of $9\,\text{fb}^{-1}$.

4.2.1 Events Simulation

Samples of simulated events, generally referred to as *Monte Carlo* simulation (MC), are used in several steps of the analysis. They are necessary to compute the efficiencies appearing in Eq. 4.2, and they are also used to extract information about the expected distributions of various features, *e.g.* momenta, masses *etc.*, for signal and background events.

In the simulation used in this work, the pp collisions are generated using PYTHIA [80] with a specific configuration for the LHCb environment [81]. The decays of the produced particles are simulated by the EvtGen package [82], with the PHOTOS [83] tool used to take into account possible final state radiation. The interaction of the simulated events with the LHCb detector is modelled by the GEANT4 [84] toolkit.

Given the discussed complexity of the $K\pi\pi$ hadronic system, the simulated samples are generated using a phase-space model that is flat in the $(K\pi\pi)$ mass. The simulated masses are then corrected according to the structures seen in the data. This "phase-space" correction, described in details in Section 4.4.3, is a unique feature of this analysis, and the first step of a series of corrections devoted to correct well-known differences between data and simulation, as it will be described in Section 4.4.

4.2.2 Dilepton invariant mass regions

One of the most powerful variables used to discriminate between the decays of interest and the backgrounds is the invariant mass of the final state particles, *i.e.* $m(K^+\pi^+\pi^-\ell^+\ell^-)$. In fact, for $B^+ \to K^+\pi^+\pi^-\ell^+\ell^-$ decays, one can expect the invariant mass of the final state particles to be

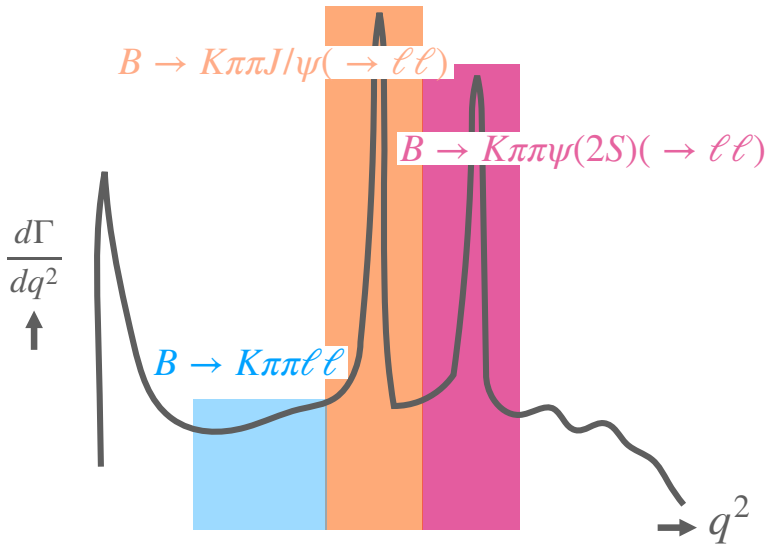

Figure 4.3: Sketch showing the branching fraction of $B^+ \to K^+\pi^+\pi^-\ell^+\ell^-$ decays with respect to $q^2 = m^2(\ell^+\ell^-)$. The three boxes represent the three q^2 regions used in the measurement: the *signal*-q^2 region (blue), the J/ψ-q^2 region (orange) and the $\psi(2S)$-q^2 region (purple).

distributed as a Gaussian with a mean equal to the B meson mass $m(B) = 5279.34\,\text{MeV}/c$ and a resolution due to detector and reconstruction effects. Thus, one can select *signal* candidates by choosing only events with a $m(K^+\pi^+\pi^-\ell^+\ell^-)$ value close to the $m(B)$.

Following the same logic, one can make use of the invariant mass of the final state leptons $m^2(\ell^+\ell^-) = q^2$ to separate the rare modes from the more abundant resonant decays. In fact, if the leptons come from a J/ψ resonance, the q^2 of the final state leptons will be around $q^2 = m^2(J/\psi) = 9.6\,\text{GeV}^2/c^4$. The same will hold for the $\psi(2S)$ resonance, where $m^2(\psi(2S)) = 13.6\,\text{GeV}^2/c^4$. A sketch of the rare and resonant branching fractions with respect to q^2 is shown in Figure 4.3, where the three boxes highlight the three q^2 regions used in this work:

- *signal*-q^2: $1.1 < q^2 < 7.0\,\text{GeV}^2/c^4$, where the rare $B^+ \to K^+\pi^+\pi^-\ell^+\ell^-$ decays are selected. The lower bound is such that background coming from $\phi \to e^+e^-$ decays is not expected to contribute, while the upper bound is chosen to avoid contamination from the resonant $B^+ \to K^+\pi^+\pi^- J/\psi\,(\to \ell^+\ell^-)$ decays.
- J/ψ-q^2: $7 < q^2 < 11\,\text{GeV}^2/c^4$, where the resonant $B^+ \to K^+\pi^+\pi^- J/\psi\,(\to \ell^+\ell^-)$ decays are selected.
- $\psi(2S)$-q^2: $11 < q^2 < 15\,\text{GeV}^2/c^4$, where the resonant $B^+ \to K^+\pi^+\pi^-\psi(2S)(\to \ell^+\ell^-)$ decays are selected.

Figure 4.4 shows how events with a $K^+\pi^+\pi^-\ell^+\ell^-$ final state are distributed with respect to the discriminating variables just defined, q^2 and $m(K^+\pi^+\pi^-\ell^+\ell^-)$, for both decays to electrons and to muons. The $B^+ \to K^+\pi^+\pi^-\ell^+\ell^-$ decays are visible as a vertical band centred at

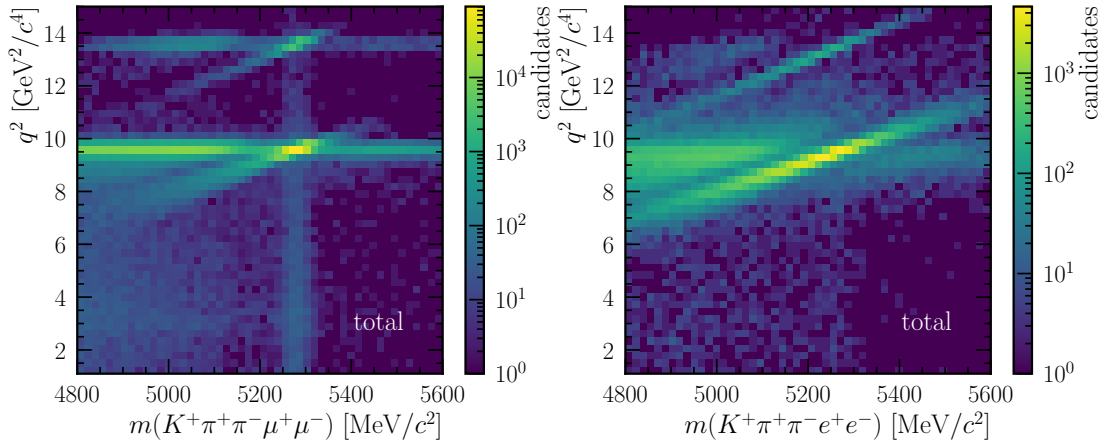

Figure 4.4: Invariant mass of the final state particles for the (left) $B^+ \to K^+\pi^+\pi^-\mu^+\mu^-$ and the (right) $B^+ \to K^+\pi^+\pi^-e^+e^-$ decays, for different values of the dilepton invariant mass squared ($q^2 = m^2(\ell^+\ell^-)$), for the whole dataset (Run1 +Run2). The decay $B^+ \to K^+\pi^+\pi^-\ell^+\ell^-$, corresponding to a vertical band at the B^+ meson mass value, is much clearer in the muon than in the electron decays, mainly due to Bremsstrahlung effects. The degradation of the electron resolution is visible also in correspondence of the J/ψ and $\psi(2S)$ resonance regions ($q^2 = m^2(J/\psi)$ and $q^2 = m^2(\psi(2S))$).

$m(K^+\pi^+\pi^-\ell^+\ell^-) = m(B)$, much clearer for the muon case than for the electron one, mainly due to Bremsstrahlung effects (described in Section 3.2.2). The $B^+ \to K^+\pi^+\pi^- J/\psi\,(\to \ell^+\ell^-)$ and $B^+ \to K^+\pi^+\pi^-\psi(2S)(\to \ell^+\ell^-)$ resonant decays are visible, on the vertical band, as accumulation of events at $q^2 = m^2(J/\psi)$ and $q^2 = m^2(\psi(2S))$. Even here it is possible to notice the degradation of the electron resolution with respect to the muon one, where the radiative tails, created by Bremsstrahlung photons that take energy away from the final state particles, are much more evident in the electron case, showing up in the figure as diagonal lines from the resonance to lower q^2 and $m(B)$ values.

It is worth to mention that the *signal*-q^2 regions studied in similar LFU analysis (described in Section 2.2) are usually defined as [1.1, 6] GeV$^2/c^4$, while in this work the region is extended to [1.1,7] GeV$^2/c^4$, adding 1 GeV$^2/c^2$ towards the J/ψ-q^2 region. This choice leads to an increase of the event yield of the rare electron mode by roughly 20%, but at the same time it exposes the measurement to the risk of a significant leakage of $B^+ \to K^+\pi^+\pi^- J/\psi\,(\to \ell^+\ell^-)$ events from the J/ψ-q^2 region to the *signal* region. In order to reduce the size of this potential leakage, an additional criterion on the invariant mass of the final state particles is imposed,

$$\left(m^{J/\psi}(K\pi\pi\ell\ell) < 5139.3\,\text{MeV}\right) \text{ and } \left(m^{J/\psi}(K\pi\pi\ell\ell) > 5476.2\,\text{MeV}\right) \tag{4.5}$$

where $m^{J/\psi}$ indicates that for this mass estimation, during the reconstruction process, the dilepton system is *constrained* to have a mass equal to the one of the J/ψ. These kinds of masses, that can be constructed also for the $\psi(2S)$ cases $m^{\psi(2S)}$, are usually referred to as "constrained" masses, having as main advantage a better resolution than the "unconstrained"

ones. Thus, the constrained mass is used in the mentioned cut to remove events where the leptons come from the J/ψ, by discarding as few as possible signal events.

A more comprehensive discussion of the impact of this strategy, and possible J/ψ leakage in the *signal*-q^2 region, is given in Section 4.3.4.

4.3 Selection

An overview of the selection applied to the data and to the simulated samples is given in detail in the following sections. The general flow of the requirements can be summarised as:

i. Stripping, which includes loose requirements to improve the quality of the events. They are applied at the stripping level (mentioned in Section 3.2.3), and thus they can not be removed by the analysts during the offline selection.

ii. Trigger, following the two-stage approach composed by the `L0` and `HLT` used by the LHCb detector to reduce the event rates, as explained in Section 3.2.3. Different `L0` and `HLT` decisions are available to the analysts, depending on the type of particle that fired the trigger.

iii. Preselection, composed by high-efficiency requirements, mostly aiming to ensure the quality of the tracks and in general of the reconstructed particles composing the event, plus requirements on particle identification.

iv. Background, where various categories of background contributions are examined. In addition, the impact of the choice on the central q^2 range with consequent possible leakage from $B^+ \to K^+\pi^+\pi^- J/\psi\,(\to \ell^+\ell^-)$ in the signal region is studied.

v. Multivariate analysis (MVA), where a classifier is trained to suppress background coming from a random combination of tracks, usually referred to as *combinatorial* background.

4.3.1 Stripping

An overview of the requirements applied at the Stripping level is given in Table 4.1. The stripping is run centrally, thus these selections cannot be removed when performing an offline analysis. The requirements are listed for each particle composing the $B^+ \to K^+\pi^+\pi^-\ell^+\ell^-$ decays, where the hadronic $K^+\pi^+\pi^-$ system is collectively referred to as K_1 for simplicity, with some selections being applied to the muons or the electrons as a pair. In addition to loose selections on the transverse momentum p_T or on the invariant masses m, other variables are used to ensure the quality of the reconstructed decay, such as the flight distance (FD), *i.e.* the distance between the primary vertex (PV) and the decay vertex (DV) of the B meson; the direction angle (`DIRA`) variable, *i.e.* the cosine of the angle between the reconstructed momentum of the B^+ meson and the FD; and the impact parameter (IP), *i.e.* the minimum distance between the PV and the direction of the B^+ meson momentum.

In the stripping selection, the B^+ is required to be compatible with being produced in the proton-proton collision, and thus to have a low value of the χ^2_{IP} [1], to have flown for a significant distance from the primary vertex before decaying, ensured by a high χ^2_{FD} [2], to have a good

[1] The χ^2_{IP} is computed as the difference of the χ^2 of the PV fit when considering or not an additional track. It basically gives an estimation on how worse the fit to the PV becomes if a tracks not coming from the PV is included.

[2] The χ^2_{FD} is a measure of the change in χ^2 when the PV and DV are combined in a single vertex fit. It thus gives a measure of how well the two vertices are separated.

fitted decay vertex, controlled by the χ^2_{vtx}/ndof metric, and to have DIRA close to unity, since the momentum of the B will be collinear to its direction of flight. For what concerns the final state particles, they are required to not be produced at the primary vertex, thus with a large χ^2_{IP}, and to have well-fitted tracks, *i.e.* with a small χ^2_{trk}/ndof. The K and the pions are also required to have a small probability to be a ghost P_{ghost}, *i.e.* a fake track created from noise hits or from hits left by multiple particles[3]. In addition, particle identification requirements are applied to the leptons. The criterion for electron uses the likelihood of electron versus pion mass hypothesis, *i.e.* $\texttt{DLL}_e > 0$. Two other requirements are applied to muons, which are required to be associated with hits in the muon subsystem (hasMuon) consistent with a muon track (isMuon). Finally, for Run1 samples, an upper limit is imposed on the number of hits in the SPD system, described in Section 3.2.1, to reject events with too many simultaneous tracks. In Run2 a similar requirement ($n_{\text{SPD}} < 450$) is added at the preselection stage.

4.3.2 Trigger

As described in Section 3.2.3, the first step of the LHCb trigger in the Run1 -2 periods, is the L0 trigger, which uses fast estimations of the particles energies and momenta to decide whether to keep or reject an event. In this analysis two L0 trigger requirements are used, depending on the type of particle that fired the L0 trigger.

The first requirement selects those events where the trigger has been fired by at least one of the leptons of the signal decay, in the following referred to as the "TOS" (Trigger On Signal) requirement. For the muon modes this translates into requiring a track with a transverse momentum p_{T} greater than a threshold and hits in the muon subsystem. Such requirements are applied in the so-called L0Muon trigger line. Similarly, the L0Electron trigger line requires, for the electron modes, to have a track compatible with hits in the electromagnetic calorimeter ECAL corresponding to a particle who has deposited in the ECAL a transverse energy E_{T} greater than a threshold. It is worth to note that, given the higher occupancy of the ECAL with respect to the muon stations and the Bremsstrahlung effects affecting the electron energy estimation (described in Section 3.2.2), the L0Electron line has a higher energy threshold than the L0Muon line, leading to a decrease of the event yield of the electron modes by a factor ~ 2 with respect to the muon ones.

The second trigger requirement selects events where the trigger has been fired by particles not belonging to the signal decay, in the following referred to as the "TIS" (Trigger Independent from Signal) category. This category is considered mainly to increase the event yield of the electron modes.

In practical terms, the dataset is split into mutually exclusive categories. The first one is the L0TIS category, which contains events that fired the "TIS" trigger. The L0TIS category can be seen as the "inclusive" category, given the absence of additional L0 requirements. The second

[3]The P_{ghost} is computed through a neural network combining various track variables, as the number of tracks in an event or the number of hits in the tracking stations.

Table 4.1: Summary of requirements from the stripping lines chosen in this thesis work. The χ^2_{FD} and χ^2_{IP} are computed with respect to the primary vertex.

Particle or event	Variable	Requirement
Event	n_{SPD}	< 600 (for `Run1`)
B	$\lvert m(K\pi\pi ee) - m_{\text{PDG}}\rvert$	$< 1500\,\text{MeV}/c^2$
	$\chi^2_{\text{vtx}}/n_{\text{dof}}$	< 9
	χ^2_{FD}	> 100
	χ^2_{IP}	< 25
	DIRA	> 0.9995
K	$\chi^2_{\text{trk}}/n_{\text{dof}}$	< 3
	P_{ghost}	< 0.4
	p_{T}	$> 250\,\text{MeV}/c$
	χ^2_{IP}	> 4
π	$\chi^2_{\text{trk}}/n_{\text{dof}}$	< 3
	P_{ghost}	< 0.4
	p_{T}	$> 250\,\text{MeV}/c$
	χ^2_{IP}	> 4
K_1	$m(K\pi\pi)$	$> 0\,\text{MeV}/c^2$
	$m(K\pi\pi)$	$< 6000\,\text{MeV}/c^2$
	$\sum_{K,\pi,\pi} p_{\text{T}}$	$> 800\,\text{MeV}/c$
	χ^2_{vtx}	< 12
	$\sum_{K,\pi,\pi} \chi^2_{\text{IP}}$	> 48
e	p_{T}	$> 300\,\text{MeV}/c$
	χ^2_{IP}	> 9
	$\texttt{DLL}_e$	> 0
μ	p_{T}	$> 300\,\text{MeV}/c$
	χ^2_{IP}	> 9
	`isMuon`	True
	`hasMuon`	True
Muon pair	p_{T}	$> 0\,\text{MeV}/c$
	m	$< 5500\,\text{MeV}/c^2$
	χ^2_{vtx}/dof	< 9
	χ^2_{FD}	> 16
	χ^2_{IP}	> 0
Electron pair	p_{T}	$> 0\,\text{MeV}/c$
	m	$< 5500\,\text{MeV}/c^2$
	χ^2_{vtx}/dof	< 9
	χ^2_{FD}	> 16
	χ^2_{IP}	> 0

category is the L0ETOS or the L0MTOS category, depending on the lepton type of the final state, which contains events that did not fire the L0TIS trigger, and where at least one of the leptons in the final state fired the L0Electron or L0Muon trigger respectively. For this reason, this second category is seen as the "exclusive" category (*i.e.* where events are TOS && !TIS), where the requirement of not falling into the L0TIS category is needed in order to avoid the double counting of the same data.

During the data-taking periods the thresholds on the $p_{\mathrm{T}}(\mu)$ and on the $E_{\mathrm{T}}(e)$ of the L0Muon and L0Electron trigger lines have been frequently changed. This is not the case for the simulated events, which are generated using only one threshold. In order to align as much as possible the data and the simulation samples, all the events in the L0ETOS category whose electron transverse energy does not satisfy the strictest threshold amongst those applied in data and simulation are removed. The electron considered for this alignment is the one with the largest E_{T}, under the reasonable assumption that it is the responsible for firing the trigger line. Similarly, the events in the L0MTOS category where the muon transverse momentum does not satisfy the hardest threshold applied in data and simulation are removed.

Table 4.2 summarises the additional requirements applied on the electron transverse energy and on the muon transverse momentum introduced to take into account these differences in the trigger thresholds.

Table 4.2: Additional requirements used to align simulated and data samples given the use of different trigger thresholds during the data-taking periods.

	$E_{\mathrm{T}}(e)$	$p_{\mathrm{T}}(\mu)$
2011	2.96 GeV	1.76 GeV/c
2012	2.96 GeV	1.76 GeV/c
2015	2.70 GeV	2.85 GeV/c
2016	2.70 GeV	1.85 GeV/c
2017	2.95 GeV	1.95 GeV/c
2018	3.15 GeV	1.80 GeV/c

After the L0 stage, the events need to pass through the software trigger filter, which is divided in two steps, the HLT1 and HLT2. The first one uses information provided only by the tracking system, while the second one exploits information from all the subdetectors, performing full event reconstruction. The HLT1 line used in this work mainly selects displaced tracks with high momenta, acting on the p_{T} and the χ^2_{IP} variables, thus compatible with tracks from B mesons. The HLT2 line requires the B vertices to be significantly displaced from the PV, and reconstructed from two, three or four charged tracks, of which at least one is compatible with an electron, when selecting $B^+ \to K^+\pi^+\pi^- e^+ e^-$ decays, or a muon, when selecting $B^+ \to K^+\pi^+\pi^-\mu^+\mu^-$.

4.3.3 Preselection

Preselection requirements are aimed at assessing that the selected particles come from well-reconstructed tracks and are of the correct particle type. For these reasons, all the signal candidates are required to have a small probability to be a ghost. In addition, electrons are required to have associated clusters in the calorimeters, while hadrons are required to be inside the geometrical acceptance of the muon system, to ensure that their tracks have reliable information from the different subdetectors. Finally, the kaon, pion and electron candidates are required to have associated hits in the RICH detectors. These properties are controlled by the boolean `hasCalo`, `hasRICH` and `InAccMuon` variables.

It has been shown in Ref. [85] that in the very centre of the ECAL calorimeter the cells have not been read-out. This results in some discrepancies between the data and simulated events. Therefore, a fiducial volume requirement is introduced on the (x, y) coordinates of the electron tracks intersecting the ECAL plane, in order to remove the region defined as $|\mathrm{x}_{\mathrm{ECAL}}| < 363.6\,\mathrm{mm}$ & $|\mathrm{y}_{\mathrm{ECAL}}| < 282.6\,\mathrm{mm}$.

Of particular concern for decays containing electrons in the final state is the presence of clone tracks, as the track quality is reduced by Bremsstrahlung effects. A pair of tracks is defined as clones when they share at least 70% of the hits in the VELO and part of the T-stations. An efficient strategy to avoid these contributions is to remove events that have angles between final state particles close to zero. In the requirement against clone tracks, the minimum angle between each pair of tracks is required to be at least 0.5 mrad. This requirement is highly efficient for the signal, retaining more than 99 % of selected signal candidates in simulation, and it is effective in vetoing candidates containing clone tracks.

Finally, PID requirements are applied to the tracks, to select the specific particle species of interest. These selections rely on the likelihood of a track to be of a given species against the pion hypothesis, as explained in Section 3.2.2, referred to as $\texttt{DLL}_X$, where X stands for the species hypothesis to be evaluated. The `DLL`s use information from the RICH, the calorimeter and the muon systems. In addition, this analysis makes use of a neural network-based variable, $\texttt{ProbNN}_X$, which is the output of a neural network trained on information from all the subdetectors and the `DLL`s. The `ProbNN` values range between 0 and 1 and can be treated as probabilities of a particle to be of a specific type. It has to be mentioned that distributions of the PID variables are particularly problematic to model in the simulation, thus a dedicated treatment is needed to calibrate the PID responses. The calibration, described in details in Section 4.4.2, uses samples from high-yield control channels. In order to align the analysis samples to these calibration samples, thresholds on the particles p and p_{T} are applied, as shown in Table 4.3.

Table 4.3: Summary of the preselection requirements discussed in Section 4.3.3.

Type		**Requirement**
Fiducial, Calibration	all tracks	`GhostProb` < 0.3

	K, π	$p_{\mathrm{T}} > 250$ MeV/c
		$p > 2000$ MeV/c
		`InAccMuon==1`
		`hasRICH==1`

	e	$p_{\mathrm{T}} > 500$ MeV/c
		$p > 3000$ MeV/c
		`hasCalo==1`
		`hasRICH==1`

	μ	$p_{\mathrm{T}} > 800$ MeV/c $p > 3000$ MeV/c `IsMuon==1`
	$J/\psi(\rightarrow e^+e^-)$	$p_{\mathrm{T}} > 500$ MeV/c
	B	$\chi^2_{\mathrm{vtx}}/\mathrm{dof} < 4.5$
	$K\pi\pi$	$1.1 < m(K\pi\pi) < 2.4$ GeV/c^2
Fiducial, Acceptance	e	$!(x_{ECAL} < 363.6\,\mathrm{mm}$ && $y_{ECAL} < 282.6\,\mathrm{mm})$
	`Run2`	nSPDHits < 450
Clones	all tracks	$\theta(\mathrm{track}_i, \mathrm{track}_j) > 0.5$ mrad with $i \neq j$
PID	K	$\mathrm{DLL}_K > -5$ `ProbNNk` > 0.2
	π	`ProbNNpi` > 0.2
	μ	`ProbNNmu` > 0.2
	e	$\mathrm{DLL}_e > 0$ `ProbNNe` > 0.2

4.3.4 Background studies

The underlying composition of backgrounds that pollutes a 5-body decay is very rich. Background contributions can arise from misidentification of final state particles, *e.g.* a hadron can be misreconstructed as a lepton; from the partial reconstruction of a different B decay, *e.g.* a $B \rightarrow K\pi\pi\ell\ell X$ decay where X is lost; and from the combinations of random tracks, usually referred to as combinatorial background.

In the following, different types of background that remain after the selections described in

Table 4.4: Summary of the vetoes applied against peaking backgrounds.

Decay	Requirement
$B^+ \to D^0(\to K^+\pi^-)\pi^+\pi^-_{\to\ell^+}\pi^+_{\to\ell^-}$	$!\lvert m(K\pi) - m^{PDG}(D^0)\rvert < 30$ MeV/c^2
$B^+ \to D^0(\to K^+\pi^-_{\to\ell^-})\pi^+\pi^-\pi^+_{\to\ell^+}$	$!\lvert m(K\pi_{\to\ell^-}) - m^{PDG}(D^0)\rvert < 30$ MeV/c^2
$B^+ \to D^0(\to K^+\pi^-_{\to\ell^-}\pi^+\pi^-)\pi^+_{\to\ell^+}$	$!\lvert m(K^+\pi^-_{\to\ell^-}\pi^+\pi^-) - m^{PDG}(D^0)\rvert < 30$ MeV/c^2
$B^+ \to D^-(\to K^+\pi^-\pi^-_{\to\ell^-})\pi^+_{\to\ell^+}\pi^+$	$!\lvert m(K^+\pi^-\pi^-_{\to\ell^-}) - m^{PDG}(D^+)\rvert < 30$ MeV/c^2
charmonium $e-h$ swap	$!\lvert m_{J\psi\,cons.}(K_{\to e}\pi\pi e_{\to K}) - m^{PDG}(B^+)\rvert < 60$ MeV/c^2 & `lProbNNl<0.8`
	$!\lvert m_{J\psi\,cons.}(K^+\pi^\pm_{\to e}\pi^\mp e^\pm_{\to\pi}e^\mp) - m^{PDG}(B^+)\rvert < 60$ MeV/c^2 & `lProbNNl<0.8`
charmonium $\mu-h$ swap	$!\lvert m(K_{\to\mu}\mu) - m^{PDG}(J/\psi)\rvert < 60$ MeV/c^2
	$!\lvert m(\pi^\pm_{\to\mu}\mu^\mp) - m^{PDG}(J/\psi)\rvert < 60$ MeV/c^2
$B^+ \to K^+\psi(2S)(\to \pi^+\pi^- J/\psi\,(\to \ell^+\ell^-))$	$!\lvert m_{J\psi\,cons.}(\pi\pi\ell\ell) - m^{PDG}(\psi(2S))\rvert < 23$ MeV/c^2
$B^+ \to K^+\chi_{c1}(3872)(\to \pi^+\pi^- J/\psi\,(\to \ell^+\ell^-))$	$!\lvert m_{J\psi\,cons.}(\pi\pi\ell\ell) - m^{PDG}(\chi_{c1})\rvert < 23$ MeV/c^2

the previous sections are discussed. In particular, backgrounds that proceed to the same final state as the signal mode via a charmonium resonance or an intermediate charm particle, such as the D meson, are the main peaking contributions for this analysis. Those are usually removed by reconstructing the invariant mass of the final-state daughters of the resonance and by explicitly applying a veto around the resonance mass.

Table 4.4 gathers the list of the vetoes used in this analysis, that will be described in detail in the following sections.

Misidentification

Detector inefficiencies can lead to possible misidentification of the final state particles with a probability that depends on their types and momenta. For this reason, it can happen that final state particles of a different decay, with branching ratios typically larger than that of the signal, are wrongly selected as signal candidates, significantly modifying the signal mass line shape. In order to reduce this kind of background, the invariant mass distributions of several combinations of final state particles can be studied in simulation/data, where the misidentification can be reverted. In this way, it is possible to reconstruct intermediate resonances from which the misidentified particles come, and to define vetoes to remove them.

$K \to \pi$ misidentification.

The decay $B^+ \to \phi K^+\ell^+\ell^-$ has been observed at LHCb [79] with muons in the final state, with a branching fraction of $\mathscr{B}\left(B^+ \to \phi K^+\mu^+\mu^-\right) = 0.82^{+0.34}_{-0.32} \times 10^{-7}$. Since the ϕ resonance decays into two kaons of opposite sign in approximately 50% of the cases [10], the decay $B^+ \to K^+K^+K^-\mu^+\mu^-$, where two kaons are misidentified as pions, can be a possible source of background. Figure 4.5 shows the $m(K^+K^+_{\to\pi^+}K^-_{\to\pi^-}\mu^+\mu^-)$ invariant mass distribution in

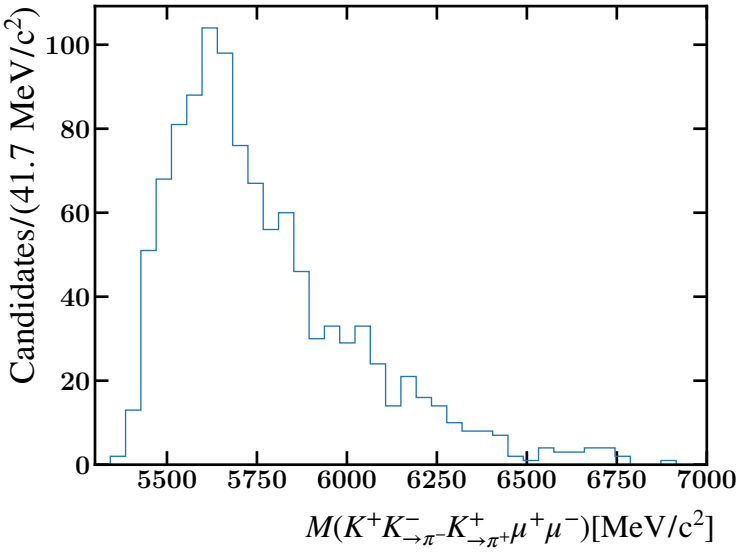

Figure 4.5: Invariant B^+ mass distributions in data in the $B^+ \to K^+K^+_{\to\pi^+}K^-_{\to\pi^-}\mu^+\mu^-$ hypothesis, where the two pions are assumed to be kaons misidentified as pions. No peaks where found pointing to possible $B^+ \to \phi K^+\mu^+\mu^-$ backgrounds.

data, where $K_{\to\pi}$ stands for a kaon reconstructed under pion mass hypothesis. No visible peak is observed in the distribution, which was expected given the initial suppression of $\mathcal{B}_{B\to\phi K\mu\mu}/\mathcal{B}_{B\to K\pi\pi\mu\mu} \sim 0.2$ and the PID requirements on the final state particles (listed in Table 4.3), which reduced this contribution to a negligible level.

***p* → *K* misidentification**.

The baryon Λ_c^+ decays into $\Lambda_c^+ \to pK^-\pi^+$ with a branching fraction of $(6.23 \pm 0.33)\%$ and into $\Lambda_c^+ \to pK_s^0(\to \pi^+\pi^-)$ with a branching fraction of $(1.59 \pm 0.08)\%$. Therefore, the Λ_c^+ could be a source of peaking background when the proton is reconstructed under the kaon mass hypothesis. Figure 4.6 show the $m(K^+\pi^+\pi^-)$ invariant mass distribution in electron and muon data, with the preselection applied, with possible combination of wrong mass hypotheses. No visible Λ_c peak is observed and thus no veto against the Λ_c is included in the selection.

Misidentified fully hadronic decays. There can be several possible contaminations from purely hadronic decays that can mimic the final state of interest with a double misidentification of two pions as leptons. This includes contributions such as $B^+ \to \overline{D}^0(\to K^+\pi^-)\pi^+\pi^-\pi^+$; $B^+ \to D^-(\to K^+\pi^-\pi^-)\pi^+\pi^+$; and $B^+ \to \overline{D}^0(\to K^+\pi^-\pi^+\pi^-)\pi^+$. While PID requirements strongly suppress these type of decays, due to their large branching fractions, of the order of 10^{-4}, these backgrounds can still contribute to the signal region. Since these backgrounds can be fully reconstructed under the correct mass hypothesis, the several hadronic combinations in data can be examined, to apply the appropriate veto around the charm meson. Figure 4.7 and 4.8

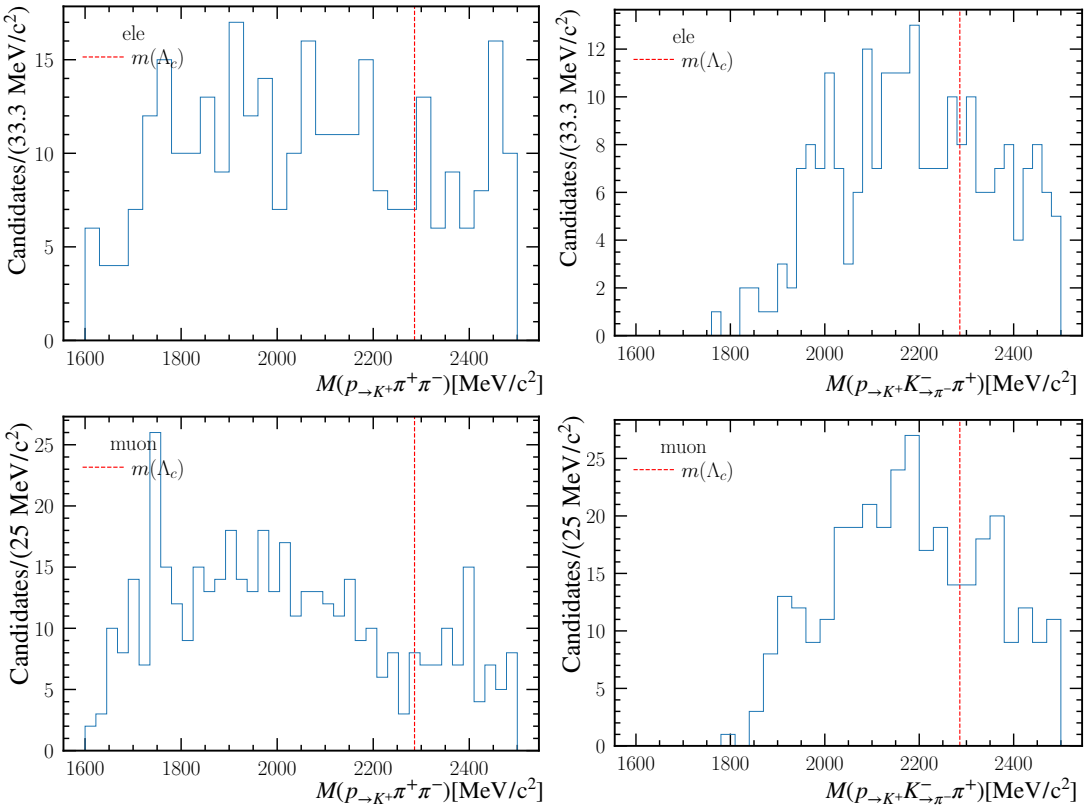

Figure 4.6: Distributions of $m(K^+\pi^+\pi^-)$ in $B^+ \to K^+\pi^+\pi^- e^+ e^-$ (top) and $B^+ \to K^+\pi^+\pi^-\mu^+\mu^-$ (bottom) decays in data, for all the possible proton reconstructions under wrong mass hypothesis.

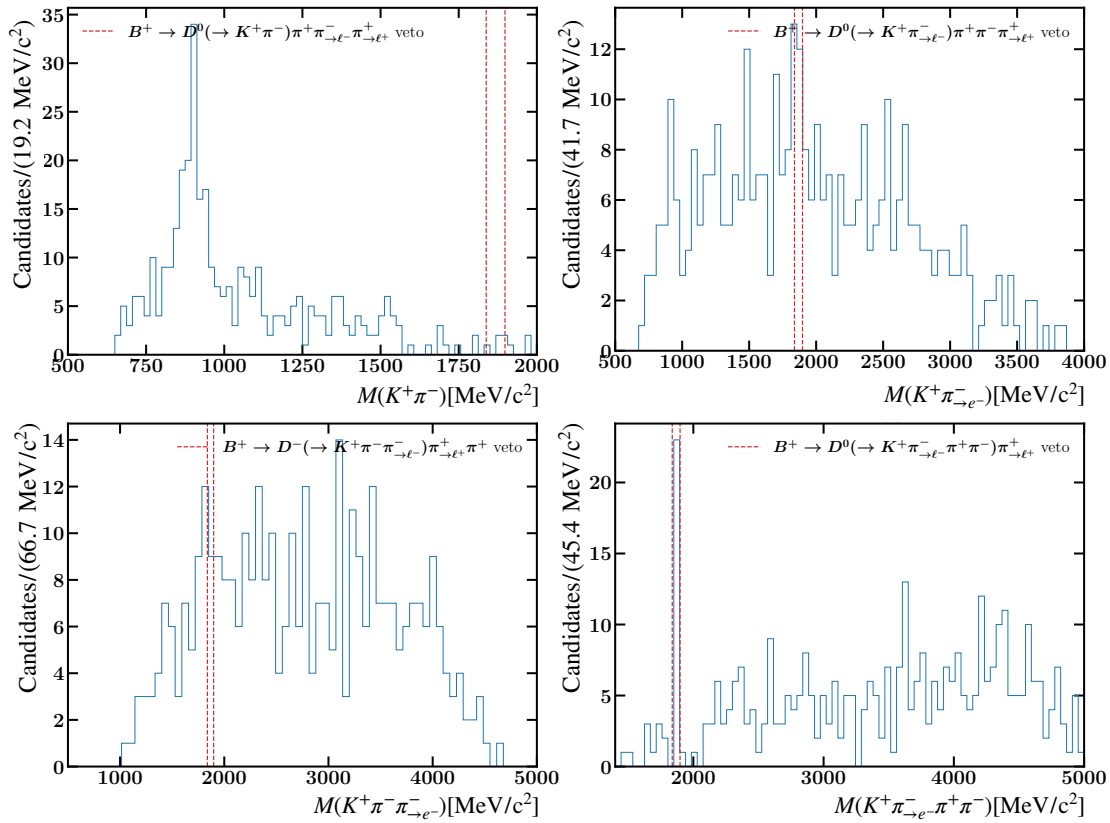

Figure 4.7: $B^+ \to K^+\pi^+\pi^-e^+e^-$ distributions for the $K\pi$, $K\pi\pi$ and $K\pi\pi\pi$ invariant masses in data, with possible misidentification of the final state particles. The data used for these plots are selected in a 100 MeV window around the B mass. The corresponding vetoed regions are shown in red.

show these invariant mass distributions for the electron and muon channels, respectively. The veto considered in this analysis consists in removing candidates in a 30 MeV window around the D meson mass, as summarised in Table 4.4. These criteria result in a signal loss of $(0.62\pm0.17)\times10^{-3}$ for the $K\pi$ veto, $(5.23\pm0.16)\%$ for the $K\pi\pi$ veto and $(2.51\pm0.25)\times10^{-3}$ for the $K\pi\pi\pi$ veto. In addition, these vetoes also remove contributions from semileptonic decays in which the charm meson decays to fully hadronic final state, *i.e.* $B^+ \to \overline{D}^0(\to K^+\pi^-\pi^+\pi^-)\ell^+\nu_\ell$ decays.

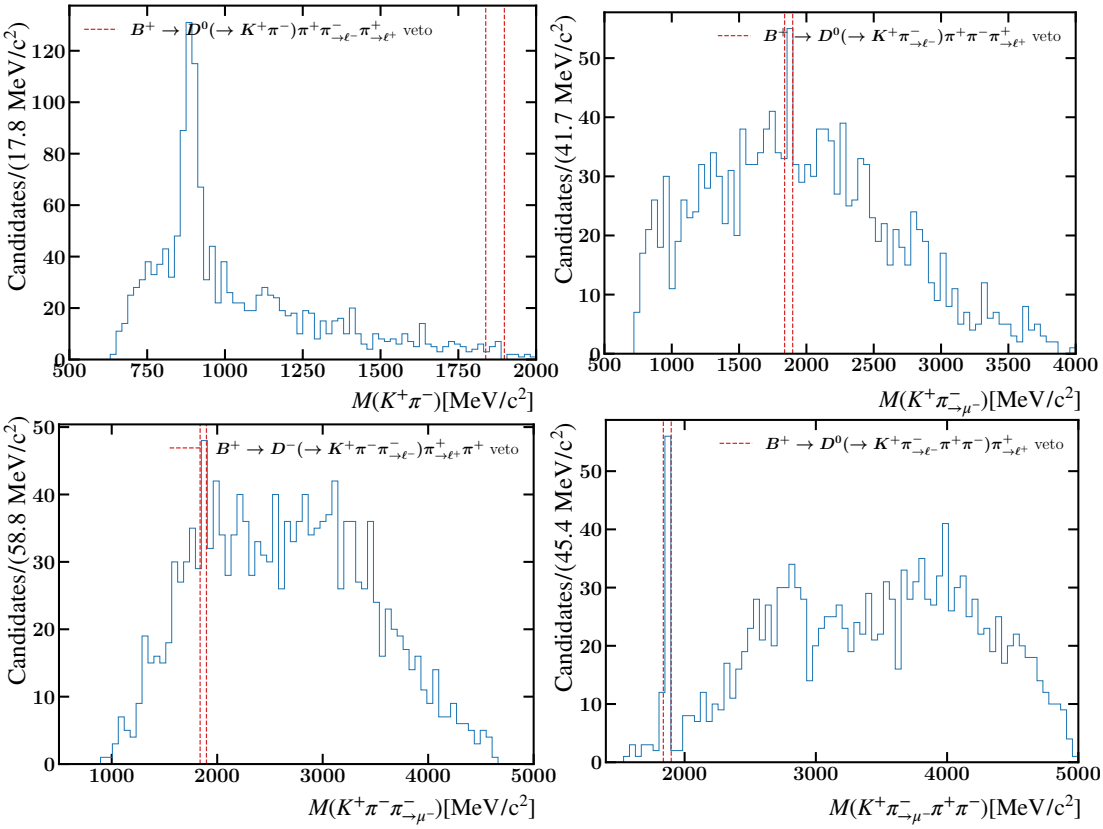

Figure 4.8: $B^+ \to K^+\pi^+\pi^-\mu^+\mu^-$ distributions for the $K\pi$, $K\pi\pi$ and $K\pi\pi\pi$ invariant masses in data, with possible misidentification of the final state particles. The data used for these plots are selected in a 100 MeV window around the B mass. The corresponding vetoed regions are shown in red.

***h*↔ℓ swap**. The rejection of events such as the resonant decay $B^+ \to K^+\pi^+\pi^- J/\psi\,(\to \ell^+\ell^-)$ in the presence of a double lepton-hadron misidentification, *e.g.* $B \to K^+_{\to \ell^+}\pi^+\pi^- e^+_{\to K^+} e^-$, is highly dependent on the mass resolution. Therefore, simple vetoes on $m(h_{\to \ell}\ell)$ around the J/ψ mass, although working well enough for muons as shown on the left side of Figure 4.9, tend to lack in signal efficiency and/or background rejection power for modes including electrons. One proposed method, adopted in the recent update of R_{K^*} [33], is to make use of the invariant mass of all the final states particles, calculated by constraining the invariant mass of the possible misidentified couples $m(h_{\to \ell}\ell)$ to that of the J/ψ. Such masses are shown on the right side of Figure 4.9 for all the possible misidentifications. The requirement used for the rejection of lepton-hadron swaps requires the exclusion of events within 60 MeV around the charmonium mass for the muons and within 60 MeV around the B meson mass for the electrons. An additional requirement on the identification of the electron, `ProbNNe` < 0.8, is applied for the events to be removed by the veto. This allows to improve the signal yield in the electron modes while maintaining the purity of the samples, since electrons with higher values of `ProbNNe` are more likely to be real electrons. These requirements have a high signal efficiency in simulation and reduce background contributions to a negligible level. Distributions and vetoes applied are shown in Figure 4.9. Figure 4.10 shows the combination of the vetoes on the electron constrained masses and on the identification requirements.

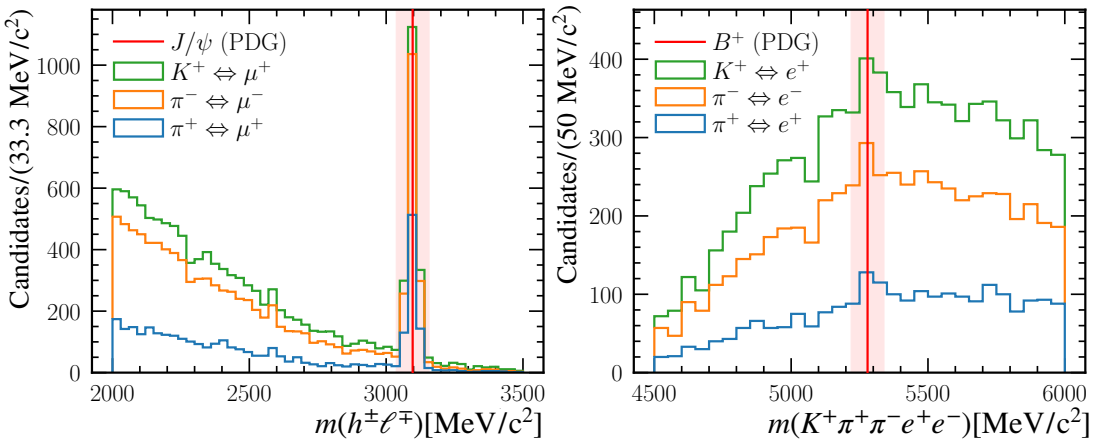

Figure 4.9: Invariant mass distributions of one hadron and the muon of opposite charge where the hadron is reconstructed as a muon (left); and invariant mass of the B meson calculated by constraining one hadron and one electron to originate from a J/ψ (right). Both distributions use `Run2` data. The histograms are stacked and the corresponding vetoed regions are shown in red.

Residual $h_{\to \ell}$ misidentified backgrounds: Residual backgrounds arising from decays where a single or a double misidentification of $\pi_{\to e}$ and/or $K_{\to e}$ is present can still pollute the signal region. We estimate such backgrounds with the same data-driven method as used in the RX analysis [33], referred to as the `PassFail` method. The method can be divided in three steps:

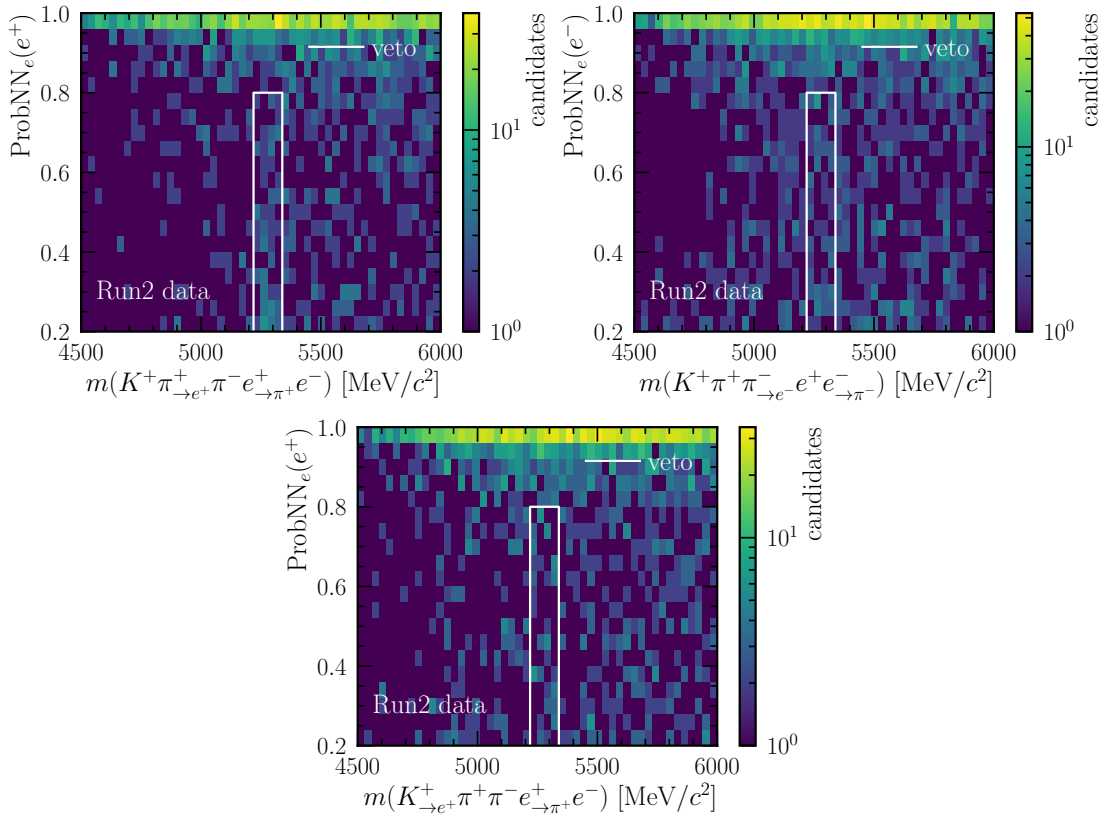

Figure 4.10: Two-dimensional plots of the invariant masses of the B meson calculated by constraining one hadron and one electron to originate from a J/ψ and of the `ProbNN`ℓ of the misidentified lepton, on `Run2` data. The vetoed regions are shown in white.

i. Defining a region enriched in misidentified decays, in the following referred to as *control* region. The control region is selected by inverting the requirement on the particle identification criteria, while keeping the rest of the selection unchanged. The choice of the inverted requirements must result in a dataset with enough event yield but still representative of the signal region, *i.e.* the identification criteria must be not too far from the nominal ones. In the following, the inverted requirements of the *control* region are referred to as the `Fail` selection, while the nominal criteria of the *signal* region are referred to as the `Pass` selection. The control region dataset will be used to obtain an estimation of the shape and the amount of the background coming from misidentification in the signal region.

ii. Computing a transfer function, needed to transfer the knowledge of the background coming from misidentifications *from* the control *to* the signal region. This is achieved by reweighting every event of the `Fail` dataset. The weights are computed as 2D maps in electron transverse momentum and rapidity, exploiting the large samples of $D^{*+} \to D^0(\to K^-\pi^+)\pi^+$ decays collected by LHCb, used also to calibrate the PID responses in simulation (described in Section 4.4.2). The weights are defined as

$$w_{\text{fake}} = \frac{\varepsilon_{\texttt{Pass}}}{\varepsilon_{\texttt{Fail}}}(p_{\text{T}}, \eta), \tag{4.6}$$

where $\varepsilon_{\texttt{Pass}}$ and $\varepsilon_{\texttt{Fail}}$ stand for the efficiency of the `Pass` and `Fail` selections computed on the calibration samples. The weights are estimated separately for the two `L0` trigger categories, `L0TOS` and `L0TIS`, and for the type of particle being misidentified as an electron (*i.e.* the K or the π). The latter is achieved by arbitrarily assigning the particles in the `Fail` region to be a K or a π based on their `ProbNNk` score, *i.e.* they are assumed to be kaons if their ProbNNk > 0.1 and pions otherwise. The weights used in this analysis are the ones already computed and validated in the RX analysis [33]. An example of the transfer functions computed using 2017 data is shown in Figure 4.11.

iii. Applying the transfer function, by assigning the weights computed in the step above to every event of the control regions, based on the electron transverse momentum and rapidity. The electron ProbNNk value is used to choose if the K or the π map is used. Since there are two electrons in the final state, all the possible combinations of particles failing the criteria must be taken into account. For this purpose, multiple control regions are defined: when the positron fails the identification and the electron passes it (`PassFail`), when the electron fails the identification and the positron passes it (`FailPass`) and when both fail the identification criteria (`FailFail`). To avoid double counting, and assuming factorization in the case of double misidentification, one has:

$$N^*_{\text{misID}} = \sum_i^{PF} w^i_{\text{fake}}(e^+) + \sum_i^{FP} w^i_{\text{fake}}(e^-) - \sum_i^{FF} w^i_{\text{fake}}(e^+) \cdot w^i_{\text{fake}}(e^-), \tag{4.7}$$

where the sums run over the events in the `PassFail` (PF), `FailPass` (FP) and `FailFail` (FF) regions. Nevertheless, the N^*_{misID} events as defined above can still be polluted by

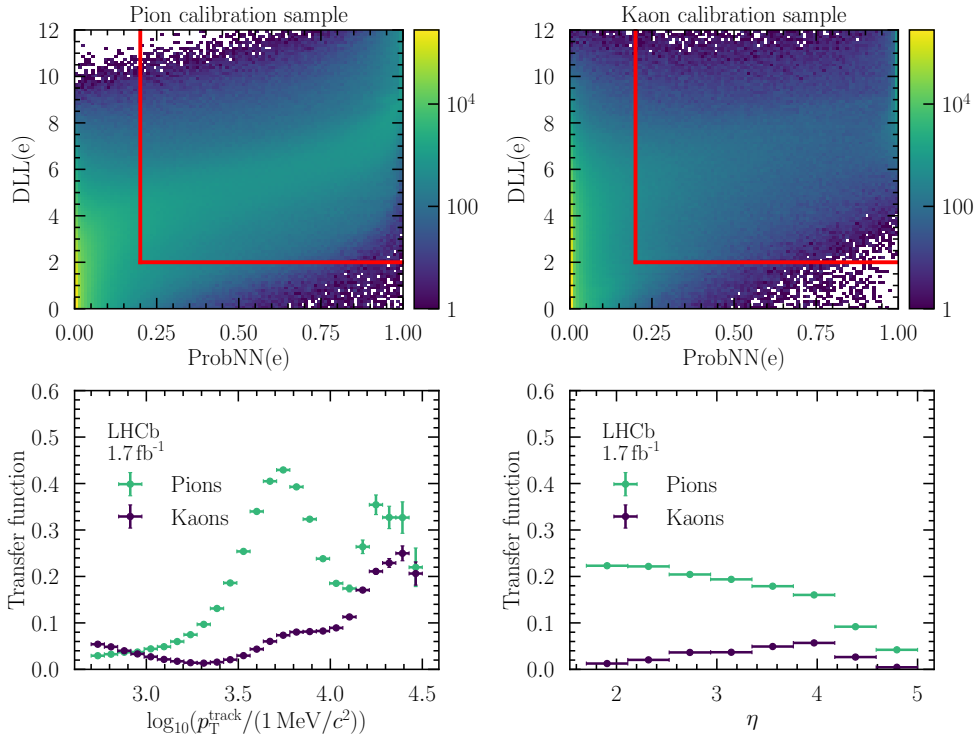

Figure 4.11: Distributions of events in the (top left) pion and (top right) kaon 2017 calibration samples with respect to the electron PID variables. The red lines show the `Pass` region (top right corner) and the `Fail` region (outside the `Pass` region). In addition, the fraction of control region events that is expected to appear in the fit region (transfer function) is shown as functions of track p_T (bottom left) and η (bottom right) [33].

real electrons (*signal*) and by electrons from the J/ψ resonant channel (*leakage*). In order to estimate these contributions one can define the same FP, PF and FF control regions in the resonant and rare mode simulated samples. Then, one can scale the yields obtained from the fits to the invariant masses of the final state particles in the data samples (described in Section 4.6.1) by the relative efficiencies of the FP, PF and FF control region selections with respect to the nominal selection (`PassPass`). This is possible because the inversion of the identification criteria is the only difference with respect to the selection applied when performing the fits. For example, the expected contribution of real electrons (signal) in the FP control region is given by:

$$\mathcal{N}^{\text{est}}_{\text{FP}}(\text{signal}) = \mathcal{N}_{\text{fit}}(\text{K}\pi\pi\text{ee}) \cdot \frac{1}{\sum_{\text{i}}^{\text{FP}} \text{i}^{\text{MC}}_{\text{sig}}} \cdot \frac{\varepsilon^{\text{MC}}_{\text{sig}}(\text{FP})}{\varepsilon^{\text{MC}}_{\text{sig}}(\text{PP})}, \tag{4.8}$$

where the sum at the denominator is necessary for the normalisation of the yield of the simulated samples.
Taking into account all the control regions, the total number of events with real signal electrons polluting N^{*}_{misID} can be estimated as:

$$\begin{aligned} N_{\text{misID}}(\text{signal}) = &\sum_{i}^{PF} \mathcal{N}^{\text{est}}_{\text{PF}}(\text{signal}) \cdot \text{w}^{\text{i}}_{\text{fake}}(\text{e}^{+}) + \sum_{\text{i}}^{\text{FP}} \mathcal{N}^{\text{est}}_{\text{FP}}(\text{signal}) \cdot \text{w}^{\text{i}}_{\text{fake}}(\text{e}^{-}) \\ &- \sum_{i}^{FF} \mathcal{N}^{\text{est}}_{\text{FF}}(\text{signal}) \cdot w^{i}_{\text{fake}}(e^{+}) \cdot w^{i}_{\text{fake}}(e^{-}), \end{aligned} \tag{4.9}$$

where the $\mathcal{N}^{\text{est}}_{\text{FF(PF)}}(\text{signal})$ terms are computed in the same way as $\mathcal{N}^{\text{est}}_{\text{FP}}(\text{signal})$ in Eq. 4.8, but with the respective efficiencies of the different control regions.
The same can be easily translated when estimating the leakage from the J/ψ mode, using the resonant simulation and the resonant yields.
Finally, taking into account all contributions, N_{misID} is estimated as:

$$N_{\text{misID}} = N^{*}_{\text{misID}} - N_{\text{misID}}(\text{signal}) - N_{\text{misID}}(\text{leakage}) \tag{4.10}$$

The application of the `PassFail` method just described to the $B^{+} \to K^{+}\pi^{+}\pi^{-}e^{+}e^{-}$ samples is shown in Figure 4.12 for `Run2` data and for the `L0TOS` trigger category. In the figure, the invariant mass distributions in the several control regions in data and in signal and resonant simulations are shown, as well as their combination obtained as in Eq. 4.7. The final estimation of possible misidentified background in the signal region is shown in Figure 4.13, where the contribution of real electrons from signal and from the resonant decays are subtracted and the two trigger categories `L0TOS` and `L0TIS` are merged. The final expected line-shape of background coming from misidentification in the signal region is shown in Figure 4.13. The expected amount of such background for the different data-taking periods and trigger categories is shown in Table 4.5.

This contribution is included in the nominal fit model, in addition to the combinatorial

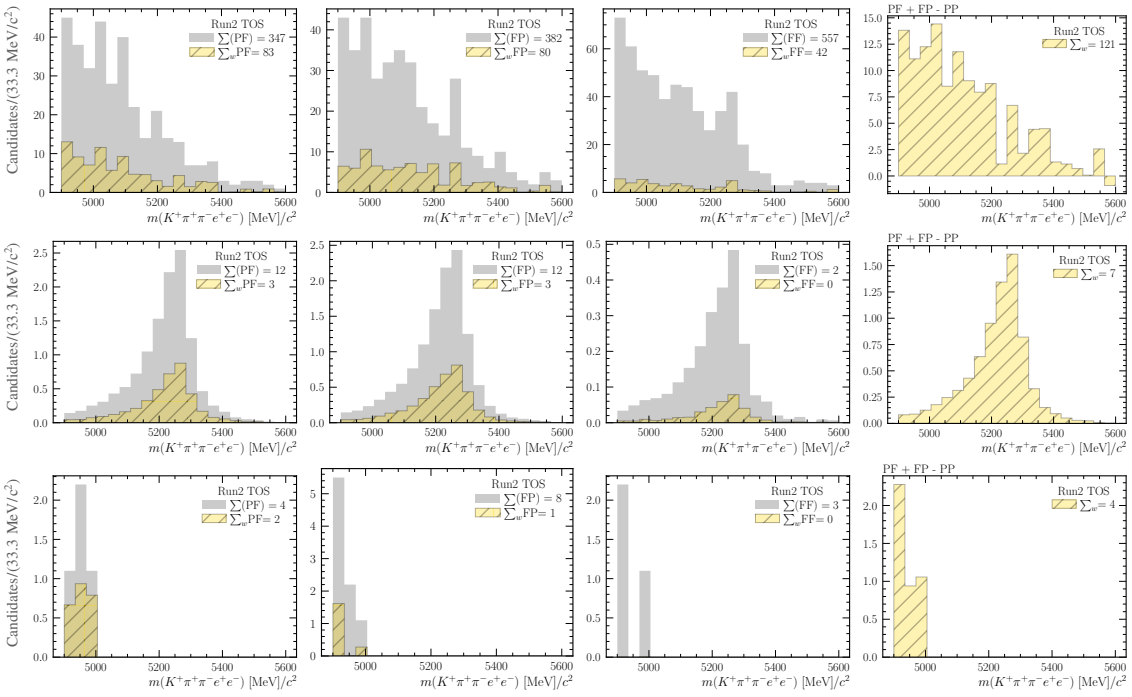

Figure 4.12: Invariant mass distributions for the PF (first column), FP (second column) and FF (third column) control regions before (grey) and after (yellow) w_{fake} are applied. The control regions are defined in Run2 data (first row), signal simulation (middle row) and resonant J/ψ simulation, selected with the L0TOS trigger. The fourth column shows the expected yield and distribution in the signal region of each component, computed as in Eq. 4.7.

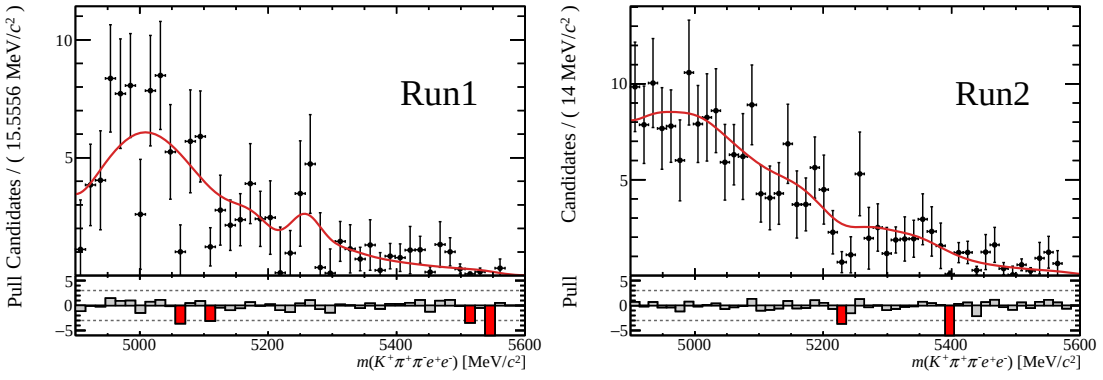

Figure 4.13: The invariant mass distributions of misID background predicted by the PassFail method for Run1 (left) and Run2 (right). The TOS and TIS trigger categories have been merged in each data-taking period.

Table 4.5: Estimated amount of background coming from $h \to e$ misidentification in the signal region.

$N(h \to e)$	TOS	TIS
Run1	39 ± 5	71 ± 8
Run2p1	36 ± 5	24 ± 2
Run2p2	77 ± 8	48 ± 3

background. The line-shape is fixed to what it is obtained when fitting the distributions (as shown in Figure 4.13) with a kernel density estimator function. Its amount is also fixed to the estimations given by the PassFail method, shown in Table 4.5. Systematic uncertainties due to this choice are evaluated by either using another empirical shape to model the line-shapes, or by constraining the yield to be gaussian-distributed with mean and resolution equal to the yield and error predicted by the method, respectively, as explained in Section 4.8.1.

Partially reconstructed decays

In a multi-body decay such as $B^+ \to K^+\pi^+\pi^-\ell^+\ell^-$, the presence of background coming from higher multiplicity decays where some tracks of the event are not reconstructed is expected, *i.e.* $B \to K^+\pi^+\pi^-\ell^+\ell^- X$, where X is missing. These types of background usually accumulate at lower B^+ mass with respect to the signal, due to the missing energy, but some leakage can still pollute the signal region. They are particularly difficult to estimate, since the decays from which they originate have different branching ratios and contribute at different masses. Therefore, due to this partial knowledge which makes it difficult to quantify the partially reconstructed background contribution, a dedicated selection for this type of background is not added to the selection, but rather a data-driven strategy is derived to model this contribution in the fit to the B meson mass shape, using data from the resonant J/ψ channels. This strategy is explained in detail in Section 4.6.2.

Semileptonic decays

Semileptonic decay chains such as $B^+ \to D^-\left(\to K^+\pi^-\ell^-\bar{\nu}\right)\pi^+\ell^+\nu$, $B^+ \to D^0\left(\to K^-\ell^+\nu\right)\pi^+\pi^+\pi^-_{\to\ell^-}$ and $B^+ \to D^-\left(\to K^+\pi^-\ell^-\bar{\nu}\right)\pi^+\pi^+_{\to\ell^+}$ can be a source of background either with the same final states of interest (plus missing neutrinos) or when one pion is misreconstructed as a lepton. Figure 4.14 shows the typical exponential-like distribution of the $K\pi\pi ee$ invariant mass for this family of backgrounds. While their core distribution are mainly populating very low mass regions, the long tail can still contribute in the invariant mass region of interest. The cumulative branching fractions for these processes are about 1.6×10^{-4}, 2×10^{-4} and 4×10^{-5}, respectively, but the latter two additionally require the reconstruction of one pion under the lepton mass hypothesis. These numbers are further reduced by a factor of $\mathcal{O}(10^{-2} - 10^{-3})$ by several elements in the selection: track quality requirements, PID identification (for the

misidentified decays), q^2 and invariant mass range, and MVA/trigger criteria. As a result, one can conclude that

- the effective branching ratios for both $B^+ \to D^- \left(\to K^+\pi^-\ell^-\bar{\nu}\right)\pi^+\pi^+_{\to\ell^+}$ and $B^+ \to D^0 \left(\to K^-\ell^+\nu\right)\pi^+\pi^+\pi^-_{\to\ell^-}$ backgrounds are suppressed to a negligible level by the full selection chain used in the analysis, and any remaining contamination is accommodated in the combinatorial background model;
- the $B^+ \to D^- \left(\to K^+\pi^-\ell^-\bar{\nu}\right)\pi^+\ell^+\nu$ background is also expected to be small and additional data-driven studies are performed, in order to gain some further confidence on the level of contamination of $B^+ \to D^- \left(\to K^+\pi^-\ell^-\bar{\nu}\right)\pi^+\ell^+\nu$ background in the data. In fact, it is possible to define an angular basis in which the angle θ_ℓ is defined as the angle between the direction of the $\ell^+(\ell^-)$ in the dilepton rest frame and the direction of the dilepton in the $B^+(B^-)$ rest frame. This definition is the same as used in previous LHCb angular analyses, such as Ref. [86]. Due to the energy loss from the missing neutrinos, this background has a distribution in $K\pi\pi\ell\ell$ mass similar to that of the combinatorial one as shown in Fig. 4.14, but with a slope that drops at the mass of the B. This similarity is however not mirrored in the angular distribution of θ_ℓ: as the antilepton (lepton) from the $B^+(B^-)$ tends to have higher momentum than the one from the D, and θ_ℓ by definition will always refer to the angle between the B and this antilepton/lepton, it will generally take on values close to zero, giving rise to a distinctive, asymmetric $\cos\theta_\ell$ distribution peaked near unity. Figure 4.15 shows the $\cos\theta_\ell$ distribution in slices of the invariant mass using data. While at very low mass region there are clearly visible contributions from double semileptonic decays, in the mass region used in this analysis no prominent asymmetry pattern is observed. To conclude, this contribution is expected to be absorbed by the combinatorial background component in the fit to the invariant mass of the final state particles.

Direct contributions

The decays $B^+ \to K^+\psi(2S)(\to \pi^+\pi^- J/\psi)$ and $B \to K^+\chi_{c1}(3872)(\to \pi^+\pi^- J/\psi)$, where the J/ψ decays into a pair of muons or electrons, are already removed from the rare signal sample with the q^2 selection (Section 4.2.2), but they must be explicitly suppressed for the normalisation mode $B^+ \to K^+\pi^+\pi^- J/\psi$. The $\psi(2S)$ and the $\chi_{c1}(3872)$ resonances are removed by imposing a veto on $m^{J/\psi}(\pi\pi\ell\ell)$, where, as usual, $m^{J/\psi}$ is the invariant mass obtained by constraining the two leptons to originate from a J/ψ. These invariant mass distributions and the respective vetoes are shown in Figure 4.16.

Charmonium contribution

The value of the invariant mass squared $m^2(\ell^+\ell^-)$ of the pair of leptons in the final state, *i.e.* the q^2, is expected to be different for signal decays and for the decays involving charmonium resonances. This is why, in the analysis, distinct dilepton mass windows are defined

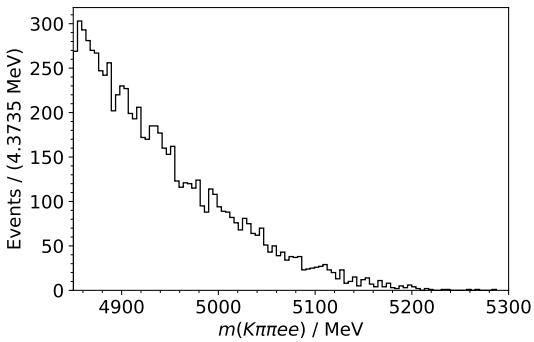

(a) $B^+ \to D^-\pi^+e^+\nu_e$, with $D^- \to K^+\pi^-e^-\overline{\nu}_e$

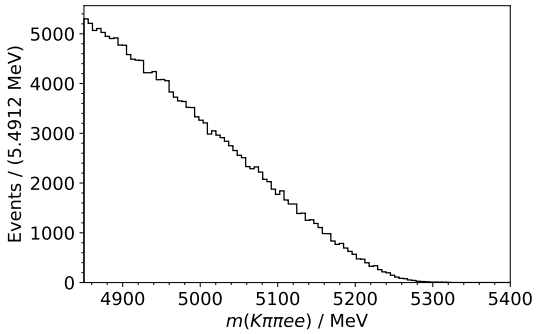

(b) $B^+ \to D^-\pi^+\pi^+$, with $D^- \to K^+\pi^-e^-\overline{\nu}_e$

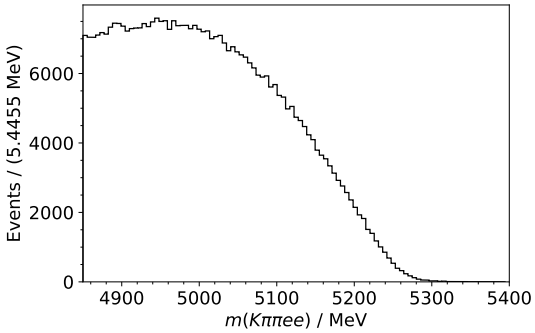

(c) $B^+ \to D^0\pi^+\pi^-\pi^+$, with $D^0 \to K^-e^+\nu_e$

Figure 4.14: Invariant mass distribution of the $K\pi\pi ee$ system for the semileptonic background processes described in the text. 1M events are simulated per process. For reference: the nominal B mass range used in the fit to the signal $B^+ \to K^+\pi^+\pi^-\ell^+\ell^-$ decays is $4900 < m_{K\pi\pi\ell\ell} < 5600\,\text{MeV}/c^2$.

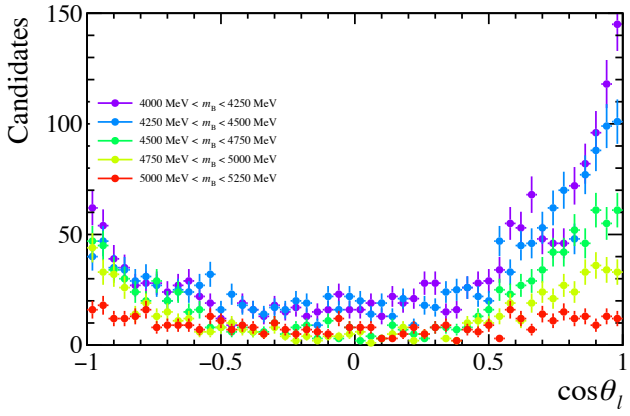

Figure 4.15: $\cos(\theta_\ell)$ distribution in Run2 $B^+ \to K^+\pi^+\pi^-e^+e^-$ data samples. The distribution is shown for different B meson mass windows, from the furthest (violet) to the nearest (red) to the nominal signal region.

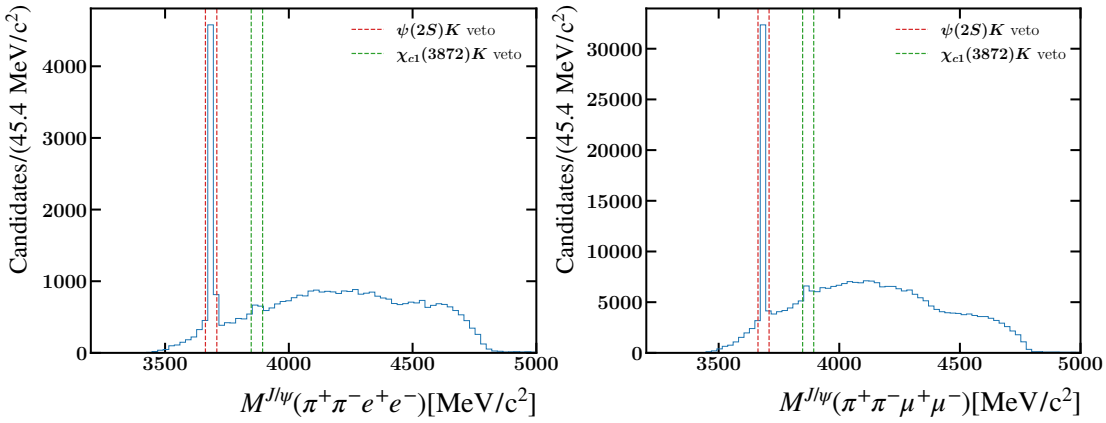

Figure 4.16: Invariant mass distributions in data for the $m^{J/\psi}(\pi\pi\ell\ell)$ system with the corresponding vetoed regions between 3663 MeV and 3709 MeV in red (to remove the $\psi(2S)$ resonance), and between 3848 MeV and 3894 MeV in green (to remove the $\chi_{c1}(3872)$).

(for signal, J/ψ or $\psi(2S)$ regions), by applying different cuts on the q^2, as explained in Section 4.2.2. Nevertheless, it could happen that decays involving nearby resonances, mainly the J/ψ, are not completely removed from the signal region by these requirements, leading to possible leakage into the signal q^2 range. In order to evaluate this contribution, the efficiency of the full selection for signal decays, including the q^2 requirement, is computed with the $B^+ \to K^+\pi^+\pi^- J/\psi\,(\to \ell^+\ell^-)$ simulated samples (applying the full correction chain to simulation samples, as described in Section 4.4). Figures 4.17 and 4.18 show the distributions of simulated resonant events surviving after the full rare mode selection is applied, for electron and muon final states respectively. Then, the number of $B^+ \to K^+\pi^+\pi^- J/\psi\,(\to \ell^+\ell^-)$ events falling into the signal region is evaluated as

$$N_{J/\psi\,\text{leak}}(\ell\ell) = \frac{\varepsilon^{J/\psi}(\text{rare})}{\varepsilon^{J/\psi}(\text{reso})} \cdot \mathcal{N}(B \to K\pi\pi J/\psi\,(\to \ell\ell)), \tag{4.11}$$

where $\varepsilon^{J/\psi}(\text{rare})$ and $\varepsilon^{J/\psi}(\text{reso})$ are the efficiencies of the signal and resonant selections calculated on J/ψ resonant simulated samples, and $\mathcal{N}(B \to K\pi\pi J/\psi\,(\to \ell\ell))$ is the yield obtained from fits to the reconstructed B^+ invariant mass in data (see Section 4.6.1). The estimated number of J/ψ-leakage events into the signal region is shown in Table 4.6, for all the trigger categories and run periods. Since the contribution is found to be nonnegligible in the electron mode, it is included as an additional component in the fit model for the rare mode signal, as described in Section 4.6.2.

Furthermore, the electron distributions and the leakage estimation change significantly (Table 4.6), especially in the `Run2` datasets, if one applies or not a correction to the resolution of the dielectron invariant mass, which is usually worse in data than in simulated samples (see the details of the *smearing* correction in Section 4.4.8). That is why this discrepancy in the J/ψ leakage evaluation will be assessed as a systematic effect (described in Section 4.8.1).

Table 4.6: Estimated number of J/ψ events leaking into the signal region, for the electron (with and without the smearing correction of the dilepton mass) and muon modes, split by data-taking period and trigger category.

$N(J/\psi)_{leak}$	Run1		Run2p1		Run2p2	
	TOS	TIS	TOS	TIS	TOS	TIS
$N_{\text{leak}}(ee)$	4.0 ± 1.0	4.0 ± 2.0	4.0 ± 1.0	6.0 ± 2.0	9.0 ± 2.0	14.0 ± 3.0
$N_{\text{leak}}(ee)$-smeared	5.0 ± 2.0	4.0 ± 2.0	11.0 ± 2.0	18.0 ± 4.0	41.0 ± 8.0	35.0 ± 7.0
$N_{\text{leak}}(\mu\mu)$	4.0 ± 3.0	0.0 ± 0.0	9.0 ± 5.0	8.0 ± 3.0	17.0 ± 6.0	10.0 ± 5.0

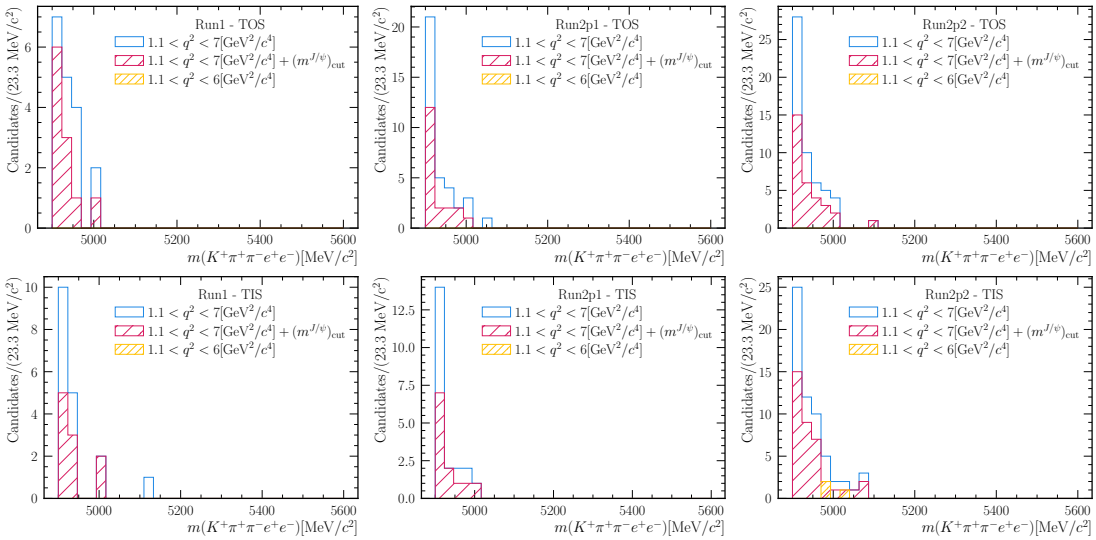

Figure 4.17: Distributions of simulated $B^+ \to K^+\pi^+\pi^- J/\psi\,(\to e^+e^-)$ events remaining after the full selection for the signal mode has been applied. Different q^2 selections are shown: in yellow $q^2 \in [1.1, 6]$ GeV$^2/c^4$, a range usually employed in similar LHCb analyses; in blue $q^2 \in [1.1, 7]$ GeV$^2/c^4$, a range widened by 1 GeV$^2/c^4$ towards the J/ψ region; in purple the selection used in this analysis. The latter consists in the wider [1.1, 7] GeV$^2/c^4$ q^2 range, on top of which a requirement on the reconstructed B^+ mass ($m^{J/\psi}$), where the two leptons are constrained to come from a J/ψ, is applied. This additional requirement ($5139.3 < m^{J/\psi} < 5476.2$) further suppresses the charmonium contribution in the signal region.

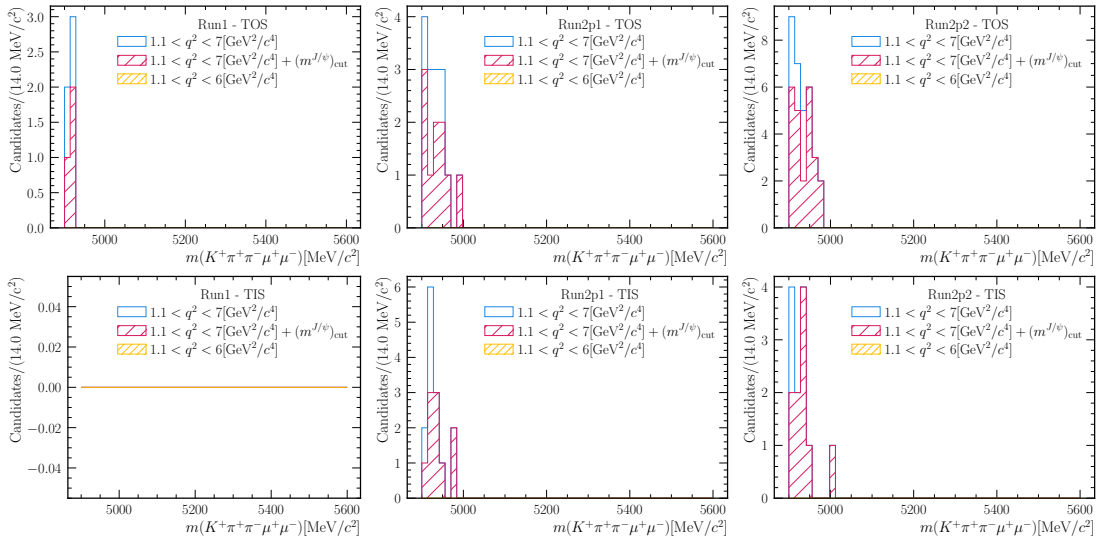

Figure 4.18: Distributions of simulated $B^+ \to K^+\pi^+\pi^- J/\psi\,(\to \mu^+\mu^-)$ events remaining after the full selection for the signal mode has been applied. Different q^2 selections are shown: in yellow $q^2 \in [1.1, 6]$ GeV$^2/c^4$, a range usually employed in similar LHCb analyses; in blue $q^2 \in [1.1, 7]$ GeV$^2/c^4$, a range widened by 1 GeV$^2/c^4$ towards the J/ψ region; in purple the selection used in this analysis. The latter consists in the wider [1.1, 7] GeV$^2/c^4$ q^2 range, on top of which a requirement on the reconstructed B^+ mass ($m^{J/\psi}$), where the two leptons are constrained to come from a J/ψ, is applied. This additional requirement ($5139.3 < m^{J/\psi} < 5476.2$) further suppresses the charmonium contribution in the signal region.

4.3.5 Multivariate Selection

Training strategy

In order to suppress contamination from combinatorial background, a boosted decision tree (BDT) from the `LightGBM` implementation [87] is used. To prevent any bias that could arise from training the classifier with the same events as it is applied to, the k-fold technique is used [88] with $k = 10$. Classifiers are trained on signal simulation and on background from the upper B-mass sideband ($m(K^+\pi^+\pi^-\ell^+\ell^-) > 5650$ MeV) in signal data; for the electron mode classifiers, the lower mass sideband (4700 MeV $< m(K^+\pi^+\pi^-\ell^+\ell^-) <$ 4900 MeV) is also used. The choice of including the additional lower mass sideband is driven by the small size of the available dataset for the electron modes in the upper mass sideband only. Therefore, the addition of the lower sideband, where the majority of the events present are expected to still be coming from combinatorial background, allows for a better training of the algorithm. Additional studies on the gain in sensitivity resulting from this choice are shown in Appendix A.

The algorithm features are chosen by recursive feature elimination, which means that in each iteration a BDT is trained on selected features, the importance of each feature is calculated, and the least important feature is dropped from the set of features for the next iteration. This procedure is repeated until only one feature is left. The whole procedure is repeated ten times with different splits among the ten folds in order to minimize statistical fluctuation. The number of training features for the final classifier is chosen by eye to be the point where the average BDT performance starts dropping significantly, which happens when 10 or fewer features are selected (see Figure 4.19). The feature ranking shown in Table 4.7 is created by calculating the mean rank of each feature candidate. The first 11 features are retained for the classifier training. After choosing the final set of features, the classifier used to discriminate signal from background is trained. For `Run1`, one classifier for the electron mode and one classifier for the muon mode are trained, for the whole data taking period. For `Run2`, one classifier for the electron mode is trained for the whole data taking period, whereas classifiers for the muon mode are trained separately for each year of data taking, yielding a 2016, a 2017 and a 2018 classifier. The 2016 classifier is also used for 2015, as the size of the 2015 dataset is very small and presents the same characteristic as the 2016 one. The performance of the classifiers is shown in Figure 4.20.

The possibility to implement a similar approach against background coming from partially reconstructed B decays has also been investigated. Nevertheless, such BDT classifier was found to be inefficient in terms of signal retention and background rejection, thus it was decided to treat the partially reconstructed background contribution directly in the fit model, as explained in Section 4.6.2.

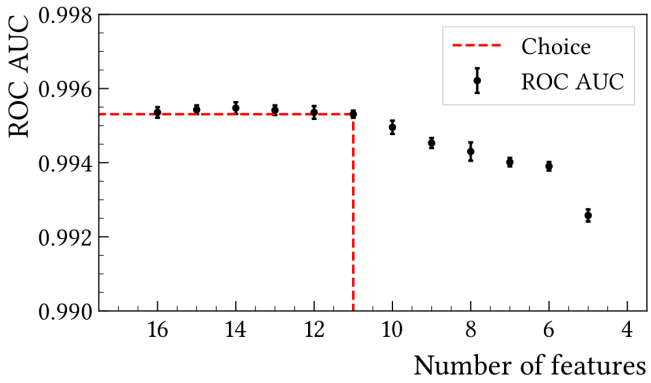

Figure 4.19: The area under the so-called "ROC" curve (receiver operating characteristic), *i.e.* a curve describing the background rejection *vs.* the signal efficiency of the BDT, as a function of the number of features the BDT is trained on.

Table 4.7: Result of the recursive feature elimination used in the classifiers. Most of the variables were already defined in the previous sections, describing the topology of the decays. In addition the `DOCA` variable is present, *i.e.* distance of closest approach between all possible pairs of particles, and the ISO_2^{vtx} variable. *i.e.* the χ^2 of the reconstructed B^+ vertex in the presence of two missing tracks.

Rank	Variable
1	$p_{\text{T}}\,(B^+)$
2	$\chi^2_{\text{FD}}\,(J/\psi\,,\text{PV})$
3	$\chi^2_{\text{vtx}}/\text{ndf}\,(B^+)$
4	$\chi^2_{\text{IP}}\,(B^+,\text{PV})$
5	$\chi^2_{\text{FD}}\,(K^+\pi^+\pi^-,\text{PV})$
6	ISO_2^{vtx}
7	$\left\lvert\text{DIRA}(K^+\pi^+\pi^-,\text{PV})\right\rvert$
8	$\max_{\text{DOCA}}(K^+,\pi^+,\pi^-,\mu^+,\mu^-)$
9	$\min_{\text{IP(PV)}}(K^+,\pi^+,\pi^-,\mu^+,\mu^-)$
10	$p\,(B^+)$
11	$\sum_{K^+,\pi^+,\pi^-,\ell^+,\ell^-} p_{\text{T}}$

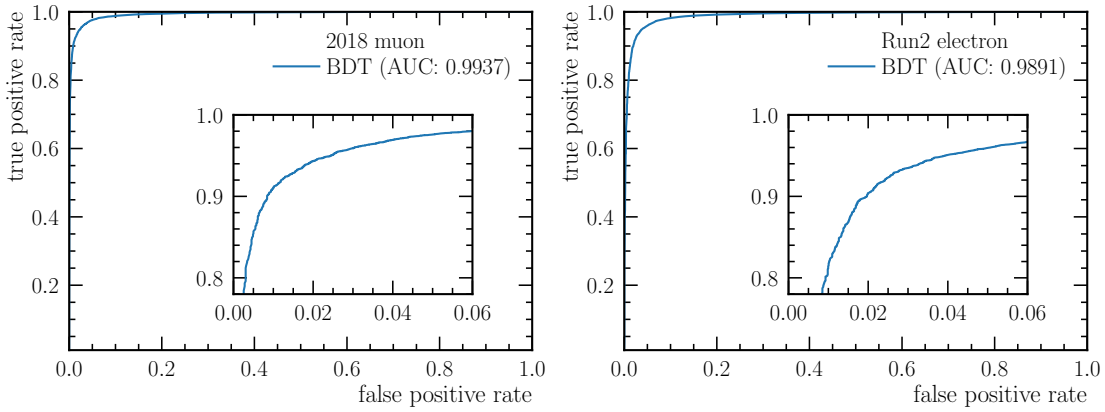

Figure 4.20: ROC curves for some of the classifiers used in this analysis, *i.e.* the one trained on Run2 electron mode samples and the one trained on 2018 muon mode samples.

BDT selection optimisation

The BDT response thresholds are chosen by optimising the figure of merit

$$\text{FoM} = \frac{S}{\sqrt{S+B}}, \tag{4.12}$$

where S and B are the expected number of signal and background events for a given requirement on BDT classifier response. The signal S is estimated from the number of $\mathcal{N}\left(B^+ \to K^+\pi^+\pi^- J/\psi\,(\to \ell^+\ell^-)\right)$ obtained by a fit to the B^+ meson invariant mass in the resonant modes. To extrapolate the number of signal decays, the resonant yields are then scaled by the branching fractions and the selection efficiencies of the signal[4] and resonant modes. Finally, the efficiency of the BDT selection considered $\varepsilon_{\text{rare}}(\text{BDT})$ needs to be included, which is evaluated on signal mode simulated samples, that allow to compute S for different BDT requirements:

$$S = \mathcal{N}\left(B^+ \to K^+\pi^+\pi^- J/\psi\,(\to \ell^+\ell^-)\right) \cdot \frac{\varepsilon_{\text{rare}}}{\varepsilon_{J/\psi}} \cdot \frac{\mathcal{B}_{\text{rare}}}{\mathcal{B}_{J/\psi}} \cdot \varepsilon_{\text{rare}}(\text{BDT}). \tag{4.13}$$

The expected background yield B is measured for every considered BDT requirement by modelling the upper mass sideband with an exponential function and calculating its integral over the signal range. The optimised selections for both final states are presented in Table 4.8. During the optimisation, the total selection efficiency for the rare channels, which is kept blinded according to the analysis strategy, needs to be calculated. This is done internally and only the efficiency of the optimal selection requirements are reported here. The results of the optimisation are shown in Table 4.8.

[4]The $\mathcal{B}(B^+ \to K^+\pi^+\pi^-\mu^+\mu^-)$ is taken as the signal branching fraction for both the muon and the electron decay modes, since the $B^+ \to K^+\pi^+\pi^- e^+ e^-$ decay has not been observed yet.

Table 4.8: Results of the BDT optimisation. Shown are optimal BDT requirement, signal estimate, background estimate in signal window, signal efficiency (not including pre-selection requirements) and the value of the figure of merit.

Decay	Year	BDT selection	S	B	ε_{BDT}	FOM
$B^+ \to K^+\pi^+\pi^- e^+ e^-$	Run1	0.878	34	15	0.71	5.0
$B^+ \to K^+\pi^+\pi^- e^+ e^-$	Run2	0.920	161	122	0.71	9.6
$B^+ \to K^+\pi^+\pi^- \mu^+ \mu^-$	Run1	0.976	195	42	0.70	12.8
$B^+ \to K^+\pi^+\pi^- \mu^+ \mu^-$	2016	0.964	254	77	0.75	14.0
$B^+ \to K^+\pi^+\pi^- \mu^+ \mu^-$	2017	0.958	252	111	0.78	13.2
$B^+ \to K^+\pi^+\pi^- \mu^+ \mu^-$	2018	0.981	262	80	0.67	14.2

4.4 Corrections to the simulation

It is a well known fact that the Monte Carlo simulated samples in LHCb suffer from several mismodelling issues, mainly concerning the simulation of the underlying pp collision, the B production kinematics and the description of the detector material. These effects result in discrepancies between data and simulation in the distributions of variables related to the track multiplicity in the event, to the momentum of the B meson, to the track reconstruction and to the particles identification. Additionally, the simulated samples used in this analysis were generated assuming a phase-space model for the hadronic system, which is flat in the $K\pi\pi$ mass between 1.1 GeV/c^2 and 2.4 GeV/c^2, the region in which LHCb is sensitive as demonstrated in [89]. In fact, as discussed in Section 4.1, the studied decay presents a complicated structure with contributions from several K^*, K_1 and K_2 states [77], where no *a priori* knowledge on the hadronic system is available.

In order to account for these issues, the simulated samples undergo a series of corrections before they are used to calculate the selection efficiencies. The various steps are detailed in the following sections, while a general overview of the correction chain is given below, where each step includes the corrections from the steps above. In general the simulated resonant $B^+ \to K^+\pi^+\pi^- J/\psi\,(\to \ell^+\ell^-)$ decays are used as control channels to compute the corrections, which are in turn applied also to the simulated samples of the rare $B^+ \to K^+\pi^+\pi^-\ell^+\ell^-$ and resonant $B^+ \to K^+\pi^+\pi^-\psi(2S)(\to \ell^+\ell^-)$ decays.

i. **PID resampling.** The first stage of corrections is implemented using a resampling procedure from the particle identification responses of high-yield calibration channels. New PID responses are added to every simulated sample so that whenever a selection containing particle identification criteria is applied to a simulated sample, the requirement is applied to the corresponding resampled variables.

ii. **Tracking efficiency.** The reconstruction efficiency of electron tracks differs in data and simulation. This has been calibrated by the LHCb tracking group [90], which produced 3-dimensional correction maps in $p_{\mathrm{T}}(e^\pm)$, $\eta(e^\pm)$ and $\phi(e^\pm)$. The e^+ and e^- weights are fetched from these maps and used as event-by-event simulation correction weight.

iii. **Phase-space correction.** The simulated samples are produced with a phase-space model for the $K^+\pi^+\pi^-$ system which does not match the complicated hadronic structure seen in data. A 3-dimensional BDT reweighter is trained on the $m(K^+\pi^-)$, $m(\pi^+\pi^-)$ and $m(K^+\pi^+\pi^-)$ distributions of $B^+ \to K^+\pi^+\pi^- J/\psi\,(\to \mu^+\mu^-)$ decays, in data and simulation, producing event-by-event weights which are applied to all the simulated samples used in the analysis.

iv. **Kinematics and multiplicity corrections.** As done in the step before, a 3-dimensional BDT reweighter is trained on $p_{\mathrm{T}}(B)$, $\eta(B)$ and and the number of tracks in the event `nTracks` distributions, producing event-by-event weights applied to the simulated sample, in order to correct the mismodelling of the B production kinematics. These corrections are calculated comparing $B^+ \to K^+\pi^+\pi^- J/\psi\,(\to \mu^+\mu^-)$ data and simulation.

v. **Trigger corrections.** A so-called "tag&probe"' approach is used to calibrate the efficiency of the trigger selections. For each trigger category used in the analysis (described in Section 4.3.2), a corresponding efficiency is calculated separately on data and on simulated samples by applying a "probe" requirement, *i.e.* the trigger decision one wants to correct, on a "tag" sample, *i.e.* composed by events with a looser selection, and evaluating the efficiency of this requirement as a function of the relevant observables which correlate with the considered trigger category. The ratio of efficiency in data and in simulation is taken as event-by-event weight and applied to the simulated samples.

vi. **Residual reconstruction effects.** This stage addresses residual differences in quantities computed during the reconstruction process. Again, a BDT reweighter is trained on data and simulated samples for the variables related to the quality of the reconstructed B vertex $\chi^2_{\text{vtx}}(B)$ and $\chi^2_{\text{IP}}(B)$. All the previously calculated corrections are applied to the simulated samples used in training.

vii. **q^2 smearing.** In general, the resolution of the dilepton invariant mass $m(ee)$ is better in simulation than in data. That is why the $m(ee)$ is transformed using the resonant $B^+ \to K^+\pi^+\pi^- J/\psi\,(\to e^+e^-)$ data and simulation samples, by means of a series of smearing parameters extracted from fits to the J/ψ mass line shape. The transformed $m_{\text{smeared}}(ee)$ is then used when calculating the efficiencies of the selections in q^2 (described in Section 4.2.2).

A sketch of the full correction chain described above, with examples of corrected simulated distributions for each step, is shown in Figure 4.21.

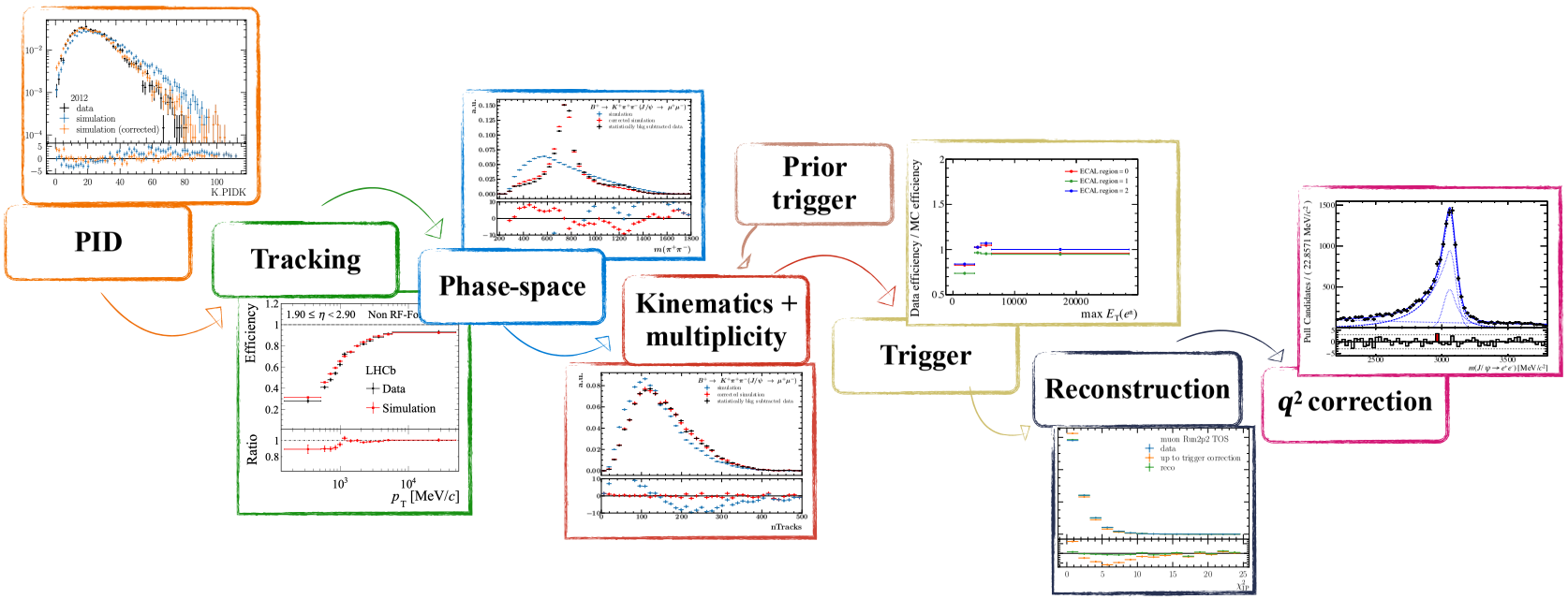

Figure 4.21: Sketch of the full correction chain applied to the simulated sample to correct for well-known data-simulation differences. For each step an example distribution of the observable being corrected is also shown.

4.4.1 Statistical background subtraction

The correction chain applied to the simulated samples is based on the comparison of distribution of variables between data and simulation. In order to obtain a fair comparison between the two, a necessary step is to remove the background contribution from the data. A well suited technique to subtract the background components is the *sPlot* method [91], which requires fitting a probability density function (PDF), including signal and background components, to a chosen variable distribution in order to extract the so-called *sWeight*s. These weights give an estimation on whether an event is more likely to be signal or background. The weights can in turn be used to obtain only signal distributions, in the following referred to as "s-Weighted" distributions, for any other variables, as long as they are uncorrelated with the one from which the *sWeight*s have been extracted.

In this case the variable chosen to perform the fit is the B-mass distribution observed in data, built with J/ψ -mass-constraint, in the $J/\psi\, q^2$ region. The data are required to pass the trigger (Section 4.3.2) and preselection (Section 4.3.3) requirements. Contributions from $B^+ \to \psi(2S)(\to J/\psi\,\pi^+\pi^-)K^+$ decays are removed as described in Section 4.3.4.

For the electron mode case, the fit model consists of three Hypatia functions, modelling the candidates where additional contribution from bremsstrahlung photons is added to none, one or both final state electrons. The Hypatia function used in these fits is the one defined in the `RooHypatia2` class within the `ROOT` data-analysis framework [92], which follows the distribution described in Ref. [93]. It is modelled as a hyperbolic core of a Crystal-Ball-like function G (described by the mean μ, resolution σ, tail parameters a, n and peak asymmetry ζ parameter), and two tails:

$$\text{Hypatia}(x,\mu,\sigma,\lambda,\zeta,\beta,a_1,n_1,a_2,n_2) = \begin{cases} \frac{G(\mu-\alpha_1\sigma,\mu,\sigma,\lambda,\zeta,\beta)}{\left(1-\frac{x}{n_1 G(\ldots)/G'(\ldots)-\alpha_1\sigma}\right)^{n_1}} & \text{if } \frac{x-\mu}{\sigma} < \alpha_1 \\ G(x,\mu,\ldots) & \text{otherwise} \\ \frac{G(\mu+\alpha_2\sigma,\mu,\sigma,\lambda,\zeta,\beta)}{\left(1-\frac{x}{-n_2 G(\ldots)/G'(\ldots)-\alpha_2\sigma}\right)^{n_2}} & \text{if } \frac{x-\mu}{\sigma} < \alpha_2, \end{cases} \tag{4.14}$$

where the core function is defined as:

$$G(x,\mu,\ldots) \equiv ((x-\mu)^2 + A_\lambda^2(\zeta)\sigma^2)^{\frac{1}{2}\lambda-\frac{1}{4}} e^{\beta(x-\mu)} K_{\lambda-\frac{1}{2}}\left(\zeta\sqrt{1+\left(\frac{x-\mu}{A_\lambda(\zeta)\sigma}\right)^2}\right)$$

with K_λ being the cylindrical harmonics or special Bessel functions of third kind and $A_\lambda^2(\zeta)$ a ratio of these: $A_\lambda^2(\zeta) = \zeta K_\lambda(\zeta)/K_{\lambda+1}(\zeta)$.

First the simulated data are split by bremsstrahlung categories, depending on the bremsstrahlung photons added to the electrons, and one Hypatia function is fit to each category. After that the same is done for data, where the tail parameters a_1, a_2, n_1, n_2 and also the parameter describing the asymmetry of the peak, ζ, are fixed from the values obtained in simulation.

The combinatorial background is modelled by an exponential function and background from partially reconstructed decays is excluded by using a fit range limited to $m(B) > 5175\,\text{MeV}/c^2$. After that the full model, consisting of three Hypatia and one exponential function, is used to fit the mass line shape in the data samples, where the bremsstrahlung categories have been merged. Here, all the shape parameters of the Hypatia functions are fixed to values obtained from the previous steps and the relative normalization of each bremsstrahlung categories is fixed from the corresponding signal yields obtained from the individual fit to each category. Thus, the only parameters, allowed to vary in the fit, are the signal yield, the background yield and the exponential parameter. An example of the fits to the simulation and to the data, for 2018 data-taking conditions, is shown in Figure 4.22.

The same procedure is applied to the $B^+ \to K^+\pi^+\pi^- J/\psi\,(\to \mu^+\mu^-)$ samples, where only one Hypatia function is fit to the simulation and data, given that muons are not needed to be separated in bremsstrahlung categories. Figure 4.23 shows the fit to the simulation and to the data for 2018 data-taking conditions in J/ψ muon samples.

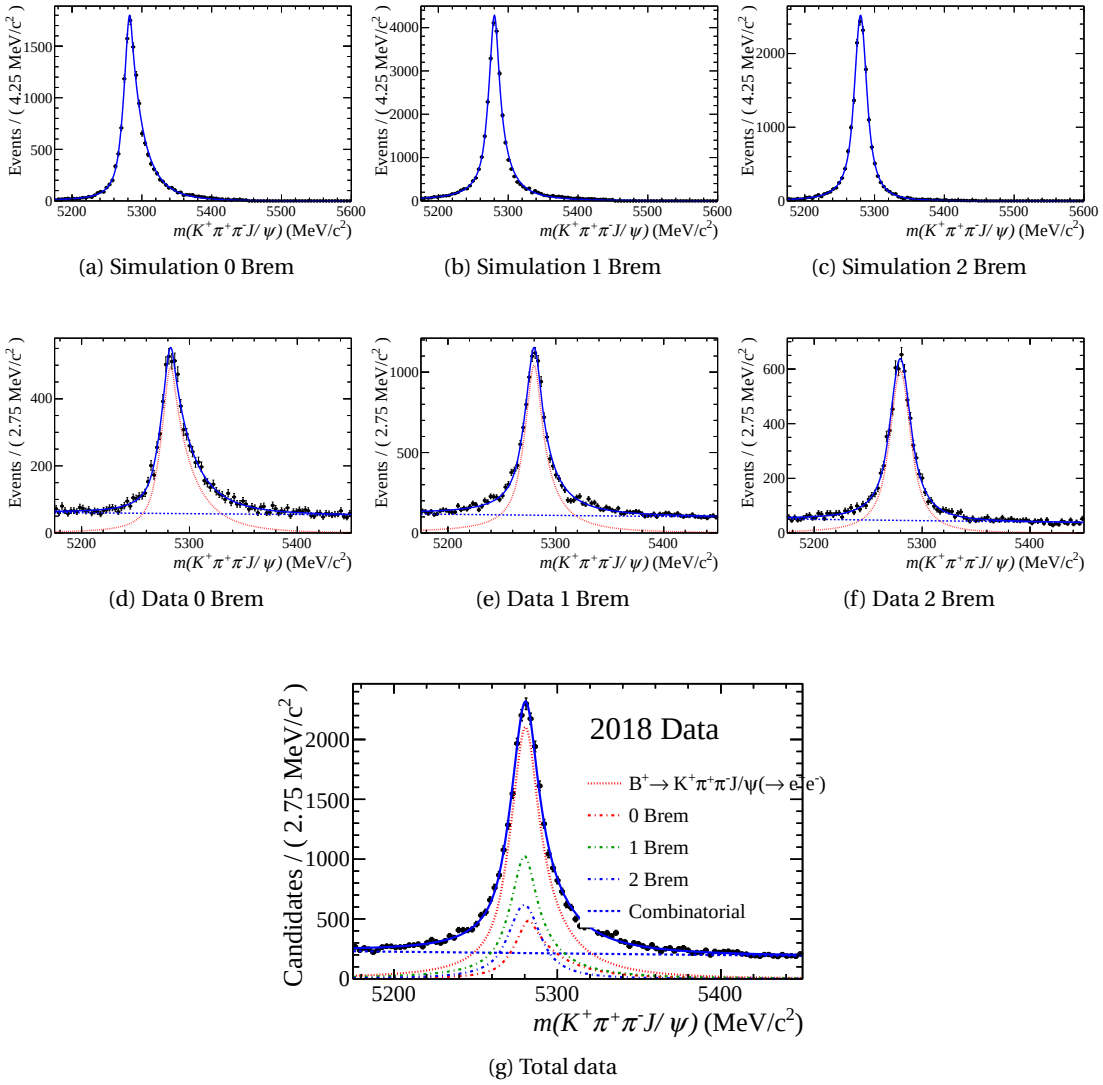

(a) Simulation 0 Brem (b) Simulation 1 Brem (c) Simulation 2 Brem

(d) Data 0 Brem (e) Data 1 Brem (f) Data 2 Brem

(g) Total data

Figure 4.22: Fit to the invariant mass of the reconstructed B meson using the J/ψ mass constraint in $B^+ \to K^+\pi^+\pi^- J/\psi\,(\to e^+e^-)$ decays. Simulation samples (top) and data samples (middle) are divided in bremsstrahlung categories: from left to right, contribution from bremsstrahlung photons has been added to none, one or both electrons in the final state. The final fit to the data, combining the three bremsstrahlung categories, is shown in the bottom. The samples refer to 2018 data-taking conditions.

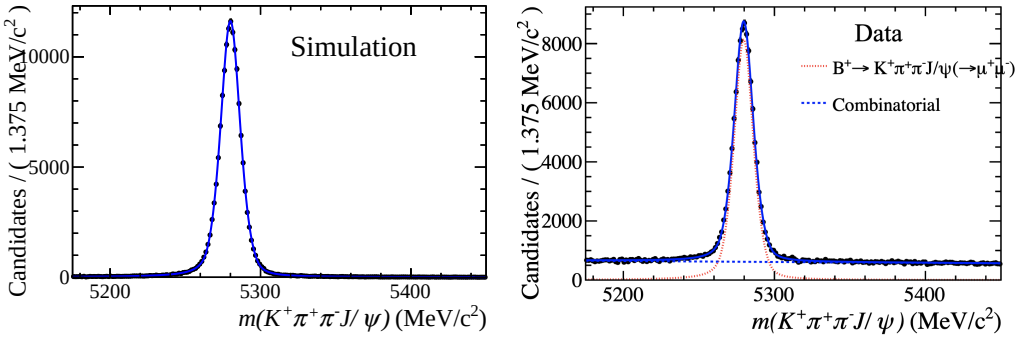

Figure 4.23: Fit to the invariant mass of the reconstructed B^+ meson, using J/ψ mass constraint, in $B^+ \to K^+\pi^+\pi^- J/\psi\,(\to \mu^+\mu^-)$ decays. Simulation (left) and data (right) refer to 2018 data-taking conditions.

4.4.2 Particle Identification response

A significant disagreement is observed between the simulation and the actual detector response for the variables used in the selection (detailed in Section 4.3.3) related to the particle identification, *i.e.* the `DLLs` and the `ProbNNs` (defined in Section 3.2.2). This is in general caused by several second-order effects (*e.g.* detector occupancy) and changes in the detector conditions during the data-taking that are not properly described in the simulation. A common practice to improve this performance consists of a data-driven approach, which exploits high-purity control samples, *i.e.* $D^{*+} \to D^{0*}(\to K^-\pi^+)\pi^+$ for hadrons, $J/\psi \to \mu^+\mu^-$ for muons, and $B^+ \to J/\psi\left(\to e^+e^-\right)K^+$ for electrons, where the background components have been subtracted via the *sPlot* technique, as explained in Section 4.4.1. These samples are processed by a dedicated working group and made available to the analysts, and they can then be used to correct the known poorly modelled distributions in the LHCb simulation.

There are two common ways to proceed: the first one is to draw the simulated distribution of the PID variable randomly from the PDF of the same variable observed in the calibration samples, where the PDF usually depends on the event kinematics and multiplicity. In this way, the original simulated distribution is completely discarded. Although this method provides a good approximation for most distributions, it does not take into account some effects. Firstly, that the neural-network based variables, *i.e.* the `ProbNNs`, depend on more variables than only the p_T, η or the number of tracks in the event. Secondly, that the different PID responses for the same track are strongly correlated, *e.g.* the ones related to the likelihood to be a kaon or a pion. For this reason, this approach is used only to correct the muon particle identification responses. For all the other responses another approach is used, whose basic idea is to transform a simulated PID variable in such a way that its distribution matches the one seen in the calibration sample (for any kinematics of the track), including the information of the simulated PDF when resampling from the data PDF (both evaluated with a kernel-based technique [94]). In this case, the correlations of the PID variable present in simulation, with other PID variables for the same track, or other parameters of the track and the event in

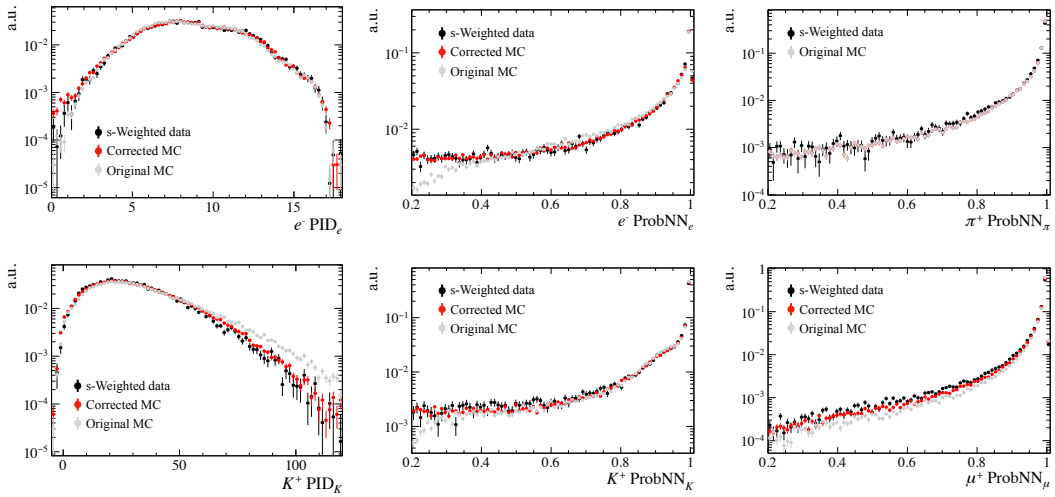

Figure 4.24: Examples of distributions of particle identification responses used in the analysis. The three distributions for each variable represent s-Weighted data (black), original simulation (grey) and corrected simulation (red). The datasets come from 2018 $B^+ \to K^+\pi^+\pi^- J/\psi\,(\to e^+e^-)$ samples, except for the muon PID response μ`ProbNN`$_\mu$, which is taken from 2018 $B^+ \to K^+\pi^+\pi^- J/\psi\,(\to \mu^+\mu^-)$ samples.

general, will be preserved. This second way of correcting the PID responses is implemented by the Meerkat tool, the details of which are given in [95].

Examples of simulated PID distributions, before and after being corrected, together with the distributions observed in s-Weighted data, are shown in Figure 4.24, where a generally good agreement is observed between data and corrected simulation.

4.4.3 $K^+\pi^+\pi^-$ resonance structure

As introduced in Section 4.1, the simulated samples do not correctly model the resonance structure of the $K^+\pi^+\pi^-$ hadronic system that is observed in data. In order to reproduce this structure, the simulated samples are reweighted by using a gradient boosted reweighter (`GBR`) from the `HEP-ml` software package [96]. The `GBR` compares the simulated and data distributions of one or more given variables. It then computes weights that can be assigned to each event of the simulated sample, to make the simulated distributions resemble the ones observed in data. The weights are thus very dependent on the choice of the variables used in the `GBR` training step. In order to make a good choice of these variables, it is important to note that the $B^+ \to K^+\pi^+\pi^-\ell^+\ell^-$ decay is completely described by eight degrees of freedom. These are the q^2, the three mass variables $m(K^+\pi^+\pi^-)$, $m(K^+\pi^-)$, $m(\pi^+\pi^-)$, and four decay angles, that are: θ_L, *i.e.* the direction of ℓ^+ in the $\ell^+\ell^-$ rest frame; θ_K, *i.e.* the direction of the kaon in the $K^+\pi^-$ rest frame; θ_V, *i.e.* the direction of the $K^+\pi^-$ system in the $K^+\pi^+\pi^-$ rest frame; and ϕ, *i.e.* the angle between the planes of the $K^+\pi^+\pi^-$ and $\ell^+\ell^-$ systems in the B rest frame. The

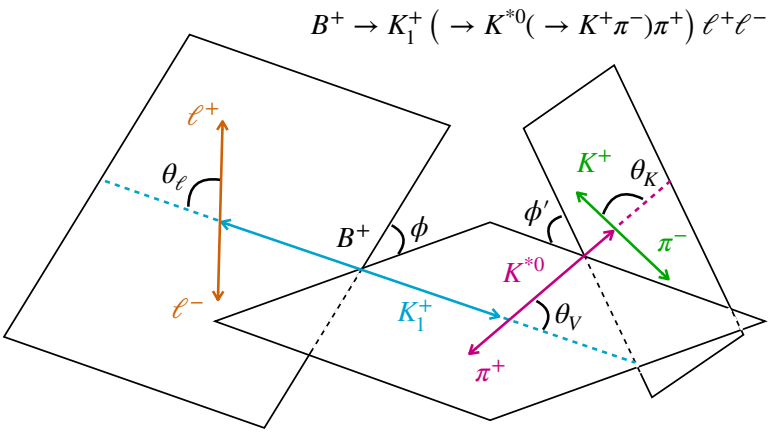

Figure 4.25: A sketch showing the angular variables needed to describe a $B^+ \to K^+\pi^+\pi^-\ell^+\ell^-$ decay.

described variables are visualised in Figure 4.25, where a sketch of a $B^+ \to K^+\pi^+\pi^-\ell^+\ell^-$ decay is shown. Among these, the three invariant masses $m(K^+\pi^-)$, $m(\pi^+\pi^-)$ and $m(K^+\pi^+\pi^-)$ are chosen as input variables for the GBR. The change in the outcome of the correction when adding also the distributions of the three angles θ_ℓ, θ_K and θ_V as input to the GBR is taken into account as a systematic effect, as discussed in Section 4.8.2.

The GBR compares $B^+ \to K^+\pi^+\pi^- J/\psi\,(\to \mu^+\mu^-)$ samples from simulation and data, where the background components have been subtracted from the data distributions using the *sPlot* technique described in Section 4.4.1. Furthermore, to account for acceptance effects due to the reconstruction process, efficiency maps of the Stripping (Section 4.3.1) and the preselection (Section 4.3.3) requirements are calculated in bins of the $K^+\pi^-$ and $\pi^+\pi^-$ invariant masses, using simulated samples. These maps are then used to unfold the data distributions given in input to the GBR.

Figure 4.26 shows an example of the $m(K^+\pi^-)$ $m(\pi^+\pi^-)$ and $m(K^+\pi^+\pi^-)$ distributions for $B^+ \to K^+\pi^+\pi^- J/\psi\,(\to \mu^+\mu^-)$ decays in s-Weighted and unfolded data and in simulation, before and after the correction for the hadronic system structure has been applied. A generally good agreement is observed between data and corrected simulation.

The same set of weights are then applied to each simulated event of all the other decays used in the analysis, *i.e.* to the rare modes and to the J/ψ and $\psi(2S)$ resonant modes, with electrons or muons in the final state. While the portability of the weights from the muon to the electron modes is ensured by the same $K^+\pi^+\pi^-$ structure in the two cases, which is independent of the type of the leptons in the final state, the validity of the weights throughout the q^2 range is not as straightforward. In fact, further studies have been performed, by re-training the GBR on $B \to K\pi\pi\gamma$ decays instead of $B^+ \to K^+\pi^+\pi^- J/\psi\,(\to \mu^+\mu^-)$ decays, thus in an even lower q^2 region than the signal one. As for the inclusion of the angles in the training procedure, any

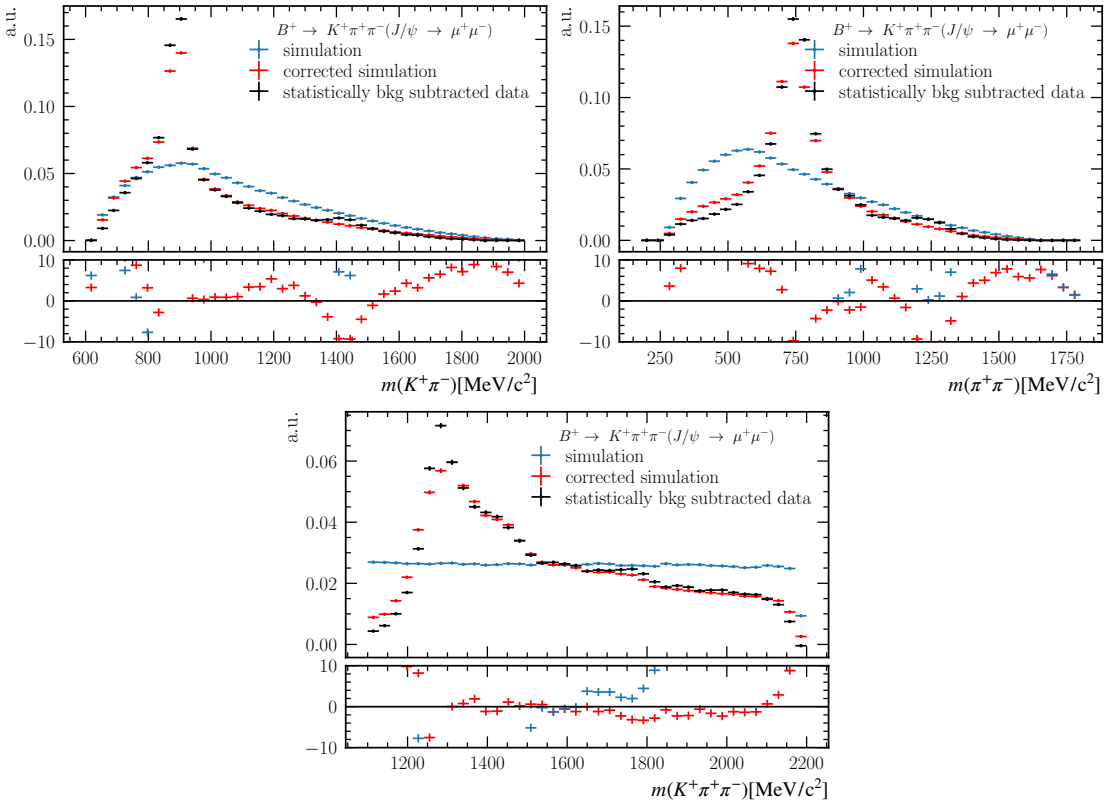

Figure 4.26: Comparison of the $m(K^+\pi^-)$, $m(\pi^+\pi^-)$ and $m(K^+\pi^+\pi^-)$ distributions between background-subtracted data (black), unweighted simulation (blue) and reweighted simulation (red) for $B^+ \to K^+\pi^+\pi^- J/\psi\,(\to \mu^+\mu^-)$ decays in the 2018 data sample.

differences in the reweighting outcome due to the different q^2 region used are included as systematic effects, as discussed in Section 4.8.2.

4.4.4 Electron tracking efficiency

Due to the small electron mass, the efficiency of reconstructing an electron as a `long track` (track definitions in Section 3.2.1) is known to depend on the amount of material crossed by the electron, which varies with its rapidity. Due to the imperfect description of the material distribution in simulation, it is necessary to reweight the simulated samples for the electron tracking efficiency distribution to match what is observed in data. To do so, the LHCb tracking group computed calibration maps with a tag&probe approach, described in [97], using $B^+ \to J/\psi(\to e^+e^-)K^+$ decays, where one of the electrons and the kaon (reconstructed as `long tracks`) define the *tag* candidate and the other electron (with opposite charge with respect to the *tag* electron) reconstructed as a `VELO track` defines the *probe*. The efficiencies are thus determined as the fraction of decays where the *probe* track is further reconstructed as a `long track` with the expected electric charge. The provided maps are 3-dimensional data-over-simulation efficiency ratios in $p_{\mathrm{T}}(e^{\pm})$, $\eta(e^{\pm})$ and the azimuthal angle $\phi(e^{\pm})$ of the probe electron. From these maps, the efficiencies ratios, *i.e.* $\varepsilon_{\mathrm{trk}}(\mathrm{data})/\varepsilon_{\mathrm{trk}}(\mathrm{simulation})$, are taken as a weight w_{trk} and applied separately to each electron, as a function of its p_{T}, η and ϕ. The final weight applied to the reconstructed candidate is then the product of the two electron weights,

$$w_{\mathrm{trk}} = w_{\mathrm{trk}}\left(e^+\right) \times w_{\mathrm{trk}}\left(e^-\right). \tag{4.15}$$

Examples of the LHCb track reconstruction efficiencies in data and in simulation, together with the tracking weights used in the calibration process, are shown in Figure 4.27.

4.4.5 B^+ kinematics and multiplicity

Observables related to detector occupancy and track multiplicity are poorly reproduced in the simulation due to several effects not completely accounted for when generating the pp underlying event, such as low-momentum particles, secondary interactions or mismodelling of the detector material. This causes significant deviations in the distributions of the observables related to the event multiplicity and the kinematics of the B^+ meson in simulation from the one measured in data. The correction process is carried out similarly to the one described for the correction of the $K^+\pi^+\pi^-$ hadronic system in Section 4.4.3. A gradient boosted reweighter (`GBR`) is used, where the training variables chosen are: $p_{\mathrm{T}}(B)$ and $\eta(B)$, as proxies to correct the B^+ kinematics; and the number of tracks in the event, as a proxy of the event multiplicity. As for the $K^+\pi^+\pi^-$ system correction, only $B^+ \to K^+\pi^+\pi^- J/\psi\,(\to \mu^+\mu^-)$ samples are used, since corrections related to effects due to the simulation of the pp underlying event are expected to be portable between the muon and electron decay modes.

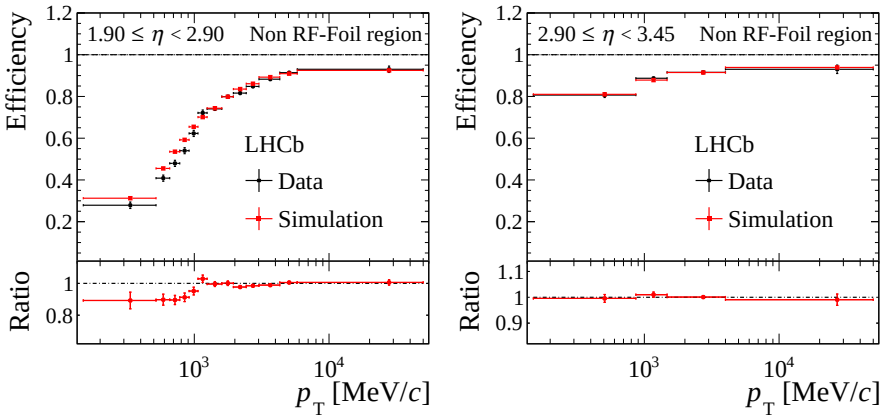

Figure 4.27: LHCb tracking efficiencies in data (black) and simulation (red) in two bins of pseudorapidity (η intervals are quoted in the top left corner of each figure). The "non RF-Foil" quote indicates that the corresponding ϕ interval does not include the foil dividing the VELO from the beam vacuum, which is treated separately. The efficiencies ratios, *i.e.* the w_{trk} applied to the final state electrons, are also shown at the bottom of each plot.

However, attention must be used when preparing the input samples for the reweighter. $B^+ \to K^+\pi^+\pi^- J/\psi\,(\to \mu^+\mu^-)$ samples are selected with the inclusive L0Muon trigger category, as the highest yield and cleanest sample available. Possible background is reduced by requiring the output of the MVA (described in Section 4.3.5) BDT > 0.5, nTracks < 400 and that candidates fall into a window of ±25 MeV around the reconstructed B^+ meson mass. The simulated samples are in addition corrected for effects due to PID mismodelling (resampled as explained in Section 4.4.2), phase-space reweighted (described in Section 4.4.3), and corrected for the poor modelling of the efficiencies of the L0 requirement used. For the latter, a "prior" trigger correction step is applied, using the same procedure described in the following Section 4.4.6, where the corrections are obtained by taking ratios of the L0 efficiencies in data and simulated samples.

Examples of comparison between reweighted simulation, to which PID (Section 4.4.2), phase-space (Section 4.4.3) and kinematics and multiplicity corrections are applied, and background-subtracted data distributions are shown in Figure 4.28, for the variables employed in the reweighter. As a cross-check, in the same figure there are also shown the outcomes of the same reweighter trained by using higher-yield channels as $B^+ \to K^+ J/\psi(\to \mu^+\mu^-)$ or $B^0 \to K^{*0} J/\psi(\to \mu^+\mu^-)$, instead of the nominal $B^+ \to K^+\pi^+\pi^- J/\psi\,(\to \mu^+\mu^-)$. A generally good agreement is observed between the data and the simulation distributions, corrected with any of these three different control channels.

The kinematic and multiplicity correction weights calculated with the inclusive L0Muon $B^+ \to K^+\pi^+\pi^- J/\psi\,(\to \mu^+\mu^-)$ samples are then propagated to all resonant (J/ψ and $\psi(2S)$) and rare decay simulated samples.

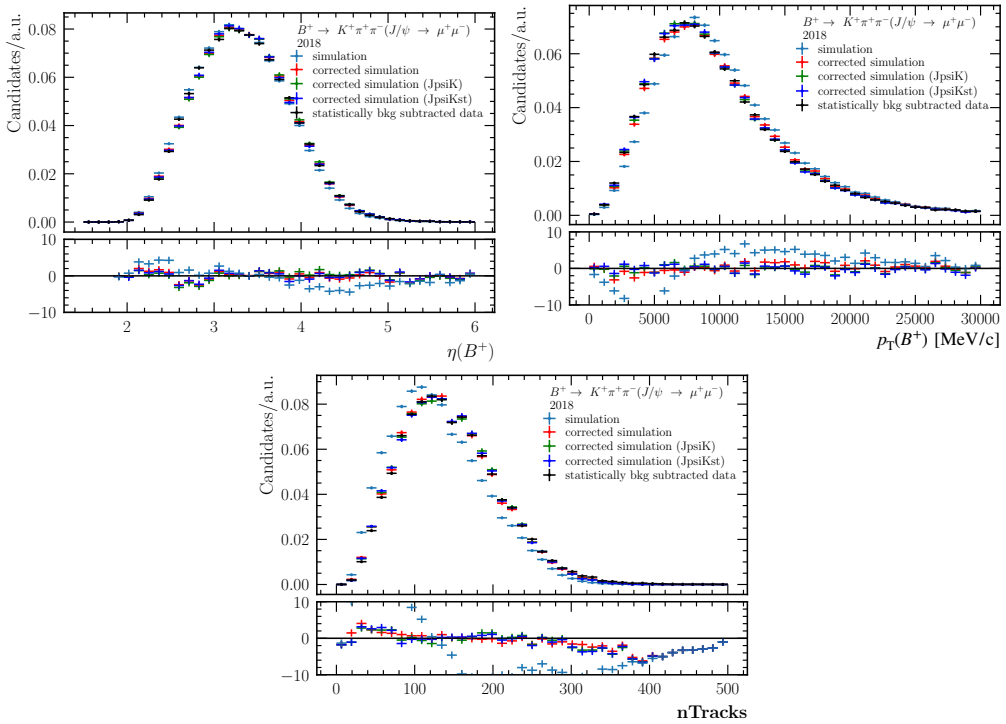

Figure 4.28: Effect of the kinematic and multiplicity corrections on $p_T(B)$, $\eta(B)$ and the number of tracks in the event nTracks. The original simulated distributions are shown in light blue. The corrected simulated distributions are shown in red, if using $B^+ \to K^+\pi^+\pi^- J/\psi\,(\to \mu^+\mu^-)$ decays in the training of the reweighter, in green, when using $B^+ \to K^+ J/\psi(\to \mu^+\mu^-)$, and in dark blue when using $B^0 \to K^{*0} J/\psi(\to \mu^+\mu^-)$. Background-subtracted data are shown in black. All the figures refer to 2018 samples.

4.4.6 Trigger efficiencies

Since the response of the trigger is not perfectly modelled in simulation, the calculation of the trigger efficiency can be affected by possible bias. This problem is overcome by applying appropriate corrections to the simulation, which are calculated in a similar way to what was explained for the correction of the electron tracking efficiency in Section 4.4.4. In practical terms, the efficiency of a trigger requirement X is calculated in data (ϵ_X^{data}) and simulation (ϵ_X^{MC}) via a tag&probe approach, and the ratio $w_X \equiv \epsilon_X^{\text{data}}/\epsilon_X^{\text{MC}}$ is applied as an event-by-event weight to the simulated samples.

For the corrections of the trigger efficiencies, $B^+ \to K^+\pi^+\pi^- J/\psi\,(\to \ell^+\ell^-)$ data and simulation samples are used, with $\ell = e, \mu$, to which the whole selection discussed in Section 4.3 is applied, except for the trigger requirements. In addition, it is required that the reconstructed B mass falls in a window of ± 50 MeV from the known B mass, to avoid possible background contributions in data. The simulated samples used are corrected with all the steps described in the previous sections, concerning the PID responses (Section 4.4.2), the phase-space modelling (Section 4.4.3), the electron tracking efficiency (Section 4.4.4) and the generation of the pp underlying event (Section 4.4.5). The weights computed with the J/ψ resonant samples are then also applied to the samples of $\psi(2S)$ resonant mode decays and of rare mode decays.

The correction procedure needs to be repeated for all the trigger categories considered in the measurements (described Section 4.3.2), as it will be described in the following subsections.

TIS calibration

The L0 efficiency of events falling in the `L0TIS` category, *i.e.* when the trigger is fired by particles independent from the signal decay, is evaluated as a function of the transverse momentum of the B^+ candidate. In addition, given the known dependence of the "TIS" efficiency on the multiplicity of the events, the binning is further split into three ranges depending on the number of tracks observed in the event.

The efficiency of the `L0TIS` requirement is computed by selecting a *tag* sample composed by events triggered by at least one of the leptons of the final state, *i.e.* where an electron fired the `L0Electron` trigger line or where a muon fired the `L0Muon` trigger line. In addition, the tag sample events have to satisfy also the software trigger requirements of the selection (Section 4.3.2). Then, the events of the *tag* sample are required to pass a *probe* selection, which is to have fired also the `L0TIS` trigger line. The `L0TIS` efficiency is then given by $\epsilon = N_{probe}/N_{tag}$ and the ratios between the data and simulation efficiencies are taken as weights to be applied to the simulated samples $w_{\text{TIS}} = \epsilon_{\text{TIS}}^{\text{data}}/\epsilon_{\text{TIS}}^{\text{MC}}$.

Examples of data and simulation efficiencies and the corresponding weights are shown in Figs. 4.29 and 4.30 for the electron and muon modes, respectively.

A good agreement is observed between the weights for the electrons and for the muon data

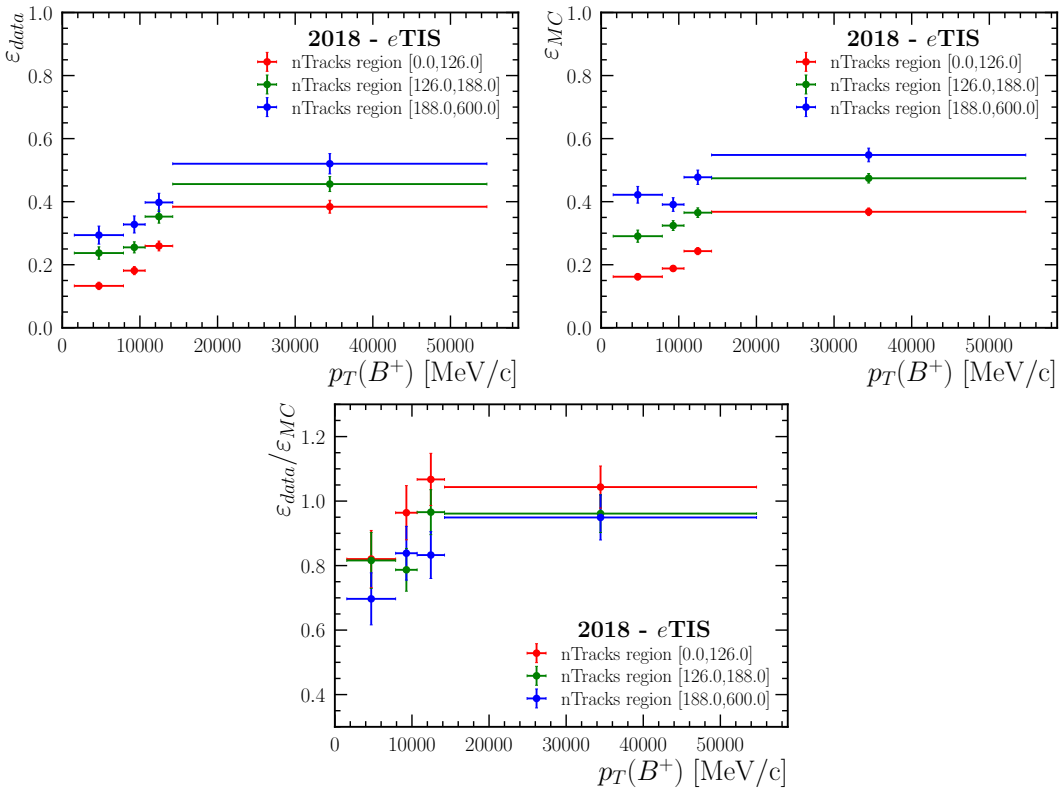

Figure 4.29: Efficiency of the `L0TIS` trigger category in data (upper left) and in simulated (upper right) $B^+ \to K^+\pi^+\pi^- J/\psi\,(\to e^+e^-)$ 2018 samples, calculated as a function of the transverse momentum of the reconstructed B^+ candidate and divided in three regions of `nTracks`, shown in blue, green and red. The bottom panel shows the corresponding weights w_{TIS}.

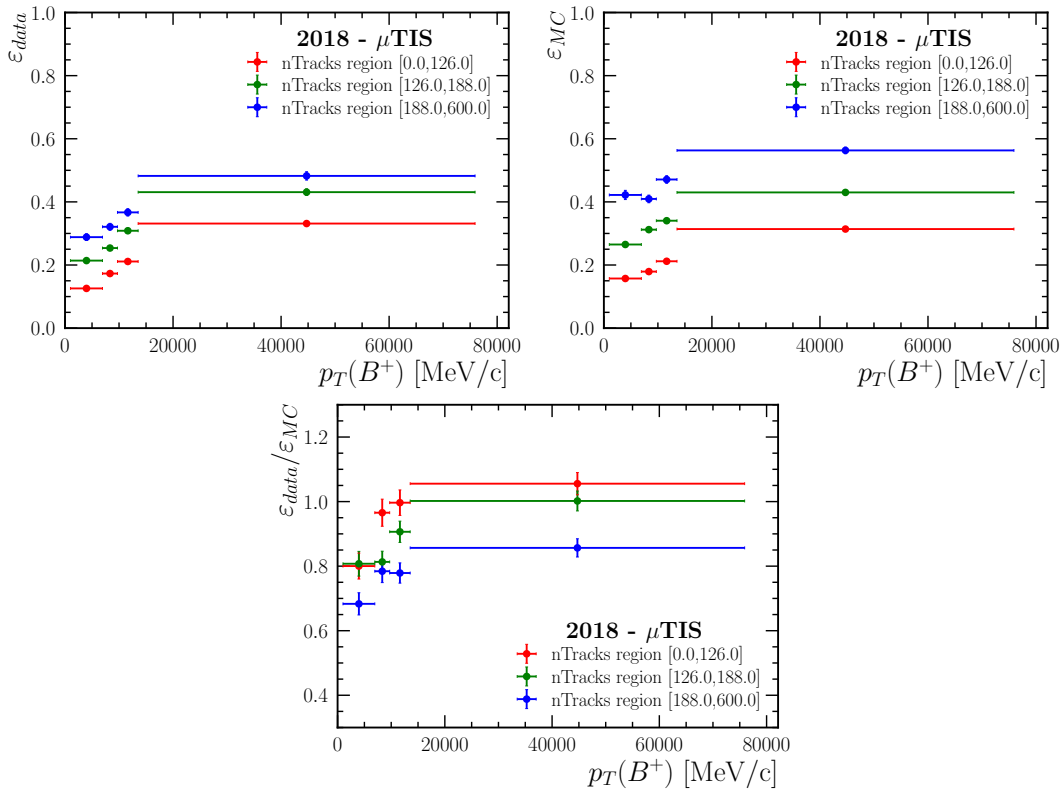

Figure 4.30: Efficiency of the `L0TIS` trigger category in data (upper left) and in simulated (upper right) $B^+ \to K^+\pi^+\pi^- J/\psi\,(\to \mu^+\mu^-)$ 2018 samples, calculated as a function of the transverse momentum of the reconstructed B^+ candidate and divided in three regions of `nTracks`, shown in blue, green and red. The bottom panel shows the corresponding weights w_{TIS}.

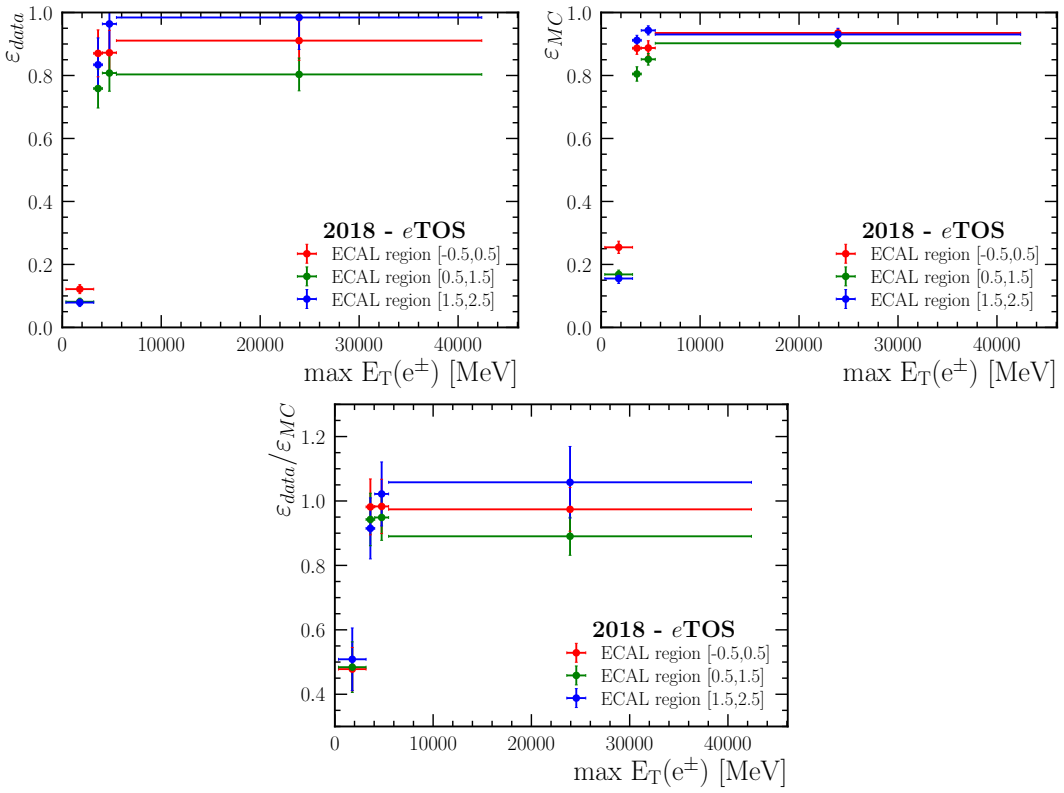

Figure 4.31: Efficiency of the L0ETOS "inclusive" trigger category in collision (upper left) and in simulated (upper right) $B^+ \to K^+\pi^+\pi^- J/\psi\,(\to e^+e^-)$ data in 2018, calculated as a function of the maximum ECAL energy deposit among the two electrons and of the ECAL region where such deposit is measured. The bottom side panel shows the corresponding weights w_{TOS}.

sets, which is in fact expected, given that the L0TIS requirement is independent from the type of the final state leptons.

Electron TOS calibration

Similarly to the L0TIS calibration, the efficiencies of the L0ETOS trigger category are evaluated by defining *tag* and *probe* samples. In this case, the *tag* events are the ones satisfying the L0TIS requirements, while the *probe* sample is a subset of the *tag* events, where the L0Electron trigger line is fired at least by the electron with the largest energy deposit in the calorimeter. The efficiencies in data and simulation are calculated as a function of the latter quantity, separately for three ECAL regions, according to the position in the calorimeter where this higher energy electron is recorded. Once again, the efficiencies are computed as the ratios of the number of events in the *probe* over the *tag* samples, and the weights w_{TOS} are given by the data over simulation efficiencies ratios. Figure 4.31 shows the data and simulation efficiencies, and the corresponding weights.

However, the L0ETOS trigger category used in the analysis is an "exclusive" category (Sec-

tion 4.3.2), meaning that the events falling in the category are also required to not have fired the L0TIS trigger, while the w_{TOS} weights just described do not take into account this additional requirement. For this reason the final weight of the "exclusive" L0ETOS trigger category $w_{\text{TOS,excl}}$ are computed as: $w_{\text{TOS,excl}} = w_{\text{TOS}} \cdot w_{\text{!TIS}}$, where

$$w_{\text{!TIS}} = \frac{1-\epsilon_{\text{TIS}}^{\text{data}}}{1-\epsilon_{\text{TIS}}^{\text{MC}}}, \tag{4.16}$$

with $\epsilon_{\text{TIS}}^{\text{data}}$ and $\epsilon_{\text{TIS}}^{\text{MC}}$ being the efficiencies of the TIS selection in data and in simulated electron samples, as described for the L0TIS calibration.

Muon TOS calibration

The L0MTOS calibration proceeds exactly as the L0ETOS calibration just described. To evaluate the efficiency of the L0MTOS category, a *tag* sample of events is defined, containing events that satisfy the L0TIS trigger condition, while the *probe* sample is defined as a subset of the *tag* events, where the L0Muon trigger line is fired at least by the muon with the largest transverse momentum $p_{\text{T}}(\mu^{\pm})$. The efficiency is calculated in data and simulation as a function of the latter quantity. Figure 4.32 shows the data and simulation efficiencies, and the corresponding weights.

As discussed in the previous section, also the L0MTOS is used in the analysis as an "exclusive" category, therefore the respective trigger weight must be computed as $w_{\text{TOS,excl}} = w_{\text{TOS}}(\mu) \cdot w_{\text{!TIS}}(\mu)$, where

$$w_{\text{!TIS}} = \frac{1-\epsilon_{\text{TIS}}^{\text{data}}}{1-\epsilon_{\text{TIS}}^{\text{MC}}}, \tag{4.17}$$

with $\epsilon_{\text{TIS}}^{\text{data}}$ and $\epsilon_{\text{TIS}}^{\text{MC}}$ being the efficiencies of the L0TIS requirements in data and simulated muon samples.

HLT calibration

The efficiency of the high level trigger is calibrated separately for events falling in exclusive L0ETOS and L0MTOS and inclusive L0TIS trigger categories (Section 4.3.2). To calculate the HLT efficiency in simulated samples, all the correction steps described previously are applied, including the L0 trigger weights. Again, a tag&probe strategy is used. The *probe* sample is defined by events that satisfy the nominal HLT lines, which by definition are fired only by particles belonging to the final state of interest. That is why it is possible to use the same HLT lines but fired from particles not included in the signal decays to define the *tag* sample. As usual, the HLT weights are given by $w_{\text{HLT}} = \epsilon_{\text{HLT}}^{\text{data}}/\epsilon_{\text{HLT}}^{\text{MC}}$. The computed w_{HLT} for the categories considered are found to be all compatible with unity, within their errors.

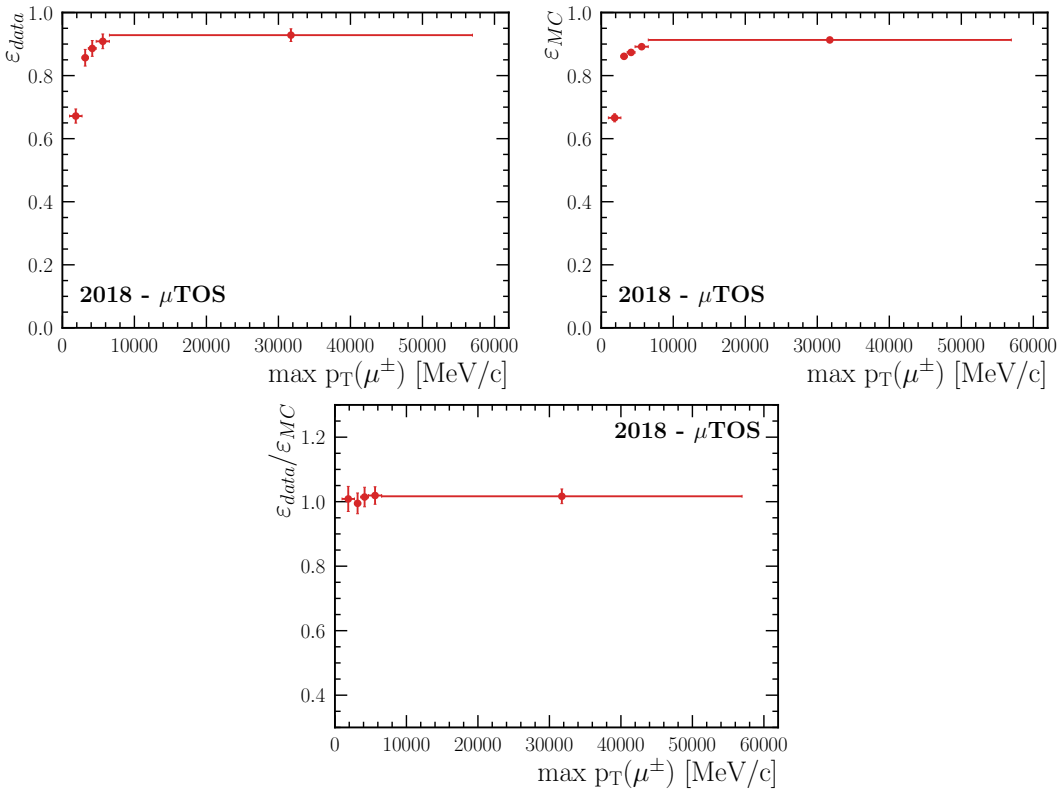

Figure 4.32: Efficiency of the `L0MTOS` "inclusive" trigger category in collision (upper left) and in simulated (upper right) $B^+ \to K^+\pi^+\pi^- J/\psi\,(\to \mu^+\mu^-)$ data in 2018, calculated as a function of the maximum p_T among the two muons. The bottom side panel shows the corresponding weights $w_{TOS}(\mu)$.

4.4.7 Residual reconstruction effects

The corrections calculated in Sections 4.4.2 to 4.4.6 leave some residual discrepancies to be corrected, due to the differences arising at the track and event reconstruction level. As described in Section 4.4.5, where discrepancies at the generator level have been corrected, a GBR is trained to evaluate data-simulation differences on typical variables related to the reconstruction process, *i.e.* the χ^2 of the fit to the B vertex ($\chi^2_{\text{vtx}}(B)/n_{\text{dof}}$) and of the impact parameter ($\chi^2_{\text{IP}}(B)$). Since reconstruction effects are expected to diverge between electron and muon decay modes, $B^+ \to K^+\pi^+\pi^- J/\psi\,(\to e^+e^-)$ and $B^+ \to K^+\pi^+\pi^- J/\psi\,(\to \mu^+\mu^-)$ are used as proxies, respectively. The full nominal selection is applied to the samples, as described in Section 4.3, which are further cleaned by selecting a window of ± 60 MeV around the B mass with J/ψ-constraint. This is done because the usual *sPlot* background subtraction technique, described in Section 4.4.1, cannot be used to subtract background contributions due to the correlation between the *sWeight*s and the variables used for the `GBR` training. The samples are further split in trigger categories, and weights are computed separately for each of those.

The effect of the reweighting is shown in Figure 4.33. Once again, the computed weights are also applied to the resonant $\psi(2S)$ and rare decay modes.

4.4.8 Smearing of the $J/\psi \to e^+e^-$ mass

The resolution of $m(ee)$ is generally better in simulated samples than it is in data. Possible causes are:

- an inaccurate description of the detector material, which in turn provokes a difference in bremsstrahlung emissions, leading to inaccurate momentum resolution;
- a mismodelling of the occupancy response of the ECAL, which leads to inaccurate energy estimation.

This difference in resolution affects the calculation of the efficiency of the q^2 requirements used to separate the rare decay from the resonant modes (described in Section 4.2.2). This effect is addressed by smearing the dilepton mass in simulated $B^+ \to K^+\pi^+\pi^- e^+e^-$ and $B^+ \to K^+\pi^+\pi^- J/\psi\,(\to e^+e^-)$ samples with this formula:

$$m_{\text{smeared}} \equiv m_{\text{gen}} + \Delta\mu + s_\sigma\,(m_{\text{reco}} - m_{\text{true}}) + (1 - s_\sigma)\left(\mu_{MC} - m_{J/\psi,\text{PDG}}\right), \tag{4.18}$$

where m_{gen} is the generated dilepton mass in simulation, m_{reco} is the dilepton mass in simulation after the reconstruction process, $m_{J/\psi,\text{PDG}}$ is the known J/ψ mass [10]; μ_{MC}, $\Delta\mu$ and s_σ are parameters obtained from fits to the J/ψ mass line shape in $B^+ \to K^+\pi^+\pi^- J/\psi\,(\to e^+e^-)$ simulated and data samples, as explained in the following. In order to perform the fits, the full selection (Section 4.3) is applied to the data sets, except for the q^2 selection and the BDT selection. In addition, to further clean the samples, a selection on the B^+ mass with J/ψ-constraint is applied, requiring it to lie in the $(5150\ \text{MeV}/c^2; 5680\ \text{MeV}/c^2)$ range. The samples are further divided in trigger categories, *i.e.* if the events are in the `L0ETOS` or in the

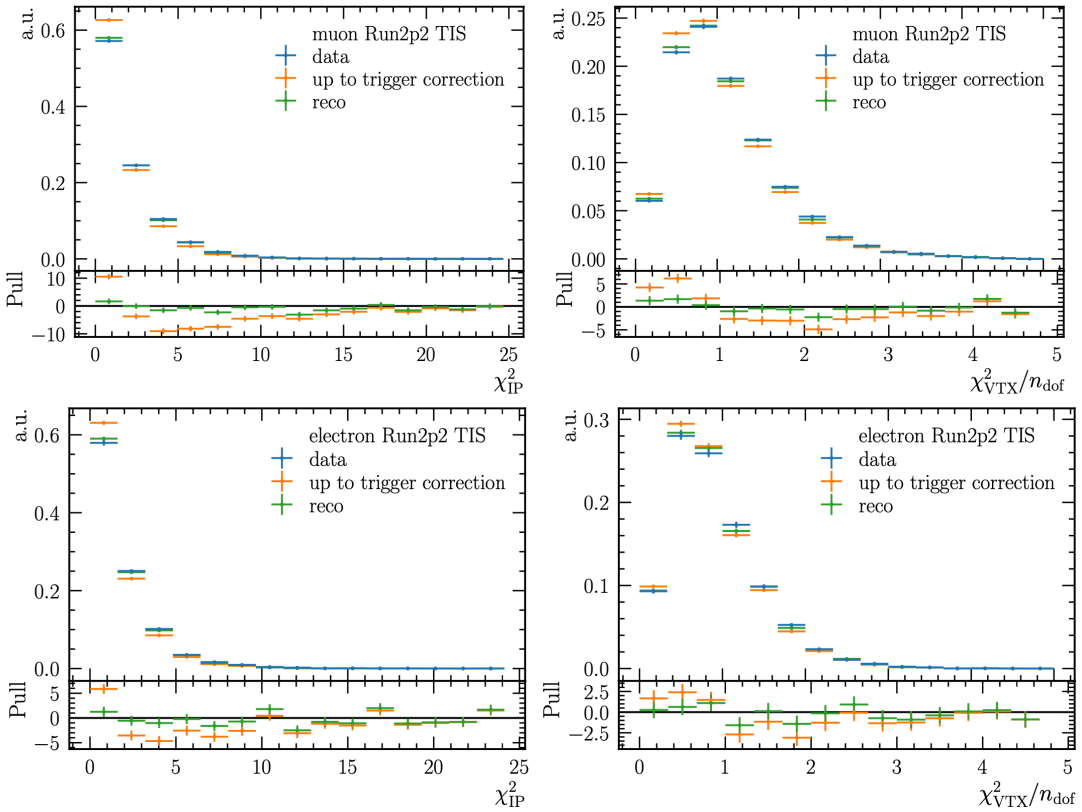

Figure 4.33: Effect of the reweighting of the residual reconstruction differences on Run2p2 muon (top) and electron (bottom) samples selected by the L0TIS requirement. The resonant simulations are shown when corrected up to the trigger step (orange), and with the addition of the residual reconstruction weights (green). Data distributions are also shown (blue).

LOTIS category, and in bremsstrahlung categories, *i.e.* if bremsstrahlung photons are added to none, one or both of the electrons. The fitted parameters are then averaged between the trigger categories, weighted for the observed yields. The signal component is modelled using the Crystal Ball shape as defined in the RooCBShape class within the ROOT framework [92], following the description in [98]:

$$\mathrm{CB}(m,\mu,\sigma,\alpha,n) = \begin{cases} \exp\left(-\dfrac{(x-\mu)^2}{2\sigma^2}\right), & \text{for} \quad \dfrac{\mathrm{x}-\mu}{\sigma} > -\alpha \\ A\cdot\left(B-\dfrac{x-\mu}{\sigma}\right)^{-n}, & \text{for} \quad \dfrac{\mathrm{x}-\mu}{\sigma} \leq -\alpha, \end{cases} \tag{4.19}$$

with

$$A = \left(\frac{n}{|\alpha|}\right)^n \cdot \exp\left(-\frac{|\alpha|^2}{2}\right), \quad \mathrm{B} = \frac{\mathrm{n}}{|\alpha|} - |\alpha|\,, \tag{4.20}$$

where μ and σ are the mean and the resolution of the distribution, α a parameter that controls the asymmetry between the right and the left tails, and n the order of the function. To describe the signal component, a linear combination of two CB functions is used, *i.e.* a double Crystal Ball shape (DCB), to better model the differences between the right and the left side of the invariant mass distributions, with a common mean and resolution for both shapes.

The DCB is at first used to fit the dilepton mass $m(ee)$ in simulated samples, where all the previous reweighting steps have been applied. In these fits all parameters are allowed to vary, so that the mean μ_{MC} and the resolution σ_{MC} of the DCB are extracted. The fit in data is performed with the same line shape combined with an exponential, to model the background coming from a random combination of tracks. All the signal parameters are fixed from the fit to simulation, except a scale factor for the resolution $s_\sigma = \sigma_{\mathrm{data}}/\sigma_{\mathrm{MC}}$ and a mean shift $\Delta\mu = \mu_{\mathrm{data}} - \mu_{\mathrm{MC}}$, to take into account the possible differences between the data and simulated samples (note that μ_{MC}, s_σ and $\Delta\mu$ are the ones used in Eq. 4.18). An example of fits to simulated and data samples can be found in Figure 4.34 and Figure 4.35 respectively. The parameter values obtained from the fits are shown in Table 4.9.

The smearing procedure can be then validated in the following way: the fits to the simulated samples are repeated, but this time on the dielectron mass smeared as in Eq. 4.18. This means having new initial parameters for the signal shape in the fit to data. Once the fits in data are also repeated, it is expected the new fitted values for $\Delta\mu$ and s_σ are 0 and 1, respectively, given that the aim of the smearing procedure is to align dielectron mass distributions in simulation and data. The values found for these parameters after the smearing correction are shown in Table 4.10, demonstrating that the smearing procedure is indeed performed correctly.

Once the procedure is completed, the efficiency of the q^2 selections is evaluated with the $(m_{\mathrm{smeared}})^2$ variable from Eq. 4.18.

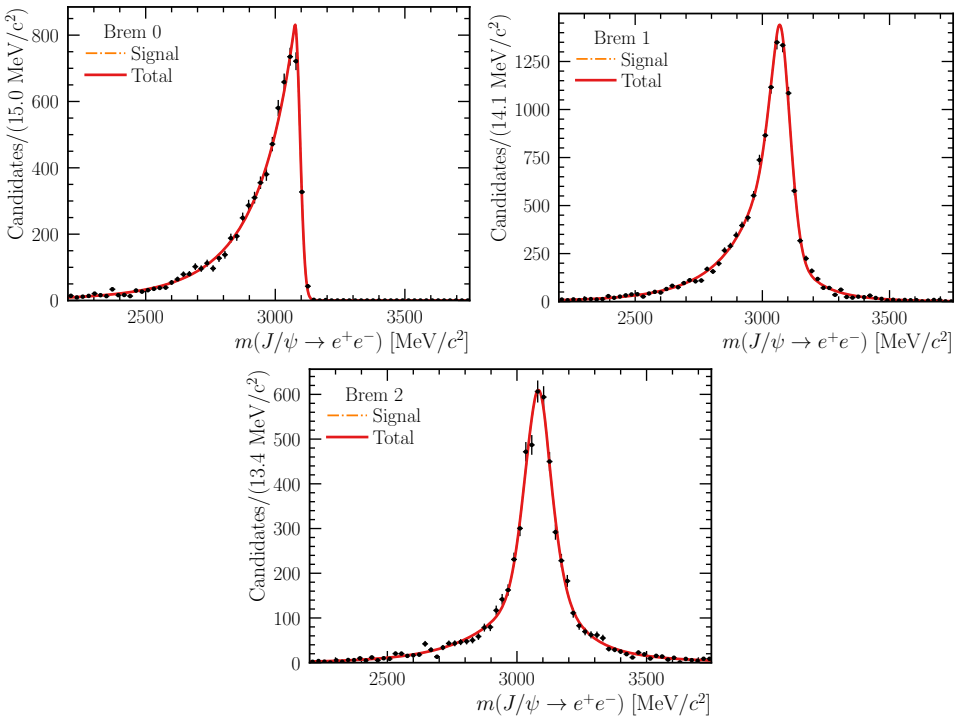

Figure 4.34: Fits to the J/ψ mass line shape in 2018 $B^+ \to K^+\pi^+\pi^- J/\psi\,(\to e^+e^-)$ simulated sample, selected in the L0ETOS category and divided in bremsstrahlung categories, *i.e.* if a bremsstrahlung photon is added to none (Brem 0), one (Brem 1) or both electrons (Brem 2). The fits are performed to evaluate the mean parameter μ_{MC}, used to smear the J/ψ mass in simulated samples, and to extract the signal shapes used in the fits to the data samples.

Table 4.9: Values of the resolution scale s_σ and mean shift $\Delta\mu$ parameters obtained from fits of the dilepton mass $m(ee)$ (before the smearing correction being applied) in simulated and data samples. The values of the parameters are shown for different years and bremsstrahlung categories, where a weighted average between the L0ETOS and L0TIS trigger categories has been performed.

	Brem 0		Brem 1		Brem 2	
Year	s_σ	$\Delta\mu$	s_σ	$\Delta\mu$	s_σ	$\Delta\mu$
2011	1.09 ± 0.05	-2.2 ± 1.5	1.07 ± 0.04	-1.9 ± 1.6	1.21 ± 0.07	-0.7 ± 2.5
2012	0.97 ± 0.03	3.0 ± 0.9	1.12 ± 0.03	0.5 ± 1.0	1.05 ± 0.04	7.8 ± 1.7
2015	1.20 ± 0.06	-9.3 ± 1.7	1.38 ± 0.07	-18.4 ± 2.4	1.17 ± 0.05	-8.7 ± 2.0
2016	1.20 ± 0.02	-7.8 ± 0.7	1.23 ± 0.02	-14.1 ± 0.8	1.07 ± 0.03	-17.3 ± 1.2
2017	1.16 ± 0.02	-6.3 ± 0.7	1.19 ± 0.02	-11.3 ± 0.8	1.04 ± 0.03	-9.0 ± 1.3
2018	1.20 ± 0.02	-6.7 ± 0.6	1.13 ± 0.02	-11.2 ± 0.7	1.11 ± 0.03	-8.1 ± 1.1

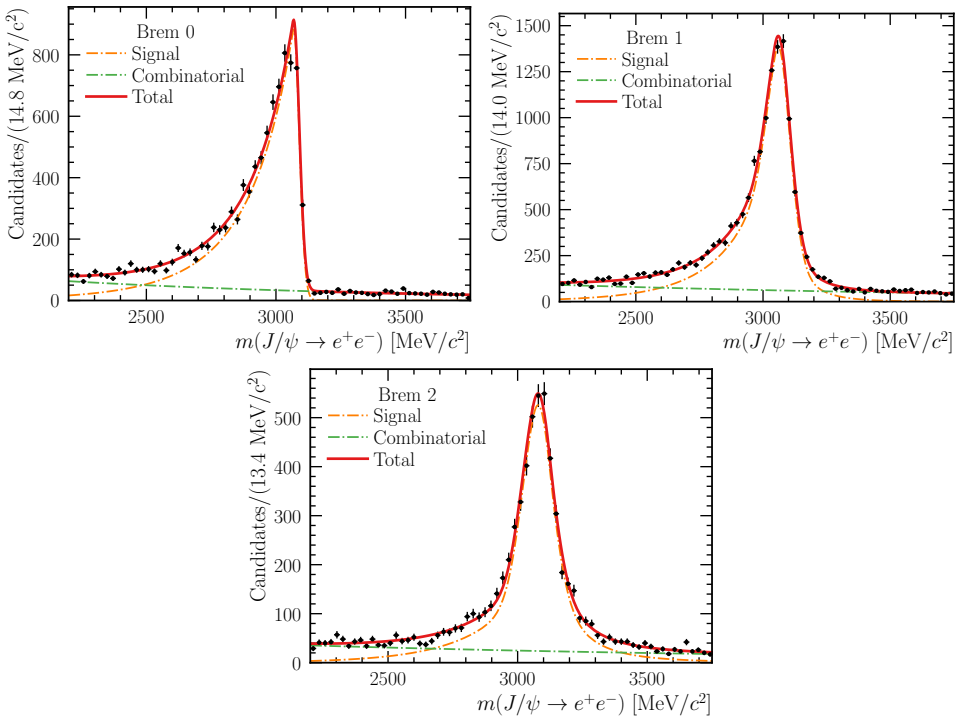

Figure 4.35: Fits to the J/ψ mass line shape in 2018 $B^+ \to K^+\pi^+\pi^- J/\psi\,(\to e^+e^-)$ data sample, selected in the `L0ETOS` category and divided in bremsstrahlung categories, *i.e.* if a bremsstrahlung photon is added to none (Brem 0), one (Brem 1) or both of the electrons (Brem 2). The fits are performed to evaluate the mean shift $\Delta\mu$ and resolution scale s_σ parameters used to smear the J/ψ mass in simulated samples.

Table 4.10: Values of the resolution scale s_σ and mean shift $\Delta\mu$ parameters obtained from fits of the smeared dilepton mass $m(ee)$ in simulated and data samples. The values of the parameters are shown for different years and bremsstrahlung categories, where a weighted average between the `L0ETOS` and `L0TIS` trigger categories has been performed.

	Brem 0		Brem 1		Brem 2	
Year	s_σ	$\Delta\mu$	s_σ	$\Delta\mu$	s_σ	$\Delta\mu$
2011	1.00 ± 0.04	-0.1 ± 1.5	1.00 ± 0.04	0.5 ± 1.6	1.04 ± 0.07	-0.1 ± 2.5
2012	0.99 ± 0.03	0.2 ± 0.9	1.00 ± 0.02	-0.1 ± 1.0	0.99 ± 0.04	0.5 ± 1.7
2015	0.99 ± 0.05	0.3 ± 1.7	1.02 ± 0.05	-3.3 ± 2.3	0.93 ± 0.07	-0.4 ± 3.4
2016	1.02 ± 0.02	-0.2 ± 0.6	1.03 ± 0.02	-5.0 ± 0.8	0.97 ± 0.03	-0.8 ± 1.3
2017	0.99 ± 0.02	0.4 ± 0.7	1.01 ± 0.02	-1.1 ± 0.8	1.00 ± 0.03	0.0 ± 1.2
2018	1.12 ± 0.03	0.1 ± 0.4	1.01 ± 0.02	-1.3 ± 0.7	1.01 ± 0.03	0.2 ± 1.2

4.5 Calculation of the event selection efficiency

In order to evaluate the observable $R_{K\pi\pi}$, as explained in Section 4.2, it is important to determine the ratio between the experimental acceptance for the rare modes and that of the resonant modes. The total acceptance can be decomposed in three factors:

$$\varepsilon = \epsilon^{\text{geom}} \cdot \epsilon^{\text{reco\&strip}} \cdot \epsilon^{\text{sel}}, \tag{4.21}$$

where:

- ϵ^{geom} is the geometrical acceptance of the LHCb detector;
- $\epsilon^{\text{reco\&strip}}$ is the efficiency of the tracking and event reconstruction chain, up to the selection applied in the stripping (Section 4.3.1);
- ϵ^{sel} is the efficiency of the selection chain, which includes the q^2 range (Section 4.2.2), the `L0` and `HLT` trigger selections (Section 4.3.2), the preselection requirements (Section 4.3.3), the multivariate selection (Section 4.3.5) and finally the selection of the reconstructed B^+ mass range where the fit to the B^+ mass line shape is performed in order to extract the resonant and the rare yields.

The computation of the above efficiencies relies on simulated samples, which have passed through the whole reweighting process described in Section 4.4.

In the following, these three efficiency contributions are described, showing the computed efficiencies only for the resonant $B^+ \to K^+\pi^+\pi^- J/\psi\,(\to \ell^+\ell^-)$ and $B^+ \to K^+\pi^+\pi^-\psi(2S)(\to \ell^+\ell^-)$ modes since, as stated in Section 4.2, the efficiencies of the rare modes are kept blinded to avoid injecting bias in the measurement and are only looked at after the full analysis is validated by the LHCb collaboration.

4.5.1 Geometrical acceptance

As simulated events are generated already in the LHCb acceptance to save resources, an estimation of the geometric efficiency cannot be obtained directly from the simulated samples used in the analysis. Therefore, efficiency tables, specific for each year and polarity of the LHCb magnet (Section 3.2.1), are produced during the simulation process. These efficiencies represent the probability to have each of the final state particles of the decay of interest with a polar angle θ between 10 and 400 mrad with respect to the axis of the detector. The geometrical acceptance, shown in Table 4.11, is reported for both the signal modes and the resonant channels used in the analysis.

Table 4.11: Geometrical acceptance of the LHCb detector for the resonant and the rare channels. The efficiencies are shown for each year of data taking and polarity of the LHCb magnet, where the values +1 or −1 stand for the `MagUp` and `MagDown` configurations (Section 3.2.1).

Year	Mag	$B \to K\pi\pi J/\psi(\to ee)$	$B \to K\pi\pi J/\psi(\to \mu\mu)$
2011	+1	$(14.705 \pm 0.033)\%$	$(14.764 \pm 0.035)\%$
2011	−1	$(14.658 \pm 0.033)\%$	$(14.760 \pm 0.040)\%$
2012	+1	$(14.914 \pm 0.035)\%$	$(15.060 \pm 0.040)\%$
2012	−1	$(15.010 \pm 0.040)\%$	$(15.040 \pm 0.040)\%$
2015	+1	$(15.975 \pm 0.035)\%$	$(16.076 \pm 0.035)\%$
2015	−1	$(16.004 \pm 0.035)\%$	$(16.009 \pm 0.036)\%$
2016	+1	$(15.954 \pm 0.035)\%$	$(16.049 \pm 0.035)\%$
2016	−1	$(15.963 \pm 0.036)\%$	$(15.087 \pm 0.035)\%$
2017	+1	$(15.870 \pm 0.050)\%$	$(16.090 \pm 0.050)\%$
2017	−1	$(15.870 \pm 0.050)\%$	$(16.020 \pm 0.050)\%$
2018	+1	$(15.960 \pm 0.050)\%$	$(16.040 \pm 0.050)\%$
2018	−1	$(16.050 \pm 0.050)\%$	$(16.120 \pm 0.060)\%$
Year	Mag	$B \to K\pi\pi\psi(2S)(\to ee)$	$B \to K\pi\pi\psi(2S)(\to \mu\mu)$
2011	+1	$(15.181 \pm 0.039)\%$	$(15.240 \pm 0.040)\%$
2011	−1	$(15.165 \pm 0.027)\%$	$(15.240 \pm 0.040)\%$
2012	+1	$(15.502 \pm 0.025)\%$	$(15.560 \pm 0.050)\%$
2012	−1	$(15.491 \pm 0.025)\%$	$(15.500 \pm 0.050)\%$
2015	+1	$(16.272 \pm 0.052)\%$	$(16.076 \pm 0.035)\%$
2015	−1	$(16.294 \pm 0.048)\%$	$(16.009 \pm 0.036)\%$
2016	+1	$(16.375 \pm 0.034)\%$	$(16.498 \pm 0.050)\%$
2016	−1	$(16.350 \pm 0.040)\%$	$(16.367 \pm 0.055)\%$
2017	+1	$(16.380 \pm 0.040)\%$	$(16.420 \pm 0.040)\%$
2017	−1	$(16.350 \pm 0.040)\%$	$(16.470 \pm 0.040)\%$
2018	+1	$(16.410 \pm 0.040)\%$	$(16.380 \pm 0.040)\%$
2018	−1	$(16.410 \pm 0.040)\%$	$(16.460 \pm 0.040)\%$
Year	Mag	$B \to K\pi\pi ee$	$B \to K\pi\pi\mu\mu$
2011	+1	$(14.796 \pm 0.023)\%$	$(14.588 \pm 0.035)\%$
2011	−1	$(14.781 \pm 0.023)\%$	$(14.642 \pm 0.035)\%$
2012	+1	$(15.092 \pm 0.025)\%$	$(14.880 \pm 0.040)\%$
2012	−1	$(15.042 \pm 0.024)\%$	$(14.980 \pm 0.040)\%$
2015	+1	$(15.775 \pm 0.039)\%$	$(15.922 \pm 0.037)\%$
2015	−1	$(15.755 \pm 0.038)\%$	$(15.908 \pm 0.035)\%$
2016	+1	$(15.843 \pm 0.037)\%$	$(15.906 \pm 0.035)\%$
2016	−1	$(15.693 \pm 0.037)\%$	$(15.956 \pm 0.035)\%$
2017	+1	$(15.735 \pm 0.034)\%$	$(15.910 \pm 0.050)\%$
2017	−1	$(15.731 \pm 0.033)\%$	$(15.920 \pm 0.050)\%$
2018	+1	$(15.790 \pm 0.050)\%$	$(15.940 \pm 0.050)\%$
2018	−1	$(15.790 \pm 0.050)\%$	$(15.860 \pm 0.050)\%$

4.5.2 Reconstruction and stripping efficiency

The efficiencies of the reconstruction process and of the stripping selection (Section 4.3.1) are calculated together using the simulated samples. The stripping and reconstruction efficiency is computed as the ratio between the sum of the weights of all the generated events and the sum of the weights of the events that are reconstructed and pass the stripping requirements. For the simulated samples, only the first reweighting step is used at this level, *i.e.* the three-dimensional reweighting of the $K\pi$, $\pi\pi$ and $K\pi\pi$ invariant mass (Section 4.4.3), both for the numerator and denominator. For the electron samples, the tracking efficiency weights (discussed in Section 4.4.4) are considered too, when computing the sum over the reconstructed events (numerator),

$$\epsilon^{\text{reco\&strip}} = \frac{\sum_{\text{reco\&strip}}(w_{\text{phsp}} \cdot w^{\text{ele}}_{\text{trk}})}{\sum_{\text{gen}}(w_{\text{phsp}})}. \tag{4.22}$$

The B^+ kinematics and multiplicity weights (discussed in Section 4.4.5), as well as the following correction steps described in Section 4.4, are not included in the calculation, given that, in order to save disk space, the majority of the simulated samples used in the analysis is produced by saving the multiplicity information only for the events passing the reconstruction process, and not for all the generated ones. An exception to this are the 2011 and 2012 J/ψ modes samples, where this information is accessible even for the generated events before being reconstructed. These samples are thus used to estimate the effects of including the B^+ kinematics and multiplicity corrections in the stripping and reconstruction efficiencies computation. The efficiency differences were found to be smaller than 0.01% for the 2011 sample and smaller than 0.05% for the 2012 samples, for both the electron and the muon modes.

The stripping and reconstruction efficiencies for the resonant J/ψ and $\psi(2S)$ channels are shown in Table 4.12, while the ones of the rare decay modes are kept blinded according to the analysis strategy.

4.5.3 Selection efficiency

Simulated samples passed through the reconstruction process and the stripping selections (Section 4.3.1) are used for the calculation of the selection efficiency. In addition, to each sample the full set of weights coming from the reweighting procedures described in Section 4.4 is associated:

- w_{phsp}, from the reweighting of the phase-space modelling (Section 4.4.3),
- $w^{\text{ele}}_{\text{track}}$, from the correction of the `long-track` reconstruction efficiencies, only when considering electron samples (Section 4.4.4),
- w_{kinmult}, from the reweighting of the B^+ kinematics and occupancy distributions (Section 4.4.5),
- $w_{\text{L0*HLT}}$, from the correction of the trigger responses (Section 4.4.6),
- w_{reco}, from the reweighting of the residual reconstruction effects (Section 4.4.7).

Table 4.12: Stripping and reconstruction efficiencies for resonant channels. Efficiencies are shown both when applying the correction to the $K^+\pi^+\pi^-$ hadronic system and to the electron tracking efficiency (weighted) or not (unweighted).

	$B\to K\pi\pi J/\psi(\to ee)$		$B\to K\pi\pi J/\psi(\to \mu\mu)$	
Year	**Unweighted**	**Weighted**	**Unweighted**	**Weighted**
2011	$(4.97\pm0.02)\%$	$(4.37\pm0.03)\%$	$(8.70\pm0.03)\%$	$(8.28\pm0.05)\%$
2012	$(4.70\pm0.01)\%$	$(4.07\pm0.02)\%$	$(8.09\pm0.02)\%$	$(7.61\pm0.03)\%$
2015	$(4.73\pm0.02)\%$	$(4.32\pm0.03)\%$	$(8.45\pm0.02)\%$	$(8.08\pm0.04)\%$
2016	$(4.93\pm0.01)\%$	$(4.45\pm0.02)\%$	$(8.43\pm0.01)\%$	$(8.12\pm0.02)\%$
2017	$(5.31\pm0.01)\%$	$(4.84\pm0.02)\%$	$(8.91\pm0.01)\%$	$(8.60\pm0.03)\%$
2018	$(5.33\pm0.01)\%$	$(4.79\pm0.02)\%$	$(8.87\pm0.01)\%$	$(8.52\pm0.03)\%$
	$B\to K\pi\pi\psi(2S)(\to ee)$		$B\to K\pi\pi\psi(2S)(\to \mu\mu)$	
Year	**Unweighted**	**Weighted**	**Unweighted**	**Weighted**
2011	$(3.90\pm0.01)\%$	$(3.58\pm0.02)\%$	$(6.25\pm0.02)\%$	$(6.25\pm0.04)\%$
2012	$(3.73\pm0.01)\%$	$(3.39\pm0.02)\%$	$(5.85\pm0.02)\%$	$(5.87\pm0.03)\%$
2015	$(3.83\pm0.02)\%$	$(3.67\pm0.04)\%$	$(6.01\pm0.04)\%$	$(6.04\pm0.07)\%$
2016	$(4.09\pm0.01)\%$	$(3.88\pm0.02)\%$	$(6.21\pm0.02)\%$	$(6.32\pm0.04)\%$
2017	$(4.15\pm0.01)\%$	$(3.99\pm0.02)\%$	$(6.31\pm0.02)\%$	$(6.42\pm0.04)\%$
2018	$(4.15\pm0.01)\%$	$(3.94\pm0.02)\%$	$(6.34\pm0.02)\%$	$(6.60\pm0.04)\%$

The correction to the $m(ee)$ resolution (Section 4.4.8) is taken into account by using $m_{\text{smeared}}(ee)$, computed as in Eq. 4.18, when evaluating the efficiency of the q^2 region selection (Section 4.2.2) on the electron modes.

The selection efficiency is computed as the ratio between the sum of weights of the events which pass the full selection (numerator), *i.e.* the q^2 range (Section 4.2.2), the `L0` and `HLT` trigger (Section 4.3.2), the preselection (Section 4.3.3), the multivariate classifier (Section 4.3.5) and the B^+ mass range requirements, and the ones which pass only the reconstruction process and the stripping selection (denominator):

$$\epsilon^{\text{sel}} = \frac{\sum_{\text{selected}} w_{\text{phsp}} \cdot w^{\text{ele}}_{\text{track}} \cdot w_{\text{kinmul}} \cdot w_{\text{L0*HLT}} \cdot w_{\text{reco}}}{\sum_{\text{reco\&strip}} w_{\text{phsp}} \cdot w^{\text{ele}}_{\text{track}} \cdot w_{\text{kinmul}} \cdot w_{\text{reco}}} \tag{4.23}$$

The reason why the weights coming from the correction of the trigger response $w_{\text{L0*HLT}}$ are used only in the numerator is that they correct for the effect of performing a trigger decision, which did not happen for the events in the denominator.

The selection efficiencies for $B^+\to K^+\pi^+\pi^- J/\psi(\to\ell^+\ell^-)$ and $B^+\to K^+\pi^+\pi^-\psi(2S)(\to\ell^+\ell^-)$ decays are shown in Tables 4.13 and 4.14 for the TOS and TIS categories respectively. Again, the selection efficiencies of the signal $B^+\to K^+\pi^+\pi^-\ell^+\ell^-$ decays are kept blinded.

Table 4.13: Efficiencies of the selection (excluded stripping and reconstruction efficiencies and geometrical acceptance) for the resonant channels. The events selected fall in the L0ETOS trigger category, for the electron modes, or in the L0MTOS, for the muon modes. Efficiency values are shown both when applying the full set of corrections described in Section 4.4 to the simulated samples (weighted) or not (unweighted).

	$B \to K\pi\pi J/\psi(\to ee)$		$B \to K\pi\pi J/\psi(\to \mu\mu)$	
Year	**Unweighted**	**Weighted**	**Unweighted**	**Weighted**
2011	0.0361 ± 0.0006	0.0319 ± 0.0009	0.1167 ± 0.0012	0.0981 ± 0.0015
2012	0.0308 ± 0.0004	0.0257 ± 0.0005	0.1167 ± 0.0009	0.0997 ± 0.0011
2015	0.0553 ± 0.0010	0.0371 ± 0.0010	0.1166 ± 0.0010	0.0839 ± 0.0011
2016	0.0555 ± 0.0004	0.0458 ± 0.0005	0.1524 ± 0.0006	0.1260 ± 0.0008
2017	0.0475 ± 0.0004	0.0392 ± 0.0005	0.1461 ± 0.0006	0.1360 ± 0.0008
2018	0.0452 ± 0.0003	0.0363 ± 0.0004	0.1402 ± 0.0006	0.1141 ± 0.0007
	$B \to K\pi\pi\psi(2S)(\to ee)$		$B \to K\pi\pi\psi(2S)(\to \mu\mu)$	
Year	**Unweighted**	**Weighted**	**Unweighted**	**Weighted**
2011	0.0392 ± 0.0007	0.0309 ± 0.0009	0.1241 ± 0.0014	0.1048 ± 0.0018
2012	0.0353 ± 0.0005	0.0272 ± 0.0006	0.1267 ± 0.0011	0.1117 ± 0.0014
2015	0.0602 ± 0.0014	0.0417 ± 0.0017	0.1548 ± 0.0026	0.1153 ± 0.0029
2016	0.0562 ± 0.0006	0.0435 ± 0.0008	0.1647 ± 0.0012	0.1353 ± 0.0015
2017	0.0531 ± 0.0005	0.0423 ± 0.0007	0.1621 ± 0.0013	0.1547 ± 0.0017
2018	0.0521 ± 0.0005	0.0400 ± 0.0007	0.1514 ± 0.0012	0.1299 ± 0.0015

Table 4.14: Efficiencies of the selection (excluded stripping and reconstruction efficiencies and geometrical acceptance) for the resonant channels. The events selected fall in the L0TIS trigger category. The efficiency values are shown both when applying the full set of corrections described in Section 4.4 to the simulated samples (weighted) or not (unweighted).

	$B \to K\pi\pi J/\psi(\to ee)$		$B \to K\pi\pi J/\psi(\to \mu\mu)$	
Year	**Unweighted**	**Weighted**	**Unweighted**	**Weighted**
2011	0.0274 ± 0.0005	0.0210 ± 0.0007	0.0545 ± 0.0008	0.0402 ± 0.0009
2012	0.0246 ± 0.0004	0.0229 ± 0.0005	0.0511 ± 0.0006	0.0387 ± 0.0007
2015	0.0382 ± 0.0008	0.0278 ± 0.0009	0.0670 ± 0.0007	0.0527 ± 0.0009
2016	0.0435 ± 0.0004	0.0373 ± 0.0005	0.0797 ± 0.0004	0.0613 ± 0.0005
2017	0.0491 ± 0.0004	0.0359 ± 0.0004	0.0939 ± 0.0005	0.0669 ± 0.0005
2018	0.0388 ± 0.0003	0.0321 ± 0.0004	0.0650 ± 0.0004	0.0486 ± 0.0004
	$B \to K\pi\pi\psi(2S)(\to ee)$		$B \to K\pi\pi\psi(2S)(\to \mu\mu)$	
Year	**Unweighted**	**Weighted**	**Unweighted**	**Weighted**
2011	0.0241 ± 0.0006	0.0165 ± 0.0006	0.0579 ± 0.0009	0.0448 ± 0.0011
2012	0.0217 ± 0.0004	0.0180 ± 0.0005	0.0564 ± 0.0007	0.0445 ± 0.0009
2015	0.0389 ± 0.0011	0.0295 ± 0.0016	0.0735 ± 0.0018	0.0627 ± 0.0024
2016	0.0420 ± 0.0005	0.0323 ± 0.0006	0.0886 ± 0.0009	0.0706 ± 0.0011
2017	0.0470 ± 0.0005	0.0311 ± 0.0005	0.0996 ± 0.0010	0.0743 ± 0.0011
2018	0.0373 ± 0.0004	0.0288 ± 0.0005	0.0702 ± 0.0008	0.0542 ± 0.0009

4.6 Mass modelling and fit strategy

The second ingredient needed for the $R_{K\pi\pi}$ measurements, in addition to the efficiencies computed in the previous section, is the double ratio of the yield of the $B^+ \to K^+\pi^+\pi^- J/\psi\,(\to \ell^+\ell^-)$ and the $B^+ \to K^+\pi^+\pi^-\ell^+\ell^-$ modes, with $\ell = e, \mu$, as shown in Eq. 4.2. The yields are measured from maximum likelihood fits to the invariant mass of the reconstructed B^+ meson, implemented with the `RooFit` package [99] within the `ROOT` data-analysis framework [92].

Several components are expected to contribute to the B^+ mass line shape, *i.e.* a signal component plus different sources of background, the latter varying with respect to the decay mode considered. In this section, the mass models used to describe these different contributions, and thus to extract the event yield for each of the different decay modes, are presented, together with the respective fit results.

The first fit models presented in Section 4.6.1 are the ones used to measure the yields in the resonant channels $B^+ \to K^+\pi^+\pi^- J/\psi\,(\to \mu^+\mu^-)$ and $B^+ \to K^+\pi^+\pi^- J/\psi\,(\to e^+e^-)$. Those fits are performed on the reconstructed B^+ mass $m^{J/\psi}(K\pi\pi\ell\ell)$, where the two leptons are constrained to be originated from a J/ψ (a definition already introduced in Section 4.2.2). Since the ratio of the efficiency-corrected yields of these two decay modes is used in the $r_{J/\psi}$ cross-check (see Section 4.7.1), which is a crucial step to validate the correctness of the analysis procedure, the two modes are fitted simultaneously. In this way, the ratio of the electron and muon yields can be measured directly as a parameter of the fit, reducing possible uncertainties that could arise from further calculation.

In the same section, the models used to extract the yields of the $B^+ \to K^+\pi^+\pi^-\psi(2S)(\to \ell^+\ell^-)$ resonant channels are described. These yields, even if not included in the definition of the $R^{-1}_{K\pi\pi}$ observable, are combined with the ones of the $B^+ \to K^+\pi^+\pi^- J/\psi\,(\to \ell^+\ell^-)$ channels in the $R_{\psi(2S)}$ cross-check, described in Section 4.7.2. The $R_{\psi(2S)}$ cross-check is an important test for the effective cancellation of the systematic uncertainties in the double ratio. For this reason, a simultaneous fit of the of the four resonant decay modes is performed, in order to measure directly the double ratio of the yields, avoiding further computation. Again, the *constrained* B^+ mass is used both when fitting $B^+ \to K^+\pi^+\pi^- J/\psi\,(\to \ell^+\ell^-)$ and $B^+ \to K^+\pi^+\pi^-\psi(2S)(\to \ell^+\ell^-)$, where naturally in the latter the two leptons are constrained to originate from a $\psi(2S)$ decay. In this case, the variable is denoted $m^{\psi(2S)}(K\pi\pi\ell\ell)$.

In all the fits mentioned so far, the variable describing the reconstructed B^+ mass line shape was obtained by constraining the dilepton mass to that of the charmonium resonance, either the J/ψ or the $\psi(2S)$ state. This is done because the constraint provides a cleaner signal peak, with a better signal-to-background ratio, which is therefore easier to model. Nevertheless, also the reconstructed B^+ mass without imposing any constrains on the dilepton mass, in the following referred to as *unconstrained* mass, can be studied to obtain information from the $B^+ \to K^+\pi^+\pi^- J/\psi\,(\to \ell^+\ell^-)$ control modes, especially to understand the contribution of partially reconstructed backgrounds (Section 4.3.4). In fact, this type of contamination is difficult to disentangle directly in the fit to the rare mode data (given the limited event

yield), and thus it requires insights that can be gained by studying the resonant modes first, as described in detail in Section 4.6.2.

Finally, a simultaneous fit to the $B^+ \to K^+\pi^+\pi^-\ell^+\ell^-$ and $B^+ \to K^+\pi^+\pi^- J/\psi\,(\to \ell^+\ell^-)\; B^+$ mass line shapes is described in Section 4.6.2, where the experimental efficiencies of the rare and resonant modes are included as parameters. In this way, the $R^{-1}_{K\pi\pi}$ observable is measured directly as a parameter of the fit, simplifying the treatment of the associated uncertainties.

4.6.1 Fit of the resonant decay modes

The fits to the resonant modes are performed on the distribution of the reconstructed B^+ meson mass line shape where the dilepton mass is constrained to that of a resonance: J/ψ or $\psi(2S)$. The *constrained* B^+ masses are required to be in a range of (5150, 5600) MeV/c^2, to exclude contributions from partially reconstructed B^+ decays that would accumulate in the lower part of the mass range. In this way, the contributions expected in the selected mass window are

- a background component, originating predominantly from random combinations of tracks, hereinafter referred to as *combinatorial*. This component is modelled in the fits with an exponential function where the exponent and the normalisation are allowed to vary;
- the signal component, modelled in the fits using a linear combination of two Crystal Ball functions (see Eq. 4.19) sharing the same mean and resolution, *i.e.* the double Crystal Ball shape (DCB) already introduced in Section 4.4.8 and hereinafter referred to as $\mathscr{P}_{\rm DCB}$. The shape parameters are all fixed from fits to the simulated samples, with the addition of a mean shift $\mu^{\rm shift} = \mu^{\rm data} - \mu^{\rm MC}$ and a resolution scale $\sigma^{\rm scale} = \sigma^{\rm data}/\sigma^{\rm MC}$, which are allowed to vary in the fit, to take into account possible differences between data and simulation.

For the electron mode, the bremsstrahlung recovery procedure (described in Section 3.2.2) creates a significant impact on the shape of the signal mass distribution, as already observed in Section 4.4.8, and thus the following three categories are parameterised separately:

- 0γ – corrections to no electron;
- 1γ – one electron received a momentum correction;
- 2γ – momentum corrections to both electrons.

The full mass model is then

$$S(m) = f_{0\gamma}S_{0\gamma}(m) + f_{1\gamma}S_{1\gamma}(m) + (1 - f_{0\gamma} - f_{1\gamma})S_{2\gamma}(m)\,, \tag{4.24}$$

where $f_{0\gamma}$ and $f_{1\gamma}$ – the fractions of events belonging to the 0γ and 1γ categories – are calculated from simulation and $S_{i\gamma}(m) = \mathscr{P}_{\rm DCB}(m|\mu^{i\gamma}, \sigma^{i\gamma}, \alpha_L^{i\gamma}, \alpha_R^{i\gamma}, n_L^{i\gamma}, n_R^{i\gamma})$, with the mean and the

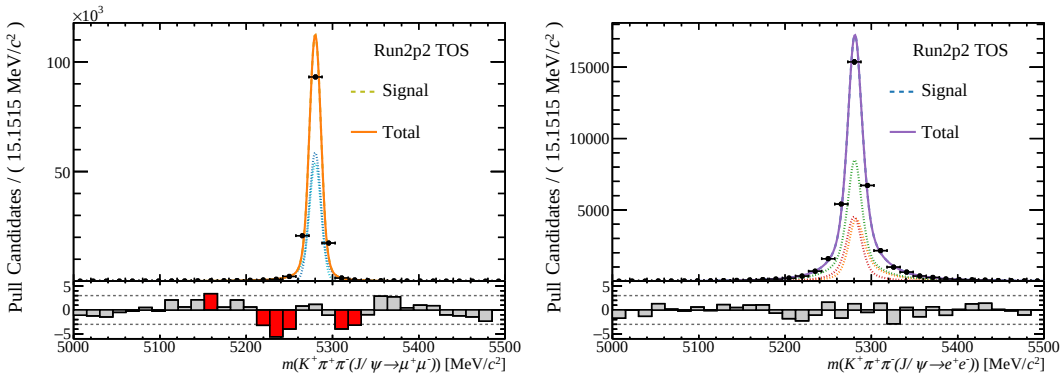

Figure 4.36: Fit to simulated $B^+ \to K^+\pi^+\pi^- J/\psi\,(\to \mu^+\mu^-)$ (left) and $B^+ \to K^+\pi^+\pi^- J/\psi\,(\to e^+e^-)$ (right) samples selected in the TOS trigger category. The events were generated using `Run2p2` conditions. For the muon case, the dotted lines show the contribution of a single side of the double Crystal Ball (DCB). In the electron case each dotted line represents a DCB modelling the three different bremsstrahlung categories (when 0γ, 1γ, 2γ have been added to the electrons).

resolution $\mu^{i\gamma}, \sigma^{i\gamma}$ shared among the right and left sides of the DCB of each bremsstrahlung category $i\gamma$.

Simultaneous fits to $B^+ \to K^+\pi^+\pi^- J/\psi\,(\to \ell^+\ell^-)$, $\ell = e, \mu$

A simultaneous fit in the J/ψ q^2 region to $m^{J/\psi}(K\pi\pi\mu\mu)$ and $m^{J/\psi}(K\pi\pi ee)$ is performed with the models described in the previous section. Fitting the two final states simultaneously allows to treat the muon yield and the ratio of the muon and electron yields as parameters, and to express the electron yield as a function of these two. In this way the yields ratio, r_{yields}, which is the quantity needed to perform the $r_{J/\psi}$ cross-check (described in Section 4.7.1), comes directly from the fit simplifying the propagation of uncertainties.

Figure 4.36 shows an example of fit to simulated samples for $B^+ \to K^+\pi^+\pi^- J/\psi\,(\to \mu^+\mu^-)$ and $B^+ \to K^+\pi^+\pi^- J/\psi\,(\to e^+e^-)$ decays, from which the signal shape parameters are extracted. Figure 4.37 shows an example of fit to the data samples, where the signal shape parameters are fixed from the fits shown in Figure 4.36 (with μ^{shift} and σ^{scale}, which are allowed to vary, to account for simulation/data differences) and a component describing the combinatorial background is added.

Table 4.15 shows the r_{yields} parameter and the yields for the muon and the electron modes extracted from fits to each data taking period and trigger category.

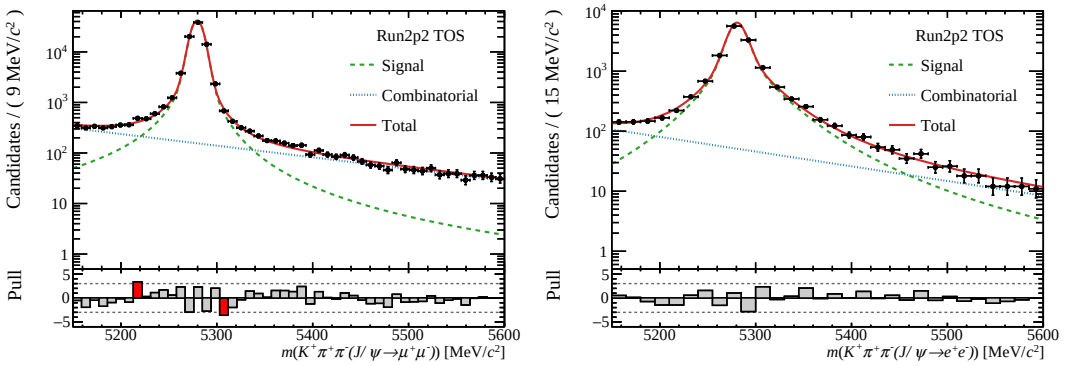

Figure 4.37: Fits to $B^+ \to K^+\pi^+\pi^- J/\psi\,(\to \mu^+\mu^-)$ (left) and $B^+ \to K^+\pi^+\pi^- J/\psi\,(\to e^+e^-)$ (right) data samples from the simultaneous fit to $m^{J/\psi}(K\pi\pi ee)$ and $m^{J/\psi}(K\pi\pi\mu\mu)$ in data collected in the Run2p2 period and selected in the TOS trigger category. The combinatorial and the signal components are shown in dotted lines, while the solid line shows the sum of these two contributions.

Table 4.15: Electron and muon $B^+ \to K^+\pi^+\pi^- J/\psi\,(\to \ell^+\ell^-)$ yields obtained from the simultaneous fits to $m^{J/\psi}(K\pi\pi ee)$ and $m^{J/\psi}(K\pi\pi\mu\mu)$ for data samples for all the data taking periods and trigger categories. The ratio of the yields of the two decay modes involved (r_{yields}) is also shown.

Period - Trigger	$\mathcal{N}\left(K\pi\pi J/\psi(\to \mu\mu)\right)$	$\mathcal{N}\left(K\pi\pi J/\psi(\to ee)\right)$	r_{yields}
Run1 TOS	33923 ± 190	4798 ± 86	7.07 ± 0.12
Run1 TIS	14422 ± 124	3972 ± 83	3.63 ± 0.07
Run2p1 TOS	42002 ± 212	7924 ± 112	5.30 ± 0.07
Run2p1 TIS	21211 ± 151	6607 ± 113	3.21 ± 0.05
Run2p2 TOS	82872 ± 297	14538 ± 162	5.70 ± 0.06
Run2p2 TIS	39251 ± 205	13127 ± 148	2.99 ± 0.034
Total	233682 ± 499	50944 ± 302	4.58 ± 0.02

Simultaneous fits to $B^+ \to K^+\pi^+\pi^- J/\psi(\to \ell^+\ell^-)$ and $B^+ \to K^+\pi^+\pi^-\psi(2S)(\to \ell^+\ell^-)$, $\ell = e,\mu$

The models used to extract the yields of the $B^+ \to K^+\pi^+\pi^-\psi(2S)(\to \ell^+\ell^-)$ decay modes are similar to the ones used to fit the $B^+ \to K^+\pi^+\pi^- J/\psi(\to \ell^+\ell^-)$ decays, described in the previous section. The main differences are that the $B^+ \to K^+\pi^+\pi^-\psi(2S)(\to \ell^+\ell^-)$ fits are performed on the B^+ meson mass variable reconstructed by constraining the dilepton to come from a $\psi(2S)$ decay, *i.e.* $m^{\psi(2S)}(K\pi\pi\ell\ell)$, and that the 11 GeV$^2/c^4 < q^2 < 15$ GeV$^2/c^4$ dilepton invariant mass range is selected (Section 4.2.2). With the full selection applied and requiring the constrained B^+ mass to lie within the 5150 MeV$/c^2 < m^{\psi(2S)}(K\pi\pi\ell\ell) < 5600$ MeV$/c^2$ mass window, the background composition is expected to be dominated by combinatorial, as for the $B^+ \to K^+\pi^+\pi^- J/\psi(\to \ell^+\ell^-)$ case.

Figure 4.38 shows an example of the fits to simulated $B^+ \to K^+\pi^+\pi^-\psi(2S)(\to e^+e^-)$ and $B^+ \to K^+\pi^+\pi^-\psi(2S)(\to \mu^+\mu^-)$ decays. As described above, the parameters obtained from such fits are in turn used to fix the signal shapes in the fits to the data samples, shown in Figure 4.39, with the addition of μ^{shift} and σ^{scale}, which are allowed to vary, to account for simulation/data differences, and a combinatorial component. The fits are performed simultaneously to the four invariant masses $m^{J/\psi}(K\pi\pi\ell\ell)$ and $m^{\psi(2S)}(K\pi\pi\ell\ell)$, with $\ell = e,\mu$. The double ratio of yields

$$R_{\text{yields}} = \frac{\mathcal{N}\left(B^+ \to K^+\pi^+\pi^-\psi(2S)(\to \mu^+\mu^-)\right)}{\mathcal{N}\left(B^+ \to K^+\pi^+\pi^- J/\psi(\to \mu^+\mu^-)\right)} \cdot \frac{\mathcal{N}\left(B^+ \to K^+\pi^+\pi^- J/\psi(\to e^+e^-)\right)}{\mathcal{N}\left(B^+ \to K^+\pi^+\pi^-\psi(2S)(\to e^+e^-)\right)} \tag{4.25}$$

is fitted directly as a parameter, while the electron yield $\mathcal{N}\left(K\pi\pi(\psi(2S) \to ee)\right)$ is derived from R_{yields} and the yields of the other three decay modes.

The yields of the $B^+ \to K^+\pi^+\pi^-\psi(2S)(\to \ell^+\ell^-)$ modes obtained from these fits, together with the double ratio of the J/ψ and $\psi(2S)$ resonant yields, are shown in Table 4.16 for each data taking period and trigger category. The reliability of the double ratio procedure is already appreciable from the R_{yields} values, which are already all compatible with unity within 2σ, even without efficiency corrections, unlike the single ratio case (Table 4.15).

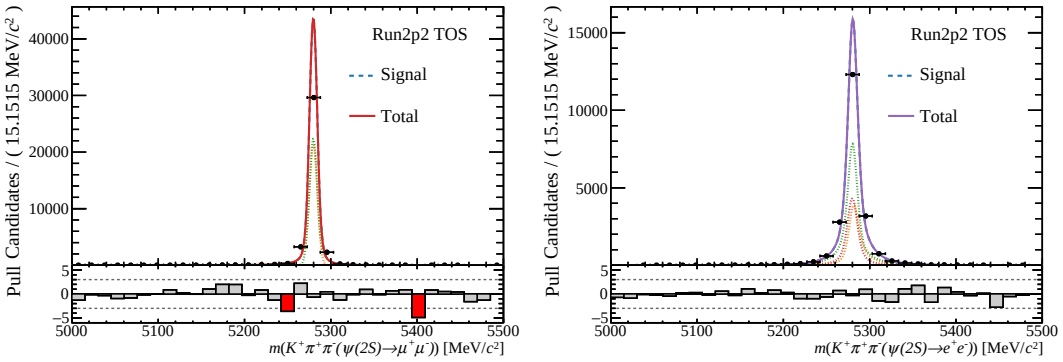

Figure 4.38: Fit to simulated resonant $B^+ \to K^+\pi^+\pi^-\psi(2S)(\to \mu^+\mu^-)$ (left) and $B^+ \to K^+\pi^+\pi^-\psi(2S)(\to e^+e^-)$ (right) samples selected in the TOS trigger category. The events were generated using Run2p2 conditions. For the muon case, the dotted lines show the contribution of a single side of the double Crystal Ball (DCB). In the electron case each dashed line represents a DCB modelling for the three different bremsstrahlung categories (when 0γ, 1γ, 2γ have been added to the electrons).

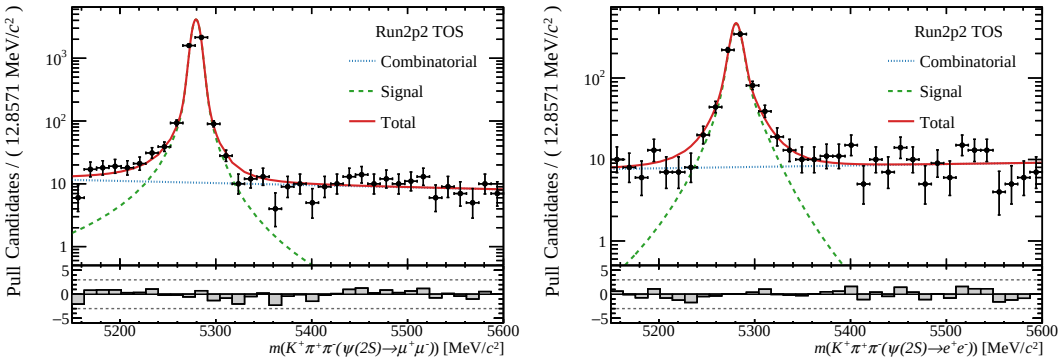

Figure 4.39: Fits to $B^+ \to K^+\pi^+\pi^-\psi(2S)(\to \mu^+\mu^-)$ (left) and $B^+ \to K^+\pi^+\pi^-\psi(2S)(\to e^+e^-)$ (right) data samples from the simultaneous fit to $m^{J/\psi}(K\pi\pi ee)$, $m^{J/\psi}(K\pi\pi\mu\mu)$, $m^{\psi(2S)}(K\pi\pi ee)$ and $m^{\psi(2S)}(K\pi\pi\mu\mu)$ in data collected in the Run2p2 period and selected with the TOS trigger category. The combinatorial and the signal components are shown in dotted lines, while the solid line shows the sum of these two contributions.

Table 4.16: Electron and muon $B^+ \to K^+\pi^+\pi^-\psi(2S)(\to \ell^+\ell^-)$ yields obtained from the simultaneous fits to $m^{J/\psi}(K\pi\pi ee)$, $m^{J/\psi}(K\pi\pi\mu\mu)$, $m^{\psi(2S)}(K\pi\pi ee)$ and $m^{\psi(2S)}(K\pi\pi\mu\mu)$ for data samples for all the data taking periods and trigger categories. The double ratio of the four decay modes involved (R_{yields}) is also shown.

Period - Trigger	$\mathcal{N}\left(K\pi\pi\psi(2S)(\to \mu\mu)\right)$	$\mathcal{N}\left(K\pi\pi\psi(2S)(\to ee)\right)$	R_{yields}
Run1 TOS	1551 ± 40	247 ± 21	0.90 ± 0.07
Run1 TIS	632 ± 26	146 ± 16	1.22 ± 0.12
Run2p1 TOS	2060 ± 46	344 ± 24	1.12 ± 0.07
Run2p1 TIS	977 ± 32	248 ± 22	1.22 ± 0.10
Run2p2 TOS	3986 ± 64	740 ± 40	0.95 ± 0.04
Run2p2 TIS	1844 ± 44	519 ± 32	1.19 ± 0.07
Total	11052 ± 107	2240 ± 64	1.07 ± 0.03

4.6.2 Fit of the rare decay modes

In this section, the strategy used to fit the reconstructed B^+ invariant mass in the rare $B^+ \to K^+\pi^+\pi^-\ell^+\ell^-$ decays is presented. To perform these fits, the full selection for the rare mode is applied to the simulated and the data samples (Section 4.3), including the q^2 selection of the signal region (Section 4.2.2). In this case, the *unconstrained* B^+ invariant mass m_B is used, *i.e.* no constraints are applied to the lepton pair, and the mass range adopted for the fit is $4900\,\text{MeV}/c^2 < m_B < 5600\,\text{MeV}/c^2$.

In addition to the combinatorial background discussed for the resonant modes, other sources of background are expected to contribute to the mass line shapes in the signal region. This is due to the topology of the decay, since the two leptons do not come from a resonance anymore and thus live in a different q^2 region, and to the extension of the mass range towards the lower side, which is made necessary by the much lower yield of the rare modes. The components of the PDF used to model the reconstructed B^+ invariant mass shape are as follows.

- The signal component, which is modelled in the fit with the same double Crystal Ball shape as used for the resonant modes (Section 4.6.1). The signal shape parameters are fixed from fits to $B^+ \to K^+\pi^+\pi^-\ell^+\ell^-$ simulated samples, an example of which is shown in Figure 4.40. In the fits to data, a mean shift $\mu^{\text{shift}} = \mu^{\text{data}} - \mu^{\text{MC}}$ and a resolution scale $\sigma^{\text{scale}} = \sigma^{\text{data}}/\sigma^{\text{MC}}$ are added, to take into account possible differences between simulation and data samples. Here, the μ^{shift} and σ^{scale} can not be allowed to vary freely as it was done for the resonant case, due to the small yield of the rare mode which undermines the stability of the fit. That is why the μ^{shift} and σ^{scale} are fixed to values extracted from fits to the unconstrained B^+ mass in $B^+ \to K^+\pi^+\pi^- J/\psi\,(\to \ell^+\ell^-)$ modes, as it will be detailed in the following section.
- The combinatorial component, described by an exponential function where the exponent and the normalisation are allowed to vary freely.

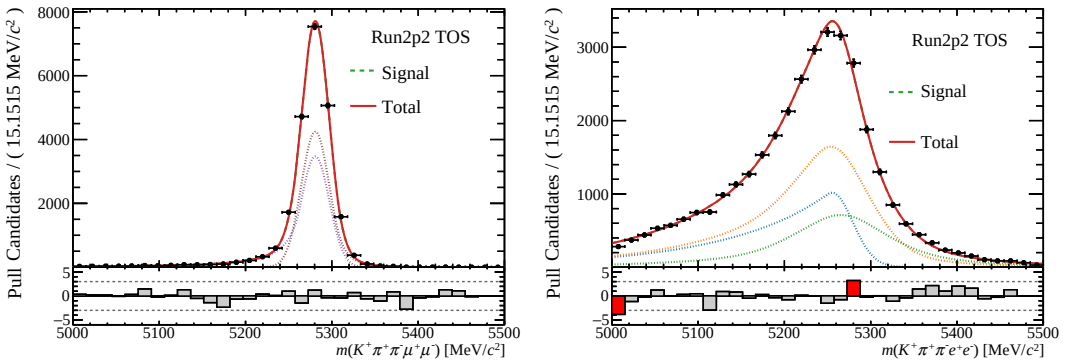

Figure 4.40: Fit to simulated $B^+ \to K^+\pi^+\pi^-\mu^+\mu^-$ (left) and $B^+ \to K^+\pi^+\pi^-e^+e^-$ (right) samples selected in the TOS trigger category. The events were generated using `Run2p2` conditions. For the muon case, the dotted lines show the contribution of a single side of the double Crystal Ball (DCB). In the electron case each dotted line represents a DCB modelling the three different bremsstrahlung categories (when 0γ, 1γ, 2γ have been added to the electrons).

- The leakage from $B^+ \to K^+\pi^+\pi^- J/\psi\,(\to e^+e^-)$ decays (only when fitting the $B^+ \to K^+\pi^+\pi^-e^+e^-$ mode due to the lower mass resolution), already introduced in the background discussion in Section 4.3.4. The leakage shape is taken from the resonant data samples to which the full rare mode selection has been applied. The remaining events, shown in Figure 4.17, are modelled with a kernel density estimator function from the `RooKeysPdf` class within the `ROOT` data analysis framework [92]. The resulting shape is then used to fix the leakage component in the fits to the rare mode data. The amount of $B^+ \to K^+\pi^+\pi^- J/\psi\,(\to e^+e^-)$ events leaking into the signal region is fixed to the estimates shown in Table 4.6.
- The residual $h \to e$ misidentification component, with amount and shape fixed to the estimates given by the PassFail method, extensively described in Section 4.3.4.
- The background component coming from partially reconstructed B^+ decays, with final states such as $K^+\pi^+\pi^-\ell^+\ell^-X$, where X is missing. This type of background is particularly challenging to model, due to its non-peaking nature and to the unknown underlying structure of all the possible decays that could contribute. That is why a dedicated data-driven procedure is designed specifically to model this contribution, by determining the partially-reconstructed line shape and its amount using the resonant $B^+ \to K^+\pi^+\pi^- J/\psi\,(\to \ell^+\ell^-)$ modes as a proxy. More details on this procedure are given in the following section.

Modelling of the partially reconstructed background contribution

Since the underlying structure of partially reconstructed (PR) backgrounds is unknown, there are no *a priori* information that can be used to model this type of contribution. The methodology designed in this analysis consists in determining the PR line shape and the fraction of

PR events with respect to the signal events using the J/ψ channel as a proxy. The strategy to model the partially reconstructed backgrounds is summarised as follows:

i. The **PR shape parameters** are extracted from fits to the *unconstrained* B^+ invariant mass in $B^+ \to K^+\pi^+\pi^- J/\psi\,(\to \ell^+\ell^-)$ decays. The unconstrained mass is used in order to have a similar mass line shape to the one expected in the rare $B^+ \to K^+\pi^+\pi^-\ell^+\ell^-$ modes, given that the constraint on the pair of leptons to come from the J/ψ resonance would act on the dilepton resolution and thus also on the shape of the PR background or of the signal component. Examples of the fits to the $m(K\pi\pi\ell\ell)$ invariant masses in the $J/\psi\, q^2$ region, used to extract the PR shape parameters, are shown in Figure 4.41 for resonant muon decays. In the fits, the PR background contribution is modelled with a convolution between a Gaussian function, with resolution σ^{PR} and a fixed null mean, and an Argus probability density function (implemented by the `RooArgusBG` class within the `ROOT` framework [92]),

$$\text{Argus}(m, m_0, c) = N \cdot m \cdot \left[1 - \left(\frac{m}{m_0}\right)^2\right] \cdot \exp\left[c \cdot \left(1 - \left(\frac{m}{m_0}\right)^2\right)\right], \tag{4.26}$$

where m_0 is the cut-off mass of the distribution and c is a slope parameter.
For muon decays, the resolution of the reconstructed B^+ invariant mass is sufficient to determine the PR shape, while for the electron modes it is necessary to first remove the signal events by applying a requirement on $m^{J/\psi}\,(K\pi\pi ee) < 5150\,\text{MeV}$, as shown on the left side of Figure 4.42.
In addition, also the mean shift μ^{shift} and resolution scale σ^{scale} of the signal component in the rare modes are obtained from the same type of fits. In particular, the μ^{shift} and σ^{scale} for muon decays are extracted from the same fit to the unconstrained mass used to estimate the PR shape parameters (Figure 4.41). For the electron modes, the μ^{shift} and σ^{scale} are extracted from fits in a dataset complementary to the one used to extract the PR shape parameters, applying thus a requirement on $m^{J/\psi}\,(K\pi\pi ee) > 5150\,\text{MeV}$ (right-hand panel of Figure 4.42). The values of the PR shape parameters and the μ^{shift} and σ^{scale}, used to fix the same parameters in the fits to the rare modes, are shown in Table 4.17, where a generally good stability can be observed between data taking periods and trigger conditions. Systematic uncertainties associated to the use of this data-driven strategy to model the partially reconstructed background contribution to the B^+ mass line shape will be evaluated as explained in Section 4.8.1.

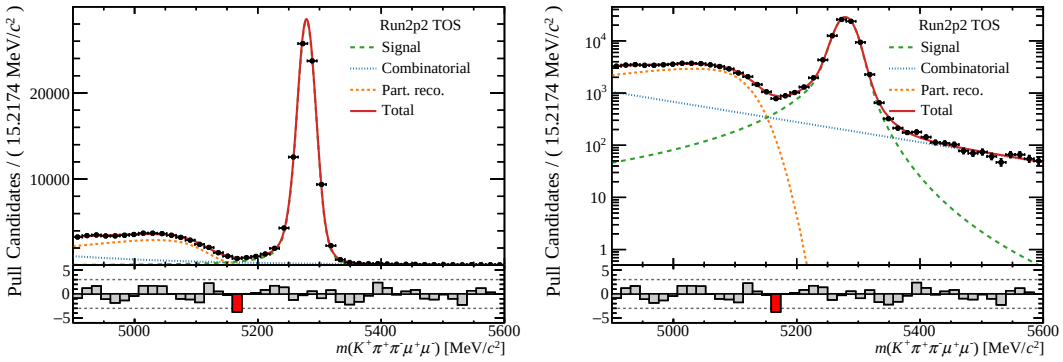

Figure 4.41: An example of the fit in linear (left) and logarithmic (right) scale to the unconstrained B^+ meson mass $m(K\pi\pi\mu\mu)$ in $B^+ \to K^+\pi^+\pi^- J/\psi\,(\to \mu^+\mu^-)$ data samples, with data collected in the Run2p2 period and selected with the TOS trigger category. The dotted lines show the contribution of the combinatorial, partially reconstructed and signal components, while the solid line shows their sum. From this type of fit, the PR shape parameters and the signal $\mu^{\text{shift}}, \sigma^{\text{scale}}$ are extracted and used to fix the same parameters in the fits to the rare $B^+ \to K^+\pi^+\pi^-\mu^+\mu^-$ mode.

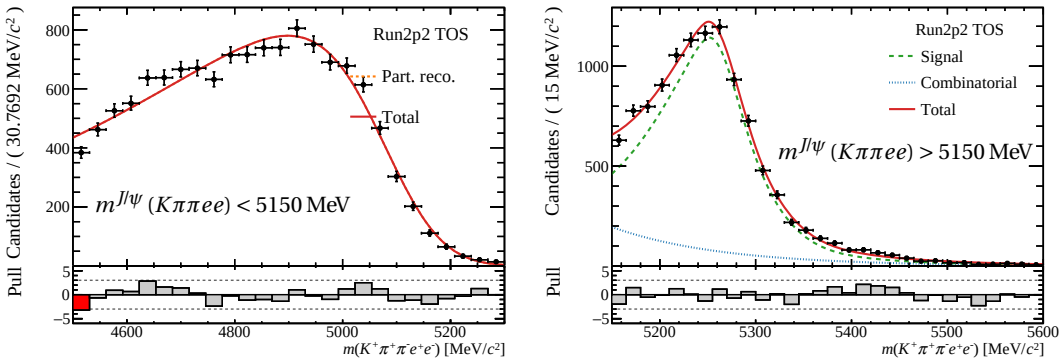

Figure 4.42: An example of the fit to the partially reconstructed background contribution, isolated requiring $m^{J/\psi}(K\pi\pi ee) < 5150\,\text{MeV}/c^2$ (left), and the fit to the signal and combinatorial shapes in the complementary dataset, selected requiring $m^{J/\psi}(K\pi\pi ee) > 5150\,\text{MeV}/c^2$ (right) for $B^+ \to K^+\pi^+\pi^- J/\psi\,(\to e^+e^-)$ data samples. The fits shown are performed in data collected in the Run2p2 period and selected with the TOS trigger category. The PR shape parameters are extracted from the left side fit, while the signal $\mu^{\text{shift}}, \sigma^{\text{scale}}$ from the right side fit. The values are used to fix the same parameters in the fits to the rare $B^+ \to K^+\pi^+\pi^- e^+e^-$ mode.

Table 4.17: Parameters extracted from the fits to the unconstrained B^+ meson masses $m(K\pi\pi ee)$ and $m(K\pi\pi\mu\mu)$ for $B^+ \to K^+\pi^+\pi^- J/\psi(\to \ell^+\ell^-)$ decays, for all the data taking periods and trigger categories. The parameters of the partially reconstructed background model ($m_0^{\rm PR}$, $c^{\rm PR}$ and $\sigma^{\rm PR}$) and the mean shift and resolution scale of the signal component with respect to the fitted values in simulated samples ($\mu^{\rm shift}$ and $\sigma^{\rm scale}$) are used to fix the same quantities in the fits to the rare modes.

Electron mode					
Period - Trigger	$\sigma^{\rm PR}$	$c^{\rm PR}$	$m_0^{\rm PR}$	$\mu^{\rm shift}$	$\sigma^{\rm scale}$
Run1 TOS	84.6 ± 5.3	-8.3 ± 0.6	5103 ± 8	2.1 ± 2.5	1.20 ± 0.09
Run1 TIS	90.1 ± 5.7	-9.3 ± 0.6	5109 ± 8	0.3 ± 3.4	1.15 ± 0.09
Run2p1 TOS	82.7 ± 3.9	-8.3 ± 0.4	5095 ± 6	-4.4 ± 2.2	1.02 ± 0.07
Run2p1 TIS	93.8 ± 4.6	-9.3 ± 0.5	5089 ± 7	-12.9 ± 1.7	1.18 ± 0.03
Run2p2 TOS	80.2 ± 3.1	-7.5 ± 0.3	5104 ± 5	-3.7 ± 1.6	1.06 ± 0.05
Run2p2 TIS	87.4 ± 3.1	-8.0 ± 0.2	5102 ± 5	-4.4 ± 1.8	0.99 ± 0.05
Muon mode					
Period - Trigger	$\sigma^{\rm PR}$	$c^{\rm PR}$	$m_0^{\rm PR}$	$\mu^{\rm shift}$	$\sigma^{\rm scale}$
Run1 TOS	30.0 ± 2.2	-14.4 ± 1.2	5128 ± 2	-2.98 ± 0.11	0.985 ± 0.006
Run1 TIS	26.0 ± 4.0	-13.8 ± 1.7	5131 ± 3	-2.93 ± 0.17	0.986 ± 0.009
Run2p1 TOS	27.3 ± 1.9	-13.3 ± 1.0	5131 ± 2	-1.80 ± 0.10	0.989 ± 0.005
Run2p1 TIS	30.3 ± 2.7	-14.0 ± 1.6	5128 ± 3	-1.69 ± 0.15	1.005 ± 0.008
Run2p2 TOS	25.7 ± 1.3	-13.9 ± 0.7	5131 ± 1	-1.64 ± 0.07	0.965 ± 0.004
Run2p2 TIS	29.9 ± 2.1	-13.2 ± 0.9	5131 ± 1	-1.97 ± 0.10	0.975 ± 0.006

ii. The **PR scale** ($s_{\rm PR}$). Like for the previous step, insights on the fraction of the PR contribution in the signal region can in principle be determined from fits to the reconstructed B^+ invariant masses in the J/ψ q^2 region. The basic idea is that the relative amount of partially reconstructed background with respect to the signal, referred to in the following as partially reconstructed scale $s_{\rm PR}$, is similar in the resonant and rare modes. To increase the stability of the fit, given that all the parameters modelling the PR contribution are allowed to vary freely, the fit is performed simultaneously between all data taking periods of the same trigger categories, sharing the same $s_{\rm PR}$, on the *constrained* B^+ invariant mass $m^{J/\psi}(K\pi\pi\ell\ell)$. An example of these fits for the electron mode selected in the TOS trigger category can be found in Figure 4.43, while the $s_{\rm PR}$ extracted for all the categories are listed in Table 4.18.
Further studies are performed using different fit configurations, *i.e.* with or without the mass constraints being applied and with or without the $s_{\rm PR}$ parameter being shared between data taking periods. A good agreement is observed between the fractions obtained with or without imposing the $s_{\rm PR}$ to be shared among different years in the same trigger conditions, when using the constrained masses. On the other hand, the fits to the unconstrained $m(K\pi\pi\mu\mu)$ invariant mass show a typical increase of 8-14 % in the fraction of partially reconstructed background, depending on the data taking period and on the trigger categories considered. The same fits to the unconstrained $m(K\pi\pi ee)$ invariant mass are extremely challenging in terms of the interplay between the different species of backgrounds and the signal. While some of these difficulties can be tackled by imposing a common $s_{\rm PR}$ value between years, there are still some remaining instabilities in the determination of the parameters of the combinatorial background shape. In fact, the solution of these fits indicates the absence of this contribution, in contrast to what is observed for the fits on the J/ψ constrained mass. This clearly prevents an unbiased extraction of the $s_{\rm PR}$ parameter. Given the above, the estimations of the $s_{\rm PR}$ shown are not used in the rare mode to fix the same parameter, but as the mean value of a Gaussian constraint. The width of the Gaussian constraint is set to 20% of $s_{\rm PR}$, in order to cover the differences in the $s_{\rm PR}$ estimations observed in the different fit configurations for the muon case. The effects of varying the mean or the width of the Gaussian constraint will be treated as systematic uncertainties, as explained in Section 4.8.1.

Table 4.18: Fractions of PR events with respect to signal events, $s_{\rm PR}$, extracted from fits to the J/ψ constrained B^+ meson mass $m^{J/\psi}(K\pi\pi\ell\ell)$ in $B^+ \to K^+\pi^+\pi^- J/\psi\,(\to \ell^+\ell^-)$ data samples. The fits are done simultaneously for a given trigger category, sharing the partially reconstructed scale among data taking periods $s_{\rm PR}$.

Trigger	$s_{\rm PR}\left(K\pi\pi\mu\mu\right)$	$s_{\rm PR}\left(K\pi\pi ee\right)$
TOS	0.433 ± 0.005	0.325 ± 0.018
TIS	0.436 ± 0.008	0.286 ± 0.015

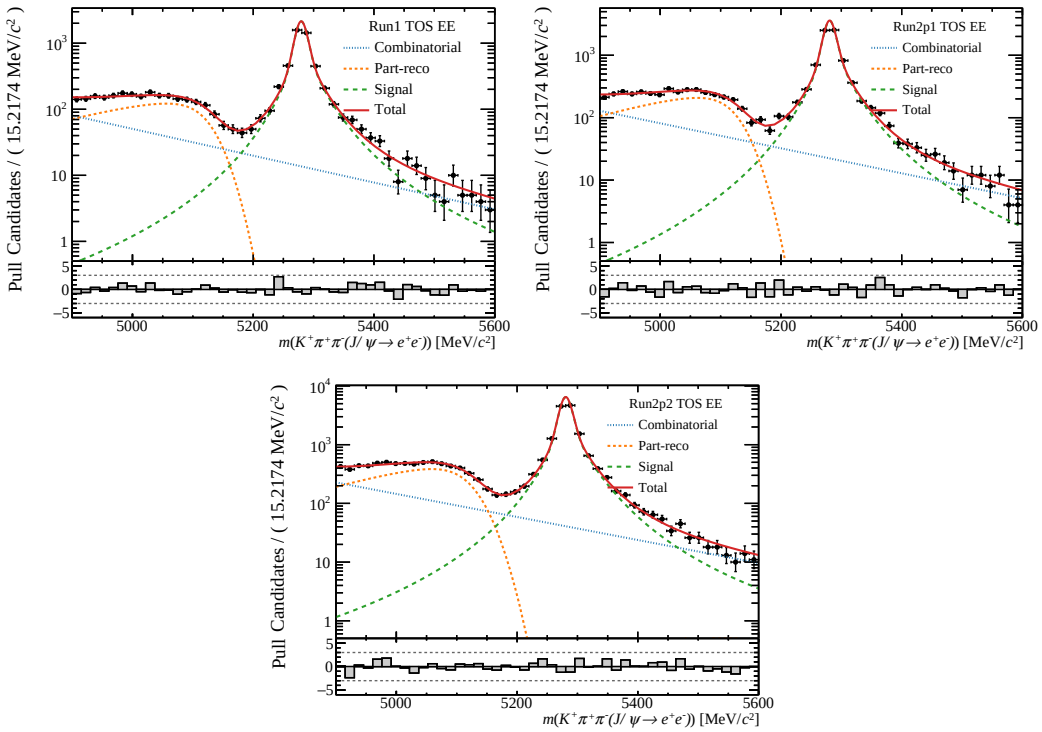

Figure 4.43: Fit of the J/ψ-constrained B^+ meson mass, for $B^+ \to K^+\pi^+\pi^- J/\psi\,(\to e^+e^-)$ data samples. The fit is performed simultaneously among the data taking periods for a given trigger category, sharing the partially reconstructed background scale, *i.e.* one s_{PR} value is extracted from the three fits shown.

Simultaneous fits to $B^+ \to K^+\pi^+\pi^-\ell^+\ell^-$ and $B^+ \to K^+\pi^+\pi^- J/\psi(\to \ell^+\ell^-)$, $\ell = e,\mu$

The $R^{-1}_{K\pi\pi}$ value is extracted by means of a simultaneous fit to all the subsets of the resonant $B^+ \to K^+\pi^+\pi^- J/\psi(\to \ell^+\ell^-)$ and rare $B^+ \to K^+\pi^+\pi^-\ell^+\ell^-$ data samples. Both the resonant and the rare mode samples are in fact divided in data taking periods and trigger categories, *i.e.* `Run1 TIS`, `Run1 TOS`, `Run2p1 TIS`, `Run2p1 TOS`, `Run2p2 TIS` and `Run2p2 TIS`. In the simultaneous fit, all the subsets are fitted simultaneously by sharing the same $R^{-1}_{K\pi\pi}$ parameter, as defined in Eq. 4.2. The total efficiencies of all the decay modes involved, which are necessary for the $R^{-1}_{K\pi\pi}$ estimation, are included directly in the fit as parameters. The efficiency parameters are constrained to follow a Gaussian distribution with mean and standard deviation being the efficiency and the associated uncertainty for the considered subsample, calculated using the reweighted simulated samples as described in Section 4.5. In order to ensure the blinding, the efficiencies of the rare modes and the $R^{-1}_{K\pi\pi}$ parameter are scaled by an unknown factor.

The fits to the resonant modes are performed using the constrained reconstructed B^+ mass in a window of (5150 MeV/c^2, 5600 MeV/c^2) selected in the $J/\psi\, q^2$ region. The model of the B^+ mass line shape follows the same strategy already described in Section 4.6.1, *e.g.* a signal shape fixed from fits to simulated samples, with a mean shift and resolution scale allowed to vary, plus a combinatorial background component, described by an exponential function with yield and decay parameter allowed to vary.

The fits to the rare modes use the unconstrained B^+ mass and in a window of (4900 MeV/c^2, 5600 MeV/c^2), selected in the signal q^2 region. The modelling of the signal and background contributions to the B^+ mass line shape are the ones described in the previous sections, summarised here for the benefit of the reader.

- The signal shape is fixed from fits to simulated samples of the rare modes, examples of which are shown in Figure 4.40. The mean shift and resolution scale, with respect to the MC values, are fixed to the parameters extracted from fits to the unconstrained B^+ invariant mass in $B^+ \to K^+\pi^+\pi^- J/\psi(\to \ell^+\ell^-)$ decays (reported in Table 4.17). Examples of these fits were shown in Figure 4.41 and in Figure 4.42 (right).
- The combinatorial component is modelled with an exponential function with exponent and normalisation allowed to vary freely.
- The partially reconstructed background shape parameters are fixed to the values shown in Table 4.17, and are extracted from fits to the unconstrained B^+ invariant mass in $B^+ \to K^+\pi^+\pi^- J/\psi(\to \ell^+\ell^-)$ decays. Examples of these fits were shown in Figure 4.41 and in Figure 4.42 (left). The relative ratio of partially reconstructed background to signal yield is constrained to lay in a Gaussian with the mean fixed to the value of Table 4.18 and the standard deviation set to 20% of the mean value. The values of the PR scale parameters are extracted from fits to the constrained B^+ invariant mass in $B^+ \to K^+\pi^+\pi^- J/\psi(\to \ell^+\ell^-)$ decays, examples of which are shown in Figure 4.43.
- The J/ψ-leakage component, only for the electron modes, is fixed to the shape shown

Table 4.19: Rare mode yields extracted from the simultaneous fit to the unconstrained B^+ meson masses $m(K\pi\pi\ell\ell)$ in $B^+ \to K^+\pi^+\pi^-\ell^+\ell^-$ signal samples in data and to the constrained mass $m^{J/\psi}(K\pi\pi\ell\ell)$ in $B^+ \to K^+\pi^+\pi^- J/\psi(\to \ell^+\ell^-)$ samples. All the data taking periods and trigger categories shares the same $R^{-1}_{K\pi\pi}$ parameter.

Period - Trigger	$\mathcal{N}\left(B^+ \to K^+\pi^+\pi^-\mu^+\mu^-\right)$	$\mathcal{N}\left(B^+ \to K^+\pi^+\pi^- e^+e^-\right)$
Run1 TOS	113 ± 12	30 ± 5
Run1 TIS	53 ± 8	27 ± 6
Run2p1 TOS	139 ± 13	47 ± 7
Run2p1 TIS	77 ± 10	44 ± 7
Run2p2 TOS	229 ± 17	69 ± 9
Run2p2 TIS	171 ± 14	104 ± 13
Total	782 ± 31	323 ± 20

in Figure 4.3.4, that gathers the remaining events of the resonant modes passing the selection of the rare modes. The J/ψ -leakage yields are fixed to the estimates in Table 4.6.

- The residual $h \to e$ misidentification component, with shape and amount fixed from the estimates given by the PassFail method (shown in Figure 4.13).

Figure 4.44 shows the fits to the rare modes by combining all the datasets and the fitted PDFs from each subcategory. The observed electron and muon yields of the rare modes are listed in Table 4.19. The blinded $R^{-1}_{K\pi\pi}$ parameter value, found by the minimisation process, is measured to be $R^{-1}_{K\pi\pi} = 2.83 \pm 0.34$. From this, since the blinding procedure is done in a way that maintains the relative uncertainty on the parameter, a statistical sensitivity of ~12% can be estimated.

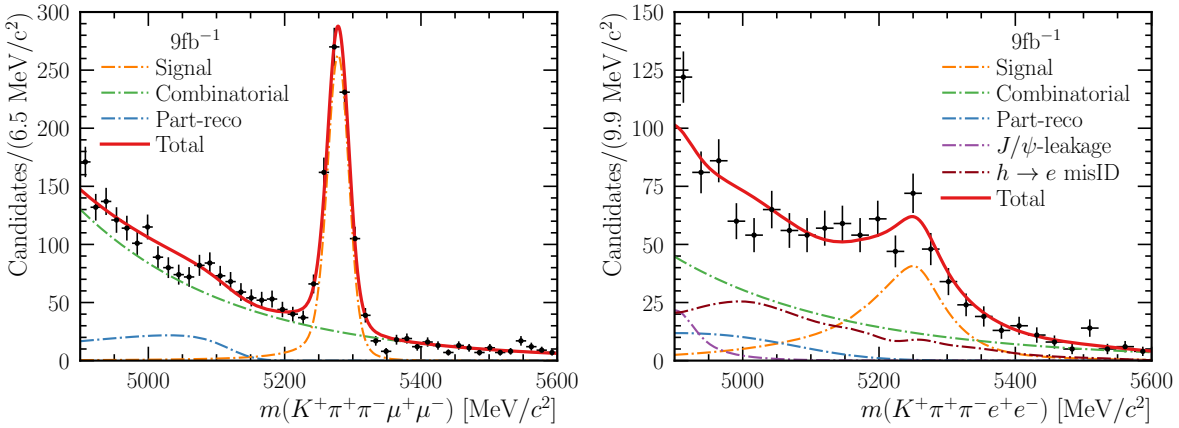

Figure 4.44: Fit to the unconstrained B^+ meson mass in $B^+ \to K^+\pi^+\pi^-\mu^+\mu^-$ (left) and $B^+ \to K^+\pi^+\pi^- e^+e^-$ (right) data samples, combining all the data taking periods and trigger categories.

4.6.3 Fit stability

The stability of each fit strategy presented so far, together with the absence of bias in the yield estimations, has been studied by generating N random pseudoexperiments, also called "toys". Each toy dataset is generated from the distributions modelling the different components of the B^+ invariant mass line shapes, by letting the fitted signal and background yields fluctuate as Poisson random variables. For each parameter of the mass model (*e.g.* the combinatorial exponent, the signal yield *etc.*) the so-called "pulls" can be calculated as the difference between the parameter value found from the fit to the toy dataset and the parameter value from which the toy dataset is generated, divided by the parameter's uncertainty in the fit to the toy dataset. For large N and in absence of bias, the pulls of all the parameters are expected to be Gaussian-distributed with $\mu = 0$ and $\sigma = 1$.

The pulls evaluation needs a more careful treatment for those parameters to which a Gaussian constraint is applied, like the efficiencies or the PR scale $s_{\rm PR}$ parameters in the fits to the rare modes. In this case, the procedure is as follows.

- The toy dataset is generated by initialising the constrained parameter p to the value extracted from the nominal fit: $p_{\rm nom}$.
- The mean value of the Gaussian constraint on the parameter, when fitting the toy dataset, is each time chosen randomly from a Gaussian distribution with $\text{Gauss}(\mu,\sigma) = \text{Gauss}(p_{\rm nom}, p_{\rm err})$, where $p_{\rm err}$ is the width of the nominal constraint calculated on the $p_{\rm nom}$ value (*e.g.* $p_{\rm err} = 20\% \cdot p_{\rm nom}$ in the case of the PR scale parameter). The computed $p_{\rm err}$ is also used as the width of the constraint in fit to the toy dataset.

The pulls of all the parameters involved in the several fits are found to be Gaussian-distributed with mean and standard deviation compatible with the values of $\mu = 0$ and $\sigma = 1$, validating the fit procedure. Figure 4.45 shows, as an example, the pull of the $R^{-1}_{K\pi\pi}$ parameter obtained from the simultaneous fit to the resonant J/ψ modes and the rare modes. To calculate this pull, 500 toys were generated, out of which only 40 *failed* (*i.e.* the minimisation procedure did not converge), proving a good stability of the fit model. The remaining non-Gaussian behaviour of the $R^{-1}_{K\pi\pi}$ pull is included as a systematic uncertainty in the final measurement, as explained in Section 4.8.1.

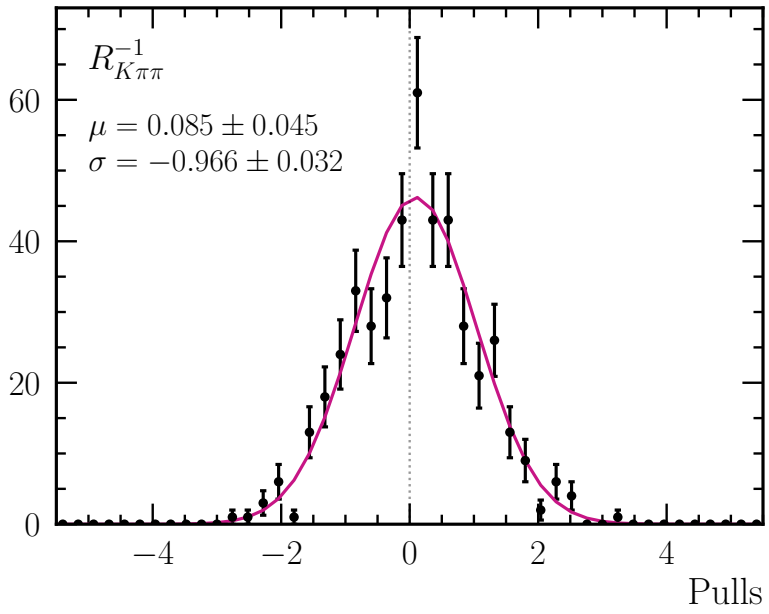

Figure 4.45: Pulls of the $R^{-1}_{K\pi\pi}$ parameter from the simultaneous fit to the resonant $B^+ \to K^+\pi^+\pi^- J/\psi\,(\to \ell^+\ell^-)$ and rare $B^+ \to K^+\pi^+\pi^-\ell^+\ell^-$ decays.

4.7 Cross-checks

Since the analysis is performed by blinding the efficiencies of the rare modes, cross-checks are needed to validate the analysis procedure before unblinding the final result. The cross-checks described in this section are useful to test the correctness of the efficiencies computation, that relies on the reweighting procedure described in Section 4.4, and of the yields estimation, extracted from the fit to the reconstructed B^+ invariant mass described in Section 4.6.1.

The first cross-check is performed by computing the ratio of the branching fractions of the resonant J/ψ decay modes, with electrons and muons in the final state. This quantity, usually referred to as $r_{J/\psi}$, is supposed to be equal to one and independent on the event kinematics, as J/ψ decays satisfy lepton universality [10].

Additionally, a double ratio between the branching fractions of the J/ψ and $\psi(2S)$ decays into muons and electrons is evaluated, usually referred to as $R_{\psi(2S)}$. With the $R_{\psi(2S)}$ cross-check it is possible to validate the robustness of the double ratio structure, which leads to the cancellation of most of the systematic effects due to differences in lepton reconstruction in the LHCb detector (Section 3.2.2).

4.7.1 $r_{J/\psi}$

In order to test that all the differences due to the electron and muon reconstruction processes are under control, the ratio $r_{J/\psi}$ is evaluated for each data taking period and trigger category as

$$\begin{aligned} r_{J/\psi} &\equiv \frac{\mathscr{B}\left(B^+ \to K^+\pi^+\pi^- J/\psi\,(\to \mu^+\mu^-)\right)}{\mathscr{B}\left(B^+ \to K^+\pi^+\pi^- J/\psi\,(\to e^+e^-)\right)} \\ &= \underbrace{\frac{\mathscr{N}\left(B^+ \to K^+\pi^+\pi^- J/\psi\,(\to \mu^+\mu^-)\right)}{\mathscr{N}\left(B^+ \to K^+\pi^+\pi^- J/\psi\,(\to e^+e^-)\right)}}_{r_{\text{yields}}} \times \frac{\varepsilon\left(B^+ \to K^+\pi^+\pi^- J/\psi\,(\to e^+e^-)\right)}{\varepsilon\left(B^+ \to K^+\pi^+\pi^- J/\psi\,(\to \mu^+\mu^-)\right)}, \end{aligned} \tag{4.27}$$

which is known to be equal to 1 with a precision of less than 1% [10].

In the above expression, the ratio of the yields r_{yields} is extracted directly as a parameter from a simultaneous fit to $B^+ \to K^+\pi^+\pi^- J/\psi\,(\to \mu^+\mu^-)$ and $B^+ \to K^+\pi^+\pi^- J/\psi\,(\to e^+e^-)$ decay modes as described in Section 4.6.1 (where the measured r_{yields} values are shown in Table 4.15). The efficiencies ε of the two decay modes are calculated as described in Section 4.5, by applying to the simulated samples all the correction steps detailed in Section 4.4.

The trend of the measured $r_{J/\psi}$ values, with respect to the MC correction step considered when computing the efficiencies, is shown in Figure 4.46. In the same figure the values of $r_{J/\psi}$ obtained when using a different control channel for the MC corrections are also shown. As alternatives to the nominal correction chain with $B^+ \to K^+\pi^+\pi^- J/\psi\,(\to \ell^+\ell^-)$ decays, another one using the higher yield channels $B^+ \to K^+ J/\psi(\to \ell^+\ell^-)$ and $B^0 \to K^{*0} J/\psi(\to \ell^+\ell^-)$ is considered. The $r_{J/\psi}$ values obtained using the three different set of weights calculated from

Table 4.20: Values of $r_{J/\psi}$ for all the different data-taking periods and trigger categories, with and without the correction steps described in Section 4.4 (PID, phase-space, kinematical and multiplicity, trigger, reconstruction and q^2 smearing corrections) being applied to the simulated sample. The quoted uncertainties include the statistical uncertainty and the systematic uncertainty due to the finite size of the simulated samples.

Period - Trigger	$r_{J/\psi}$ - Uncorrected	$r_{J/\psi}$ - Corrected
Run1 TOS	1.123 ± 0.028	1.052 ± 0.058
Run1 TIS	1.017 ± 0.031	1.104 ± 0.083
Run2p1 TOS	1.200 ± 0.021	1.077 ± 0.044
Run2p1 TIS	1.060 ± 0.022	1.049 ± 0.038
Run2p2 TOS	1.136 ± 0.013	0.973 ± 0.025
Run2p2 TIS	1.023 ± 0.015	1.003 ± 0.029

the alternative correction chains are found to be in very good agreement with each other for all the data taking periods and trigger categories, further validating the correctness of the reweighting procedure.

A summary of the measured $r_{J/\psi}$ values can be found in Table 4.20. The quoted uncertainties include the statistical as well as the systematic uncertainty related to the finite size of the simulated samples. This systematic uncertainty is evaluated with the bootstrapping method, which consists in recomputing the event selection efficiencies using 100 different datasets. In practical terms, this is achieved by assigning to each simulated event a weight, sampled from a Poisson distribution with unitary mean. This procedure is repeated 100 times leading to the generation of 100 different simulated datasets. All the corrections to the simulation (Section 4.4) are then recalculated using these 100 alternative samples and, finally, each of the 100 sets of weights is used to calculate the efficiencies. The average of the differences between the nominal efficiency and the ones computed on the bootstrapped samples is taken as systematic uncertainty.

From Figure 4.46 and Table 4.20 the effect of the reweighting procedure is clearly appreciable, where the $r_{J/\psi}$ values computed at the end of the correction chain are found to be compatible with unity within two standard deviations for all the data-taking periods and trigger categories considered.

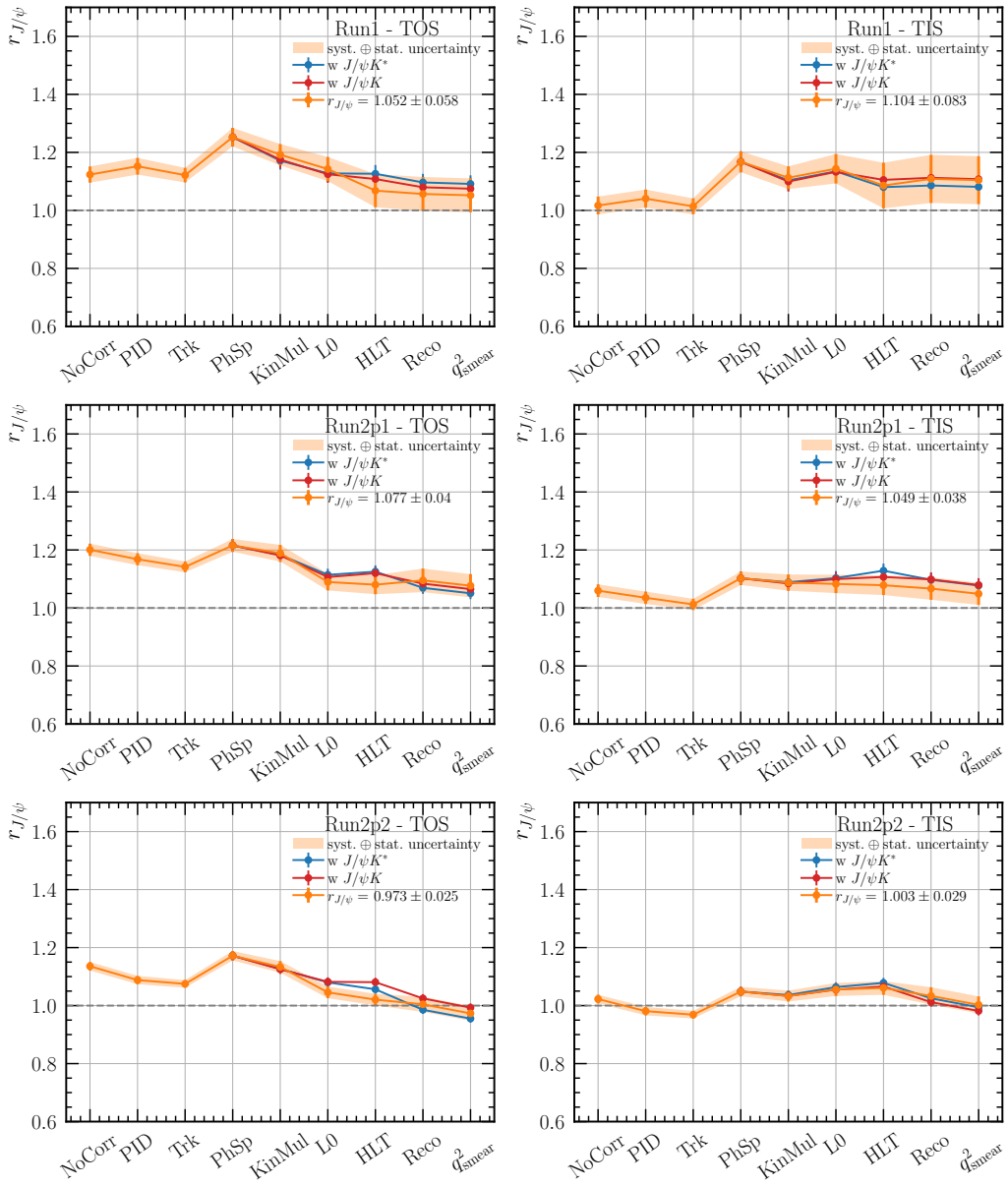

Figure 4.46: Values of the $r_{J/\psi}$ ratio with respect to the incremental correction step applied to the simulated samples for `Run1` (top), `Run2p1` (centre), `Run2p2` (bottom), for the TOS (left) and TIS (right) trigger categories. The uncertainties shown include the statistical uncertainty and the systematic uncertainty due to the finite size of the simulated samples. The different colours show the $r_{J/\psi}$ values when the efficiencies are computed using the nominal simulation weights (orange), the weights extracted from $B^+ \to K^+ J/\psi(\to \ell^+\ell^-)$ decays (red) and the weights extracted from $B^0 \to K^{*0} J/\psi(\to \ell^+\ell^-)$ decays (blue).

4.7.2 $r_{\psi(2S)}$ and $R_{\psi(2S)}$

In order to cross-check the analysis procedure, the resonant $B^+ \to K^+\pi^+\pi^-\psi(2S)(\to \ell^+\ell^-)$ mode is exploited too. In fact, since the $\psi(2S)$ meson, like the J/ψ, verifies lepton flavour universality to a precision of $\approx 10\%$ [10], one can study (as already done for $r_{J/\psi}$) the ratio:

$$\begin{aligned} r_{\psi(2S)} &\equiv \frac{\mathscr{B}\left(B^+ \to K^+\pi^+\pi^-\psi(2S)(\to \mu^+\mu^-)\right)}{\mathscr{B}\left(B^+ \to K^+\pi^+\pi^-\psi(2S)(\to e^+e^-)\right)} \\ &= \frac{\mathscr{N}\left(B^+ \to K^+\pi^+\pi^-\psi(2S)(\to \mu^+\mu^-)\right)}{\mathscr{N}\left(B^+ \to K^+\pi^+\pi^-\psi(2S)(\to e^+e^-)\right)} \times \frac{\varepsilon\left(B^+ \to K^+\pi^+\pi^-\psi(2S)(\to e^+e^-)\right)}{\varepsilon\left(B^+ \to K^+\pi^+\pi^-\psi(2S)(\to \mu^+\mu^-)\right)} \equiv 1. \end{aligned} \tag{4.28}$$

Furthermore, the $\psi(2S)$ resonant modes can be used, combined with the J/ψ modes, in the validation of the double ratio procedure, by studying the quantity:

$$\begin{aligned} R_{\psi(2S)} &\equiv \frac{\mathscr{B}\left(B^+ \to K^+\pi^+\pi^-\psi(2S)(\to \mu^+\mu^-)\right)}{\mathscr{B}\left(B^+ \to K^+\pi^+\pi^- J/\psi\,(\to \mu^+\mu^-)\right)} \cdot \frac{\mathscr{B}\left(B^+ \to K^+\pi^+\pi^- J/\psi\,(\to e^+e^-)\right)}{\mathscr{B}\left(B^+ \to K^+\pi^+\pi^-\psi(2S)(\to e^+e^-)\right)} \\ &\equiv \underbrace{\frac{\mathscr{N}\left(B^+ \to K^+\pi^+\pi^-\psi(2S)(\to \mu^+\mu^-)\right)}{\mathscr{N}\left(B^+ \to K^+\pi^+\pi^-\psi(2S)(\to e^+e^-)\right)} \frac{\mathscr{N}\left(B^+ \to K^+\pi^+\pi^- J/\psi\,(\to e^+e^-)\right)}{\mathscr{N}\left(B^+ \to K^+\pi^+\pi^- J/\psi\,(\to \mu^+\mu^-)\right)}}_{R_{\text{yields}}} \\ &\times \frac{\varepsilon\left(B^+ \to K^+\pi^+\pi^-\psi(2S)(\to e^+e^-)\right)}{\varepsilon\left(B^+ \to K^+\pi^+\pi^-\psi(2S)(\to \mu^+\mu^-)\right)} \frac{\varepsilon\left(B^+ \to K^+\pi^+\pi^- J/\psi\,(\to \mu^+\mu^-)\right)}{\varepsilon\left(B^+ \to K^+\pi^+\pi^- J/\psi\,(\to e^+e^-)\right)} \equiv 1. \end{aligned} \tag{4.29}$$

Verifying that the $R_{\psi(2S)}$ value is equal to unity and independent from the corrections applied to the simulated samples is a good check of the robustness of the double ratio strategy.

The $R_{\psi(2S)}$ quantity can be seen as the product of the double ratio of the yields of the four resonant modes involved R_{yields} and the double ratio of the efficiencies. R_{yields} is measured directly as a parameter from simultaneous fits to the $B^+ \to K^+\pi^+\pi^- J/\psi\,(\to \ell^+\ell^-)$ and $B^+ \to K^+\pi^+\pi^-\psi(2S)(\to \ell^+\ell^-)$ decays modes, as described in Section 4.6.1, where the observed R_{yields} are shown in Table 4.16. The efficiency of each decay mode is computed as explained in Section 4.5, for each step of the correction procedure detailed in Section 4.4.

The values of both the single $r_{\psi(2S)}$ and the double $R_{\psi(2S)}$ ratios, with respect to the correction step applied to the simulated samples, are shown in Figure 4.47. The measured values of the $r_{\psi(2S)}$ and $R_{\psi(2S)}$ ratios are summarised in Table 4.21. As expected, the $R_{\psi(2S)}$ trend is found to be reasonably flat with respect to the correction steps applied to the simulation, while the effect of the reweighting procedure are much more visible on the single $r_{\psi(2S)}$ ratio. In both cases, the final values are found to be compatible with unity within two standard deviations for all the trigger categories and data taking periods. The quoted uncertainties include the statistical as well as systematic uncertainties, related to the finite size of the simulated samples used, evaluated with the bootstrapping method, as already described in Section 4.7.1.

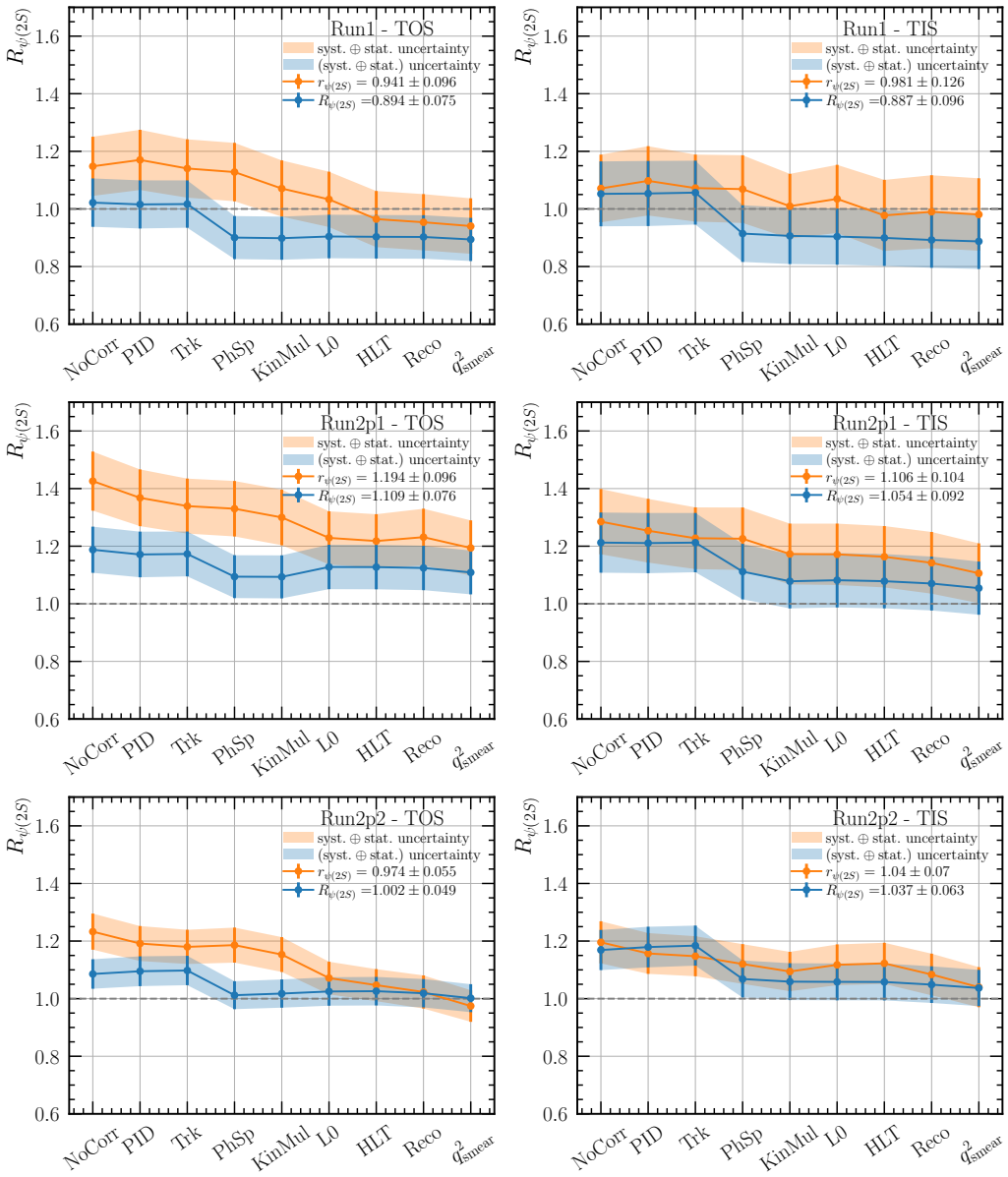

Figure 4.47: Values of the single $r_{\psi(2S)}$ (orange) and the double $R_{\psi(2S)}$ (blue) ratios with respect to the different correction steps applied to simulated samples for `Run1` (top), `Run2p1` (center), `Run2p2` (bottom), for TOS (left) and TIS (right) trigger categories. The quoted uncertainties include the statistical uncertainty and the systematic uncertainty due to the finite size of the simulation.

Table 4.21: Values of the single $r_{\psi(2S)}$ (top) and double $R_{\psi(2S)}$ ratios for `Run1`, `Run2p1` and `Run2p2` and for different trigger categories, with and without the correction weights (PID, phase-space, kinematics and multiplicity, trigger, reconstruction and q^2 smearing corrections) being applied to the simulated sample. The quoted uncertainties include the statistical uncertainty and the systematic uncertainty due to the finite size of the simulated samples.

Period - Trigger	$r_{\psi(2S)}$ - Uncorrected	$r_{\psi(2S)}$ - Corrected
Run1 TOS	1.15 ± 0.10	0.94 ± 0.10
Run1 TIS	1.07 ± 0.12	0.98 ± 0.13
Run2p1 TOS	1.42 ± 0.10	1.19 ± 0.10
Run2p1 TIS	1.28 ± 0.11	1.11 ± 0.10
Run2p2 TOS	1.14 ± 0.01	0.97 ± 0.02
Run2p2 TIS	1.23 ± 0.06	0.97 ± 0.05
	$R_{\psi(2S)}$ - Uncorrected	$R_{\psi(2S)}$ - Corrected
Run1 TOS	1.02 ± 0.08	0.89 ± 0.07
Run1 TIS	1.05 ± 0.11	0.89 ± 0.10
Run2p1 TOS	1.18 ± 0.08	1.10 ± 0.08
Run2p1 TIS	1.21 ± 0.10	1.05 ± 0.09
Run2p2 TOS	1.09 ± 0.05	1.00 ± 0.05
Run2p2 TIS	1.17 ± 0.07	1.04 ± 0.06

4.8 Systematic uncertainties

This section presents the systematic uncertainties associated to the $R^{-1}_{K\pi\pi}$ measurement, *i.e.* errors that do not scale in a Poisson sense with the amount of data available. Several sources of systematic uncertainty are identified, summarised in Table 4.22, which are described in detail in the following sections.

The systematic uncertainties can be mainly divided in two groups. The first one is related to the process of reweighting the simulated samples, *i.e.* possible differences not accounted for between the control and signal modes or electron and muon modes (see Section 4.4), which would lead to systematic inaccuracies in the efficiency computation. The second group is related to the strategy used to fit the reconstructed B^+ invariant mass, such as the definitions of the line shape models used for the various datasets, background estimations *etc.*, which would thus impact the measurement of the yields.

It is worth to stress that, given the low yield of the rare $B^+ \to K^+\pi^+\pi^-\ell^+\ell^-$ modes, the systematic uncertainties are expected to play a minor role with respect to the statistical one on the final $R^{-1}_{K\pi\pi}$ measurement.

4.8.1 Systematic uncertainties associated to the fit model

In this section the systematic effects that could arise from the arbitrary choice of a given model to fit the line shape of the B^+ invariant mass (Section 4.6) are described. In general, such systematics are evaluated by generating 500 pseudoexperiments from the nominal fit model used for the data samples by letting the signal and background yields fluctuate following a Poisson distribution around the fitted values, according to the fit error. The pseudoexperiments, also called *toys*, are then fitted both with the nominal model and with an alternative one, which is constructed depending on the systematic effect to be evaluated. The difference in the $R^{-1}_{K\pi\pi}$ estimation is computed for each toy i: $\Delta_i = y_i^{\text{nom}} - y_i^{\text{alt}}$, and the average of the Δ_i over all the pseudoexperiments is retained as a systematic uncertainty.

Bias in the signal yield

To test the absence of bias in the models used to extract the $R^{-1}_{K\pi\pi}$ parameter (described in Section 4.6.2), pseudoexperiments were generated and the $R^{-1}_{K\pi\pi}$ pulls values computed, as shown in Section 4.6.3. As already introduced, the pulls are expected to be normally distributed around zero, with unit standard deviation, where residual shifts from these values would indicate a bias in the parameter estimation. For the $R^{-1}_{K\pi\pi}$ case, for which the pulls have already been shown in Figure 4.45, a shift of 3% of the pulls mean value is observed, which, given the relative uncertainty of 12% on the $R^{-1}_{K\pi\pi}$ parameter, leads to a systematic uncertainty of $\sim 0.4\%$. In Table 4.22 this systematic uncertainty is indicated as *Fit bias in* $R^{-1}_{K\pi\pi}$.

Signal shape parameters fixed from simulation

In all the fits to the $m(K^+\pi^+\pi^-\ell^+\ell^-)$ distribution in data, the shape parameters of the signal component are fixed from the line shape obtained in the respective fits to simulated samples. Systematic uncertainty due to possible data/simulation differences in the signal line shape is thus evaluated by fitting the pseudoexperiments, generated from the nominal fit model, both with the nominal model and an alternative one, which is constructed by poissonianly fluctuating the signal shape parameters around their nominal fitted values in simulation, taking into account their fit errors and correlations. The average difference between the $R^{-1}_{K\pi\pi}$ values obtained when using the nominal or the alternative signal shape parameters when fitting the toys, found to be $\sim 0.5\%$, is taken as systematic uncertainty.

Signal mean shift and resolution scale parameters fixed from resonant modes

When fitting the signal component in collision data, a mean shift parameter and a resolution scale parameter are allowed, with respect to the values fitted in simulated samples, to account for possible data/simulation differences. In the fits to the signal modes, these values are fixed from fits to the unconstrained B^+ invariant mass in resonant decay modes. Systematic uncertainty due to this choice has not been evaluated yet. The plan is to generate pseudoexperiments and let the μ^{shift} and the σ^{scale} parameters fluctuate around their nominal values every time a toy dataset is fitted. The average difference between the $R^{-1}_{K\pi\pi}$ values obtained when fitting the toy datasets with the nominal and the alternative model will be taken as systematic uncertainty.

Modelling of the partially reconstructed background

The background coming from partially reconstructed B decays is the most challenging to model, due to the different branching ratios and peaking values of the decays that can pollute such a multi-body channel. The data-driven strategy developed in this analysis, described in Section 4.6.2, aims at extracting information on the PR from the resonant modes, like the line shape parameters and the relative amount of PR events with respect to signal events. However, this strategy heavily relies on the assumption to have a similar PR contribution in the rare and in the resonant decay modes. Unaccounted effects arising from possible differences between these decay modes are taken as systematic uncertainties, and they are estimated as described below.

- **PR line shape model.** The nominal fit model used for the PR line shape is a convolution between an Argus and a Gaussian function. An alternative model is studied in order to evaluate the systematic uncertainty due to this choice, which is a kernel density estimator function (implemented by the `RooKDE` ROOT class [92]). The average difference in the fitted $R^{-1}_{K\pi\pi}$ parameter, when fitting the toys with the nominal and the alternative model is found to be $\sim 0.3\%$, and it is taken as systematic uncertainty.

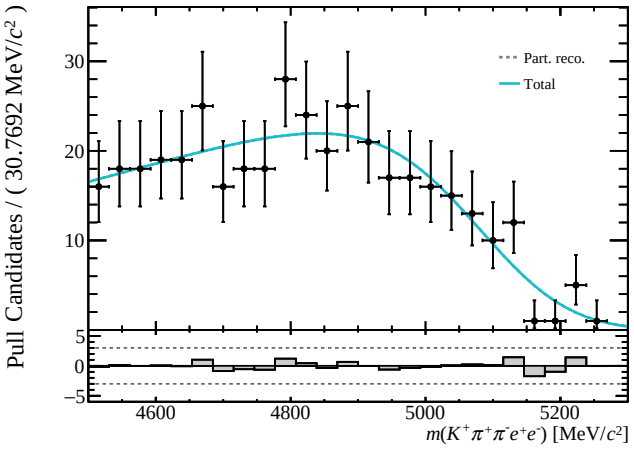

Figure 4.48: Fit to the reconstructed $m(K\pi\pi ee)$ invariant mass for $B \to K\pi\pi\pi ee$ events.

- **PR line shape extraction.** The nominal parameters of the PR line shape, discussed in the previous point, are fixed from fits to the unconstrained B^+ invariant mass in resonant decays (example in Figure 4.42, left panel). As an alternative, it was considered to fix them from fitting a sample of 1M simulated $B \to K\pi\pi\pi ee$ events, in 2017 data taking condition. Given its limited size, a selection looser than the one used for the signal mode is applied to this sample, *i.e.* only the preselection and the BDT > 0.4 requirement (Section 4.3). The selected events are then fitted with the usual convolution between an Argus and a Gaussian function. The PR shape parameters extracted from this fit, shown in Figure 4.48, are: $\sigma^{\rm PR} = 99 \pm 98$, $c^{\rm PR} = -5.2 \pm 2.0$ and $m_0^{\rm PR} = 5115 \pm 37$, to be compared with the nominal PR line shape parameters shown in Table 4.17. The average of the differences in the $R^{-1}_{K\pi\pi}$ estimations when fitting the toys with the nominal and the alternative PR shape from $B^+ \to K\pi\pi\pi ee$ events is found to be 1.7%, and it is taken as a systematic uncertainty.
- **PR scale parameter $s^{\rm PR}$.** In the fit to the signal decay modes the ratio between PR yield and signal yield is constrained to lie in a Gaussian with a mean equal to the same value as fitted in the resonant decay modes, and a standard deviation equal to 20% of this value. Possible systematic uncertainties can thus arise from the mean and the width chosen for the constraint. These systematics are assessed by fitting the pseudoexperiment, generated from the nominal fitted PR yield, either with a larger width for the constraint (σ = 50%) or with an increased mean value of the constraint (μ = 0.44). The latter value chosen is the largest $s^{\rm PR}$ observed among all fitted subsamples used to extract the $s^{\rm PR}$ parameter from the resonant decay mode, with the fits repeated using both the constrained and unconstrained B^+ invariant masses. The systematics due to the mean and the width of the $s^{\rm PR}$ constraint are found to be 1.9% and 0.1% respectively, again taken as the average difference between the $R^{-1}_{K\pi\pi}$ estimates when fitting the toys with the nominal and the alternative mean and width values of the constraint.

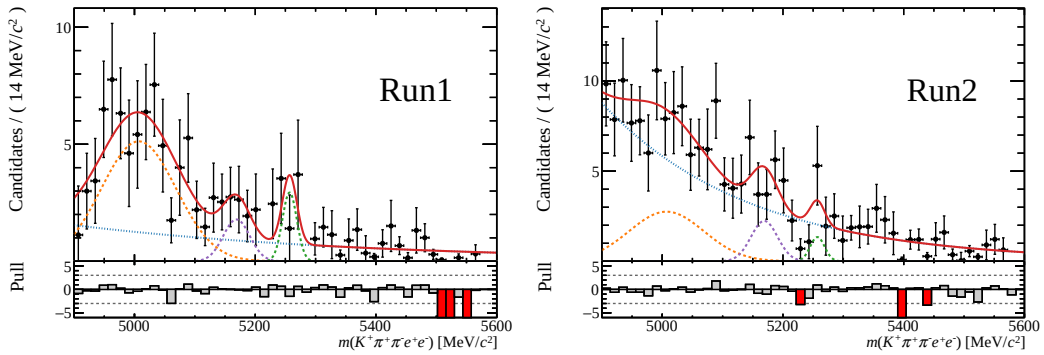

Figure 4.49: Alternative empirical models for the $h \to e$ misID line-shapes used to estimate the systematic uncertainties due to the KDE shapes used in the nominal fit model (shown in Figure 4.13).

Residual $h_{\to e}$ misidentified backgrounds

The background contribution due to hadrons being misidentified as electrons is included in the nominal fit model by fixing its amount and shape to the estimations from the PassFail method, explained in Section 4.3.4. The nominal shape for this contribution is a kernel density estimator (KDE) function, as shown in Figure 4.13. The systematic uncertainties due to this choice are studied by using an alternative empirical shape consisting of three Gaussian functions, as shown in Figure 4.49. The systematic uncertainty is then evaluated by fitting 500 pseudoexperiments, generated from the nominal fitted values and distributions, with this alternative model. The average difference between the $R^{-1}_{K\pi\pi}$ values obtained using the nominal and the alternative model is taken as systematic uncertainty. In the same way, the systematic uncertainty arising from fixing the yield of this contribution is studied, by fitting the pseudo-experiments with a Gaussian constraint on the misidentification yield, with the mean and the resolution of the constraints being the amounts and errors estimated by the PassFail method.

Modelling of combinatorial background

The systematics due to the choice of using an exponential function to model the background coming from random combination of tracks has not been estimated yet. The plan is to assess this systematics by using $B \to KKK\ell\ell$ samples with the two electrons having the same charge, and where two opposite-charged kaons can be considered as misreconstructed pions in order to match the signal channels. The use of those samples is made necessary by the fact that the simple use of an alternative model (*e.g.* a Chebychev polynomial implemented by the `RooChebychev` ROOT class [92]) was found to be not reliable in the estimation of the fitted yields, resulting in unphysical shapes. The systematics will be evaluated using the shape obtained from $B^+ \to K^+K^+K^-\ell^+\ell^-$ events passing the signal selection, as alternative model to fit pseudoexperiments.

Fixing the J/ψ leakage component

The systematics due to the choice of fixing the yield of $B^+ \to K^+\pi^+\pi^- J/\psi\,(\to e^+e^-)$ leaking into the signal region will be estimated by imposing a Gaussian constraint on this yield. The systematics will be evaluated again by generating toy datasets using the fixed J/ψ leakage values, which will then be fitted by fixing or imposing a Gaussian constraint on the leakage component, taking the average difference of the obtained $R^{-1}_{K\pi\pi}$ values as systematic uncertainty.

4.8.2 Systematic uncertainties related to the calculation of the efficiency

The systematic uncertainties that affect the efficiency computation mainly arise from the corrections steps applied to the simulated samples, described in Section 4.4. The systematic uncertainties derive in general from two sources:

- from the finite size of the control samples used in the correction procedure;
- from the choice of the correction strategy (*e.g.* binning scheme or training variables in the `GBR`).

In Section 4.7.1 the bootstrapping method has been introduced (*i.e.* generate 100 datasets by assigning random Poissonian weights to each simulated event), which already addresses the first point, since the systematic uncertainty can be computed as the average of the differences between the nominal efficiency and the one computed on bootstrapped samples. Thus, the following sections will focus on the methods to estimate the main systematic effects due to the correction strategy.

PID resampling

The PID response of the detector is corrected in simulated samples by resampling the PID distributions from calibration samples using kernel density estimator functions, as described in Section 4.4.2. The possible sources of systematic uncertainty in this approach are the limited size of the calibration samples and the width of the kernel used to describe the PID distributions. The two sources are addressed as follows.

- To evaluate the effect of the finite size of the calibration samples on the PID correction procedure, the bootstrapping method is applied. PID corrections are computed for each set of Poisson weights, and the selection efficiency is computed for each set of the resulting PID corrections. The average difference between the nominal double ratio of the efficiencies of the resonant and the rare modes and the double ratio of the efficiencies computed with the bootstrapped corrections is taken as systematic uncertainty.
- During the PID resampling, multi-dimensional PID distributions are used, both in data and simulation, described with a kernel-based model. The systematic uncertainty

due to this parameterisation is evaluated by increasing the width of the kernel by 50%, creating new transformed PID variables and comparing the obtained double ratio of the efficiencies of the resonant and rare modes to the nominal one.

Both systematic uncertainties are found to be ∼ 5%.

Phase-space reweighting

The novel data-driven approach used to correct the underlying dynamics of the multibody phase space of $B^+ \to K^+\pi^+\pi^-\ell^+\ell^-$ decays has a number of caveats that need to be investigated as possible sources of systematic uncertainty. First, as described in Section 4.4.3, the methodology relies on the ability to describe the key aspects of these decays in terms of the hadronic system, *e.g.* using only $m(K^+\pi^-)$, $m(\pi^+\pi^-)$ and $m(K^+\pi^+\pi^-)$ as training variables for the GBR, thus ignoring any angular dependence. The impact on the efficiency of not including angular variables in the correction procedure is investigated by recalculating the phase-space corrections adding either only $\cos\theta_L$ or all three angles $\cos\theta_L$, $\cos\theta_K$ and $\cos\theta_V$ (refer to Figure 4.25 for the definition of the angles). Then the double ratio of the efficiencies of the resonant and the rare modes, entering the $R^{-1}_{K\pi\pi}$ definition in Eq. 4.2, can be compared between the nominal correction and the variants including more angular information. The results are shown in the top panels of Figure 4.50.

In addition, the reweighting of the hadronic system is determined using data and simulation samples of $B^+ \to K^+\pi^+\pi^- J/\psi\,(\to \mu^+\mu^-)$ decays and the findings are then applied also to the simulated samples of the rare $B^+ \to K^+\pi^+\pi^-\ell^+\ell^-$ modes, selected in a different q^2 region. The systematic uncertainty due to this change of the q^2 region is estimated by retraining the phase-space correction procedure using a specific decay chain with an even lower q^2 than the signal modes. The chosen decay is $B \to (X \to K\pi\pi)\,\gamma$, which is thus used as an alternative dataset in the GBR training to compute the phase-space weights. Also here, the systematic uncertainty can be evaluated as the difference in double ratio of the efficiencies when using the nominal correction chain or the $K\pi\pi\gamma$ variant. The results are shown in the bottom panel of Figure 4.50.

The total systematic uncertainty is estimated using the maximum relative difference of the double ratio of the efficiencies found with the three correction variants explained above. The systematic uncertainty is thus found to be 6%, driven by the variant using the three decay angles.

Kinematics and multiplicity corrections

The B kinematics and multiplicity distributions in simulated samples are reweighted through a gradient booster reweighter, trained on $B^+ \to K^+\pi^+\pi^- J/\psi\,(\to \mu^+\mu^-)$ control samples (Section 4.4.5). The planned systematics to be assessed for this correction are related to the type of selection applied to the control sample and to the choice of multiplicity variable used in the

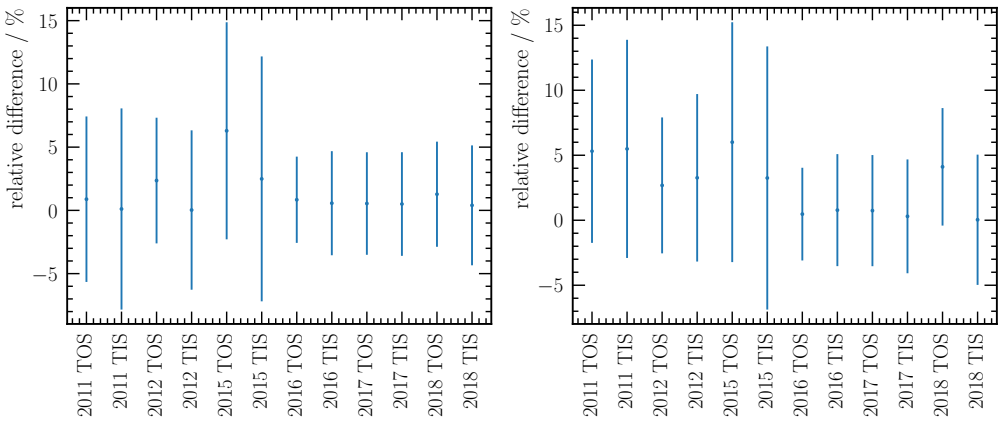

(a) $\cos\theta_L$

(b) $\cos\theta_L$, $\cos\theta_K$ and $\cos\theta_V$

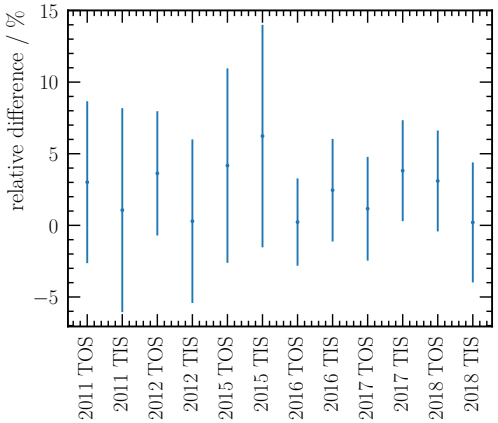

(c) $B^+ \to K^+\pi^+\pi^-\gamma$

Figure 4.50: Relative differences in double ratio of efficiencies of the rare $B^+ \to K^+\pi^+\pi^-\ell^+\ell^-$ and resonant $B^+ \to K^+\pi^+\pi^- J/\psi\,(\to \ell^+\ell^-)$ modes, with $\ell = e, \mu$, when computed on simulated samples with the nominal reweighting process applied and alternative corrections of the hadronic system. Top left: differences when adding $\cos\theta_L$ in the training of the GBR. Top right: differences when adding all the $\cos\theta_L$, $\cos\theta_K$ and $\cos\theta_V$ angles describing the $B^+ \to K^+\pi^+\pi^-\ell^+\ell^-$ decays. Bottom: differences when using $B^+ \to K^+\pi^+\pi^-\gamma$, instead of $B^+ \to K^+\pi^+\pi^- J/\psi\,(\to \mu^+\mu^-)$ decays, as control channel. The errors shown are only statistical, thus relative to the size of the simulated samples used to compute the efficiencies.

training process, as explained in the following.

- The nominal method used to correct the generation of the pp underlying event in simulated samples makes use of the $B^+ \to K^+\pi^+\pi^- J/\psi\,(\to \mu^+\mu^-)$ decay mode, selected with the `L0Muon` inclusive trigger. Such weights are then applied also to the electrons, assuming such generator-level corrections can be ported between electron and muon modes. Recomputing the corrections by training the GBR with $B^+ \to K^+\pi^+\pi^- J/\psi\,(\to \mu^+\mu^-)$ samples selected according to the nominal `TIS` trigger selection (which, by definition, is the same for electron and muon modes), can further validate this assumption. In order to assess the different outcome of the two methods, given the large overlap between the `TIS` sample and the inclusive `L0Muon` sample, a bootstrapping method is used. The GBR reweighter is trained on the nominal and the bootstrapped samples 100 times, one for each set of poissonian weights. The average difference between the computed double ratio of efficiencies using the bootstrapped weights and the nominal weights will be taken as systematics uncertainty.
- To correct the multiplicity distribution, the number of tracks in the event is used as a feature of the GBR reweighter. In order to assess the systematic uncertainties due to this choice, an alternative variable is chosen, *i.e.* the number of tracks reconstructed in the VELO detector. Also in this case, the nominal and the alternative reweighters are trained over the 100 bootstrapped datasets, and the average difference between the double ratio of efficiencies computed with the two reweighters will be taken as systematic uncertainty.

L0 trigger corrections

L0 efficiency maps are computed on resonant samples with a tag-and-probe approach, in order to reweight the L0 response of the detector in simulation (Section 4.4.6). The plan to estimate the systematic uncertainties due to this approach is described in the following.

- The data and simulation L0 efficiencies are calculated in iso-populated bins of kinematical variables, depending on the type of L0 response considered ($p_{\mathrm{T}}(B^+)$ and `nTracks` for `TIS`, $\max(E_{\mathrm{T}})(e^{\pm})$ –and the calorimeter region– for `ETOS` and $p_{\mathrm{T}}(\mu^{\pm})$ for `MTOS`). To evaluate the systematic uncertainty due to this choice, the trigger corrections are recalculated with a different method, by fitting the trigger turn-on curve. This curve consist of the efficiency of each trigger selection computed as a function of the same kinematical variables used in the binning strategy. The functional form used to fit the turn-on curves is a combination of an error function and a Gompertz function:

$$f(x) = f_1\left(1 + \mathrm{erf}\left(\frac{x-t}{\sqrt{2}\sigma_1}\right)\right) + f_2 s^{\exp\left(-\frac{x-t}{\sqrt{2}\sigma_2}\right)} + a, \tag{4.30}$$

  where f_1 and f_2 are the relative normalisations of the two folded functions, σ_1 and σ_2 their resolutions, t is the common threshold, s is the Gompertz skewness and a is a

constant offset. This model addresses the fact that the error function is symmetrical around the threshold, while the transition in data generally appears softer on the right-hand side of the distribution. The associated systematic uncertainty will be evaluated by taking the average of the difference between the double ratio of the efficiencies calculated with the two methods (with weights coming from the binned approach or from fitting the turn-on curve) for the 100 sets of bootstrapped weights.

- In the nominal method the efficiencies of the ETOS selection are computed considering only the electron with the largest energy deposit in the calorimeter, and using the corresponding L0ElectronTOS decision as probe. An alternative strategy can be implemented to assess the systematic uncertainties due to this choice. One can in fact use the logical OR of the L0ElectronTOS decisions of the two electrons instead, and compute the difference between the trigger efficiencies calculated with the two methods, for each bootstrapped sample.

Smearing corrections

The dielectron pair mass resolution is generally better in simulation than it is in data. This difference is corrected for by modifying the $m(ee)$ distribution, using parameters estimated from fits to the resonant samples, as described in detail in Section 4.4.8. The corrected $m(ee)$ is then used to compute the efficiency of the q^2 requirement. Systematic uncertainties that can arise from such a strategy derive from the choice of line shape used in these fits, and from averaging the smearing parameters between the TIS and TOS categories. How these effects will be assessed is described in the following.

- The fits to the resonant data samples in the different Bremsstrahlung categories use a double Crystal-Ball as nominal line shape. As an alternative, an Hypatia function is tested. The difference in the double ratio of efficiencies will be taken as systematic uncertainty.
- The systematic uncertainty arising from averaging the smearing parameters among the TIS and TOS samples can be assessed by keeping the parameters separated and recomputing the efficiencies separately for the two trigger categories, for each bootstrapped sample. The average difference in the double ratio of efficiencies computed in these two ways will be taken as systematic uncertainty.

Flatness of $r_{J/\psi}$

Several event features play a role in the analysis strategy: for example, the trigger efficiency corrections are evaluated as a function of the B^+ transverse momentum; vertex-related variables are part of the set of features on which the multivariate classifier is trained; and so on. As a further sanity check the value of $r_{J/\psi}$ is verified to not depend on these variables, nor upon other kinematical observables. To do so, for each of the considered variables the data sets

are divided in $m = 5$ bins using an isoscalar approach, *i.e.* the bin edges are defined so that a similar amount of events falls in each bin. The binning is defined on fully selected electron data samples, which suffer more from limited event yield than the muon ones.

For each bin of a given variable, the fit strategy is the same as the one discussed in Section 4.6.1, *i.e.* extract the r_{yields} from a simultaneous fit to $B^+ \to K^+\pi^+\pi^- J/\psi\,(\to e^+e^-)$ and $B^+ \to K^+\pi^+\pi^- J/\psi\,(\to \mu^+\mu^-)$ events, where this time the events are additionally required to fall in the considered bin. The efficiencies are computed using the full set of corrections from the reweighting procedure as in Section 4.5, but with the addition of the efficiency of the selection defined by the bin edges, *i.e.*

$$\varepsilon_{\text{bin}} = \varepsilon_{\ell\ell} \cdot \frac{\sum_{\text{bin}} w_{\text{phsp}} \cdot w_{\text{track}} \cdot w_{\text{kinmul}} \cdot w_{\text{L0*HLT}} \cdot w_{\text{reco}}}{\sum_{\text{full_range}} w_{\text{phsp}} \cdot w_{\text{track}} \cdot w_{\text{kinmul}} \cdot w_{\text{L0*HLT}} \cdot w_{\text{reco}}}, \tag{4.31}$$

where the sum in the numerator runs over all the event weights which lie in the selected variable bin and the sum in the denominator runs over the full range. The effect of the residual non-flatness of $r_{J/\psi}$ on the double ratio $R^{-1}_{K\pi\pi}$ is evaluated by computing a "flatness systematics" to add to the final measurement. Such systematic uncertainty is estimated by calculating a pseudo$R_{K\pi\pi}$ double ratio where the yields of the rare mode are replaced by efficiency-rescaled resonant yields:

$$r_{\text{flatness}} \equiv \frac{\sum_{i=1}^{m} \mathcal{N}^i_{K\pi\pi\mu\mu}}{\sum_{i=1}^{m} \mathcal{N}^i_{K\pi\pi ee}} \times \frac{\sum_{i=1}^{m} \varepsilon^i_{K\pi\pi ee}}{\sum_{i=1}^{m} \varepsilon^i_{K\pi\pi\mu\mu}} \times \frac{\sum_{i=1}^{m} N^i_{K\pi\pi J/\psi,ee}}{\sum_{i=1}^{m} N^i_{K\pi\pi J/\psi,\mu\mu}} \times \frac{\sum_{i=1}^{m} \varepsilon^i_{K\pi\pi J/\psi,\mu\mu}}{\sum_{i=1}^{m} \varepsilon^i_{K\pi\pi J/\psi,ee}}, \tag{4.32}$$

with the rescaled yields being

$$\mathcal{N}^i_{K\pi\pi\ell\ell} = \frac{\varepsilon^i_{K\pi\pi\ell\ell}}{\varepsilon^i_{K\pi\pi J/\psi,\ell\ell}} \times N^i_{K\pi\pi J/\psi,\ell\ell}. \tag{4.33}$$

Since $J/\psi \to \ell^+\ell^-$ decays satisfy LFU, r_{flatness} should be compatible with unity, if the rare mode efficiencies are well calibrated. Residual discrepancies are caught by the flatness systematics d_f defined as

$$d_f = r_{\text{flatness}} - 1. \tag{4.34}$$

The $r_{J/\psi}$ trends for some example variables are shown in Figure 4.51, while the flatness parameters computed for the full set of the variables considered, for the `Run2p2` data period and the TIS trigger category as an example, are shown in Figure 4.52.

The maximum of the quadratic sums of the flatness parameters among data taking periods and trigger categories is taken as systematic uncertainty, which is found to be 5% for the `Run1` TIS category, driven mainly by the angles between the several combinations of the final particles, or the DIRA between the $K^+\pi^+\pi^-$ system and the PV.

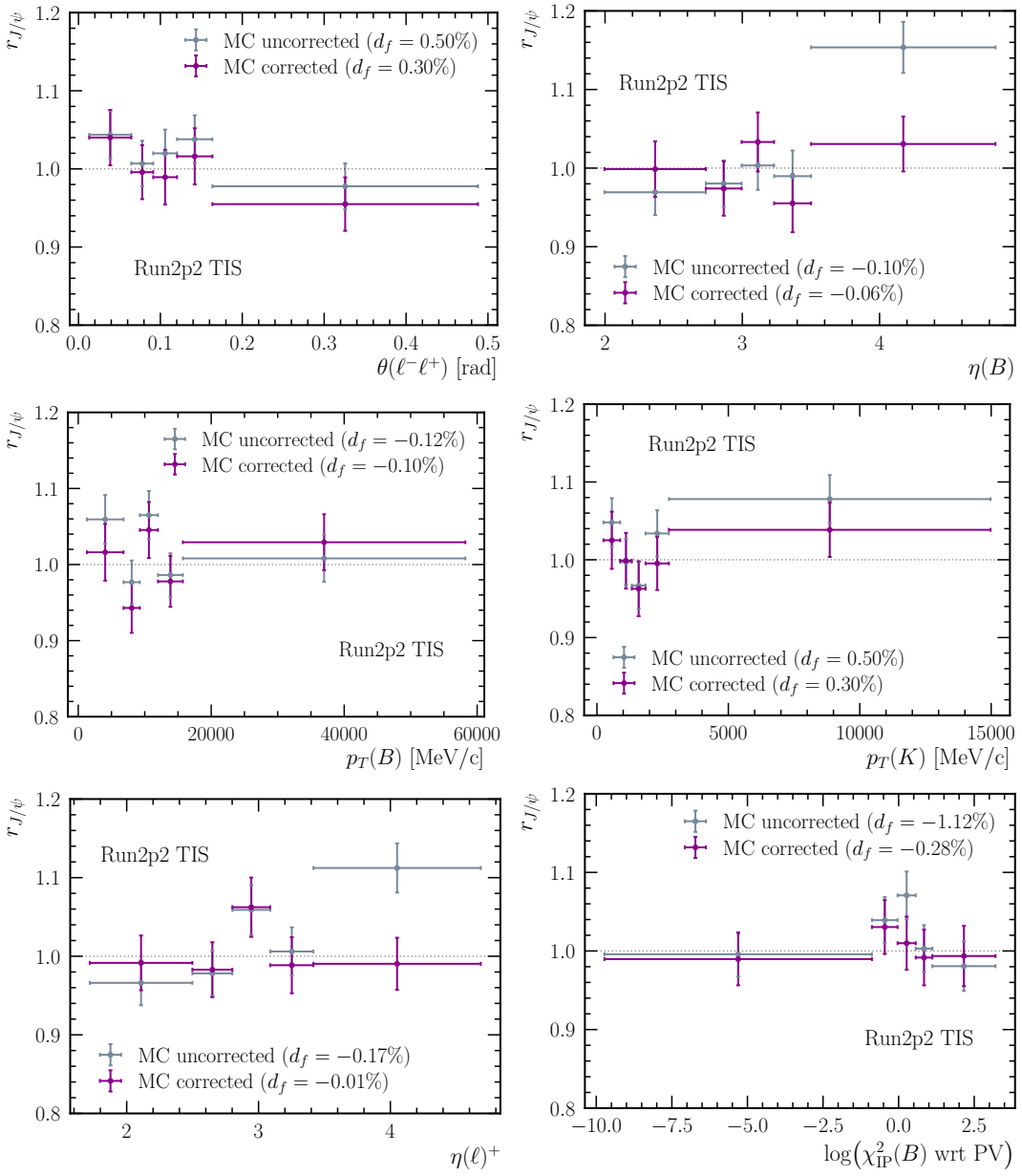

Figure 4.51: Examples of $r_{J/\psi}$ trends with respect to kinematic variables or variables related to the reconstructed process. The plots refer to data selected in the TIS trigger category for the Run2p2 data taking period. The value of $r_{J/\psi}$ for each bin, and of the integrated flatness parameter d_f, are shown both when using the original (uncorrected) or the reweighted (corrected) simulated samples in the efficiency computation.

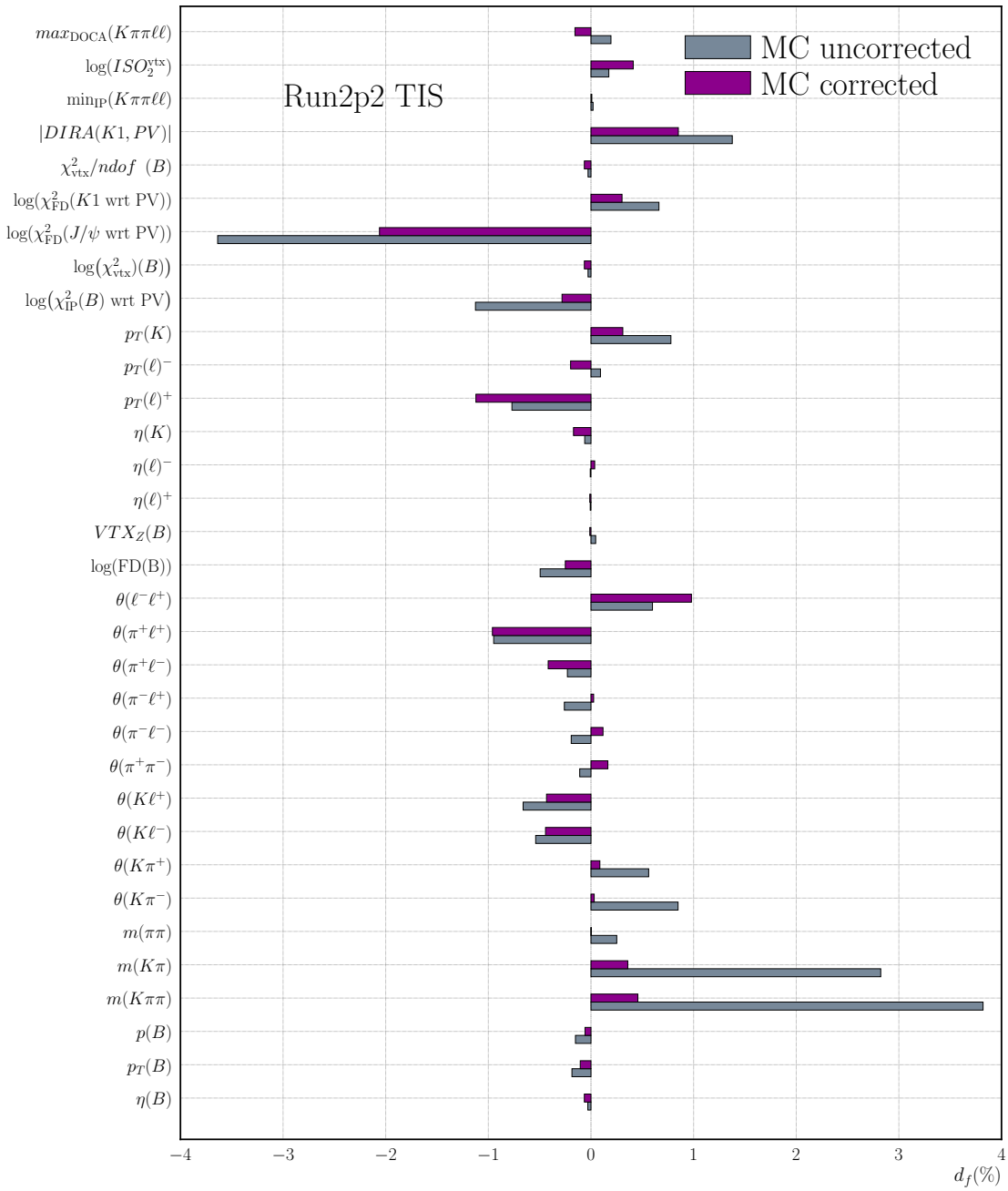

Figure 4.52: Flatness parameters computed for the full set of variables studied, with (purple) or without (gray) the reweighiting process being applied to the simulated samples. The values refer to data from the Run2p2 period and selected with the TIS category.

Table 4.22: Summary of the systematic uncertainties discussed in the section. The systematic uncertainties which have not been yet estimated are indicated as TBE.

Systematics due to the choice of the fit model	
Fit bias on $R^{-1}_{K\pi\pi}$	1.0%
Signal shape fixed from MC	0.5%
μ^{shift} and σ_{scale} fixed from resonant modes	TBE
Part-reco shape model (KDE vs Argus×Gauss)	0.3%
Part-reco shape extraction (from $K\pi\pi\pi ee$)	1.7%
s^{PR} constraint choice ($\mu = 0.44$)	1.9%
s^{PR} constraint choice ($\sigma = 50\%$)	0.1%
Empirical $h_{\to\ell}$ misID shape	6.0%
Constrain $h_{\to\ell}$ misID yields	0.3%
Fixed J/ψ -leakage yield	TBE
Combinatorial shape	TBE
Systematics due to the efficiency computation	
Phase-space corrections (variants with angles and $K\pi\pi\gamma$)	6%
PID resampling (calibration samples size)	5%
PID resampling (kernel width)	5%
B^+ kin&mult corrections (TIS vs TOS)	TBE
B^+ kin&mult corrections (`nTracks` vs `nVeloTracks`)	TBE
L0 corrections (binning vs fit turn-on curve)	TBE
L0 corrections (factorisation of TOS responses)	TBE
$m(ee)$ smearing corrections (average among TOS and TIS)	TBE
$m(ee)$ smearing corrections (different signal shape)	TBE
$r_{J/\psi}$ flatness	5%

4.9 Outlook

All the experimental steps towards the measurement of the $R^{-1}_{K\pi\pi}$ ratio have been detailed in the previous sections. The analysis has been shown to be robust both in terms of the computation of the efficiency, where possible disagreements between simulation and data have been thoroughly corrected for, and of the statistical procedure used to extract the signal yield, where the model used to fit the B^+ invariant mass line shape has been proven to provide unbiased estimations. The expected sensitivity of the measurement was shown to be of $\sim 12\%$.

The $R^{-1}_{K\pi\pi}$ value quoted in the thesis, $R^{-1}_{K\pi\pi} = 2.83 \pm 0.34$, where the uncertainty is only statistical, was multiplied by an unknown random factor. The analysis is in fact currently undergoing review within the LHCb collaboration, and the permission to unblind the final $R^{-1}_{K\pi\pi}$ value will only be granted after any additional checks requested by the collaboration are performed. Moreover, the measurement of $R^{-1}_{K\pi\pi}$ will be performed after fulfilling a series of unblinding steps, in order to ensure the absence of any artificial bias in the data analysis procedure. The unblinding steps are mainly aimed at checking the consistency of the result among the different run periods and trigger categories, and the compatibility of the measured $B^+ \to K^+\pi^+\pi^-\mu^+\mu^-$ branching fraction with the the one published by the LHCb collaboration using data collected in the `Run1` period [79]. Finally, all the missing systematic uncertainties, which are expected to play a minor role given the statistic uncertainty of the measurement, will be evaluated during the review process.

5 Conclusions

E quindi uscimmo a riveder le stelle.

— Inferno, canto XXXIV, vv 139

An *indirect* search for New Physics beyond the Standard Model was presented in this thesis, which aims at testing the lepton flavour universality of the SM by measuring the ratio $R_{K\pi\pi}$. The measurement considers the hadronic $K^+\pi^+\pi^-$ system in an inclusive way, *i.e.* by not selecting any of the several resonances contributing to the system. $R_{K\pi\pi}$ will be the first inclusive LFU ratio, and will thus provide complementary information, with respect to the other ratios, on the spin structure of possible new particles. In addition, the analysis will provide the first observation of the $B^+ \to K^+\pi^+\pi^- e^+ e^-$ decay mode.

The procedure towards the measurement of $R_{K\pi\pi}$ consists of several steps, described in great detail in this thesis.

First, the selection of signal candidates was presented, where the requirements to isolate $B^+ \to K^+\pi^+\pi^-\ell^+\ell^-$ decays, with $\ell = e, \mu$, from the environment generated by the pp collision were optimised for the electron mode, which suffers the most from limited event yield.

The efficiency of the event selection was then computed using simulated samples, which undergo a series of correction steps in order to reduce the differences between simulation and data samples. Among the correction steps, one of the novelties of this analysis was described, namely the procedure to correct the mass spectra of the $K^+\pi^+\pi^-$ hadronic system.

The correctness of the whole calibration procedure was tested by taking the $r_{J/\psi}$ and $R_{\psi(2S)}$ ratios, which were shown to be compatible with unity for all the subsets of data taking periods and trigger categories considered in the measurement.

Finally, the yields of the signal modes were extracted by means of an unbinned maximum likelihood fit to the reconstructed B^+ invariant mass line shape. The fit was performed si-

multaneously for the signal and for the normalization decay modes. The event selection efficiencies were included in the fit, in order to extract directly the $R^{-1}_{K\pi\pi}$ value as a parameter of the fit model. One of the biggest challenges in the fit procedure was to model the background coming from partially reconstructed B^+ decays. The strategy adopted, which was developed during this PhD, consists in estimating the line shape and the amount of this contribution from $B^+ \to K^+\pi^+\pi^- J/\psi\,(\to \ell^+\ell^-)$ events. In addition, the background coming from the misidentification of a hadron as an electron was studied by implementing a method known as `PassFail`.

The estimated sensitivity of the $R^{-1}_{K\pi\pi}$ measurement was shown to be $\sim 12\%$, but the $R^{-1}_{K\pi\pi}$ value is kept *blinded*, until the LHCb collaboration gives permission to *unblind* it following the successful completion of the review procedure, which is currently ongoing.

The statistical uncertainty, driven by the limited event yield available in the electron mode, is the dominant uncertainty of the measurement, as is the case for all the other LFU ratios mediated by a $b \to s\ell\ell$ quark-level transition measured by the LHCb collaboration. For this reason, it is of crucial importance to fully exploit the data that will be collected by the LHCb detector during the future periods of the LHC. As discussed in the thesis, the detector underwent major changes during the past years, in order to operate at increased luminosity during the `Run3` and the `Run4` periods. Among the upgrades, the most impactful for measurements with $b \to s\ell\ell$ decays will be the removal of the hardware trigger stage, that has been the limiting bottleneck for the collection of events with electrons during Runs 1 and 2. This, together with the complete upheaval of the tracking system (to which I contributed during the PhD), will grant the ability to collect up to $50\,\text{fb}^{-1}$ by the end of `Run4`, which will help in reducing both the statistical and the systematic uncertainties due to data-driven models, leading to an unprecedented precision for flavour measurements.

In addition, independent measurements of the LFU ratios are expected from the CMS [47] and from the Belle II [100] collaborations, the latter with an estimated precision of few percent with $50\,\text{ab}^{-1}$ of data collected, thus with completely different experimental setups and analysis strategies, which will be fundamental in order to confirm or disprove the current LFU picture.

These, together with the $R_{K\pi\pi}$ measurement and all the other previous and foreseen LFU ratios measurements of LHCb, demonstrate the crucial role of the flavour measurements in the indirect searches for New Physics scenarios.

A MVA sensitivity studies

A comparison of the performance of the nominal MVA for the electron modes, which includes the lower mass sideband in the training procedure ($4700\,\text{MeV}/c^2 < m(K^+\pi^+\pi^-\ell^+\ell^-) < 4900\,\text{MeV}/c^2$) with an alternative MVA ($\text{bdt}_{\text{OneSb}}$), where the training uses only the upper mass sideband, is described in this section. With the same procedure described in Section 4.3.5, an optimal selection value of $\text{bdt}_{\text{OneSb}} > 0.994$ is found for such MVA.

The performance of the two MVAs is validated in pseudoexperiments. Toy datasets are generated, a fit to the B^+ invariant mass is performed on these datasets, and the pull distribution for the parameter describing the yield of the rare mode is studied. These studies only use the `Run2p1` and `Run2p2` data samples for the electron mode, split in trigger categories. In order to produce realistic and unbiased toy datasets, instead of using the parameters obtained from the fits to the invariant mass of the rare modes (described in Section 4.6.2) as starting parameters to generate the toy datasets, we use the quantities estimated from fitting the resonant decay channels, as explained below. As an example, the numbers quoted in the following for the different component estimations refer to the TOS sample.

- The **signal yield** is computed as:

$$\mathcal{N}^{\text{est}}\left(B^+ \to K^+\pi^+\pi^-\ell^+\ell^-\right) = \mathcal{N}\left(B^+ \to K^+\pi^+\pi^- J/\psi\,(\to \ell^+\ell^-)\right) \cdot \frac{\varepsilon_{\text{rare}}}{\varepsilon_{J/\psi}} \cdot \frac{\mathcal{B}(\text{rare})}{\mathcal{B}(J/\psi)},$$

  where $\mathcal{N}\left(B^+ \to K^+\pi^+\pi^- J/\psi\,(\to \ell^+\ell^-)\right)$ is the signal yield of the resonant channel, as derived in Section 4.6.1, scaled by the efficiencies of the rare and the resonant selections, computed as shown in Section 4.5 without any correction applied to the MC samples, and corrected by the ratio between rare and resonant branching ratios. The estimated signal yields are 39.6 ± 0.5 in `Run2p1` and 71.9 ± 0.7 in `Run2p2` for the nominal BDT, and 36.6 ± 0.6 in `Run2p1` and 66.7 ± 0.1 in `Run2p2` for the BDT trained using only the upper B^+ mass sideband as proxy for the combinatorial background.

Table A.1: Inverse intervals of BDT requirements considered to estimate the value of the combinatorial slope used to generate the pseudoexperiments.

bdt	$\text{bdt}_{\text{OneSb}}$
$\in [0.70, 0.75]$	$\in [0.80, 0.85]$
$\in [0.75, 0.80]$	$\in [0.85, 0.90]$
$\in [0.80, 0.85]$	$\in [0.90, 0.95]$

- The background yield from **partially reconstructed** B decays is estimated as:

$$\mathcal{N}^{\text{est}}(\text{PR}) = s^{\text{PR}}(J/\psi) \cdot \mathcal{N}^{\text{est}}\left(B^+ \to K^+\pi^+\pi^-\ell^+\ell^-\right),$$

  where $s^{\text{PR}}(J/\psi)$ is the ratio between the yields of partially reconstructed background and signal observed in the resonant mode. As explained in Section 4.6.2, this parameter is extracted from a simultaneous fit of the J/ψ-constrained B mass $m^{J/\psi}(K\pi\pi\ell\ell)$ line shape among all data-taking periods, sharing the same s^{PR}. The estimated yield of background from partially reconstructed decays is 14.2 ± 0.8 in `Run2p1` and 25.7 ± 1.5 in `Run2p2` for the nominal BDT, and it is 17.6 ± 0.9 in `Run2p1` and 32.0 ± 1.7 in `Run2p2` for $\text{bdt}_{\text{OneSb}}$.

- The ***J*/*ψ*-leakage** contribution is described in Section 4.3.4, and it is found to be 6.59 ± 0.13 in `Run2p1` and 13.0 ± 0.14 in `Run2p2` for the nominal BDT, and 8.26 ± 0.13 in `Run2p1` and 19.54 ± 0.19 in `Run2p2` for $\text{bdt}_{\text{OneSb}}$ (here, MC corrections have not been used to estimate the efficiencies).

- The **combinatorial slope** is extracted from fits to the $m(K\pi\pi\ell\ell)$ distribution in the mass window used for the rare mode *i.e.* $[4900, 5600]$ MeV/c^2 (described in Section 4.6.2), where the signal contribution is removed by applying inverse BDT requirements. Three intervals of BDT values are considered, in order to understand the trend of the slopes for increasingly tighter BDT requirements. The intervals are detailed in Table A.1, where different intervals are chosen for the two MVAs due to the different efficiencies of the two BDT requirements. The signal and partially reconstructed background contributions in these inverse BDT intervals can be estimated as described previously, from fits to the resonant channels performed in the same intervals. These two contributions are found to be negligible for all the intervals and thus the only expected contributions remain the combinatorial background, modelled as an exponential, and the J/ψ-leakage (with yield and shape fixed as described in Section 4.3.4).
  The fits are shown in Figure A.1, for the two BDTs. The slopes extracted in all the intervals are listed in Table A.2. The combinatorial slopes obtained using the three intervals are found to be compatible with each other. Therefore, value from the interval closest to the nominal BDT requirement is retained and it is used to generate the toy datasets.

- The **combinatorial** background contribution is estimated by counting the remaining events in the invariant mass range once the signal, partially reconstructed background

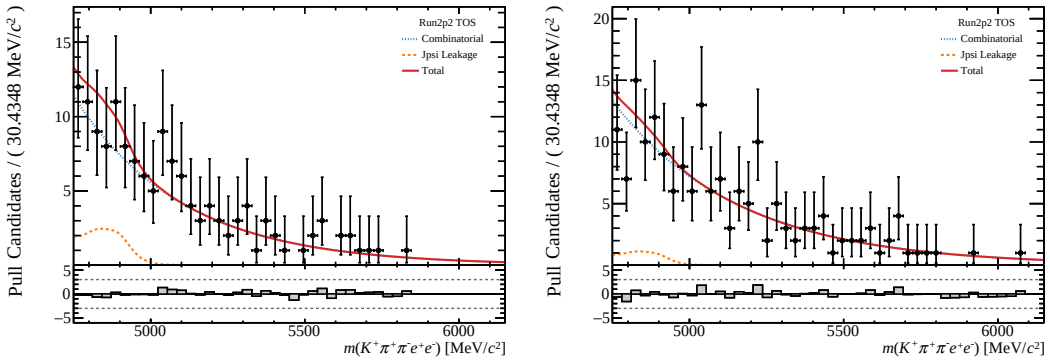

Figure A.1: Fits to the $m(K\pi\pi\ell\ell)$ line shape, where the signal is removed using an inverted cut on the BDT. The fits are shown for the nominal BDT (left), in the bdt $\in [0.75, 0.80]$ range, and for the alternative one (right), in the $\text{bdt}_{\text{OneSb}} \in [0.80, 0.85]$ range. Both fits are performed on the Run2p2 dataset. From these fits, the slope of the combinatorial model is estimated, which is then used to initialize the pseudo-experiments.

Table A.2: Combinatorial slopes in each BDT interval extracted from fits to the $m(K\pi\pi\ell\ell)$ distributions in the rare mode mass window, for Run2p1 and Run2p2 (examples of the fits are shown in Figure A.1).

Parameters	$0.70 < \text{bdt} < 0.75$	$0.75 < \text{bdt} < 0.80$	$0.80 < \text{bdt} < 0.85$
τ^{exp} - Run2p1	$(-2.62 \pm 0.36) \times 10^{-3}$	$(-3.39 \pm 0.38) \times 10^{-3}$	$(-2.96 \pm 0.36) \times 10^{-3}$
τ^{exp} - Run2p2	$(-3.15 \pm 0.31) \times 10^{-3}$	$(-2.86 \pm 0.31) \times 10^{-3}$	$(-2.56 \pm 0.24) \times 10^{-3}$
Parameters	$0.80 < \text{bdt}_{\text{OneSb}} < 0.85$	$0.85 < \text{bdt}_{\text{OneSb}} < 0.90$	$0.90 < \text{bdt}_{\text{OneSb}} < 0.95$
τ^{exp} - Run2p1	$(-2.85 \pm 0.35) \times 10^{-3}$	$(-2.62 \pm 0.31) \times 10^{-3}$	$(-2.99 \pm 0.28) \times 10^{-3}$
τ^{exp} - Run2p2	$(-2.46 \pm 0.26) \times 10^{-3}$	$(-2.46 \pm 0.24) \times 10^{-3}$	$(-2.82 \pm 0.22) \times 10^{-3}$

and J/ψ leakage contributions, obtained in the previous points, are removed:

$$\mathcal{N}^{\text{est}}(\text{comb}) = \mathcal{N}_{tot}(\text{mass range}) - \mathcal{N}^{\text{est}}(\text{rare}) - N^{\text{est}}(\text{PR}) - N(J/\psi^{leak}).$$

The estimated yield of combinatorial background is 108 ± 13 in Run2p1 and 131 ± 15 in Run2p2 for the nominal BDT, and it is 124 ± 14 in Run2p1 and 149 ± 16 in Run2p2 for the alternative one.

1000 toy datasets are generated by poissonianly fluctuating all the contributions detailed above. These datasets are then fitted with the nominal mass fit model extensively described in Section 4.6.2. The pull values for the signal yield for the nominal BDT are Gaussian-distributed, with $\mu = 0.019 \pm 0.032$ and $\sigma = 1.017 \pm 0.023$ for Run2p1, and $\mu = 0.063 \pm 0.031$ and $\sigma = 0.987 \pm 0.022$ for Run2p2. For the alternative BDT, the pulls are Gaussian-distributed with $\mu = 0.071 \pm 0.033$ and $\sigma = 1.045 \pm 0.023$ for Run2p1, and $\mu = 0.047 \pm 0.035$ and $\sigma = 1.021 \pm 0.025$ for Run2p2. Thus, both alternatives exhibit pulls with mean values compatible with zero and sigma values

compatible with unity within $\sim 2\sigma$. The sensitivity of the final measurement can be estimated by using the mean and standard deviation of the pull of the electron signal yield parameter, and by estimating the muon signal yield from the resonant mode (scaling the resonant yield by the ratio between rare and resonant efficiencies, as discussed above). These yield estimates, as well as the expected sensitivities, are shown in Table A.3, which lists the results obtained on the TOS and TIS samples separately. The estimated gain in sensitivity drove the choice to retain the nominal BDT classifier, *i.e.* the one trained using both upper and lower B^+ mass sidebands as proxy for the combinatorial background.

Table A.3: Estimation of the $R_{K\pi\pi}$ sensitivity for the two MVAs, calculated using the average signal yield obtained from pseudoexperiments $\mathcal{N}_{ee}$ and estimating $\mathcal{N}_{\mu\mu}$ by scaling the resonant yield by the ratios of efficiencies and branching ratios of the rare and resonant modes.

Nominal bdt	$\mathcal{N}_{ee}$	$\mathcal{N}_{\mu\mu}$	σ_R/R		
Run2p1 - TOS	41 ± 16	130 ± 13	47%	40%	22%
Run2p1 - TIS	29 ± 11	81 ± 10	49%		
Run2p2 - TOS	74 ± 18	242 ± 18	31%	25%	
Run2p2 - TIS	56 ± 15	173 ± 15	34%		
$\text{bdt}_{\text{OneSb}}$	$\mathcal{N}_{ee}$	$\mathcal{N}_{\mu\mu}$	σ_R/R		
Run2p1 - TOS	39 ± 18	130 ± 13	47%	47%	27%
Run2p1 - TIS	26 ± 12	81 ± 10	49%		
Run2p2 - TOS	69 ± 22	242 ± 18	31%	33%	
Run2p2 - TIS	55 ± 18	173 ± 15	34%		

It has to be noted that this is not the real sensitivity expected from the measurement, since it is computed using only estimations derived from the resonant modes. A proper assessment of the $R^{-1}_{K\pi\pi}$ sensitivity is performed in Section 4.6.2, using pseudoexperiments from the actual signal and background fitted yields.

Bibliography

[1] CMS collaboration, S. C. *et al.* , *Observation of a new boson at a mass of 125 GeV with the CMS experiment at the LHC*, Physics Letters B **716** (2012) 30.

[2] ATLAS collaboration, G. Aad *et al.* , *Observation of a new particle in the search for the Standard Model Higgs boson with the ATLAS detector at the LHC*, Physics Letters B **716** (2012) 1.

[3] C. Burgard, *Standard Model of physics programmed in TikZ*, https://texample.net/tikz/examples/model-physics/, 2016. Accessed: 2022-05-20.

[4] E. Noether, *Invariante variationsprobleme*, Nachrichten von der Gesellschaft der Wissenschaften zu Göttingen, Mathematisch-Physikalische Klasse **1918** (1918) 235.

[5] ALEPH and DELPHI and L3 and OPAL and LEP Electroweak Working Group, S. Schael *et al.* , *Electroweak measurements in electron–positron collisions at W-boson-pair energies at LEP*, Physics Reports **532** (2013) 119.

[6] ALEPH and DELPHI and L3 and OPAL and SLD Collaborations and LEP Electroweak Working Group and SLD Electroweak Group and SLD Heavy Flavour Group, S. Schael *et al.* , *Precision electroweak measurements on the Z resonance*, Physics Reports **427** (2006) 257.

[7] PiENu Collaboration, Aguilar-Arevalo *et al.* , *Improved Measurement of the* $\pi \to e\nu$ *Branching Ratio*, Phys. Rev. Lett. **115** (2015) 071801.

[8] NA62 collaboration, Lazzeroni C. *et al.* , *Precision Measurement of the Ratio of the Charged Kaon Leptonic Decay Rates*, Physics Letters B **719** (2013) 326.

[9] KEDR collaboration, V. M. Aulchenko *et al.* , *Measurement of the ratio of the lepton widths* $\Gamma_{ee}/\Gamma_{\mu\mu}$ *for the* J/ψ *meson*, Physics Letters B **731** (2014) 227.

[10] Particle Data Group, P. A. Zyla *et al.*, *Review of particle physics*, Prog. Theor. Exp. Phys. **2020** (2020) 083C01.

[11] J. Ellis, M. K. Gaillard, and D. V. Nanopoulos, *A Historical Profile of the Higgs Boson*, 2012. doi: 10.48550/ARXIV.1201.6045.

[12] Planck collaboration, *Planck 2015 results*, A&A, Section Cosmology (including clusters of galaxies) **594** (2016) .

[13] Super-Kamiokande collaboration, Y. Fukuda *et al.*, *Evidence for Oscillation of Atmospheric Neutrinos*, Phys. Rev. Lett. **81** (1998) 1562.

[14] R. Barbieri, C. W. Murphy, and F. Senia, *B-decay anomalies in a composite leptoquark model*, The European Physical Journal C **77** (2016) .

[15] W. Altmannshofer, S. Gori, M. Pospelov, and I. Yavin, *Quark flavor transitions in L_μ - L_τ models*, Phys. Rev. D **89** (2014) .

[16] A. Crivellin, G. D'Ambrosio, and J. Heeck, *Explaining $h \to \mu^\pm\tau^\mp$, $B \to K^*\mu^+\mu^-$, and $B \to K\mu^+\mu^- / B \to Ke^+e^-$ in a Two-Higgs-Doublet Model with Gauged $L_\mu - L_\tau$*, Phys. Rev. Lett. **114** (2015) .

[17] A. Celis, J. Fuentes-Martín, M. Jung, and H. Serôdio, *Family nonuniversal Z' models with protected flavor-changing interactions*, Phys. Rev. D **92** (2015) .

[18] A. Falkowski, M. Nardecchia, and R. Ziegler, *Lepton flavor non-universality in B-meson decays from a U(2) flavor model*, JHEP **2015** (2015) .

[19] M. Gell-Mann and F. E. Low, *Quantum Electrodynamics at Small Distances*, Phys. Rev. **95** (1954) 1300.

[20] LHCb collaboration, R. Aaij *et al.* , *Measurements of the S-wave fraction in $B^0 \to K^+\pi^-\mu^+\mu^-$ decays and the $B^0 \to K^*(892)^0\mu^+\mu^-$ differential branching fraction*, JHEP **11** (2016) 047. 33 p.

[21] LHCb collaboration, R. Aaij *et al.* , *Differential branching fraction and angular analysis of $\Lambda_b^0 \to \Lambda\mu^+\mu^-$ decays*, JHEP **115** (2015) .

[22] LHCb collaboration, R. Aaij *et al.* , *Differential branching fractions and isospin asymmetries of $B \to K^{(*)}\mu^+\mu^-$ decays*, JHEP **2014** (2014) .

[23] LHCb collaboration, R. Aaij *et al.* , *Branching Fraction Measurements of the Rare $B_s^0 \to \phi\mu^+\mu^-$ and $B_s^0 \to f_2'(1525)\mu^+\mu^-$ Decays*, Phys. Rev. Lett. **127** (2021) .

[24] CMS collaboration, *Measurement of the $B_S^0 \to \mu^+\mu^-$ decay properties and search for the $B^0 \to \mu^+\mu^-$ decay in proton-proton collisions at $\sqrt{s}$ = 13 TeV*, `arXiv:2212.10311`.

[25] LHCb collaboration, R. Aaij *et al.* , *Measurement of CP-Averaged Observables in the $B^0 \to K^{*0}\mu^+\mu^-$ Decay*, Phys. Rev. Lett. **125** (2020) .

[26] LHCb collaboration, R. Aaij *et al.* , *Angular Analysis of the $B^+ \to K^{*0}\mu^+\mu^-$ Decay*, Phys. Rev. Lett. **126** (2021) .

[27] Bordone, M. , Isidori, G. & Pattori, A, *On the standard model predictions for R_K and R_{K^*}*, The European Physical Journal C **76** (2016) 440.

[28] LHCb collaboration, R. Aaij *et al.*, *Test of lepton universality in beauty-quark decays*, Nature Phys. **18** (2022) 277, arXiv:2103.11769.

[29] LHCb collaboration, R. Aaij *et al.* , *Search for Lepton-Universality Violation in $B^+ \to K^+\ell^+\ell^-$ Decays*, Phys. Rev. Lett. **122** (2019) .

[30] LHCb collaboration, R. Aaij *et al.* , *Tests of lepton universality using $B^0 \to K^0_S\ell^+\ell^-$ and $B^+ \to K^{*+}\ell^+\ell^-$ decays*, Phys. Rev. Lett. **128** (2022) .

[31] LHCb collaboration, R. Aaij *et al.* , *Test of lepton universality with $B^0 \to K^{*0}\ell^+\ell^-$ decays*, JHEP **2017** (2017) .

[32] LHCb collaboration, R. Aaij *et al.* , *Test of lepton universality with $\Lambda_b^0 \to pK^-\ell^+\ell^-$ decays*, JHEP **2020** (2020) .

[33] LHCb Collaboration, *Measurement of lepton universality parameters in $B^+ \to K^+\ell^+\ell^-$ and $B^0 \to K^{*0}\ell^+\ell^-$ decays*, doi: 10.48550/ARXIV.2212.09153.

[34] Y. Amhis *et al.*, *Averages of b-hadron, c-hadron, and τ-lepton properties as of 2021*, arXiv:2206.07501.

[35] D. Bigi and P. Gambino, *Revisiting $B \to D\ell\nu$*, Phys. Rev. D **94** (2016) .

[36] F. U. Bernlochner, Z. Ligeti, M. Papucci, and D. J. Robinson, *Combined analysis of semileptonic B decays to D and D^*: $R(D^{(*)})$, $|V_{cb}|$, and new physics*, Phys. Rev. D **95** (2017) .

[37] S. Jaiswal, S. Nandi, and S. K. Patra, *Extraction of $|V_{cb}|$ from $B \to D^{(*)}\ell\nu_\ell$ and the Standard Model predictions of $R(D^{(*)})$*, JHEP **2017** (2017) .

[38] The BaBar Collaboration, J. P. Lees *et al.*, *Extraction of form Factors from a Four-Dimensional Angular Analysis of $\overline{B} \to D^*\ell^-\overline{\nu}_\ell$*, Phys. Rev. Lett. **123** (2019) 091801.

[39] G. Martinelli, S. Simula, and L. Vittorio, *$|V_{cb}|$ and $R(D^{(*)})$ using lattice QCD and unitarity*, Phys. Rev. D **105** (2022) 034503.

[40] LHCb collaboration, R. Aaij *et al*, *Measurement of the Ratio of Branching Fractions $\mathcal{B}(\overline{B}^0 \to D^{*+}\tau^-\overline{\nu}_\tau)/\mathcal{B}(\overline{B}^0 \to D^{*+}\mu^-\overline{\nu}_\mu)$*, Phys. Rev. Lett. **115** (2015) 111803.

[41] LHCb collaboration, R. Aaij *et al*, *Measurement of the Ratio of the $B^0 \to D^{*-}\tau^+\nu_\tau$ and $B^0 \to D^{*-}\mu^+\nu_\mu$ Branching Fractions Using Three-Prong τ-Lepton Decays*, Phys. Rev. Lett. **120** (2018) 171802.

[42] LHCb collaboration, R. Aaij *et al.*, *Test of lepton flavour universality using $B^0 \to D^{*-}\tau^+\nu_\tau$ decays with hadronic τ channels*, arXiv:2305.01463.

[43] A. Greljo, J. Salko, A. Smolkovič, and P. Stangl, *Rare b decays meet high-mass Drell-Yan*, 2022. doi: 10.48550/ARXIV.2212.10497.

[44] E. Mobs, *The CERN accelerator complex in 2019. Complexe des accélérateurs du CERN en 2019*, , General Photo.

[45] ALICE collaboration, K. Aamodt, *The ALICE experiment at the CERN LHC*, JINST **3** (2008) S08002.

[46] ATLAS collaboration, G. Aad, *The ATLAS Experiment at the CERN Large Hadron Collider*, JINST **3** (2008) S08003.

[47] CMS collaboration, S. Chatrchyan, *The CMS experiment at the CERN LHC*, JINST **3** (2008) S08004.

[48] LHCb collaboration, R. Aaij *et al.* , *The LHCb Detector at the LHC*, JINST **3** (2008) S08005.

[49] LHCb collaboration, R. Aaij *et al.* , *LHCb Detector Performance*, Int. J. Mod. Phys. A **30** (2015) 1530022.

[50] D. Jacquet and F. Follin, *Implementation and experience with luminosity levelling with offset beam*, 2014. doi: 10.5170/CERN-2014-004.183.

[51] LHCb collaboration, R. Aaij, *Measurements of the B^+, B_0, B_s^0 meson and Λ_b^0 baryon lifetimes*, JHEP **2014** (2014) .

[52] LHCb VELO group, R. Aaij *et al.* , *Performance of the LHCb Vertex Locator*, JINST **9** (2014) P09007.

[53] LHCb Silicon Tracker Group, M. t. Tobin, *The LHCb Silicon Tracker*, Nucl. Instrum. Methods Phys. Res. , A **831** (2016) 174.

[54] C. A. Beteta *et al.*, *Monitoring radiation damage in the LHCb Tracker Turicensis*, JINST **15** (2020) P08016.

[55] LHCb collaboration, B.-M. *et al. LHCb inner tracker: Technical Design Report*, Technical design report. LHCb, CERN, Geneva, 2002. revised version number 1 submitted on 2002-11-13 14:14:34.

[56] LHCb collaboration, B.-M. *et al. LHCb outer tracker: Technical Design Report*, Technical design report. LHCb, CERN, Geneva, 2001.

[57] M. Adinolfi *et al.*, *Performance of the LHCb RICH detector at the LHC*, The European Physical Journal C **73** (2013) .

[58] I. Machikhiliyan and L. calorimeter group, *The LHCb electromagnetic calorimeter*, Journal of Physics: Conference Series **160** (2009) 012047.

[59] R. I. Dzhelyadin, *The LHCb hadron calorimeter*, Nuclear Instruments and Methods in Physics Research Section A: Accelerators, Spectrometers, Detectors and Associated Equipment **494** (2002) 332, Proceedings of the 8th International Conference on Instrumentatio n for Colliding Beam Physics.

[60] E. P. Olloqui and (on behalf of the LHCb Collaboration), *LHCb Preshower(PS) and Scintillating Pad Detector (SPD): Commissioning, calibration, and monitoring*, Journal of Physics: Conference Series **160** (2009) 012046.

[61] A. A. A. Jr *et al.*, *Performance of the LHCb muon system*, JINST **8** (2013) P02022.

[62] F. Archilli *et al.*, *Performance of the Muon Identification at LHCb*, JINST **8** (2013) P10020.

[63] R. Aaij *et al.*, *The LHCb trigger and its performance in 2011*, JINST **8** (2013) P04022.

[64] LHCb collaboration, *Trigger schemes*, http://lhcb.web.cern.ch/lhcb/speakersbureau/html/TriggerScheme.html.

[65] LHCb collaboration, R. Aaij *et al.*, *A Comparison of CPU and GPU Implementations for the LHCb Experiment Run 3 Trigger*, Computing and Software for Big Science **6** (2021) 1.

[66] G. Dujany and B. Storaci, *Real-time alignment and calibration of the LHCb Detector in Run II*, J. Phys. : Conf. Ser. **664** (2015) 082010.

[67] *LHCb Trigger and Online Upgrade Technical Design Report* , 2014.

[68] R. Aaij *et al.*, *Allen: A High-Level Trigger on GPUs for LHCb*, Computing and Software for Big Science **4** (2020) .

[69] LHCb collaboration, *LHCb Tracker Upgrade Technical Design Report* , 2014.

[70] LHCb collaboration, *LHCb VELO Upgrade Technical Design Report* , 2013.

[71] C. Joram *et al.*, *LHCb Scintillating Fibre Tracker Engineering Design Review Report: Fibres, Mats and Modules* , CERN, Geneva, 2015.

[72] S. Jakobsen, *LHCb SciFi: From performance requirements to operational detector. CERN Detector Seminar*, https://cds.cern.ch/record/2814025, 2022.

[73] *WinCC-OA*, https://www.winccoa.com/.

[74] *JCOP framework*, https://jcop.web.cern.ch/.

[75] SciFi collaboration, *SciFi Tracker Controls and Monitoring*, https://edms.cern.ch/ui/file/2060160/0.5/SciFi-controls-design-v0.5_docx_cpdf.pdf.

[76] *Guide for ECS FSM design in LHCb detectors*, https://edms.cern.ch/ui/file/655828/3/LHCb_-ECS_FSM_Guidelines.pdf.

[77] Belle collaboration, H. Guler *et al.*, *Study of the $K^+\pi^+\pi^-$ Final State in $B^+ \to J/\psi K^+\pi^+\pi^-$ and $B^+ \to \psi' K^+\pi^+\pi^-$*, Phys. Rev. D **83** (2011) 032005, arXiv:1009.5256.

[78] G. Isidori *et al.*, *A general effective field theory description of $b \to s l^+ l^-$ lepton universality ratios*, arXiv:2110.09882.

[79] LHCb collaboration, R. Aaij *et al.*, *First observations of the rare decays* $B^+ \to K^+\pi^+\pi^-\mu^+\mu^-$ *and* $B^+ \to \phi K^+\mu^+\mu^-$, JHEP **10** (2014) 064, arXiv:1408.1137.

[80] T. Sjöstrand, S. Mrenna, and P. Skands, *A brief introduction to PYTHIA 8.1*, Computer Physics Communications **178** (2008) 852.

[81] I. Belyaev *et al.*, *Handling of the generation of primary events in Gauss, the LHCb simulation framework*, Journal of Physics: Conference Series **331** (2011) 032047.

[82] D. J. Lange, *The EvtGen particle decay simulation package*, Nuclear Instruments and Methods in Physics Research Section A: Accelerators, Spectrometers, Detectors and Associated Equipment **462** (2001) 152, BEAUTY2000, Proceedings of the 7th Int. Conf. on B-Physics at Hadron Machines.

[83] P. Golonka and Z. Was, *PHOTOS Monte Carlo: a precision tool for QED corrections in Z and W decays*, The European Physical Journal C **45** (2006) 97.

[84] J. Allison *et al.*, *Geant4 developments and applications*, IEEE Transactions on Nuclear Science **53** (2006) 270.

[85] LHCb collaboration, R. Aaij *et al.*, *Test of lepton universality with* $B^0 \to K^{*0}\ell^+\ell^-$ *decays*, JHEP **08** (2017) 055, arXiv:1705.05802.

[86] LHCb collaboration, R. Aaij *et al.*, *Angular analysis and differential branching fraction of the decay* $B_s^0 \to \phi\mu^+\mu^-$, JHEP **09** (2015) 179, arXiv:1506.08777.

[87] G. Ke *et al.*, *LightGBM: A Highly Efficient Gradient Boosting Decision Tree*, in *Advances in Neural Information Processing Systems* (I. Guyon *et al.*, eds.), **30**, Curran Associates, Inc., 2017.

[88] A. Blum, A. T. Kalai, and J. Langford, *Beating the hold-out: bounds for K-fold and progressive cross-validation*, in *Annual Conference Computational Learning Theory*, 1999.

[89] LHCb collaboration, R. Aaij *et al.*, *Precision measurement of the ratio of the* Λ_b^0 *to* $\overline{B}^0$ *lifetimes*, Phys. Lett. **B734** (2014) 122, arXiv:1402.6242.

[90] LHCb collaboration, R. Aaij, C. Abellán Beteta, and Ackernley, *Measurement of the electron reconstruction efficiency at LHCb*, JINST **14** (2019) P11023, arXiv:1909.02957, All figures and tables, along with any supplementary material and additional information, are available at https://cern.ch/lhcbproject/Publications/p/LHCb-DP-2019-003.html (LHCb public pages).

[91] M. Pivk and F. R. Le Diberder, *sPlot: A statistical tool to unfold data distributions*, Nucl. Instrum. Meth. **A555** (2005) 356, arXiv:physics/0402083.

[92] R. Brun and F. Rademakers, *ROOT — An object oriented data analysis framework*, Nuclear Instruments and Methods in Physics Research Section A: Accelerators, Spectrometers, Detectors and Associated Equipment **389** (1997) 81, New Computing Techniques in Physics Research V.

[93] A. Poluektov, *Kernel density estimation of a multidimensional efficiency profile*, JINST **10** (2015) P02011.

[94] A. Poluektov, *Correction of simulated particle identification response in LHCb using kernel density estimation.* , CERN, Geneva, 2017.

[95] A. Poluektov, *Kernel density estimation of a multidimensional efficiency profile*, JINST **10** (2015) P02011, `arXiv:1411.5528`.

[96] A. Rogozhnikov, *Reweighting with boosted decision trees*, Journal of Physics: Conference Series **762** (2016) 012036.

[97] *Measurement of the electron reconstruction efficiency at LHCb*, JINST **14** (2019) P11023.

[98] T. Skwarnicki, *A study of the radiative cascade transitions between the Upsilon-prime and Upsilon resonances*, PhD thesis, Institute of Nuclear Physics, Krakow, 1986, DESY-F31-86-02.

[99] W. Verkerke and D. Kirkby, *The RooFit toolkit for data modeling*, 2003. doi: 10.48550/ARXIV.PHYSICS/0306116.

[100] Belle II collaboration, T. Abe, I. Adachi, K. Adamczyk, and S. Ahn, *Belle II Technical Design Report*, 2010.

Personal Information

ADDRESS Avenue de Mategnin 71, 1217 Meyrin CH

PHONE / EMAIL +41 77 816 76 03 / sara.celani@cern.ch

NATIONALITY Italian

DATE OF BIRTH 07.03.1992

The research I performed during the PhD focuses on Lepton Flavour Universality tests in $b \to s\ell\ell$ decays at LHCb. During the last year I was the responsible of the development of the software interface for the control system of high voltage channels for the new LHCb scintillating fibre tracker. In 2022 I was a representative of the LHCb Early-Career Community. I have been a teaching assistant for several courses: laboratory of nuclear physics for bachelor students and particle physics I and II for master students.

Education

PHD April 2019 - Now

IN PARTICLE PHYSICS École Polytechnique Fédérale de Lausanne

Testing Lepton Universality in $B \to X\ell\ell$ ($X = K\pi\pi$, $\ell = e, \mu$) decays with LHCb

Thesis director: Lesya Shchutska

MASTER'S DEGREE 2015 - 2018

IN PHYSICS Università degli studi di Roma "La Sapienza", final mark: 110/110

A Multivariate Analysis in the Higgs production in association with a top quark pair for the multileptonic final state with two same sign light leptons plus one hadronically decaying tau with the ATLAS detector

Thesis director: Simonetta Gentile

BACHELOR'S DEGREE 2011-2015

IN PHYSICS Università degli studi di Roma "La Sapienza", final mark: 101/110

Study of the Higgs to two muons channel at the International Linear Collider

Thesis director: Simonetta Gentile

Work in arXiv:1603.04718

Teaching experience

INSTITUTION École Polytechnique Fédérale de Lausanne

Summer student supervision, Jul - Aug 2022

Exercise sessions in Particle physics II (Master course), Feb - May 2022

Exercise sessions in Particle physics I (Master course), Sep - Dec 2021

Assistant in Laboratory of nuclear physics (Bachelor course), Oct 2019 - Jun 2021

Scholarships

INSTITUTION Istituto Nazionale di Fisica Nucleare (INFN)

DATES January - April 2018

3 months fellowship at CERN ('La fisica delle particelle per esplorare l'universo')

PROJECT *Study of Yukawa coupling of the Higgs boson with the top quark through the associated production of the Higgs boson with a pair of a top quark and anti-top(ttH) in final state with two same sign light leptons and a hadronic tau*

Schools and Internships

HOME INSTITUTION Swiss Institute of Particle Physics (CHIPP), January 2022
TITLE CHIPP Winter School of Particle Physics 2022

HOME INSTITUTION Autonoma University of MADRID, August 2021
TITLE 6th Summer School INFIERI (INtelligent signal processing for FontIEr Research and Industry)
Best poster Award: *Experimental Strategy to test Lepton Flavour Universality in $b \to s\ell\ell$ decays at LHCb*

HOME INSTITUTION École Polytechnique Fédérale de Lausanne, July 2020
TITLE 6th Summer School Machine Learning in High Energy Physics
Certificate of Excellence

HOME INSTITUTION Royal Holloway University of London
TITLE Summer students funds to study $H \to \mu\mu$ at ILC, July - August 2015

Workshops and Conferences

CONFERENCE BEAUTY 2023 (Clermont-Ferrand, France), July 2023
TALK *Recent results in $b \to s\ell\ell$ transitions,* on behalf of the LHCb collaboration

CONFERENCE ICHEP2022 XLI (Bologna, Italy), July 2022
TALK *Electroweak Penguin decays at LHCb,* on behalf of the LHCb collaboration
(Proceeding published in PoS ICHEP2022 (2022) 736)

CONFERENCE TAU2021 (Indiana University, fully virtual), September 2021
TALK *Lepton Flavour Universality tests and Lepton Flavour Violation searches at LHCb,* on behalf of the LHCb collaboration
(Proceeding submitted to SciPost arXiv:2111.11105)

Internal talks

CONFERENCE 104th LHCb Week - SciFi Parallel Session, June 2022
TALK *SciFi Controls and DAQ*

CONFERENCE 98th LHCb Week, December 2020
TALK *Testing Lepton Flavour Universality with $B \to K\pi\pi\ell\ell$ decays*

Posters

CONFERENCE 148th LHCC Meeting (CERN, fully virtual), November 2021
TITLE *Lepton Flavour Universality test with $B \to K\pi\pi\ell\ell$ decays at LHCb*

CONFERENCE Annual CHIPP meeting, June 2021
TITLE *Testing Lepton Flavour Universality in $b \to s\ell\ell$ decays at LHCb*

CONFERENCE Joint SPS/OePG annual meeting, Zurich CH, August 2019
TITLE *Experimental Strategy to test Lepton Flavour Universality in $b \to s\ell\ell$ decays at LHCb*
Best-poster award

Skills and Competences

RESPONSIBILITIES

April 2020 - April 2022

MonteCarlo simulation liaison for Rare Decays working group

January 2022 - March 2023

LHCb Early Career Representative

2020-2022

Expert in control and monitoring of the high voltage channels for the SciFi tracker

MOTHER tongue: Italian

OTHER LANGUAGE(S)	Listening	Reading	Speaking	Writing	
English	C2	C2	C1	C1	(CAE certificate in 2019)
French	B1	B2	B1	B1	

COMPUTER SKILLS: C, C++, Python, ROOT Software, LaTeX, Linux, WinCC, Microsoft Office

Work Experience

EMPLOYER / ADDRESS: PricewaterhouseCoopers Advisory SpA / Largo Angelo Fochetti, 29, Roma Italy

DATES: October 2018 - March 2019

POSITION: Junior Consultant - Technology Consulting / Digital Transformation

RESPONSIBILITIES: I actively worked on the digitalisation of the public administration of the metropolitan city of Rome. Our aim was to create a Citizenship Relationship Manager easily accessible by the population which included and unified the services provided by the several public systems (civil registry, taxes, school inscriptions etc).

Additional information

VOLUNTEERING: After my father's unexpected death in 2014, I created with my mother and other friends, a voluntary association: we organise sports and cultural events to promote healthy lifestyle, to donate defibrillators to my hometown and to organise CPR (cardiopulmonary resuscitation) courses. I have obtained the license to use defibrillator and practise CPR, released by Italian Red Cross

HOBBIES: I obtained the Diploma in Solfeggio and 5th year diploma in Piano at the Conservatory "Licino Refice" FR, Italy

I practised volleyball for 13 years, and I have been a volleyball trainer for two years (with a teaching qualification, released by the Italian Volleyball Federation). I played also tennis and swimming